

**Supported Nanostructured Materials
with Enhanced Electrode-electrolyte
Interface for High Performance
Supercapacitors and Dye Sensitized
Solar Cell Counter Electrodes**

**Thesis Submitted to AcSIR for the Award of
the Degree of**

**DOCTOR OF PHILOSOPHY
In Chemical Sciences**



By

**Mr. Bihag A. M.
Registration Number: 10CC11J26085**

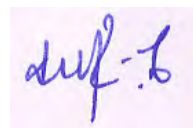
**Under the Guidance of
Dr. Sreekumar Kurungot**

CSIR-National Chemical Laboratory, Pune - 411008, India.

February 2015

CERTIFICATE

This is to certify that the work incorporated in the thesis entitled, “**Supported Nanostructured Materials with Enhanced Electrode-Electrolyte Interface for High Performance Supercapacitors and Dye Sensitized Solar Cell Counter Electrodes**” submitted by **Mr. Bihag A. M.**, has carried out by him under my supervision at the Physical and Materials Chemistry Division, CSIR-National Chemical Laboratory, Pune-411008, India. All the materials from other sources have been duly acknowledged in the thesis.



Date: February 23th, 2015

Dr. Sreekumar Kurungot

Place: Pune, India.

(Research Guide)

DECLARATION

I, hereby declare that all the experiments in this thesis entitled, “**Supported Nanostructured Materials with Enhanced Electrode-Electrolyte Interface for High Performance Supercapacitors and Dye Sensitized Solar Cell Counter Electrodes**” submitted for the degree of Doctor of Philosophy in Chemical Sciences, to the AcSIR-National Chemical Laboratory have been carried out by me at the Physical and Materials Chemistry Division, CSIR-National Chemical Laboratory, Pune-411 008, India, under the supervision of Dr. Sreekumar Kurungot. The work is original and has not been submitted in part or full by me, for any degree or diploma to this or to any other University.



Date: 23-02-2015

Mr. Bihag A. M.

Physical and Materials Chemistry Division,

CSIR-National Chemical Laboratory,

Pune-411 008, India.

ACKNOWLEDGEMENT

At this the juncture of my thesis, I take immense pleasure in thanking each and every one who has contributed for the accomplishment of my doctoral research programme at CSIR-NCL, Pune.

First of all, I would like to express my enormous gratitude to my research supervisor Dr. Sreekumar Kurungot for his cherished guidance, understanding and patience which added considerably to my graduate experience. I am also thankful to him for the freedom he gave while holding me in the right track which made me to realise my dream. Though I examined his patience several times, he made a wonderful research atmosphere during my stay at CSIR-NCL, Pune.

I devote my sincere acknowledgment to Dr. Manohar V. Badiger for his advices and fruitful discussion in the polymer electrolyte part of the thesis. He always inspired me with his energy and smiling face in and outside the lab. At this moment, I would also like to thank his student Arun Torris for the effective research collaboration in solid-state supercapacitors, which still is in continuation. I also would like to mention the warm friendship and the support he offered throughout.

I wish to thank Dr. Satish B. Ogale, for the fruitful collaboration in solar cell research which contributed heavily to my thesis. He helped me by allowing to utilise his excellent research facility and with the stimulating scientific discussions. Here, I am also conveying my gratitude to his student Onkar Game for helping in solar cell characterisations and the scientific discussions which helped me for exploring more on DSSC. Tanya also needs special mention for the help in characterisations of the DSSC systems. I would also like to thank Dhanya, with her I have done some excellent collaborative research on solid-state supercapacitors.

I wish to acknowledge Dr. Sujith K. Ghosh, IISER, Pune, and his students Sanjog, Manna, Jordar, Partha for their effective collaboration on conductivity electrochemical studies of various MOF related materials.

I take this opportunity to convey my regards to the DAC chairman Dr. Pankaj Poddar and members, Dr. B.L.V Prasad and Dr. Ulhas Kharul for all their help, support and suggestions during the PhD coursework evaluations and presentations. Further, I would like to express my sincere thanks to my PhD coursework co-ordinators, Dr. P. A Joy, Dr. Nandini Devi, Dr. Vinod and Dr. Gopinath for their excellent classes and supports during the course work.

I wish to thank Dr. Sourav Pal, Director, CSIR-NCL, for providing me all infrastructural facilities. I would also like to thank Dr. Anil Kumar, Chair, Physical and Materials Chemistry Division, for his constant and encouraging support and for the facilities under the division. I would also take this opportunity to thank the SAC office members for the support. I take this opportunity to thank Dr. K. Vijayamohanan for the fruitful scientific advises. I would also like to mention Dr. Rahul Banerjee, Dr. Suresh Bhatt and Dr. Ajith Kumar for their support.

I take this opportunity to acknowledge Dr. Patil, Sagar and Baba sahib for their help in XPS analysis and also for collaborative works.

I am forever indebted to all my former teachers as they built the foundation of knowledge for these achievements.

My Sincere thanks to all my seniors Sreekuttan, Dr. Beena, Dr. Palani, Joyashish, Dr. Dhanraj and Dr. Kannan. They helped me at the initial stage of my research by mentoring and caring. No words can suffice to acknowledge the friendly and stimulating atmosphere created by my labmates Vishal, Pandi, Santhosh, Harshitha, Siddu, Rajith, Roby, Kashyap, Pritish, Sachin, Sarath, Hari, Vidyanand, Pranav, Maya, Ruhi, Ajinkya, Samprith and Ayasha during my stay at NCL. At this time, I am remembering my friends who left our lab in between Vrushali, Ranjith, Hussain, Bipin, Neeta and Lal. I take time to convey my gratitude to Bhuvaneshwari, Sajina and Neethu who carried out their internship research projects with me.

I also wish to thank my colleagues Sharath, Unni, Joby, Manjunath, Shivakumar, Manzoor, Prabhu, Bishnu, Tanay, Arjith,

Pradip, Shubhadeep, Umesh, Harshal, Anitha, Abhik, and Rohan for creating such wonderful atmosphere around me with their support in and outside the lab and the cherished friendships.

Special gratitude to Leena, Bindu, Anumon, Jijil, Reji, Vijayadas, Sudheesh and Hari chettan for making my life in NCL more wonderful and homely.

I thank Sunil, Kiran, Vyshakh, Eldo, Alson, Rajesh, Nisha, Prajitha, Jaya, Kabeer, Jino, and Rashid for the warm friendship. I wish to thank Sanoop and Shibin along with the other members of G-1 and G-30 for making wonderful and cherished time in NCL.

I express my deep sense of gratitude to my family for the continuous support and affection. I find no word to express my feeling for my vappa and umma for their love, affection and support throughout my life. They were always behind me with all patience that made me to achieve my dreams. My sincere feelings for my sister, "sha" also arose at this time. I remember cherished time with "munnu" and his innocent love and affection.

Words are not sufficient to express my wife Biyas's enormous love, support and understanding. We started a new life together just before I joined for the PhD and she stood behind me with a great amount of patience, love and support.

Though, many have not been mentioned, none is forgotten

Bihag Anothumakkool

List of Abbreviations

Abbreviation	Expansion
0-D	Zero-Dimensional
1-D	One- Dimensional
2-D	Two- Dimensional
3-D	Three- Dimensional
DMII	1, 3-Dimethylimidazolium Iodide
ASSP	All Solid-State Supercapacitor
BDM	Bockhs-Devanathan-Muller
CCF	Conventional Carbon Fiber
CE	Counter Electrode
CNF	Carbon Nanofiber
CNT	Carbon Nanotubes
CP	Conducting Polymers
CPE	Constant Phase Element
CTR	Charge Transfer Resistance
CV	Cyclic Voltammetry
DCM	Dichloromethane
DLM	Diffuse-Layer Model
DMSO	Dimethylsulfoxide
DSSC	Dye Sensitized Solar Cell
EDAX	Energy-Dispersive X-Ray Spectroscopy
EDL	Electrical Double Layer
EDLC	Electrochemical Double Layer Capacitors
EDOT	Ethylenedioxythiophene
EIS	Electrochemical Impedance Spectroscopy

ESCA	Electron Spectroscopy for Chemical analysis
ESR	Electrochemical Series Resistance
EV	Electric Vehicle
FCNF	Functionalization of Carbon Nanofiber
FESEM	Field Emission Scanning Electron Microscopy
FF	Fill Factor
FT	Fourier Transform
FTO	Fluorine Doped Tin Oxide
FWHM	Full Width at Half Maximum
HCNF	Herringbone Carbon Nanofiber
HEV	Hybrid Electric Vehicle
HOMO	Highest Occupied Molecular Orbital
HPLC	High Performance Liquid Chromatography
HR-TEM	High-Resolution Transmission Electron Microscopy
IHP	Inner Helmholtz Layer
IR	Infra-Red
J _{sc}	Short Circuit Current Density
LCV	Linear Sweep Voltammetry
LED	Light Emitting Diode
LIC	Li-Ion Supercapacitor
NMP	N-Methyl-2-Pyrrolidone
OHP	Outer Helmholtz Plane
PANI	Polyaniline
PCNF	Platelet Carbon Nanofiber
PEDOT	Polyethylenedioxythiophene
PEDOT-p	PEDOT Film Impregnated Flexible Paper
PIAS	Polarized Infrared Absorption Spectroscopy

PPy	Polypyrrole
PTFE	Polytetrafluoroethylene
Pth	Polythiophene
PVDF	Polyvinylidenedifluoride
RTIL	Room Temperature Ionic Liquid
SAED	Selected Area Diffraction
SEM	Scanning Electron Microscopy
SSA	Specific Surface Area
TCNF	Tubular Carbon Nanofiber
TEM	Transmission Electron Microscope
TEMABF ₄	Triethylmethylammoniumtetrafluoroborate
TGA	Thermo Gravimetric Analysis
VGCF	Vapour Phase Grown Carbon Fiber
VGCNF	Vapour Phase Grown Carbon Nanofiber
V _{oc}	Open Circuit Voltage
XPS	X-Ray Photoelectron Spectroscopy
XRD	X-Ray Diffraction

Table of Contents

Abstract	1-5
Chapter-1	
Supercapacitor and Dye Sensitized Solar Cell: Importance of Supported Nanostructured Materials for Attaining Efficient Electrochemical Interfaces	6-61
1.1 Introduction	7
1.2 Electrode-Electrolyte Interface	8
1.2.1 Double Layer or Electrical Double Layer (EDL)	8
1.2.2 Different Double Layer Models	9
1.3 Supercapacitor	11
1.3.1 Historical Background	11
1.3.2 Supercapacitor vs. Other Energy Devices.....	13
1.3.3 Applications of Supercapacitor	14
1.3.4 Working Principle of a Supercapacitor	15
1.3.5 Classification of Supercapacitor	17
1.3.5.1 Electrochemical double layer capacitors (EDLCs).....	17
1.3.5.2 Pseudocapacitor	19
1.3.5.3 Hybrid composites	20
1.3.5.4 Asymmetric hybrid	20
1.3.5.5 Li-ion supercapacitor	21
1.4 Challenges of the Supercapacitors.....	21
1.5 Electrode Materials for Supercapacitors	22
1.5.1 Carbon Morphologies.....	22
1.5.1.1 Engineered carbon.....	22
1.5.1.2 Carbon nanotubes	24
1.5.1.3 Carbon fibers and carbon nanofibers	25
1.5.1.4 Graphene	27
1.5.2 Metal Oxides and Hydroxides	28
1.5.3 Conducting Polymers.....	30
1.6 Electrolyte Material	32
1.6.1. Solid Electrolytes	33
1.7 Dye Sensitized Solar Cell	34

1.7.1 Advantages and Challenges of DSSC	36
1.7.2 Mechanism of DSSC.....	37
1.7.3 Efficiency of a Solar Cell	38
1.7.3.1 Factors affecting the efficiency of a DSSC	40
1.8 Counter Electrodes for DSSCs	40
1.8.1 Low Platinum Efforts through Nanostructuring	41
1.8.2 Pt-free Metal Catalyst	41
1.8.3 Metal Compounds	42
1.8.4 Carbon Materials	42
1.8.5 Conducting Polymers.....	43
1.9 Nanostructured Materials.....	44
1.9.1 Supported Nanostructured Materials	45
1.10 1-D Supported Nanostructured Materials for Energy Applications.....	47
1.11 Scope and Objectives of the Present Thesis	51
1.12 References	53

Chapter-2

1-D Confinement of PEDOT Using Hollow Carbon Nanofiber: An Efficient Charge Storage Material with High Catalytic Activity for Tri-iodide Reduction in DSSC

62-100

2.1 Introduction.....	63
2.1.1 PEDOT as a Charge Storage Material	63
2.1.2 PEDOT as a Counter Electrode in Dye Sensitized Solar Cell (DSSC)	64
2.1.3 Solution for the Existing Problems	64
2.2 Experimental Section	65
2.2.1 Materials	65
2.2.2 Functionalization of Carbon Nanofiber (FCNF)	65
2.2.3 PEDOT-FCNF Composite Preparation.....	66
2.2.4 Counter Electrode Preparation	66
2.2.5 Dye Sensitized Solar Cell (DSSC) Fabrication.....	67
2.2.6 Characterization	67
2.2.7 Electrochemical Studies	67
2.3 Result and Discussion.....	70
2.3.1 HR-TEM and SEM Analyses	70

2.3.2 BET-Surface Area Measurements	73
2.3.3 Electrical Conductivity Measurements	74
2.3.4 XRD Analysis	76
2.3.5 Raman Spectroscopy	77
2.3.6 FT-IR Spectra	78
2.3.7 XPS Analysis.....	79
2.3.8 Thermogravimetric Analysis.....	80
2.3.9 Electrochemical Characterization of Charge Storage Properties.....	81
2.3.9.1 Cyclic voltammetry	82
2.3.9.2 Galvanostatic charge-discharge experiments	83
2.3.9.3 Impedance analysis	86
2.3.10 Electrochemical Characterisation of Counter Electrode Activity.....	88
2.3.10.1 Cyclic voltammetry analysis	88
2.3.10.2 Impedance and Tafel analysis	90
2.3.10.3 $I-V$ measurement of DSSC.....	92
2.4 Conclusions	95
2.5 References	97

Chapter-3

Active Interface Tuning Of Solid-State Supercapacitor: Studies with Carbon Fiber Supported Conducting Polymers **101-134**

3.1 Introduction	102
3.2 Experimental Section	103
3.2.1 Materials	103
3.2.2 Preparation of PVA-H ₂ SO ₄ Solutions and Film	104
3.2.3 Synthesis of Polyaniline (PANI)	104
3.2.4 Electrochemical Polymerization of EDOT.....	104
3.2.5 PANI Electrode Preparation	105
3.2.6 Device Fabrication	105
3.2.7 Characterization	106
3.3 Result and Discussion.....	107
Part A. Effect of Mass Loading of PANI in the Relative Electrode-Electrolyte Interface	107
3.3.A1 SEM and EDX Analysis	109
3.3.A2 Electrochemical Characterization	110

Part B: Electrodeposited PEDOT as a Solution for Establishing Enhanced Electrode-electrolyte Interface	117
3.3.B1 SEM and EDX Analysis	118
3.3.B2 Four Probe Conductivity Measurements	121
3.3.B3 Electrochemical Characterization	121
3.4 Conclusions.....	132
3.5 References	133

Chapter-4

Electrochemically Grown MnO₂ Nanowall Forest on a Carbon Fiber Substrate as a Supercapacitor Charge Storage Material **135-152**

4.1 Introduction	136
4.2 Experimental Section	137
4.2.1 Materials	137
4.2.2 Preparation of MnO ₂ Coated Carbon Paper.....	137
4.2.3 Characterization	138
4.2.4 Electrochemical Characterization	138
4.3 Result and Discussion.....	139
4.3.1 SEM and HR-TEM Analysis.....	139
4.3.2 Surface Area Measurements.....	141
4.3.4 Raman, XRD and XPS Spectral Analyses	142
4.3.5 Electrochemical Analysis	143
4.3.6 Application in Solid-State Supercapacitor.....	150
4.4 Conclusion.....	151
4.5 References	152

Chapter-5

Surfactant-Free Interfacial Polymerization of PEDOT through Simple Roll Coating: Scalable Method for Flexible, Conducting Substrate for Energy Conversion and Storage Applications **153-183**

5.1 Introduction	154
5.2 Experimental Section	157
5.2.1 Materials	157

5.2.2 Preparation of the PEDOT Paper.....	157
5.2.3 Preparation of PVA-H ₂ SO ₄ Solution and Film.....	161
5.2.4 Prototype Flexible Supercapacitor Fabrication.....	162
5.2.5 Characterization.....	162
5.2.6 Counter Electrode Characterization.....	163
5.2.7 Dye Sensitized Solar Cell (DSSC) Fabrication.....	163
5.3 Result and Discussion.....	163
5.3.1 Conductivity Studies.....	164
5.3.2 SEM and TEM Analysis.....	165
5.3.3 XRD Analysis.....	167
5.3.4 XPS Analysis.....	167
5.3.5 UV-Visible Spectral Analysis.....	169
5.3.6 Mechanism of Interfacial Polymerization.....	170
5.3.7 Application in Flexible Solid-State Supercapacitor.....	176
5.3.8 Pt- and TCO-Free DSSC Counter Electrode Application.....	181
5.4 Conclusion.....	184
5.5 References.....	185

Chapter-6

Summary and Conclusions 189-196

6.1 Summary.....	190
6.2 Future Prospects.....	195

List of Publication 197-199

Erratum 201

Abstract

Fast decrease of fossil energy along with its inevitable and irreversible detrimental effect on environment makes renewable energy sources as the only *messiah* for sustainable living for a better tomorrow. However, intermittent nature of such renewable energy sources imposes efficient energy storage and converting devices as integral part of the power electronics meant for the renewable energy technologies. Majority of the stationary and portable energy storage and conversion requirements are effectively satisfied by electrochemical devices such as batteries, supercapacitors, dye-sensitized solar cells (DSSCs) etc. Heart of such a system comprises a highly dynamic and augmented electrode-electrolyte interface, which requires facile ionic and electron transport throughout the materials in use. Tunable physical and chemical properties of the electrode materials *via* nanosizing look fascinating due to their possibilities in electrochemical interfaces to address the pertaining issues related to performance and durability. However, nanostructuring typically results in low electric and ionic conductivity along with stability. An ingenious way to overcome the low electric and ionic conductivity along with stability is with the help of a support material which comprises high conductivity and surface area. Among the various supported materials, 1-dimensional (1-D) structure holds superior advantages such as higher surface area with continuous electron path and facile ion transport etc. Such confined conducting fibers/tubes can be utilized to grow active materials with tunable morphology and multifunctional properties along with augment in conductivity, low charge transfer resistance and improved stability. Apart from that, high surface area associated with the 1-D structuring provides easy ion flux and buffer volume between the structures which alleviates the mechanical stress for the materials. The present thesis has successfully addressed some of the issues related to the low electrode-electrolyte interfaces of the charge storage electrodes for the supercapacitors and the counter electrodes (CEs) for DSSCs by utilizing 1-D carbon supported nanomaterials. Further, fabrication of efficient solid-state supercapacitors could be accomplished by extending the same strategy based on the 1-D carbon support owing to its ability to form better interfaces with the gel-polymer electrolytes. Along with the efficient switchover from the liquid- to the solid-state devices, future flexible electronic devices also require system flexibility for supercapacitors and

DSSCs to attain better adaptability during device fabrications. This demands highly efficient and flexible electrode materials, where a breakthrough could be achieved during the work by developing a simple and scalable method for making a highly flexible paper like electrode. The applications of this thin paper like electrode could be validated by fabricating a flexible solid-state supercapacitor and by applying as a flexible counter electrode for DSSC.

The entire thesis is spread into six chapters and an abstract of each chapter is given below:

Chapter-1: This chapter starts with an overview of the double layer structure of the electrode-electrolyte interfaces which is the heart of all electrochemical devices including supercapacitors and dye sensitized solar cells (DSSCs). This is followed by a detailed discussion about supercapacitors, their historical background, working principles, types, challenges, electrode materials, electrolytes etc. Further, a brief introduction is dedicated to DSSCs, followed by a discussion about the counter electrode reactions in DSSC and their mechanism. The above discussion includes a detailed literature survey and discussions devoted to various Pt-free counter electrode catalyst materials and their advantages and disadvantages. The detailed introduction of the supercapacitors and DSSCs follows a general discussion on various potential nanomaterials. The advantages and disadvantages of the nanomaterials as the electrode materials in electrochemical power devices are highlighted in the subsequent section with the help of detailed literature survey. Chapter also puts an effort to introduce more advanced hetero-nanostructured materials including various nano dimensions with detailed discussions by including specific examples from the literature. Finally, potential benefits of 1-D carbon supported materials and their importance in energy devices, especially their abilities to improve the electrochemical activity, charge mobility, stability etc., are also briefed. Based on the above discussions, towards the end of this chapter, scope and objectives of the present thesis are specified.

Chapter-2: In this chapter, a facile, scalable and simple strategy for making 1-D polyethedioxithiophene (PEDOT) by *in situ* polymerization using carbon nanofiber (CNF) as a solid template is reported. The above strategy is unique as it helps the hybrid (CP) to achieve excellent electrochemical properties in terms of high

conductivity and surface area with optimum porosity which make the material to be a potential candidate for supercapacitor and DSSC CE applications. Structure and the interactions of the polymer and π -electron of CNF are explained with detailed physical characterizations such as Raman, XPS and TGA analyses. Further, electrochemical characterizations of CP reveal potential charge storage properties over CNF and PEDOT in terms of high capacitance, cycling stability and excellent retention with high scan rate and current density. This is followed by electrochemical analyses of the tri-iodide catalytic activity of the above material by using cyclic voltammetry, impedance and Tafel techniques which reveal the superior catalytic activity of CP. This improved performance characteristics of the material is further confirmed realistically by deploying the material as a CE in DSSC.

Chapter-3: In this chapter, a novel method to address the low interface and high ESR of solid-state supercapacitor is described. This is achieved by judiciously employing a gel-plasticised ionomer (PVA-H₂SO₄), which is allowed to infiltrate and form a continuous solid matrix within the porous carbon paper substrate which is initially coated with a polymeric (PANI) electro active material. Cross-sectional SEM and elemental mapping reveal that the solid electrolyte was mimicking its liquid counterpart in terms of the interface. This novel strategy could significantly narrow down the difference between the charge storage properties of the solid- and liquid-state supercapacitor devices. The capacitance obtained is much superior than the convention film based solid-state supercapacitor. Using the above experiments, it is able to demonstrate the importance of porosity in the electrode for establishing enhanced interfacial network in solid-state supercapacitors for achieving high charge-storage properties. However, one challenge noticed here was that, at higher mass loading of the electro active material, the performance of the solid-state device becomes inferior to its liquid-state counterpart as the polymer infiltration becomes improper under such conditions. To address this issue, a different strategy of electrodepositing the charge storage material (PEDOT) directly onto a porous carbon current collector is adopted, which ensures a highly reproducible coating of the electro-active material over each carbon fiber backbone. This morphology and the alignment of PEDOT led to an enhanced surface area and electrical conductivity, and the pores in the system enabled effective intercalation of the polymer–gel electrolyte. Consequently, the solid device attained very low internal resistance and a high

specific capacitance for PEDOT even with high mass loading. The performance of the device was consistent even under wide-ranging humidity and temperature conditions.

Chapter-4: This chapter addresses the low electric and ionic conductivity of MnO_2 for their potential applications in supercapacitor. The strategy adopted here is a simple electrochemical deposition of 1-D aligned highly uniform MnO_2 porous nanowalls onto a conducting porous carbon fiber paper without employing any templates. The structure of the material deposited is elucidated by XRD, Raman and XPS analyses. The peculiar growth pattern of the vertical MnO_2 walls, which are microporous concomitantly, provided spacious and accessible corridors along the surface, which act as facile channels for ion transport after the electrolyte filling. At the same time, the carbon fiber backbone helped to overcome the issue of the inherent electrical resistance associated with MnO_2 . Thus, the formed electrode appeared to display higher specific capacitance which is stable in higher current density. Even after continuous cycling, the nanowalls appeared to be structurally stable with no significant degradation in capacitance. Further, the high porosity of the MnO_2 nanowall electrodes is utilised to make an efficient solid-state supercapacitor. Due to the enhanced electrode-electrolyte interface owing to the high porosity of the nanowalls, excellent capacitance could be attained even at high current density conditions with very low ESR.

Chapter-5: A single material possessing both high charge storage property, conductivity and flexibility is promising as it can play the role of both current collector and an electrode material, which results in flexible, lighter, thinner, and cheaper energy devices. This approach is very challenging in the present situation due to the lack of materials which possess the required conductivity, flexibility and capacitance concomitantly. To address this, in this chapter, a novel synthetic strategy is developed to prepare a highly conducting PEDOT phase on flexible cellulose paper formed by inducing surfactant-free interfacial polymerization at the interface of two immiscible liquids. The illustrated process is highly scalable in such a way that very large flexible PEDOT paper can be prepared in 2-3 h under laboratory conditions. The obtained PEDOT-paper possesses efficiently packed π -conjugated chains and increased doping level which are confirmed by following a set of experiments *viz* XRD, XPS, conductivity and UV-visible measurements. This favourable change has been attained by the slow polymerization coupled with the high dielectric constant of

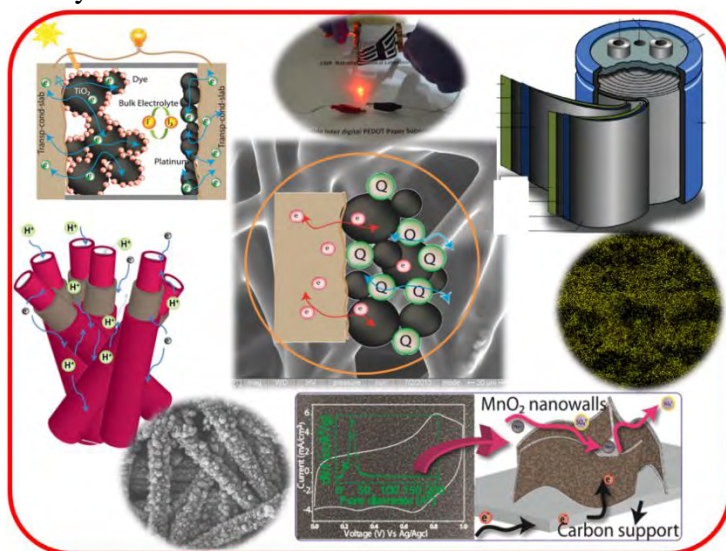
the interface, which stabilises the counter ions through hydrogen bonding. This helps for better inter-chain and intra-chain charge mobility, leading to high conductivity compared to the PEDOT prepared in n-butanol. The low sheet resistance achieved is found to be stable even after two months under ambient conditions and at various flexible and bending conditions. Further, demonstration of a high performance flexible solid-state supercapacitor and flexible DSSC CE could be made by using the PEDOT paper as the electrodes in the respective applications.

Chapter-6: This chapter gives an outline of the main observations and conclusions of the thesis spread in different chapters. Initially, a concise introduction to the present thesis by emphasizing the core theme of the 1-D supported materials is presented. Later, conclusions and main findings of each chapter are overviewed in separate sections. Final part is dedicated to the discussion on the future prospects of the present thesis. This includes importance of the present thesis in terms of materials evolved, device fabrication methodologies and their scope of improvements etc.

Chapter-1

Supercapacitor and Dye Sensitized Solar Cell: Importance of Supported Nanostructured Materials for Attaining Efficient Electrochemical Interfaces

This chapter starts with an overview of the double layer structure of electrode-electrolyte interfaces which is the heart of all electrochemical devices including supercapacitors and dye sensitized solar cells (DSSCs). This is followed by a detailed discussion about supercapacitors, their historical background, working principles, types, challenges, electrode materials, electrolyte etc. Further, a brief introduction is dedicated to DSSCs, followed by a discussion about the counter electrode reactions in DSSC and their mechanism. The above discussion includes a detailed literature survey and discussions devoted to various Pt-free counter electrode catalyst materials



and their advantages and disadvantages. The detailed introduction of the supercapacitors and DSSCs follows a general discussion on various potential nanomaterials. The advantages and disadvantages of the nanomaterials as the electrode materials in electrochemical power devices are highlighted in

the subsequent section with the help of detailed literature survey. Chapter also puts an effort to introduce more advanced hetero-nanostructured materials including various nano dimensions with detailed discussions by including specific examples from the literature. Finally, potential benefits of 1-D carbon supported materials and their importance in energy devices, especially their abilities to improve the electrochemical activity, charge mobility, stability etc., are also briefed. Based on the above discussions, towards the end of this chapter, scope and objectives of the present thesis are specified.

1.1 Introduction

Fast growing energy requirement and simultaneous fossil fuel depletion in the present scenario demand substantial reform in the future energy policies of the countries. Here, renewable energy technologies can play a pivotal role for better living through sustainable growth. Even though, major renewable energy sources such as solar, wind etc. have the potential to fulfil the entire world energy requirement, lack of efficient conversion and storage technologies creates a barrier for this revolution. Among the photo-voltaic technologies, which convert solar energy directly to electrical energy, dye sensitized solar cell (DSSC) seems to be promising over the conventional silicon technologies due to the cheap and easy processable nature. Further, solar energy can be converted into hydrogen fuel by electrolysing water using a photoelectrochemical cell^[1]. Later, the stored hydrogen can be used as fuels for fuel cells to convert it into electricity at the point of demand. However, renewable energies are not constant and reliable, which make them highly difficult to transmit these energies directly to the electrical grids. Low cost electrical energy storage devices, such as various types of batteries and supercapacitors can play a big role here by smoothing the intermittence nature of the renewable energy. Electrochemical supercapacitors or ultracapacitors are very promising at this context over batteries in terms of their high power density. Apart from the grid smoothening, electric vehicle (EV), hybrid electric vehicle (HEV), consumer electronics and various industries also require highly efficient and cheap energy storage systems.

Heart of all the above electrochemical devices like DSSCs, photoelectrochemical cells, fuel cells, supercapacitors, Li-ion batteries etc., is an efficient electrode-electrolyte interface (Figure 1.1). Proficient movement of charges at the electrode-electrolyte interfaces, including ions and electrons during the electrode reaction/adsorption, plays a pivotal role in the efficiency of the above electrochemical devices. Nano sizing of materials^[2], which forms the electrochemical interfaces in the above devices, is promising at this context as it leads to tunable physical and chemical properties. Such property changes are ideal for interfacial reactions as the reactions primarily rely on the relative interface/surface and ionic/electrical conductivity of the material along with an inherent activity. Prime objective of this chapter is thus to explore the aspects of nanostructured materials for making electrodes for efficient

electrochemical power devices by developing ideal electrode-electrolyte interfaces with special emphasis on supercapacitors and DSSCs.

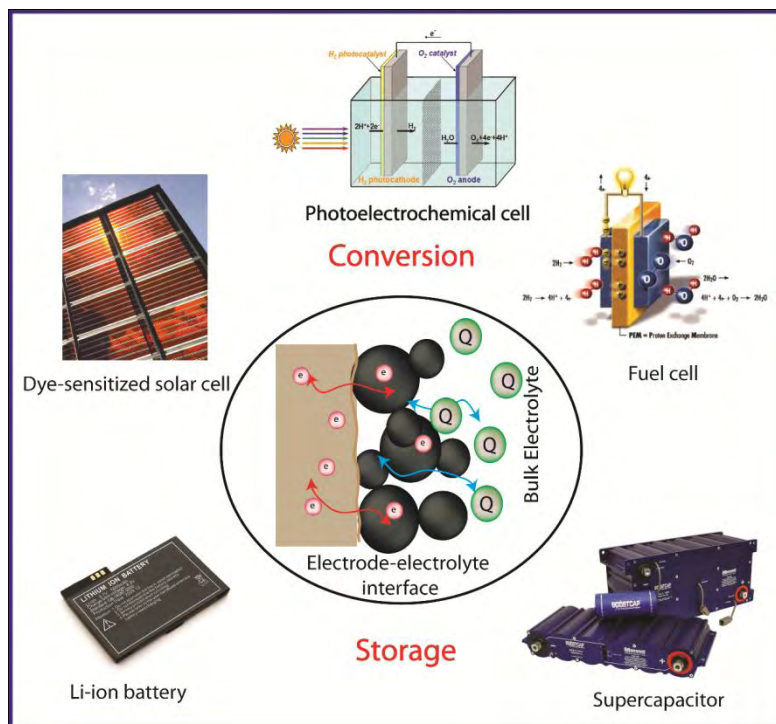


Figure 1.1: Schematics of an electrode-electrolyte interface in the general electrochemical devices.

1.2 Electrode-Electrolyte Interface

1.2.1 Double Layer or Electrical Double Layer (EDL)

Electrical double layer is any boundary between two different phases which are separated by charges. When two different conducting materials are in contact, due to the difference in the surface charges, they undergo redistribution of charges and a potential difference is developed (Figure 1.2). This potential difference between two points is defined as the galvanic potential. Galvanic potential is created by the difference in the chemical forces experienced by the electrons in the surface layer of two metals. In a similar fashion, if two conducting materials, e.g. solid electrode and liquid/solid electrolyte are in contact, the galvanic potential is created.

Such a potential creates a double layer at the interface by the redistribution of the charges. The first layer comprises of ions (positive or negative) adsorbed on the solid surface by chemical interaction, whereas the second layer composed of ions

which are loosely bound by the first layered surface charges. However, as a whole, the interface is electrically neutral. In literature, many models are available for explaining the double layer. However, a single model cannot satisfy all the experimental situations, because the double-layer structure depends on several parameters including electrode material (metals, carbons, semiconductors etc.), porosity of the electrode, electrolyte (solvent, supporting electrolyte, concentration etc.), temperature etc.

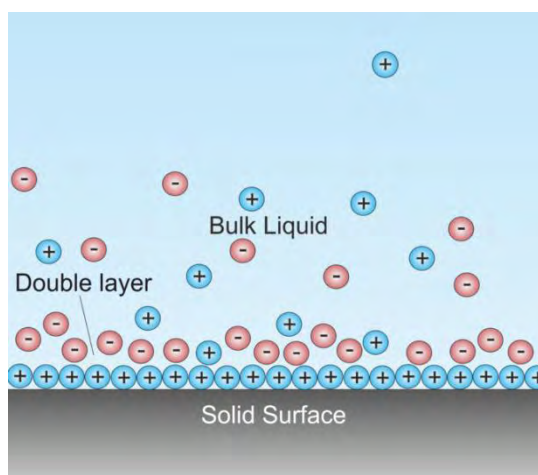


Figure 1.2: Schematics of a double layer formed at an interface of the mobile and stationary phases. (Courtesy: http://en.wikipedia.org/wiki/File:Double_Layer.png)

1.2.2 Different Double Layer Models

Helmholtz^[3] developed the first theoretical model for the double layer. This is a simple approximation that the charges are held by electrostatic forces and are separated by a distance d (Figure 1.3a). This layer is compact and potential linearly drops along the interface. However, this model does not address the effects of thermal motion, ion diffusion, adsorption onto the surface, solvent/surface interactions etc. Later, simple Helmholtz model is further modified and extended by Gouy^[4] and Chapman^[5] and is known as Diffuse-Layer Model (DLM). They considered the thermal and electric field effect on the ions in the electrolyte and thus considered that both types of ions are distributed all over the diffusive layer near to the electrode surface and obeys Maxwell-Boltzmann statistics (Figure 1.3b). However, this model fails especially at higher concentration as it does not consider the ion-ion interaction. Further, this model overlooked the EDL capacitance. Later Stern^[5] combined the Helmholtz model and Gouy and Chapman model to form a unified model. Helmholtz

recognized the electric double layer explicitly in two region of ion distribution, first the inner region is called as the compact or Stern layer and the second is the diffusive layer (Figure 1.3c). Thus, charge at the metal surface, $Q_m = Q_s = q_h + q_g$, where Q_m is the charges at the metal, which is balanced by the total charge at the solution side Q_s , consisting q_h (fixed charge distributed in Helmholtz layer) and q_g (diffusive charge distributed in Gouy and Chapman region). Total EDL capacitance is given, $C_t^{-1} = C_H^{-1} + C_G^{-1}$. In a dilute solution $C_G^{-1} \gg C_H^{-1}$ and therefore, $C_t = C_G$, indicates that it approaches DLM. This model also fails in cases where there is a specific absorbable ion in the electrolyte and further this model does not address the role of solvent [6].

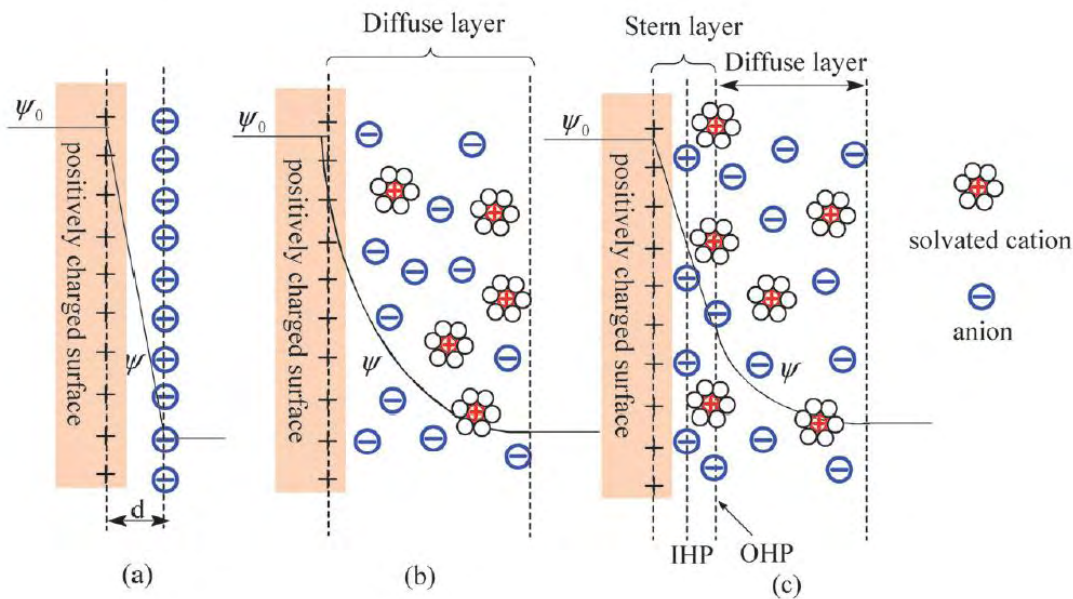


Figure 1.3: Electrical double layer models for a positively charged surface. a) The Helmholtz model, (b) the Gouy–Chapman model and (c) the Stern model, showing the inner Helmholtz plane (IHP) and outer Helmholtz plane (OHP). The IHP refers to the distance of closest approach of the specifically adsorbed ions (generally anions) and OHP refers to that of the non-specifically adsorbed ions. (Reproduced from Ref. [7] with permission of The Royal Society of Chemistry).

Later, Triple-Layer Model or Esin and Markov^[8], Grahame^[9] and Devanathan^[10] Model was proposed, which took in consideration of the specifically adsorbed molecule due to the partial dehydration at the metal surface. Larger ions with few solvent sheaths are preferably absorbed over the smaller ions having larger solvent sheath. In 1963, Bockhs-Devanathan-Muller proposed a model^[11] (BDM), which includes the interaction of solvent in the interface models. According to the above model, there will always be oriented polar solvent molecules, such as water, strongly

held at the metal surface. Because of the competitive adsorption, this layer contains specifically adsorbed ions which are partially hydrated and the centre of the locus of the above ions is called the inner Helmholtz layer (IHP). Adjacent to IHP, a layer of hydrated ions is oriented and the locus centre of this ion is called the outer Helmholtz plane (OHP). The remaining part of the electrolyte which leads to the bulk is the diffusive layer (Figure 1.3c). Later, Sergio Trasatti and Giovanni Buzzanca demonstrated that the specific adsorption of ions in a certain potential range could occur with a charge transfer between the ions and electrodes. This was the first step towards understanding the charge storage mechanism of pseudocapacitive materials. Later, B.E. Conway conducted extensive research on RuO_2 , which helped in understanding the surface reaction and in differentiating the double layer charge storage, pseudocapacitance and battery with each other. Physical and mathematical support for pseudocapacitance was developed by Rudolph A. Marcus. He explained the rate of electron transfer in redox reaction without making or breaking bonds which was initially formulated to account the outer sphere electron transfer.

1.3 Supercapacitor

1.3.1 Historical Background

Supercapacitor, also known as electrochemical capacitor or ultracapacitor, is an energy storage device which stores electricity at its electrode-electrolyte interface. In 1957, H. Becker of General Electric Corp. developed and received first patent for developing the electrolytic capacitor using a porous carbon electrode and it was the first step towards the evolution of the supercapacitor. As the double layer mechanism in electrochemistry was not known at that time, it was believed that the charges were stored in the pores of carbon. Later, Robert A. Rightmire of SOHIO Company developed modern double layer capacitor in 1966 using non aqueous electrolyte and higher surface area carbon. In 1971, Nippon Electric Company Limited (NEC) bought the licence from SOHIO and commercialised the above technology. Its initial application was restricted to backup power for computer memory due to the low energy density. Between 1975 to 1980, Prof. B. E. Conway and co-workers developed RuO_2 based supercapacitors, which helped in gaining the fundamental understanding of the charge storage mechanism inside the supercapacitor. His research led to a new

type of supercapacitor known as pseudocapacitor with high energy density than the double layer capacitors. First successful supercapacitor was marketed in 1978 by Panasonic with a brand name of "Goldcaps". For high power applications, supercapacitor with low internal resistance was developed by Pinnacle Research Institute (PRI) in 1982 for military applications under the brand name "PRI Ultracapacitor". Supercapacitor industry currently is 1000 million dollar worth and is expected to grow to 3.5 billion by 2020. Now the leading manufacturer, Maxwell industries possesses 136 million dollar share in the market (Figure 1.4a). Other major industries include Nippon Electrical Co. (Japan), Nesscap Co. Ltd. (Korea), Cap-XX (Australia), Axion Power International, Inc. (U.S.), Panasonic Electronic Devices Co. Ltd. (Japan) etc.

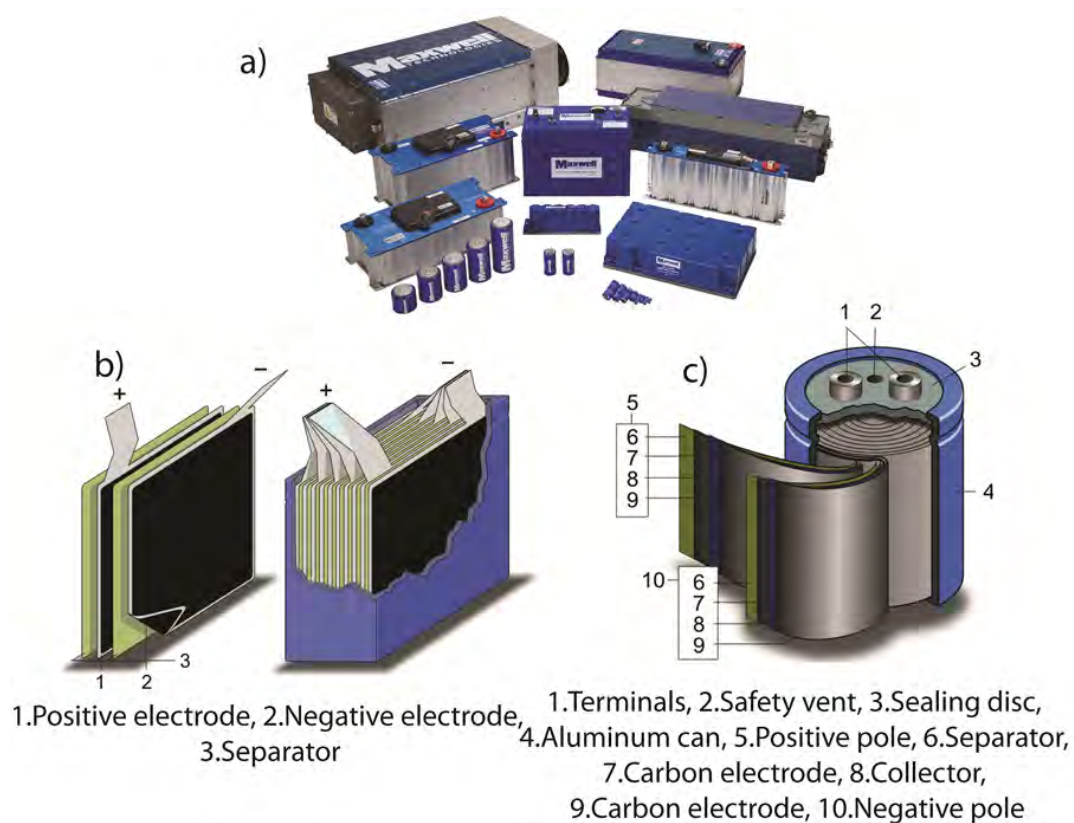


Figure 1.4: a) Different types of supercapacitor range of Maxwell Technologies. Schematic construction of a supercapacitor with b) stacked electrodes and c) wound supercapacitor. (Ref: <http://www.maxwell.com/> and <http://en.wikipedia.org/wiki/Supercapacitor.>)

1.3.2 Supercapacitor vs. Other Energy Devices

Supercapacitors store charges at the electrode-electrolyte interfaces with reversible ion adsorption. Whereas, the conventional capacitors, also known as electrostatic capacitors, store charge electrostatically between two metal plates (electrodes). Due to the low surface area of the plates, they can store only few microfarad and they are commonly used for line filtering and tuning radio frequencies, whereas, supercapacitors store charge at the electrode-electrolyte interface which is $\sim 10^5$ times more than the conventional capacitor. A comparison of power density and energy density is shown in the Ragone plot in Figure 1.5.

When we look at the supercapacitor in the Ragone plot, supercapacitor possesses an intermediate energy density and power density, which bridge the gap between the conventional capacitor and Li-ion battery. Batteries, especially lithium ion batteries^[12], have high energy density, however, they face low cycle life (~ 1000 cycles) and safety related issues due to the usage of Li metal^[13]. On the other hand, supercapacitor is a highly potential

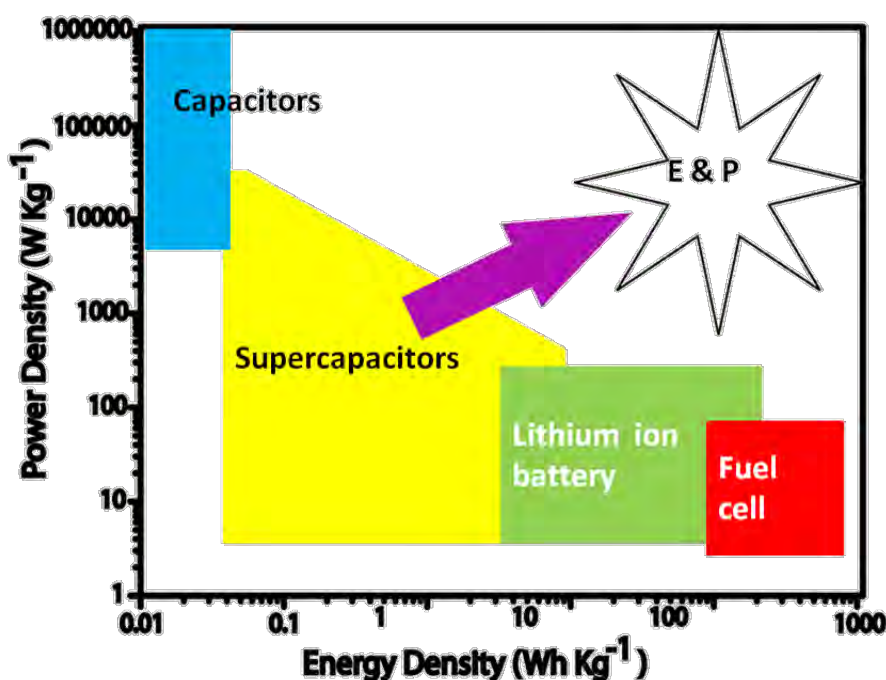


Figure 1.5: Ragone plot, which is a graphical representation of energy density vs. power density of various energy devices.

Table 1.1: Comparison of lithium-ion battery and supercapacitor (source batteryuniversity.com).

Function	Supercapacitor	Lithium-ion (general)
Charge time	1–10 seconds	10–60 minutes
Cycle life	1 million or 30,000h	500 and higher
Cell voltage (V)	2.3 to 2.75	3.6 to 3.7
Working Temperature (°C)	-40 °C to 65	5 to 45
Specific energy (Wh kg⁻¹)	5-10 (typical)	50-100
Specific power (W kg⁻¹)	Up to 10,000	1,000 to 3,000
Cost per Wh	\$20 (typical)	\$0.50-\$1.00 (large system)
Cost per kW	\$ 15-30	\$ 50-150
Service life (in vehicle)	10 to 15 years	5 to 10 years

candidate for energy storage owing to its high power density, extreme long cycle life, coulombic efficiency, varied working temperature range etc. Though current supercapacitors possess low energy density than battery, fast charging capability makes them ideal for replacing even battery as a standalone energy storage device apart from the usual high power required applications coupled with a battery. A comparison of the commercial supercapacitors and lithium batteries is given in **Table 1**.

1.3.3 Applications of Supercapacitor

Even though supercapacitors are known for their high power density, in low energy applications, a supercapacitor has the potential to replace Li-ion battery. Currently, supercapacitor possesses energy density around 5-7 Wh kg⁻¹, compared to 100-200 Wh kg⁻¹ of Li-ion battery. Some of the common applications of the supercapacitor include but not limited to back-up power solution, regenerative power, burst power solutions, quick charge solutions, cold starting solutions etc. Global market growth and forecast diagram is shown in Figure 1.6 along with other energy

devices. Apart from this, supercapacitor shows superior applications in electric vehicles where it works along with Li-ion battery to provide burst power and regenerative energy storage. Here, supercapacitor will substitute the battery at

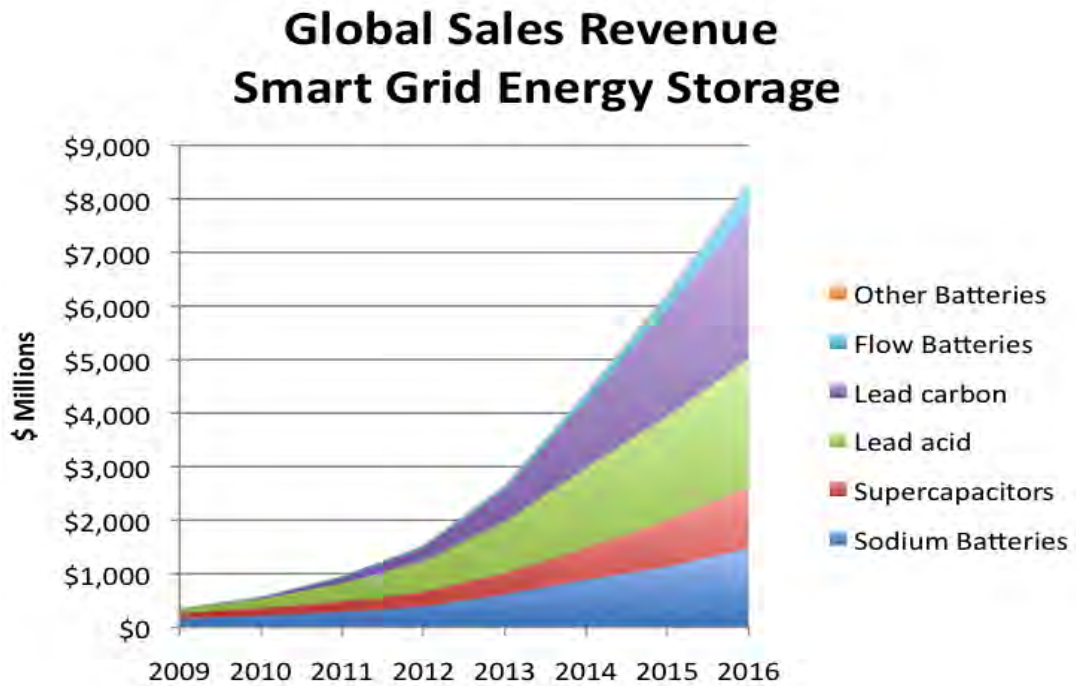


Figure 1.6: Market forecast of the supercapacitor industry along with the other storage devices (Source: altenergystocks.com).

power demanding situations such as power steering, speed up, climbing etc. Apart from this, such substitution improves the cycle life (3-5 times) of the battery, as it avoids deep cycling and fast discharge of the battery. Further, supercapacitor stacks alone can run buses and trams as showed by CSR Zhuzhou Electric Locomotive and Shanghai Sunwin Bus Corporation in China. Here, big supercapacitor stacks are charged in less than 1 minute at stops which are 2-5 km distance apart.

1.3.4 Working Principle of a Supercapacitor

Conventional capacitors, also known as electrostatic capacitors, store charge electrostatically between two metal plates (electrodes) which are separated by an insulating dielectric material. Capacitance stored (C) is related to the charge stored (Q) and voltage (V) applied by the following equation:

$$C = \frac{Q}{V}$$

In a capacitor, C is directly proportional to the area of the plates and inversely proportional to the distance between the plates

$$C = \epsilon_0 \epsilon_r \frac{A}{D}$$

where, ϵ_0 is the dielectric constant of free space and ϵ_r is the dielectric constant of the insulating material between the electrodes. The energy (E) stored and the power (P) in the capacitor are given by the following equations:

$$C = \frac{1}{2} CV^2 \quad \text{and} \quad P = \frac{V^2}{4R}$$

where, R is the resistance of the capacitor.

Working principle of a supercapacitor is very similar to electrostatic capacitors; they store charge or energy at the electrode-electrolyte interfaces with reversible ion adsorption. The dielectric material is replaced by an electrolyte and a separator in supercapacitor. Polarization of the dielectric material during the charging leads to the energy storage in conventional capacitor whereas, polarization at the two electrode-electrolyte interface results in charge storage in supercapacitor. In brief, “Supercapacitors store charges at the electrode-electrolyte interfaces with reversible ion adsorption during the polarization of the electrodes”.

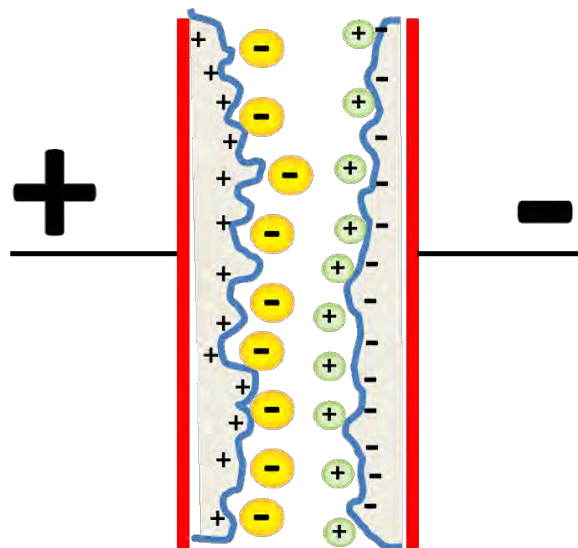


Figure 1.7: A schematic representation of the charge storage process at the two electrode-electrolyte interfaces in a supercapacitor.

Figure 1.7 shows a general picture of the electrode-electrolyte interface of the supercapacitor. Two interfaces are formed at the electrodes and they are similar to two capacitors connected in series. Thus, the capacitance obtained from a supercapacitor will be always half the capacitance of a single electrode interface as per the following equation:

$$C_{total} = \frac{C_1 * C_2}{C_1 + C_2}$$

1.3.5 Classification of Supercapacitor

Supercapacitors are broadly classified as electrochemical double layer capacitors (EDLC) and pseudocapacitors in terms of the charge storage mechanism involved in the systems. There are few other classes of supercapacitors which use one or two of the above charge storage mechanisms in different combinations. Schematic of the classification is shown in Figure 1.8.

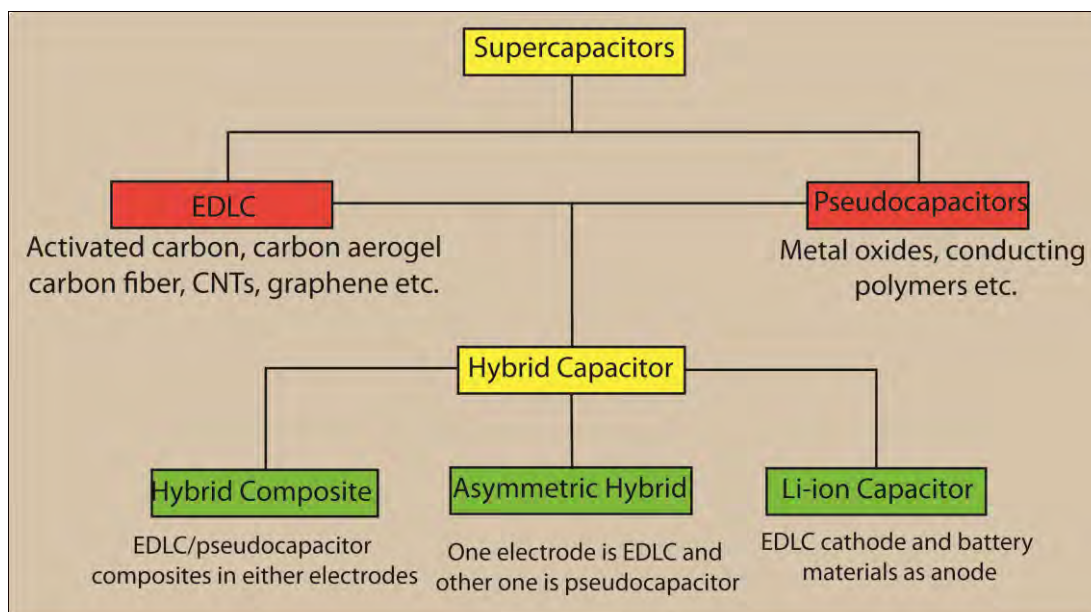


Figure 1.8: Different types of supercapacitors.

1.3.5.1 Electrochemical double layer capacitors (EDLCs)

EDLC normally stores charge electrostatically (non-faradic) at the electrode-electrolyte interface through the double layer formed (Figure 3a) in the Helmholtz region. Ideally, throughout the working potential of the EDLC, the electron transfer does not take place between the electrode and electrolyte and is purely non-faradaic. When a positive potential is applied to one of the electrodes, negative ion from the

electrolyte gets adsorbed on the electrode surface to form a double layer and the exact reverse process happens at the second electrode. Schematics of a double layer formed at a positively charged electrode are shown in Figure 1.3c. As the charge storage in EDLC is based on a surface phenomenon, the process is highly reversible and response time for the double layer changes with potential is very less. Thus, compared to batteries, which rely on redox process, EDLC has huge advantage of its high power density and cycle life. At the same time, as a demerit of the surface phenomena, inaccessible bulk part beneath the surface leads to low energy density. Thus, EDLC shows very low mass specific capacitance of the range of 80-200 F g⁻¹ or 10-50 μF cm⁻² depending on the material and testing methods. This huge values in cm² compared to the metallic capacitor is due to the close charge separation around 3 Å in the compact layer or 1000 Å over the diffusive part of the double layer. If we take an average capacitance of 30 μF cm⁻², *i.e.*, 30 μC V⁻¹ cm⁻², for a carbon surface and an average atom density of 10¹⁵ cm⁻² for a smooth electrode surface, charge accumulated per atom will be 30 x 10⁻¹⁵ μC. Thus, each atom will possess 30 x 10⁻²¹ C /1.6x10⁻¹⁹ C, *i.e.* 0.18 electron per atom in 1 V in EDLC in comparison to 1 electron or higher per atom in the case of the battery electrodes.

As the charge storage is directly proportional to the area of the surface accessible to the ion in the electrode, higher surface area carbon materials (500-3000 m² g⁻¹) are prominent in this class. This includes activated carbon, carbon aerogels, carbon nanotubes, graphene etc^[14]. As the carbon is stable at higher voltage, commercial supercapacitor based on carbon utilises the non-aqueous electrolyte to achieve a high voltage window of 2.5-3.0 V. EDLC normally shows linear charge-discharge characteristics, *i.e.*, voltage drops linearly during charging and discharging, which indicates the negligible contribution of pseudocapacitance. Compared to any other materials, this class is ideal for high power applications due to the low ESR of the device derived from the EDLC materials. Even though EDLC is considered as pure double layer charge storage or non-faradaic, there can be a contribution from non-faradaic charge storage due to the functional groups^[15], doped hetero atoms^[16] etc. present at the surface. Such non-faradic contributions can enhance the total capacitance of the materials, which can be controlled during the synthesis. Further, functionalization with redox molecules^[17] on carbon surface as well in electrolyte^[18] is also being used to improve the capacitance of EDLC.

1.3.5.2 Pseudocapacitor

Working principle of a pseudocapacitor is entirely different from EDLC. In pseudocapacitors, passage of electron across the double layer is involved which results in a current which is faradaic in nature. Thus, charge-discharge mechanism of pseudocapacitor is similar to that of battery to some extent owing to the thermodynamically originated charge storage. Thus, pseudocapacitance is potential dependent and can be ascribed from the comparative cyclic voltametry profile in Figure 1.9. Stored capacitance is thus given by $C_{\phi} = d\Delta q/dV$. Even in EDLC, some extent of pseudocapacitance contributes (1-5 %) towards the total capacitance, depending upon the extent of the functional groups on the surface (in the edge). On the other hand, pseudocapacitor or even battery shows some amount of EDLC (5-10 %), depending upon the ion accessible electrochemical interfacial surface^[19]. Thus, there is no 100 % pseudocapacitance or EDLC in reality, rather one factor dominates over the other depending upon the electrode materials and electrolytes. Some of the common processes which come under the pseudocapacitance are^[20] :

- 1) Redox systems: $Ox + ze^{-} \rightleftharpoons Red$ and $O^{2-} + H^{+} \rightleftharpoons Lattice$, e.g.: conducting polymers
- 2) Underpotential deposition of metal adatoms: $M^{z+} + S + ze \rightleftharpoons SM$ (S = surface lattice sites) or $H^{+} + e^{-} + S \rightleftharpoons SH$.^[21], e.g.: H or Cu on Pt, Pb on Au, H on Pt or Rh etc.
- 3) Intercalation process: $M^{x+} + Li^{+}/Na^{+}/K^{+} \text{ etc} + e^{-} \rightleftharpoons M^{(x-1)}Li/Na/K$, e.g.: MnO_2 , CoO_2 , MoS_2 etc.

Broad class of practically useful pseudocapacitor materials includes metal oxides, conducting polymers etc. Since, faradaic process is involved by molecules in both surface and the bulk near to the surface, pseudocapacitors show enhanced capacitance compared to EDLC. Key highlight of this type of redox materials compared to EDLC is its high mass specific capacitance. Other lineaments include the cheap synthesis cost of many members such as metal oxides (eg. MnO_2) and conducting polymers (e.g. polyaniline). However, due to slow kinetics of the Faradaic process, pseudocapacitors suffer from the low power density compared to EDLC. Apart from the low power density, Faradaic process normally results in low stability due to volume changes during the ions insertion inside the bulk of the materials resulting in phase changes. Further, compared to EDLC, the working potential of

pseudocapacitors is less due to their low redox potential which restricts their improvement in energy density.

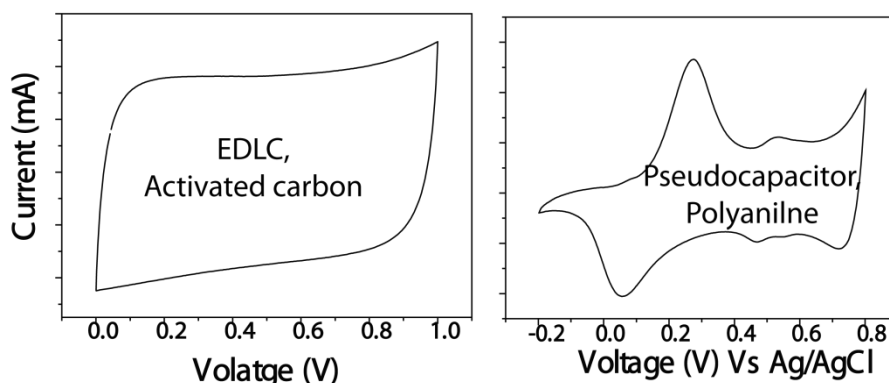


Figure 1.9: Typical cyclic voltammogram profile of the EDLC and pseudocapacitor materials.

1.3.5.3 Hybrid composites

This class comprises of composites of EDLC and pseudocapacitor materials. In general, EDLC materials possess higher SSA and comparable conductivity. Thus, such large SSA of carbon materials is utilised for making hybrid materials with other metal oxides^[22], conducting polymers^[23] etc. Apart from AC, CNT³¹, CNF, graphene^[24] etc. are also been used for making such hybrid materials. Due to the improved conductivity, surface area along with the presence of high capacitance from the pseudocapacitor, composites show superior charge storage properties in terms of low ESR, energy density and power density. Apart from the enhanced charge storage properties, low stability of the pseudocapacitive materials is also addressed by such hybrid materials to some extent^[24-25].

1.3.5.4 Asymmetric hybrid

Asymmetric capacitor is a combination of EDLC and pseudocapacitor materials. However, it is different from the conventional supercapacitor in terms of the cell configuration. It possesses an asymmetric cell configuration in which one electrode is EDLC (commonly -ve electrode) and the other comprises of a pseudocapacitor (+ve electrode). Thus, polarity of the electrode is important as that of a battery^[26]. One of the advantages of this type of combination is the extended voltage window of the cell in an environmental friendly aqueous electrolyte compared to non-aqueous electrolyte such as acetonitrile. Here, neutral salt solutions such as Li₂SO₄, Na₂SO₄, LiCl etc. are used as the electrolytes. Due to the higher over potential for

water decomposition in such electrolytes, a higher working potential of 1.6-1.8 V can be achieved which helps to increase the energy density of the devices^[27]. By proper balancing of the electrode material's mass, stable capacitors with a working voltage as high as 2 V can also be achieved^[28]. Further, superior ionic conductivity of such aqueous electrolytes in comparison to a non-aqueous electrolyte leads to low ESR for the devices. Thus, this class is ideal for high power application with comparable energy density.

1.3.5.5 Li-ion supercapacitor

Li-ion supercapacitor (LIC) utilises the high power density of a supercapacitor and superior energy density of Li-ion battery with judicious combination of the electrodes. Here, Li-battery type electrode is used as the anode and supercapacitor type electrode (EDLC) as the cathode in a Li salt containing electrolyte^[29]. Thus, anode goes through faradaic type intercalation reaction in a wider potential window which boosts the energy density in a non-aqueous electrolyte. At the same time, EDLC at the cathode gives enough power to the device due to its fast charge-discharge capability. Packed LIC shows around 10-15 Wh kg⁻¹ compared to 5-10 Wh kg⁻¹ of supercapacitor. Conventionally, activated carbons (ACs)^[30] are used as the cathode materials while other carbon morphologies like CNT^[31], graphene^[32], carbon fiber etc. have been evolved as the cathode materials in LIC. In the case of the anode materials, Li₄Ti₅O₁₂ (LTO) is the common anode material, due to its high power capability and cycle life. Apart from LTO, metal oxides^[33], graphite^[34] etc. are also being used as the anode materials in LIC.

1.4 Challenges of the Supercapacitors

Current challenges of the supercapacitors are to improve the energy density, power density and working voltage without compromising the cost, safety and environmental friendliness. Currently, supercapacitors possess energy density of around 5-10 Wh Kg⁻¹ which needs to be boosted up to ~50 Wh Kg⁻¹ for high energy stand-alone applications without compromising the power. Energy density can be increased by either improving the capacitance of the electrode material or by extending the potential window. In case of the electrode materials, novel synthetic strategies are required to fine tune the conventional EDLC carbon pore structure for possible improvement. High energy conducting polymers and metal oxides are

promising; at the same time, challenges exist due to low SSA, charge mobility and chemical stability. Higher voltage window can be achieved by utilising new electrolyte materials such as ionic liquids. However, challenges in this case are the low conductivity and viscosity of the ionic liquids which result in low capacitance and high ESR for the devices. For improving the power output, low electrical conductivity of the high SSA electrode materials needs to be addressed to reduce the internal resistance. Further, texturing and designing of novel current collectors are required for achieving low charge transfer resistance. High quality porous membrane with high ionic conductivity is also a major factor which can reduce the ESR of the supercapacitor. Apart from high energy and power densities, safety requires replacement of the volatile liquid electrolytes from the supercapacitor. Hence, polymer electrolyte is a promising alternative in this regard. However, low energy and power density due to the low electrode-electrolyte interface formation and low ionic conductivity while replacing the liquid electrolytes need to be addressed.

1.5 Electrode Materials for Supercapacitors

1.5.1 Carbon Morphologies

Carbon is a marvellous element and is essential to all living systems with vast number of allotropes. Further, by various synthetic strategies, carbon can be tailored in various myriad of structures from bulk to nano regime. They find extreme range of applications in various fields including supercapacitors and can be classified into different types, which depend on their allotropic nature.

1.5.1.1 Engineered carbon

Microporous carbon is the primary electrode material in most of the commercial supercapacitors. It possesses high conductivity and higher SSA which are essential for high power and enhanced charge storage. One of the key advantages of the carbon material is its simple and cheap production from natural abundant, renewable and cheap sources. Apart from these, these types of carbons can be engineered for specific applications through carbon texture/structure and surface modifications. Key qualities of these carbons are high conductivity, SSA range ($1-3000 \text{ m}^2 \text{ g}^{-1}$), good corrosion resistance, higher working voltage (4-5 V), temperature stability, tunable pore structure, relatively low cost, higher processability and

compatibility with other materials in composites^[35].

Generally speaking, higher SSA can accumulate larger amount of the electrolyte at the electrode-electrolyte interface which possibly leads to a larger capacitance. However, in reality, sometimes it is found that the higher SSA carbon possesses less capacitance. This is due to the less efficient utilisation of the much narrowed micropores (< 0.7 nm) due to the ion sieving effect^[14]. Thus, pore distribution also plays a remarkable role in deciding the capacitance. There are mainly three classes of pores, micropores (< 2 nm), mesopores (< 2 - 50 nm) and macropores (> 50nm)^[36]. A schematic of the carbon pore structure is given in Figure 1.10. Proper composition of micropores and mesopores is required in EDLC materials as mesopores help to decrease the diffusion resistance at higher charge-discharge time. In addition, excessive SSA leads to very low density for carbon which creates low conductivity and packing efficiency. Thus, higher SSA with proper pore size and increased conductivity are the critical parameters which need to be engineered during the carbon preparation process. Commercially available carbons for supercapacitor applications, normally known as “engineered carbon”, have an amorphous nature with more or less disordered graphitic microstructure. Amorphous carbons are hexagonal carbon layers or graphene layers with low order in parallel fashion. Whereas in other extent, the graphitised carbon is derived by more ordering and stacking of carbon layers, which is achieved by heat treatments above 2500 °C. Thus, in between the extreme graphitic and amorphous carbon, wide variety of carbon can be prepared with tunable physical and chemical properties for various applications.

In general, carbons are prepared by inert atmosphere mediated heat treatments of carbon rich precursors. Thus, the properties of the derived carbon depend upon the carbon precursors and the process undergone. During the thermal decomposition or pyrolysis, precursors eliminate volatile materials including heteroatom. Further increment in temperature leads to the condensation to form graphitic microcrystalline units. To improve the SSA of the carbon materials, many techniques are available including physical, chemical and catalytic activation. Thermal activation or physical activation is the controlled treatment of carbon with oxidising gases such as steam, CO₂, air or their mixture between 700 °C to 1000 °C^[35]. Such an atmosphere helps to burn off the volatile pyrolysis products which in turn opens up the pores and increases the SSA. Even though increased burn off improves the quality of the carbon, decreased strength, low density and low yield are negative effects of this process. On the other

side, chemical activation^[37] is done at a relatively low temperature of 400 -700 °C by treating with chemicals of dehydrating effects such as H₃PO₄, ZnCl₂, KOH etc. There are other various template assisted methods also available for proper control over the pores. This include, zeolites^[38], silica templates^[39], molecular frameworks etc^[7, 40]. Nevertheless, left over templates and their removal make the process costlier in many of the above materials. However, high control over the pores makes some of the above methods potentially important in many applications. Carbide derived carbon^[41] also is a versatile material which has shown its potential supercapacitor application. Here, metal in the carbide is selectively leached out by halogen treatment at elevated temperature to result in higher SSA carbon with proper pore size distribution^[42].



Figure 1.10: A schematic representation of the activated carbon sphere pore structure and possible EDL formed with the solvated cation.

1.5.1.2 Carbon nanotubes

Carbon nanotubes (CNT) are nanostructured cylindrical allotrope of carbon. They are entirely made up of sp² hybridised carbon layers or graphene layers which are rolled to form seamless cylinder. CNTs are prepared by methods like laser ablation, arc discharge, chemical vapour deposition (CVD) etc.^[2] One of the common methods for preparing CNTs is CVD approach in which a hydrocarbon feed along with a carrier gas is passed in a chamber containing the transition metal catalyst. Size of the catalyst particle is the crucial factor which decides the size of the nanotubes apart from the other parameters. They are divided into single wall and multiwall CNTs, depending on the layers rolled up (Figure 1.11). They possess very high length

to diameter ratio, with micron range length and ~1-100 nm diameters depending on the number of the walls in CNTs. Compared to many other materials, they have extreme high thermal, electrical and mechanical (tensile strength, 100-600 GPa) properties, which make them as versatile materials for various applications. Metallic type conductivity, high surface area ($200\text{-}900\text{ m}^2\text{ g}^{-1}$) and stability make them as ideal for polarizable electrode as in EDLC^[43]. First report in this direction came in 1997 by Niu *et al.*^[44] using MWNT of $430\text{ m}^2\text{ g}^{-1}$ giving a capacitance of 102 F g^{-1} in acid medium. Chemical functionalization^[35, 45], chopping^[46], hetero atom doping^[47] etc. have also been tried on CNTs to enhance the capacitance *via* increased wetting as well Faradaic contributions. Further, they were also used as conducting backbone to support other charge storage materials like metal oxides^[22], conducting polymers^[23] etc. The above mentioned filler effect of CNTs is very important due to their high aspect ratio, which helps to decrease the electron travel path resulting in low ESR for the supercapacitor.

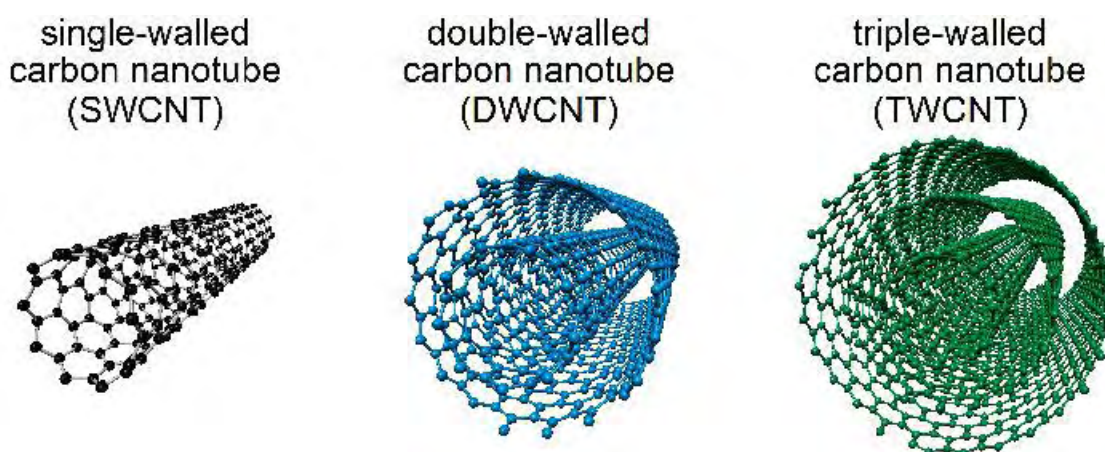


Figure 1.11: Schematic representation of the different types of the carbon nanotubes (Courtesy: T. Hirschmann).

1.5.1.3 Carbon fibers and carbon nanofibers

Carbon fibers are versatile materials in terms of easy method of preparation, high conductivity, high aspect ratio, ability to form standalone substrate etc. High conductivity and surface area make them ideal for many applications like fuel cells, Li-ion batteries etc. apart from the supercapacitor applications. Conventional carbon fiber (CCF) and vapour phase grown carbon fiber (VGCF) possess several micron sizes in diameter^[2]. However, cheap production cost makes them ideal for many

applications. CCF is synthesized by classical electro spinning method of a polymer (e.g. polyacrylonitrile). Here, fibers are extruded from a polymer solution using electrostatic forces to a conducting substrate. Carbonizations and SSA improvements by activations are followed the spinning process. Surface area can be improved up to $1000 \text{ m}^2 \text{ g}^{-1}$ via various physical and chemical activations. Proper selection of polymer and synthetic technique can prepare fibers even in nanometre regime ($>100 \text{ nm}$). Specific capacitance of 140 F g^{-1} is reported for activated carbon fibers^[48]. Applications of the high aspect ratio fibers are unique due to their ability in forming composites. They can be composited with metal oxides^[49], conducting polymers^[50] etc. by suitable *in situ* methods, electrode deposition, hydrothermal, vapour phase

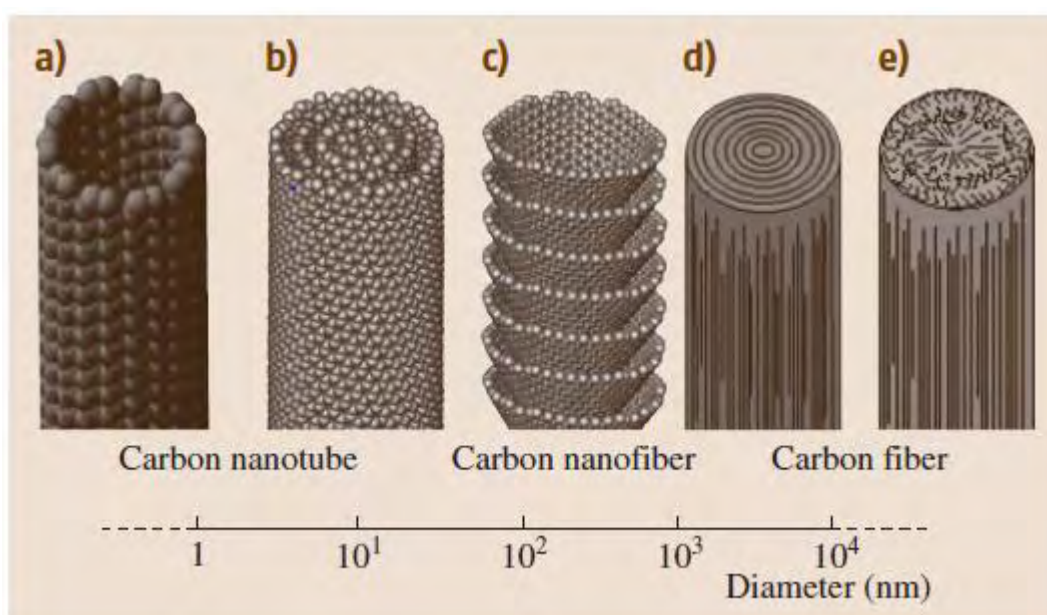


Figure 1.12: A schematic comparison of the diameter dimensions on a log scale for various types of fibrous carbon materials. (Reprinted with permission from Ref.[2], Copy right, Springer-2013).

processes etc., which find applications in supercapacitors^[51], DSSCs^[52], Li-ion batteries^[53], fuel cells^[54] etc.

In case of VGCF, carbon sources, normally hydrocarbons are vaporised and continuously feed along with a carrier gas containing vaporised catalyst (Fe, Ni, Co and Cu) to a chamber at a high temperature. Such a continuous^[50b] or floating process normally yields carbon fiber of sub-micrometre diameters and lengths of a few to 100 μm . Such continuous process is ideal for carbon fiber production in large scale. On the other side, vapour phase grown carbon nanofiber (VGCNF) is grown over the catalyst substrate which is kept inside the heating chamber. Diameter of the CNF

grown depends on the size of the catalyst particle. Advantage of such VGCNFs is their low diameter and highly graphitic nature. A schematic comparison is shown in Figure 1.12. Here, Figure 1.12c represents cup stacked CNF under the class of VGCNF, whereas, Figure 1.12d and 1.12e represent VGCF and conventional fiber, respectively.

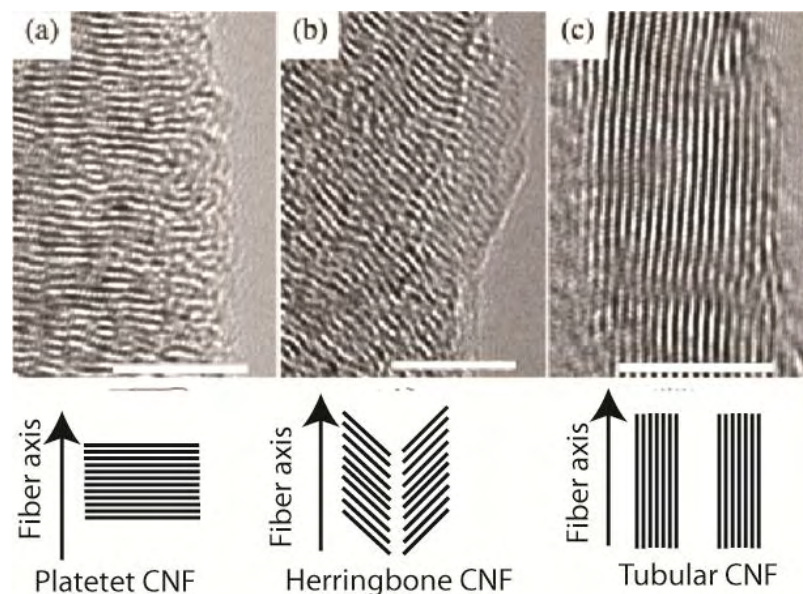


Figure 1.13: HR-TEM images of various types of vapour phase grown carbon nanofibers (VGCNFs) and schematic representations of the orientation of the graphene layers. (Adapted with permission from Ref. [55]. Copyright, American Chemical Society, 2006).

1.5.1.4 Graphene

Graphene is a 2-dimensional (2-D) sheet of sp^2 hybridised carbon network. Honeycomb structure of graphene layers is the basic building block of many other carbon allotropes like 3-D graphite, 1-D nanotubes and 0-D fullerenes (Figure 1.14). Highly delocalised electrons in the π -conjugated network of graphene result in extremely high thermal, electrical and mechanical properties. Electron mobility of a single layer graphene is measured to be $15,000 \text{ cm}^2 \text{ V}^{-1} \text{ s}^{-1}$ [56]. They can be prepared by various methods like mechanical[57] and chemical exfoliation of graphite[58], unzipping of carbon nanotubes[59], solvothermal method[60], epitaxial growth on SiC surfaces[61] and metal surfaces[62], chemical vapour deposition[63], bottom-up synthesis[64] etc. However, large scale production of high quality graphene is still a daunting challenge. Hummer's method[65] or modified Hummer's methods[66], which are based on the chemical exfoliation of graphite is considered to be the scalable methods, though the quality of the graphene produced is inferior to the other methods.

High conductivity, SSA, flexibly and mechanical properties of graphene make it as an ideal candidate for EDLC materials. The first report of graphene as an EDLC appeared in 2008 by Rao *et.al.*^[67] and later by Ruoff *et.al.*^[68]. Due to the higher electrolyte accessible SSA and conductivity, very large capacitance in comparison with CNT and carbon is reported at higher voltage window^[69].

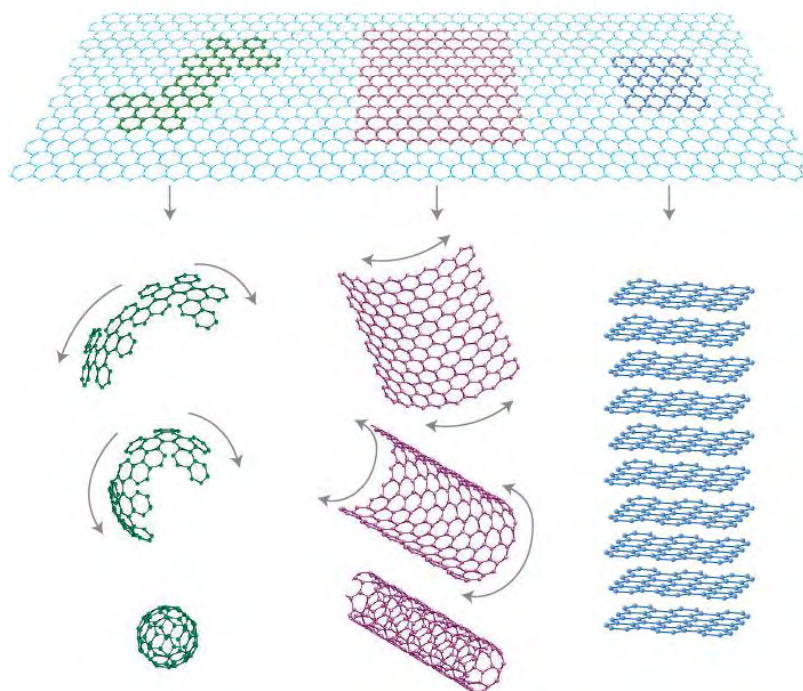
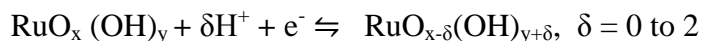


Figure 1.14: Mother of all graphitic forms. Graphene is a 2-D building material for carbon materials of all other dimensionalities. It can be wrapped up into 0-D buckyballs, rolled into 1-D nanotubes or stacked into 3-D graphite (Reprinted by permission from Macmillan Publishers Ltd: Nature Materials Ref. [56], Copyright, 2007).

1.5.2 Metal Oxides and Hydroxides

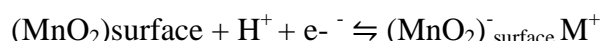
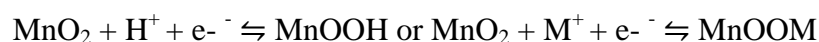
Metal oxide or hydroxide, which can store charge by Faradaic reaction through reversible oxidation state, comes under the class of pseudocapacitor. Metal oxides have the ability to store charge by reversible redox reactions in addition to the normal surface storage and thus have a high energy density than EDLC. Prime requirement of a metal oxide for this purpose is its ability to conduct charges in addition to the reversible oxidation states without undergoing any phase changes in the operating potential and electrolytes. Ruthenium oxide, manganese oxides, cobalt oxide, nickel oxide, vanadium oxides etc are well known for this type of charge storage. Apart from this, hydroxides, double metal hydroxides and mixed metal oxides are also known for charge storage. RuO_2 or $\text{RuO}_2 \cdot x\text{H}_2\text{O}$ is one of the earliest and at the same time best

pseudocapacitive materials so far. It was first reported in 1971 by Buzzanca *et al.*^[70]. The charge storage mechanism was studied in 1978 by Michell *et al.*^[71] using X-ray emission spectroscopy studies. RuO₂ undergoes redox reaction through electrochemical protonation in acidic media from Ru⁴⁺ to Ru³⁺ or even Ru²⁺ as shown below^[72]:



Theoretical maximum capacitance calculated for RuO₂ is around 2000 F g⁻¹ by considering a uniform protonation throughout the electrochemical window. They possess high practically achievable capacitance combined with chemical as well as thermal stability and quasi-metallic conductivity compared to any other metal oxide. Presence of water molecules in RuO₂.xH₂O is highly critical for the faster proton or cation movement through H₂O and OH⁻ sites inside the crystal^[73]. Thus, faster proton diffusion (H⁺ diffusion coefficient 10⁻⁸-10⁻¹² cm² s⁻¹) helps for the hydrous RuO₂ to show more capacitance than the anhydrous one^[74]. However, high cost of the material makes it less interesting for researchers in later stages even though RuO₂ was the first metal oxide used in a supercapacitor.

In 1998, Goodenough *et al.* demonstrated the charge storage properties of amorphous MnO₂.nH₂O in KCl solution having a capacitance of 200 F g⁻¹. Charge storage mechanism^[75] of MnO₂ is very similar to that of RuO₂. In general, manganese oxides (MnO_x) are low in cost, less toxic and environmental friendly materials. They can be prepared by various techniques like electro-deposition, co-precipitation, hydrothermal reaction etc. Apart from the synthesis technique, crystal structure of MnO_x depends on heat treatment and oxygen atmosphere. It is believed that two types of charge storage processes involve in MnO₂; first one is the intercalation of H⁺ or M⁺ (alkali metal cation) into the bulk and the second one is the surface adsorption as that of an EDLC.



Both mechanisms involve a redox reaction in which a shuttling of Mn oxidation state from III and IV occurs. The intercalation mechanism is limited by the diffusion of ions at high charge rate compared to faster surface charge storage as that in the second

mechanism. Pure intercalation type mechanism leads to a maximum capacitance of 1100-1350 F g⁻¹ for MnO₂. However, compared to RuO₂, electrical (10⁻⁵-10⁻⁶ S cm⁻¹) and ionic mobility of MnO₂ is very less and thus results in very low capacitance (~200 F g⁻¹) in practical conditions. Low capacitance is prominent when the MnO₂ electrode thickness is high^[76] due to high charge transfer resistance. Although, higher crystallinity can enhance the conductivity of MnO_x, poor surface area results concomitantly. Thus judicious synthetic strategies are required to attain higher SSA with comparable conductivity. Oxides and hydroxides of other metals like Ni^[77], Co^[78], Fe^[79], V^[80], Sn^[81], Ti, Cu^[82], Mo etc. also show excellent charge storage properties. However, narrow potential window of such materials limits their possibilities in real capacitors.

1.5.3 Conducting Polymers

Conducting polymers (CP) are the most recent class of polymers^[83]. They are basically electrically conducting organic polymers. They possess π -conjugating polymer chain as backbone with continuous sp² hybridized centers. However, excess +ve (p) or -ve (n) charges in CP determine the conductivity and thus called as in the doped state. P-doped CPs are more common as they can be prepared easily compared to the n-doped CP. CPs have a conducting range from semiconducting to the metallic depending upon the doping level. Conductivity of CP also depends on several factors including the method of preparation, quality of film used for the measurements etc. Oriented polyacetylene can reach a conductivity of 10⁵ S cm⁻¹, which is nearly equal to metallic conductivity. They are ideal for supercapacitor electrode due to their low cost, environmental friendly nature, high conductivity in doped state, high energy density etc. In CP, charge storage occurs through redox processes. In a reduced state, de-doping occurs and the counter ions are released to the electrolyte while in oxidised state, heavy doping occurs and thus ions are transferred back to the polymer chain to balance the excess +v charges. CP based supercapacitor can be classified in to 3 groups depending upon the configuration. In Type-1 symmetrical, both the electrodes are p-doped CP and the voltage window can go upto 1 V depending upon the materials. In Type-2 asymmetric, two different p-doped CP with different redox activities are used; e.g. polyaniline and polypyrrole. In Type-3, an n-doped and p-doped CP, which can be from the same polymer, are used as either electrode.

Table 1.2: Various conducting polymers used as the supercapacitor electrode materials and their properties.

Conducting polymer	Mw (g mol ⁻¹)	Dopant level	Conductivity γ	Potential Range	Theoretical capacitance (F g ⁻¹)
Polyaniline	93	0.5	0.1-5	0.7	964
Polypyrrole	67	0.33	10-50	0.8	620
Polythiophene	84	0.33	300-400	0.8	485
PEDOT	142	0.33	300-500	1.2	210

Advantage of Type-3 is its voltage window as high as 3.1 V in non-aqueous electrolytes. Some of the common CPs which are used in supercapacitors are shown in Table.2. Polyaniline and polypyrrole were used as pseudocapacitor initially by Gottesfeld^[84] and Conway^[85]. Among the various CPs shown in Table 1.2, polyaniline (Figure 1.15a) possesses highest capacitance owing to its low molecular weight and high doping level. However, volume expansion during the charge-discharge process due to the ion intercalation process results in serious stability issues. Such a stability issue is common for all CPs. However, polyethedioxythiophene (PEDOT)^[86] (Figure 1.15b) shows much more stability, higher electrochemical window and high conductivity even though it possesses relatively low capacitance. CPs can be prepared by various methods like chemical oxidation in solution phase, electrodeposition, vapour phase synthesis, interfacial polymerization etc. To address the low stability of CP, various composites with carbon materials and metal oxides also have been explored by researchers.

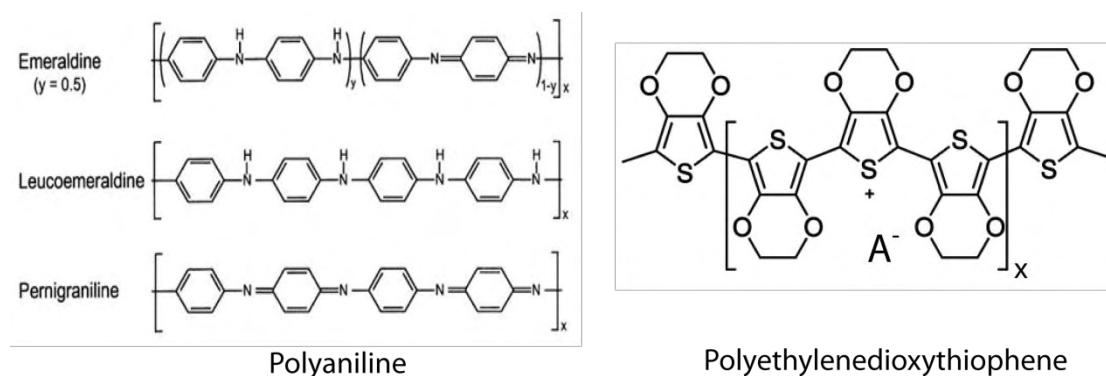


Figure 1.15: Two representative members of the conducting polymers: a) structure of polyaniline in its different forms and b) polyethylenedioxythiophene.

1.6 Electrolyte Material

The electrolytes normally used in supercapacitors are in liquid phase. They play a crucial role in the performance of the supercapacitor by attributing the ESR of the device. Further, the potential of a supercapacitor is restricted by the decomposition of the electrolyte solvent. Thus, power and energy of a supercapacitor can be largely decided by the electrolyte. The prime requirement of a supercapacitor electrolyte is its high conductivity ($\sim 1 \text{ S cm}^{-1}$) and electrochemical stability. Apart from this, wide voltage window, chemical inertness, high ionic concentration, low volatility, low viscosity, availability at high purity with low cost etc. are also required for a quality electrolyte. At very early stage, supercapacitors utilised aqueous electrolytes and later non-aqueous electrolytes came into the picture and dominated the field. Still, research is progressing on aqueous based electrolytes (such as aqueous solution of H_2SO_4 , KOH etc.) due to their unique ability to achieve low ESR for the device due to very high conductivity as well as their eco-friendly nature. Supercapacitors containing aqueous electrolytes normally display a higher capacitance owing to the higher ionic concentration with smaller ionic radius. Further, high ionic conductivity of the aqueous system, due to the large dielectric constant of water compared to the organic electrolytes, leads to higher power density. However, acid and base electrolytes have a voltage restriction of 1 V due to the water oxidation which restricts the improvement in the energy density. To mitigate the corrosive nature of acid, aqueous salt solutions are explored and are found to be promising in this context due to their ability to achieve a voltage window as high as $2.2 \text{ V}^{[28a]}$ owing to the high overpotential for water decomposition. Further, this type of neutral pH electrolyte is ideal for asymmetric capacitor with metal oxide as the positive electrode, such as MnO_2 .

Compared to the aqueous electrolytes, the main advantage of the organic electrolytes is their ability to extend the voltage window up to 2.8 V. However, the conductivity and specific capacitance obtained in the organic electrolyte will always be inferior to the aqueous electrolytes. Among the organic electrolytes, propylene carbonate (PC) and acetonitrile are the most regularly used solvents. Acetonitrile is superior to PC in terms of its low viscosity. However, it is inferior in terms of the environmental and toxic problems. On the other hand, PC-based electrolytes^[87] are environmental friendly and stable in varies temperature range with comparable

conductivity and voltage window which is similar to acetonitrile. Organic salts which are used along with the solvents include tetraethylammoniumtetrafluoroborate, tetraethylphosphoniumtetrafluoroborate, triethylmethylammoniumtetrafluoroborate (TEMABF₄) etc.

Room temperature ionic liquids (RTILs)^[88] are the molten salts which are considered to be the future electrolytes of supercapacitors due to their unique ability to achieve high voltage window up to 6 V. Since they do not require additional solvents they have low vapour pressure and high working temperature without any risk of explosion^[89]. However, present RTILs possess high viscosity and low conductivity (~1-10 mS cm⁻¹) than the commercial organic electrolytes which hamper the power performance of the RTIL based supercapacitors. They are normally based on a quaternary ammonium cation (R₄N⁺) with an anion. Physical and chemical properties strongly depend on the type of the cation and anion.

1.6.1. Solid Electrolytes

Liquid electrolytes in conventional electrochemical energy storage devices raise safety issues and thus require high-standard safety encapsulation materials and technologies. Such safety precautions are more important in organic electrolytes as they are more toxic and have high vapour pressure. They will make serious damage if they come out of the device package during a possible leakage or explosion. Replacement of the liquid electrolytes in the energy storage devices with a solid counterpart is thus very promising for developing thin, lightweight, economically viable and flexible future devices. Polymer electrolytes have been extensively studied as the electrolytes in supercapacitors and lithium batteries.

Polymer electrolytes are normally two-phase systems comprising of an ionic conducting medium entrapped in a polymer matrix. The polymer matrix normally consists of poly(ethyleneoxide) (PEO), poly(vinylalcohol) (PVA), poly(methylmethacrylate) (PMMA), poly(vinylidene fluoride) (PVDF), poly(vinylidene fluoride-hexafluoropropylene) (PVDF-co-HFP), poly(acrylonitrile) (PAN) etc. The ion conducting mediums are either from acid, alkali or salt. For improving the ionic mobility, a large amount of solvent is used during the polymer gel formation. PVA-H₂SO₄/H₃PO₄/HClO₄ is commonly used as a polymer electrolyte owing to its higher conductivity and 1 V voltage window. However, instead of acid or

alkali, usage of salts like LiCl, LiClO₄ etc. can provide wider window upto 2 V. Higher voltage can be achieved in non-aqueous polymer systems such as PVDF, PVDF-co-HFP, PEO etc. which are plasticized by solvents like acetonitrile, propylene carbonate, ethylene carbonate etc., where the commonly used salts include TEABF₄, LiBF₄, LiClO₄ etc. Researchers are also looking at the aspects of preparing solid polymer electrolytes using RTIL by blending with some of the above mentioned polymer matrices to achieve high voltage windows up to 4-5 V.

1.7 Dye Sensitized Solar Cell

Solar cells are the electrical devices which convert solar energy directly into electrical energy. The existing solar cells can be classified into two, such as the conventional solar cells and the excitonic solar cells. The most common example for the conventional solar cell is the silicon solar cell which is based on p-n junction excitation. These cells are made from crystalline silicon. Even though they have high conversion efficiency (22 %), the cost of Si processing and fabrication is very high. On the other hand, emerging technologies which include dye sensitized solar cells (DSSCs), perovskite, inorganic and quantum dot solar cells are exciting in this context and they belong to the excitonic solar cells. The excitonic solar cells work on the principle of electron-hole pair creation in photoactive materials. But, due to the strong bonding between the electron and hole, carrier materials are required to split the electron and hole. This means that they cannot travel far without recombining with each other. Whereas, the excited electron and the corresponding hole can immediately separate and easily travel away from each other in the p-n junction PVs. Among the various excitonic PV technologies, DSSC looks promising due to its simple and cheaper fabrication method and relatively high conversion efficiencies (12 %).

DSSC was invented by Michael Gratzel and it is also called as Graetzel cell. It has attracted wide attention due to its simple architecture, low cost, ease of production and high energy conversion efficiency. A DSSC is an electrochemical device that works using chemical reactions and it generates electricity when photons are absorbed by a photosensitized dye present in it. The basic structure of DSSC is based on the original Graetzel design. It consists of four main parts. First one is the glass substrate with a transparent fluorine doped tin oxide coating (FTO), counter electrodes (a platinised electrode to collect electrons and catalyze the redox couple regeneration

reaction), a semiconducting layer or film with wide band gap (most common is TiO_2), the dye molecule and a redox electrolyte (an organic solvent containing a redox system like iodide/tri-iodide couple) (Figure 1.16).

In the past decades, silicon, gallium arsenide, cadmium sulphide etc were used as the semiconductor materials in solar cells. However, the solar cells made from these semiconductor materials were less stable. Later, the use of wide band gap semiconductors such as titanium dioxide, zinc dioxide etc came to practice, which possess higher stability. Other semiconductor oxides are SnO_2 , Nb_2O_5 and they possess high resistance to photo corrosion. However, the conversion efficiency of light into current was very less due to limited surface area of the electrode and less absorption of photons.

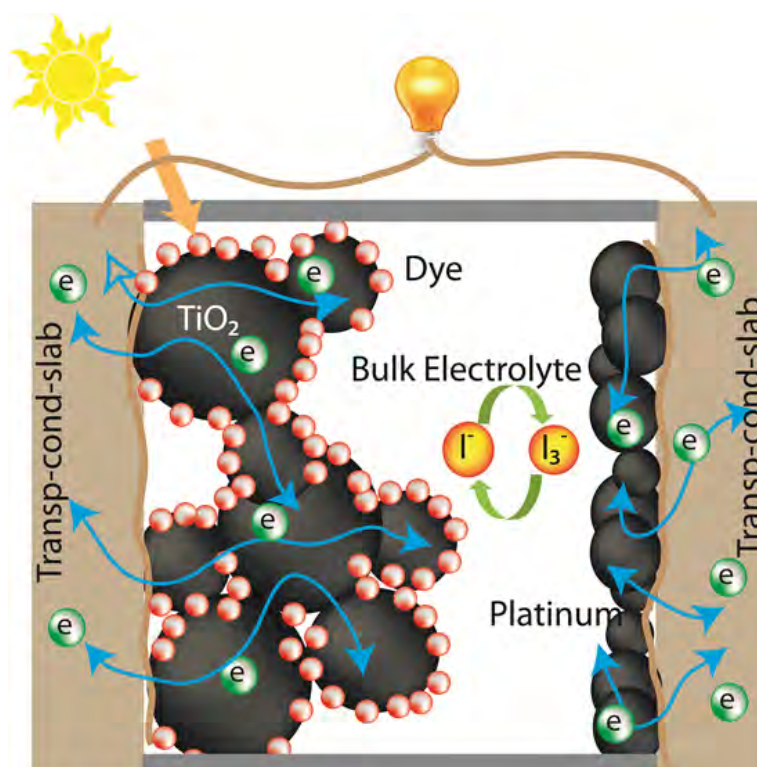


Figure 1.16: A schematic representation of a DSSC.

Different dye molecules are used as photosensitizers in DSSCs. They possess proper molecular structure. These dyes are able to absorb the incident photons and get converted into the excited states. The common dyes used in DSSCs are polypyridyl compounds of ruthenium in +2 oxidation state. There are other ruthenium complexes as well. The most common examples are $\text{Ru}(\text{dcb})(\text{bpy})_2$ studied by Kelly *et.al*^[90] and Farzad *et.al*^[91]; invented $\text{Ru}(\text{dcbH}_2)(\text{bpy})_2(\text{PF}_6)_2$ and $\text{Os}(\text{dcbH}_2)(\text{bpy})_2-(\text{PF}_6)_2$.

The electrolytes used in DSSCs are classified into liquid state, solid state or quasi solid state. DSSC electrolyte should be transparent to the visible light and must have long term stability that includes chemical, thermal and electrochemical stability. The common electrolyte used is the iodide/ tri-iodide couple made from LiI and I₂, which is superior to Br⁻/Br₂, SCN⁻/SCN₂ etc., which are the other examples for the redox couples used in DSSCs. For two decades, intensive researches established a breakthrough in the field of DSSC by using TiO₂ film as the photoanode, I³⁻/I⁻ as the redox couple and platinum as the efficient counter electrode.

1.7.1 Advantages and Challenges of DSSC

DSSCs are considered to be the most efficient third generation solar technology. The conversion efficiency of solar cells of over 12 % is reported. The cost of production of DSSC is also less, since the materials are cheap. DSSCs are alternatives for the existing technologies and they have potential applications in rooftop solar collectors. The dyes used in the solar cells are also highly efficient since the absorption of photons is high and they are converted to electrons in the titanium oxide layer. The absorption spectrum of titanium oxide layer and solar spectrum should coincide as this affects the rate of photon absorption. Maximum possible photo current depends on the overlap between these two spectra. Different dyes have different absorption in various regions of the spectrum. For example, some dye molecules have poorer absorption in the red wavelength. They can function at low light conditions also. So, they can be used in cloudy weather. DSSCs are able to radiate away the more heat produced because of the presence of thin conductive layer. Thus, they can operate at lower internal temperatures also.

Table No.1.3: Comparison of DSSCs with the traditional silicon solar cells

Properties	DSSCs	Silicon solar cells
Power generation cost	Low cost production	High cost
Transparency	Transparent	Opaque
Power generation efficiency	Normal	High
Manufacture	Simple structure ,easy to fabricate	Difficult

However, there are many challenges faced by the present architecture of DSSC. The temperature has effects on the structure and functioning of DSSC. The electrolyte used in DSSC freezes at low temperatures and can break the cells which makes the cells non-functioning. The cells can also break and which can lead to leakage of the electrolyte at higher working temperatures. Thus, physical damage of the cells and temperature sensitive electrolytes are major problems in the performance and functioning of dye sensitized solar cells. The organic solvents used in the electrolytes are volatile also. Hence, they are to be carefully sealed which contributes to higher fabrication cost. Further, the dyes will degrade when exposed to ultraviolet radiation, resulting in instability. Apart from the above issues, high cost of Pt-counter electrode also makes the cost of DSSC much higher. Thus, huge challenges and, hence, enormous scope for fundamental and applied research to explore new electrolytes with less temperature sensitivity, stable and large spectrum absorbing dye, Pt-free counter electrode etc. in DSSC are present before the researchers.

1.7.2 Mechanism of DSSC

Following are the main processes occurring in a DSSC (Figure 1.17):

- Sunlight enters the cell through the transparent region of the solar cell. The incident photons are absorbed by complex photosensitizers absorbed on the TiO_2 surface. Photosensitizers are the dye molecules. They are excited from their ground state. Ruthenium based dyes are commonly used for the light absorption.
- Thus excited electrons reach the conduction band of the TiO_2 electrode. This leads to an effective charge separation with a negative charge in the titanium phase and a positive charge in the surface adsorbed Ru^{3+} . The dye molecule strips from iodide in the electrolyte below the TiO_2 and oxidizes it into tri-iodide. Further, electrons are received by the counter electrode through the outer circuit.
- The oxidized photosensitizer accepts electrons from I^- ion and retains its ground state. Also I^- gets oxidized to I_3^- .
- I_3^- diffuses to the counter electrode and again gets reduced to I^- .

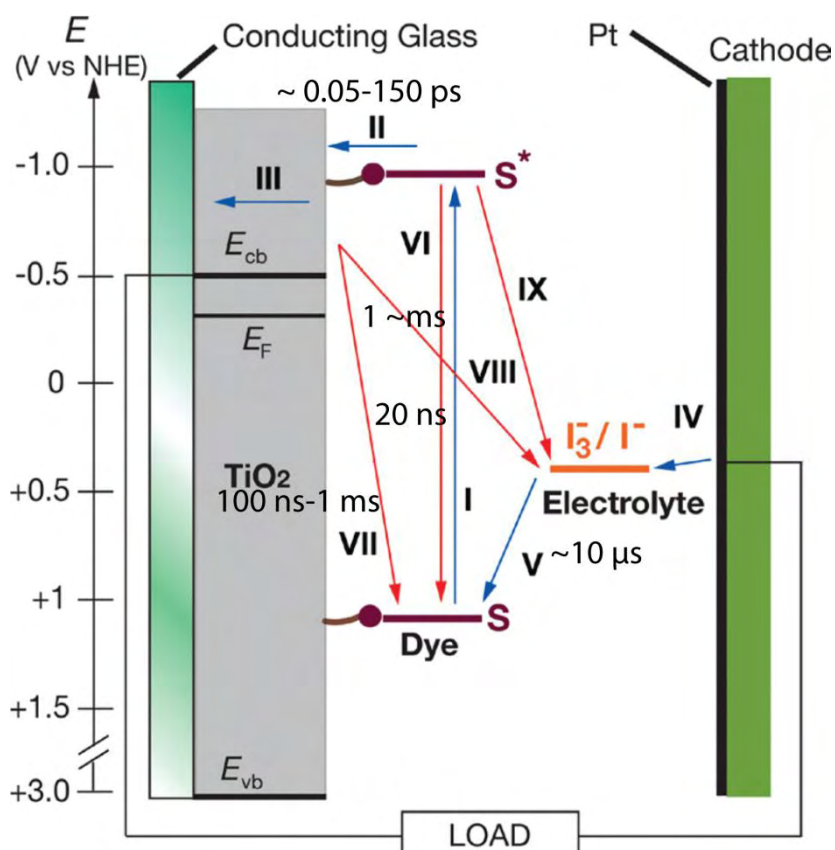


Figure 1.17: Schematic representation of the electron pathway in DSSC (Reproduced from Ref. [92] with permission of The Royal Society of Chemistry).

When light is absorbed by the dye, it goes to the excited state and the time required for the electron to reach the conduction band of TiO_2 is 0.05-150 ps. The time needed for the regeneration of the dye is 100 ns – 1 ms. The regeneration time depends on the nature of the electrolyte. The efficiency of the light conversion depends on the relative speed of the reactions and that is the kinetics. The electron injection in the conduction band of TiO_2 is much faster than the electronic relaxation processes. The tri-iodide is reduced to iodide at the counter electrode in a time interval of 10 μs . The reduction of the oxidised dye by I^- is faster than the direct recombination of the dye and the injected electron.

1.7.3 Efficiency of a Solar Cell

The total amount of the electrical power obtained for a particular solar power is expressed as a percentage called solar conversion efficiency. The performance and efficiency of a solar cell can be measured by analysing the I-V curve of a DSSC under solar simulators which provide an intensity of 100 mW cm^{-2} (one sun illumination)

which is the standard condition for reporting the efficiency of a solar cell. Figure 1.18 shows a typical I-V plot.

The current density J_{SC} , open circuit voltage V_{OC} etc. are very important features of a solar cell. The maximum voltage a cell can develop is the V_{OC} and the maximum current is the I_{SC} . Another important term related to solar cell is the fill factor that is defined as the ratio of the maximum obtainable power to the product of the open circuit voltage and short circuit current. Thus, the fill factor is calculated as follows:

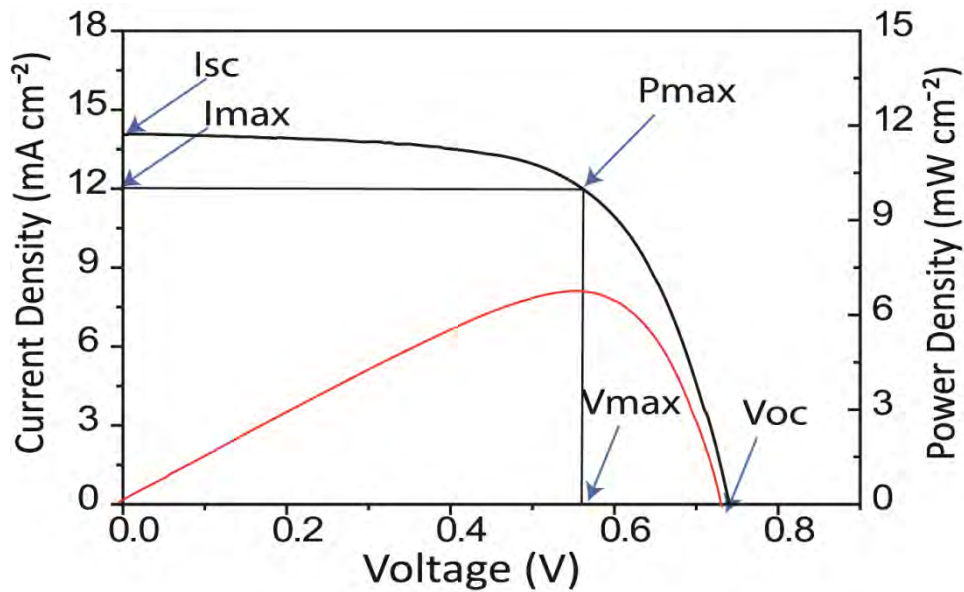


Figure 1.18: I-V Plot of a typical DSSC cell.

$$FF = \frac{V_{max}I_{max}}{V_{oc}J_{msc}}$$

The efficiency of a solar cell is represented as η , which is the percentage of power converted from the absorbed light into electrical energy, *i.e.*, $\left(\frac{P_{max}}{P_{input}}\right)$.

$$\eta = \frac{J_{sc}V_{oc}FF}{P_{input}}$$

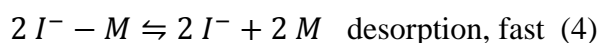
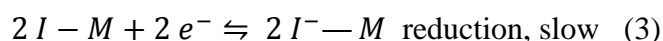
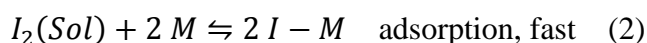
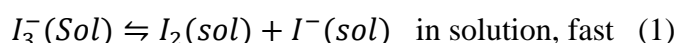
P_{input} is the input power of solar light per cm^2 .

1.7.3.1 Factors affecting the efficiency of a DSSC

The overall solar energy conversion efficiency of a DSSC is directly proportional to the efficiency of electron injection in the wide band gap of the semiconductors. Hence, researchers are forced to develop various nanostructured semiconducting materials which have higher surface area ability to load more dye molecules. Development of photosensitizers which possess extraction or absorption of the whole solar spectrum (extended to the near IR) is of high demand to enhance the efficiency. Apart from the working electrode, selection of redox couples in the electrolyte also plays a crucial role in deciding the efficiency of the cells. Apart from the other factors, an efficient counter electrode CE is also required for achieving high performance DSSCs.

1.8 Counter Electrodes for DSSCs

In a typical DSSC, the key reactions are photo induced oxidation of the dye which is coated on a polycrystalline TiO₂ at the anode and regeneration of the dye to its original state using iodide/tri-iodide (I⁻/I₃⁻) redox species at the cathode. The tri-iodide (I₃⁻) generated at the photoanode requires a highly active catalyst to convert it back to I⁻ at the cathode by collecting electrons from the outer circuit to complete the cycle. Hence, a highly efficient and stable CE catalyst is very critical for achieving competent DSSC systems. I₃⁻ reduction happening at the counter electrode in solution phase goes through the following steps:



here, -M is the catalyst surface

Among the various steps, the slowest and the rate determining step is (3); thus, molecular iodine (I₂) reduction *i.e.*, electron transfer and I₂ adsorption/I⁻ desorption play a critical role. The low charge transfer resistance is a basic parameter required for an efficient catalyst. The best known catalyst for the CE is precious platinum (Pt)

which possesses high catalytic activity and high corrosion resistance. Platinum can be prepared directly onto FTO by various methods like magnetron sputtering^[93], thermal decomposition^[94], electrochemical deposition^[95] and chemical reduction^[96]. However, the high cost of Pt metal and high energy required for the Pt electrode preparation through sputtering/thermal evaporation make Pt a less viable choice for commercial applications^[97]. Thus, replacement of Pt with a cheaper and abundant, but at the same time, highly active, stable and easily processable catalyst material is critical for improving the prospects of commercialization of DSSC.

1.8.1 Low Platinum Efforts through Nanostructuring

As a bench mark catalyst, Pt is popular at present in the CE research. Most of the Pt based researches intended to reduce the amount of Pt or to maximize its utilisation. This includes improving the surface area of Pt *via* nanostructuring, which helps for the high activity per mass of Pt. Ma *et.al*^[98] studied the effect of thickness of Pt towards the tri-iodide reduction and found that 2-50 nm Pt thickness is sufficient for comparable conversion efficiency. Jung *et.al* reported Pt nanocups^[99] having a diameter of 300 nm and a height of 400 nm showing a superior efficiency than the conventional Pt. Other efforts include compositing Pt with different carbon morphologies like graphite^[100], CNT^[101], graphene^[102] etc. Further, composites with conducting polymers^[103] are also reported. However, cost of Pt is still a persisting issue in such materials. Even though such efforts are intensely going on, substantial improvements are not yet attained to balance the cost of Pt.

1.8.2 Pt-free Metal Catalyst

Among the metal alternatives in place of Pt, nickel and palladium are the immediate choices as they are in the same group of elements. However, electroplated Ni shows poor conversion efficiency due to the low FF and V_{oc} , resulting from the reaction between I_3^- and Ni^[104]. Pd is also found to be unstable due to the formation of PdI₆^[105] with the iodine species in the electrolyte. Though gold is not catalytically active towards I_3^-/I^- couple, it is highly active towards the other redox couples like Co³⁺/Co²⁺^[106], Sn²⁺/S²⁻^[107] and thus can outperform Pt in quantum dot solar cells. Other metals like molybdenum and tungsten also show inferior efficacy^[108]. Overall, at present, apart from Pt, no other metal is looking promising as a CE in DSSC.

1.8.3 Metal Compounds

After Gratzel *et al.*^[109] introduced CoS in 2009, enormous research activities started to find facile catalyst for CE. This includes transition metal compounds like metal sulphides^[110], metal phosphides^[111], metal nitrides^[112], metal carbides^[112a] and metal oxides^[112a, 113]. The metals tried in the above compounds include cobalt, nickel, titanium, molybdenum, tungsten etc. However, metal chalcogenides are known to be very active towards the tri-iodide reduction reaction. Metal sulphides and selenides based CEs shown very high conversion efficiency. Ho *et al.*^[114] reported CoS circular nanorod arrays displaying low charge transfer resistance and an efficiency of 7.7 %, which is similar to the Pt CE. Other remarkable catalysts are Cu₂ZnSnS₄^[110a], FeS₂^[110b], Co₉S₈^[115], NiS^[116], Ni₉S₈^[117], Co_{8.4}S₈, Ni₃S₂^[118], Co_{0.85}Se & Ni_{0.85}Se^[119], Ni₃Se₄^[120]. Bang *et al.*^[121] studied NiSe₂, CoSe₂, and MoSe₂ and found that the Ni analogy is more electrocatalytically active for the I₃⁻ reduction. However, Yu *et al.*^[122] compared the performance of selenides of Co, Ni, Cu, Fe, Ru and reported that the Co system is superior among the group. Even though the transition metal compounds show superior activities, still, the cost of the metals, their processing and stability are the pertaining issues.

1.8.4 Carbon Materials

One of the earliest reports on the use of the carbonaceous materials as the CE was by Gratzel *et al.* in 1996 who used conductive graphite powder and carbon black to ease the DSSC module processability^[123]. Other noteworthy reports in this direction include the activated carbon based CE by Murata *et al.*^[124] and mesoporous carbon aerogel based CE by Tan *et al.*^[125]. Other carbon materials like carbon-nanotubes (CNTs)^[112b, 126], carbon-nanofibers (CNFs)^[127], graphene^[128] and heteroatom doped carbons^[129] are also promising due to their high conductivities and surface areas. High surface area helps to increase the roughness factor of the carbon CE which helps to attain low charge-transfer resistance (R_{ct}) in the CE/electrolyte interface. Lee *et al.*^[130] investigated the effect carbon particle size on the catalytic activity by comparing the carbon particle with an average size of 30 nm and 2–12 μm. They found that nanocarbon shows superior catalytic activity (PCE of 6.73 %) than bulk carbon. Grätzel *et al.*^[131] prepared optically transparent CEs using graphene. Aksay *et al.*^[132] studied the effect of oxygen amount in the graphene for the catalytic activity

and found that the optimum amount of oxygen is required for higher catalytic activity. This was in agreement with the positive effect of defects in CNTs for better catalytic activity^[133]. Kim *et al.* studied^[134] the effect of orientation of CNTs by preparing CNT based CEs by using screen printing and chemical vapour deposition (CVD) techniques. In the screen printed CE, CNTs are oriented randomly whereas the CVD grown CNTs are well oriented and thus result in low Rct. They found that the screen printed CNT CE can show a conversion efficiency of 8.03 %, whereas CVD grown CNTs can display an efficiency of 10.04 % due to the well aligned CNTs with high electrical and ionic conductivity. In most of the cases, carbon to substrate adhesion is poor except in cases where they are directly grown on the electrodes. Apart from these, poor catalytic activity^[112b, 126b, 128c, 128d] compared to metals, corrosion, opacity and processability issues result in diminished efficiency and stability for the carbon materials compared to Pt^[135].

1.8.5 Conducting Polymers

Structural flexibility of the DSSC makes them ideal for many flexible applications. Apart from these, integration of DSSCs in window walls of high rise building demands transparency in the cells. In such scenario, CE using conducting polymers looks promising due to their flexible nature as well as possible transparency in the electrode. Polyethylenedioxythiophene (PEDOT)^[136] is a promising conducting polymer due to its high conductivity, transparency, and stability. In 1988 Jonas *et al.*^[137] reported a possible application of PEDOT in electrochemical devices such as solid electrolytic capacitor. Application of PEDOT as a CE in DSSC is first reported by Yohannes *et al.*^[138] Later aqueous processable PEDOT having poly(styrenesulfonate) (PSS)^[139] as the counter ion was introduced as CE in DSSC which possesses an added merit of transparency. Yanagida *et al.*^[140] investigated the effect of counter ion in the PEDOT towards tri-iodide reduction and found that no impact on the conversion efficiency rather interaction between polymer and substrate (FTO) directly determines the fill factor. Further, electrodeposited PEDOT^[141], PEDOT fiber^[142], PEDOT carbon composites^[143] were also used as CE. As PEDOT possesses high conductivity, transparent conductive oxide (TCO)-free CE can be prepared by using PEDOT^[144]. Here, PEDOT will play a dual role of the catalyst as well as the current collector. In addition to PEDOT, a derivative, poly(3,3-diethyl-3,4-dihydro-2H-thieno-[3,4-b][1,4]dioxepine) (PProDOT-Et₂) has also been proposed

as a CE^[145]. Polythiophene (PTh), which is a basic unit of PEDOT, also is expected to be a good catalyst for the tri-iodide reduction. However, some literature studies indicate low catalytic activity of Pt^[146] compared to PEDOT. Wu *et al.*^[147] prepared polypyrrole (PPy) nanoparticle and used this as CE in DSSC, which showed a high PCE of 7.66 %, exceeding the value of the Pt CE (6.90 %). Recent other reports include chemical^[148], vapour phase^[149], electrochemical^[150] polymerized PPy, PPy composites with graphene^[150b, 151], CNTs^[150a, 152], freestanding PPy nanotubes^[153], polypyrrole nanosheets^[154] etc. Polyaniline (PANI) is another extensively researched CE candidate for DSSC. Wu *et al.*^[155] reported an inexpensive PANI having ClO₄⁻ counter ion prepared by chemical oxidation. Zhao *et al.*^[156] prepared transparent PANI CE for bifacial DSSC. Other reports of PANI include composites with graphene^[157], CNTs^[158], iodine doped polyaniline^[159] and double layered PANI nanostructures^[160].

Literature survey clearly reveals that PEDOT shows promising catalytic activity compared to its counterparts and sometimes its activity can even surpass the performances of the electrodes made from the metal based catalysts by inducing property modulations through proper synthetic strategies. PEDOT possesses high stability and conductivity as required for a good electrocatalyst apart from its superior inherent catalytic efficiency. Even though PEDOT possesses high catalytic activity and transparency, it can form complexes with iodide and this can tarnish the prospects for the long term catalytic activities. This was proved by XPS analysis by Girtu *et al.*^[161] which was further confirmed by Biallozor *et al.*^[162] using CV measurements.

1.9 Nanostructured Materials

Nano sizing of materials has triggered much excitement in the fundamental understanding of their properties as well their possible applications in the energy field. Nanomaterials open up tunable physical and chemical properties due to high surface/volume ratio and short charge and mass transport length. Apart from the higher surface area, optical band gap, conductivity, melting point, reactivity etc. also change along with the size reduction (Figure 1.19). However, manipulation of such properties to make them suitable for specific applications requires dedicated synthetic strategies. High surface/volume ratio along with the facile charge transport is ideal

for interfacial reactions occurring in the electrochemical devices such as supercapacitors, DSSCs, Li-ion batteries, fuel cells, electrochemical cells etc. However, nanostructured materials, especially single phase nanomaterials, suffer from serious drawbacks which limit their practical applications in energy devices. This includes low conductivity, slow kinetics, poor cycling and low mechanical properties, which are inevitable trade-off during the nanostructuring of the materials^[163]. Higher surface area imparts short electrical path for the materials which brings enlarged contact resistance between the grain boundaries. This linearly increases with SSA. Such increments in the resistance of the materials will lower the power capabilities of the energy devices. Apart from this, lack of simple and cheap methods for a large scale production is significantly restricting the applicability of the above nanomaterials from replacing the conventional materials from the energy devices.

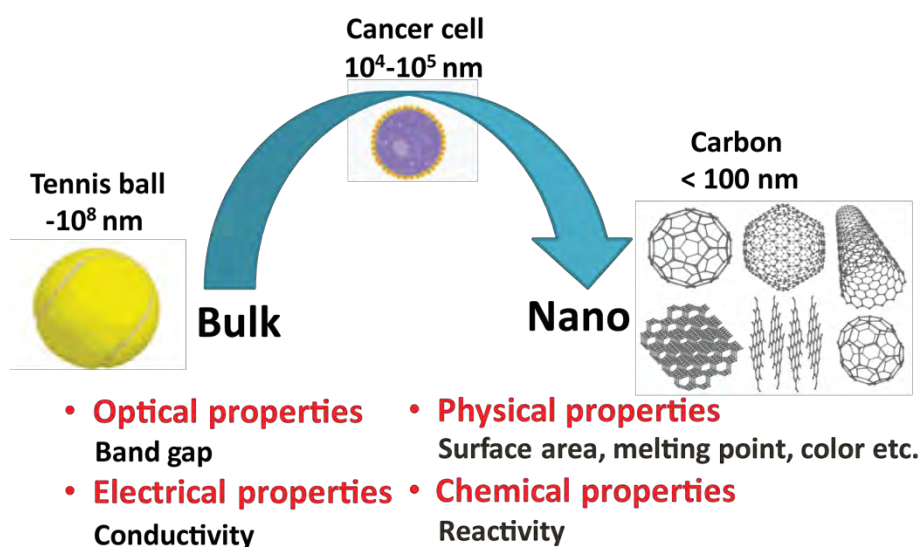


Figure 1.19: Bulk to nano: a schematic representation indicating the material property changes during the transformation of the size from bulk to nano.

1.9.1 Supported Nanostructured Materials

To address the above issues of a single phase nanomaterials, researchers are focussing on making heterogeneous nanomaterials comprised of multi-nanocomponents. They have tailored nano-composites for specific demands such as conductivity, charge mobility and improved mechanical properties. Further, experimentally proved synergic effect at nano-regime leads to excellent electrochemical properties which is beyond the integral properties of the individual materials. Successful applications of hetero-nanostructured materials in

electrochemical devices depend on 1) proper selection of the materials which are in combination, 2) deploying the desired synthetic strategies and 3) designing and optimizing the heterogeneous nanostructure. Most of the multiphase nanostructured materials utilise carbon materials as the support materials owing to their exceptional properties such as high SSA, conductivity, corrosion resistance and stability. Their ability to play as excellent support materials is well established in fuel cell as a Pt catalyst support^[6]. Heterogeneous nanomaterials can be broadly classified into 0-D, 1-D, 2-D and 3-D; a schematic representation is given in Figure 1.20. The broad class of 0-D materials includes core-shell, hollow sphere, encapsulated nanomaterials etc. They find excellent applications in battery as they address the volume expansion and low conductivity issues^[163]. Here, high energy density materials can serve as the core, meantime the shell will provide adequate conductivity and chemical stability by preventing expansion and agglomeration. Compared to 0-D hetero-nanostructures, 1-D nanomaterials can provide continuous electron path and better charge transport in a 1-D confined region resulting in better kinetics. This is highly important in case of the supercapacitor for high power and in the DSSC counter electrode for higher fill factor *via* improved kinetics facilitated by effortless charge transport. Further, in many

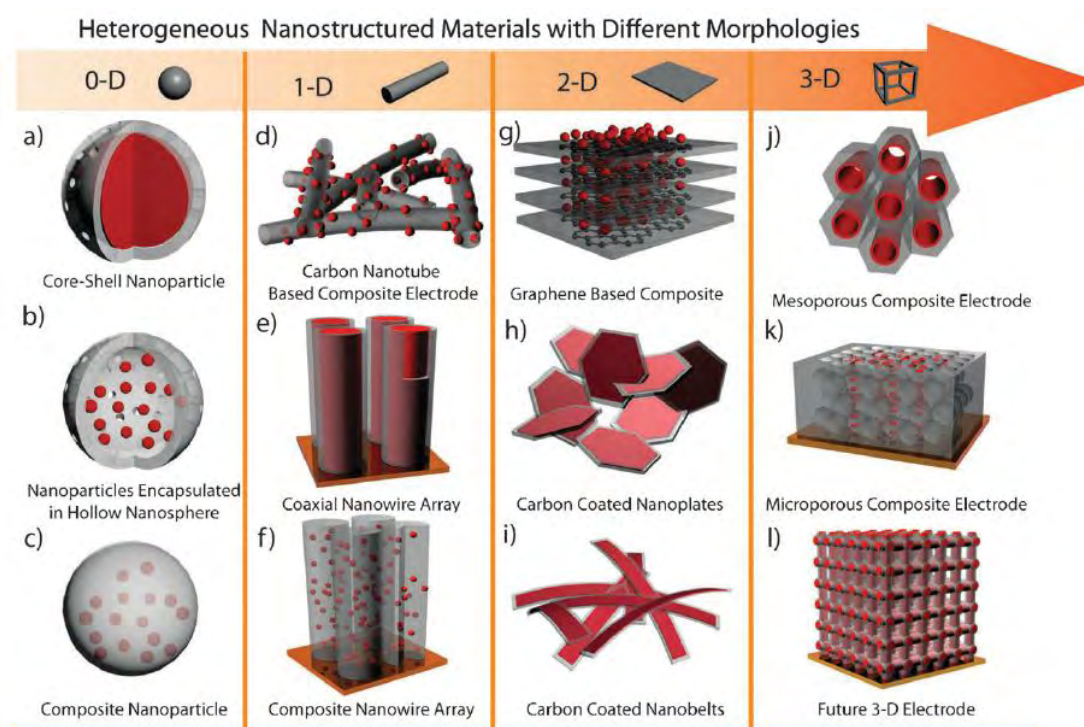


Figure 1.20: Different heterogeneous nanostructured materials based on structural complexity (Reproduced from Ref. [163] with permission of The Royal Society of Chemistry).

cases, synergic effect boost the inherent charge storage properties and catalytic properties compared to individual components. Apart from these, high surface area with 1-D structure provides easy ion flux and buffer volume between the structures, which alleviate the mechanical stress for the materials. Importantly, no need of external binder and conducting ingredients reduces the cost of the devices. Such a facile ionic and electron mobility enhancement can also be found in 2-D and 3-D hetero-nanostructures. 2-D heterostructures have attracted wide attention after the discovery of graphene. However, achieving the desired morphology of 2-D and 3-D heterostructures is tedious compared to the 1-D structures^[163]. In case of graphene, synthesis into a spatially separated high quality (extent of graphitisation) single layer graphene in large scale is challenging. Further, processability of such highly graphitized graphene is again a challenging task for anchoring a second nanomaterial on the surface. At the same time, large varieties of 1-D nanomaterials for specific applications are available with desired properties. Most of them are highly processable and cheaper in cost. Especially, 1-D carbon materials are available in various morphologies like fiber (hollow and rigid), tubular etc^[2]. Further, they have varied aspect ratio, graphitization level, surface functionalities which make the hetero-nanostructure synthetic strategies more flexible. Thus, such vast variety of 1-D carbon materials deliver possibility of myriad application in energy filed to use as support materials. Apart from 1-D carbon materials, conducting polymers and metal oxides have also shown possibilities to use as 1-D support materials though at less extent compared to 1-D carbon^[74a].

1.10 1-D Supported Nanostructured Materials for Energy Applications

In literature, a large number of reports are available for various 1-D nanostructures which are utilised in applications involving electrochemical energy conversion to energy storage devices. Zhang *et al.*^[164] reported a conformal SnO₂ decoration over CNT which provided adequate electrical contact and prevented volume expansion of SnO₂ during Li intercalation/de-intercalation process (Figure 1.21). Similarly, Lee *et al.*^[165] reported PPy coated CNT showing superior capacitance properties than the pure CNT and PPy due to 1-D nanoconfinement which provided facile ion path and electrical conductivity for the composite. Ji *et al.* prepared

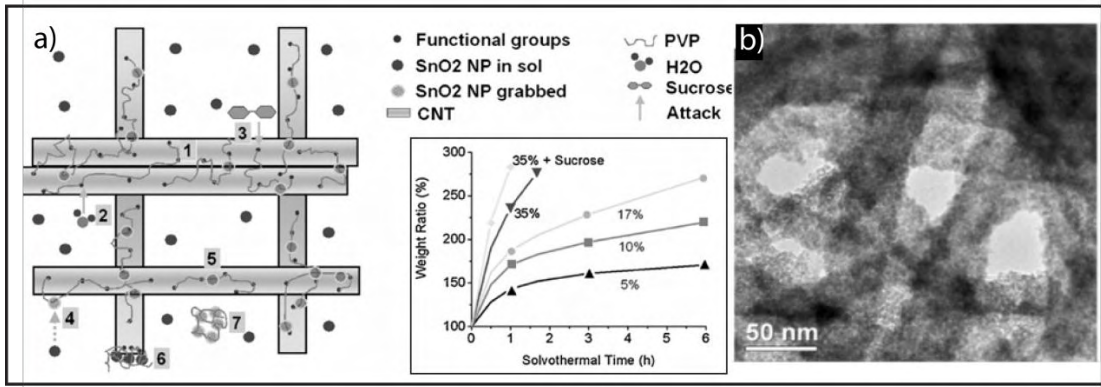


Figure 1.21: Schematic representation of the synthetic procedure of SnO_2/CNTs (Inset: weights of the composite papers versus the solvothermal treatment time when different volume ratios of water are used. Here, 100 wt.% refers to the PVP-loaded CNT sheets) and b) TEM images of the $\text{SnO}_2\text{-CNT}$ composite sheet (Adapted and reprinted with permission from Ref.[164], Copyright, Wiley-VC, 2009).

carbon/silicon (C/Si) composite nanofibers by electrospinning polyaniline nanofibers containing silicon nanoparticles, followed by carbonisation [166]. 15 % Si in the composites could provide large reversible capacities of about 1800 mAh g^{-1} . Gao *et al.* [167] reported a composite made using TiN nanoparticles on CNTs as a CE in

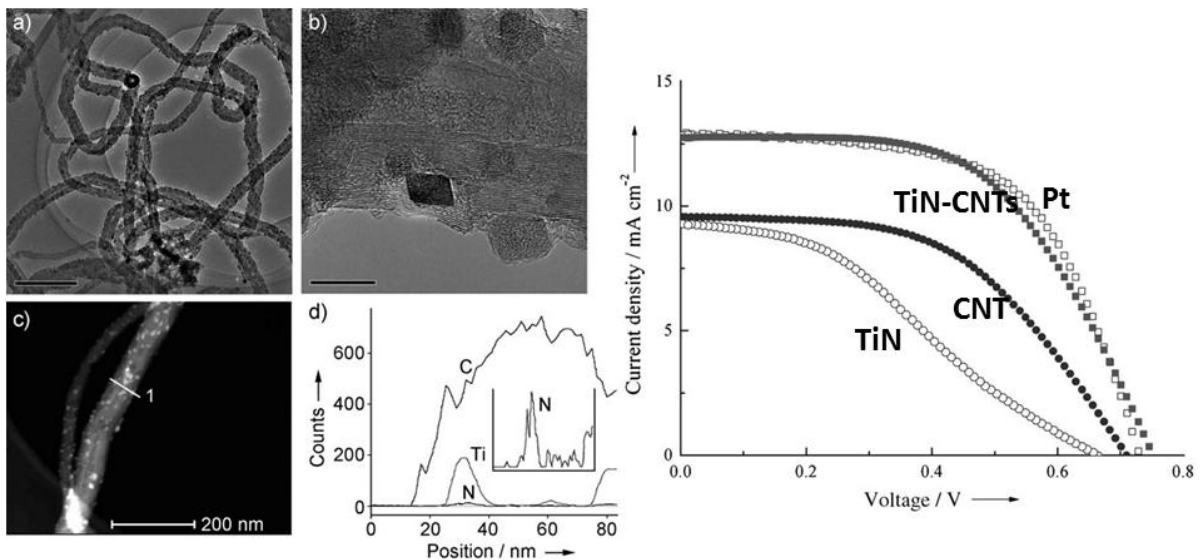


Figure 1.22: a, b) TEM images (scale bars: 200 nm (a), 10 nm (b)), c) HAADF-STEM image and d) element distribution of TiN-CNTs. Inset: spectrum of N from 0 to 80 nm expanded vertically by a factor of 57.5. The signals in (d) were obtained by line-scanning across a single carbon nanotube (line 1 in (c)) from right to left. The right images is showing the I-V polarisation (Adapted and reprinted with permission from Ref.[167], Copyright, Wiley-VC, 2010).

DSSC. The DSSC using TiN/CNT shows 5.41 % conversion efficiency, higher than the DSSCs using TiN CE and the pure CNTs. The high performance of the composites is ascribed to the combination of high catalytic activity and electrical conductivity (Figure 1.22). Basic idea of such 1-D heterostructures is to address the low charge mobility, active surface area and stability of a highly electrochemically active material *via* 1-D carbon support. Apart from the carbon, researchers also used conducting polymers as 1-D supports owing to their high conductivity. A 1-D nanostructured MnO₂/PPy composite was prepared by Li *et al.*^[168] using chemical polymerization of PPy in presence of MnO₂ nanoparticles. A high specific capacitance of 320 F/g is obtained for the composites after 500 charge–discharge cycles in the potential range of 0.4 to 0.6 V in a neutral pH KCl electrolyte. However, compared to carbon support, stability of such materials is still dubious. In most of the above examples, the derived materials possess higher disorder due to random orientation of the material during the synthesis. As a solution for this problem, template assisted methods are used by researchers to grow ordered arrays of 1-D nanostructured materials on a substrate by the “bottom-up” growth approach, *i.e.* the growth direction of the 1-D nanostructure is well controlled, in most cases, perpendicular to the substrate such as a current collector. Lee *et al.*^[163] reported coaxial nanowire comprising MnO₂ core and PEDOT shell resulting higher energy density than the individual components (Figure 1.23). In case of DSSCs CE, oriented heterostructures are very less due to difficulties in orienting concomitantly two phases together. Complete removal of the templates like alumina is hard and further large scale production is still challenging in such examples. Well interconnected carbon fiber can also be utilised to grow highly active but less conducting materials having low SSA. Due to highly ordered micron pores of carbon fibers, various type of coating techniques can be applied, such as electro-deposition, vapour phase deposition, dip coating etc. This type of 1-D oriented carbon backbone provides seamless electron path which acts as a current collector. Further, larger surface area can effectively increases the effective interfaces of the active materials along with controlling the structure during the deposition. Alshareef *et al.*^[169] reported Co₃O₄ nanowires over carbon fiber paper and showed the superior charge storage properties (Figure 1.24). Low electrical conductivity of Co₃O₄ is addressed by the carbon fiber support and the porous structure helps for easy ion transport and formation of better interfaces.

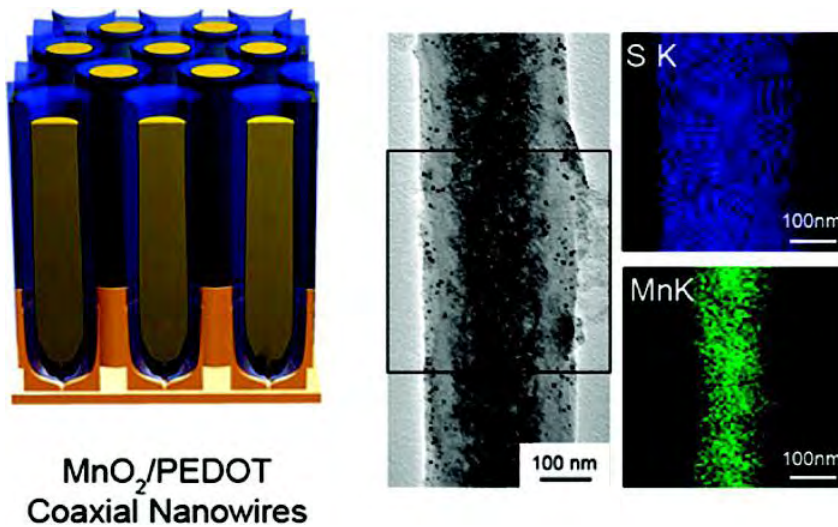


Figure 1.23: Image in the left side is the schematics of $\text{MnO}_2/\text{PEDOT}$ coaxial nanowire formed in alumina template. Images in the right side correspond to the single PEDOT coaxial nanowire and their EDS mapping (Adapted with permission from Ref.[170], Copyright, American Chemical Society, 2007).

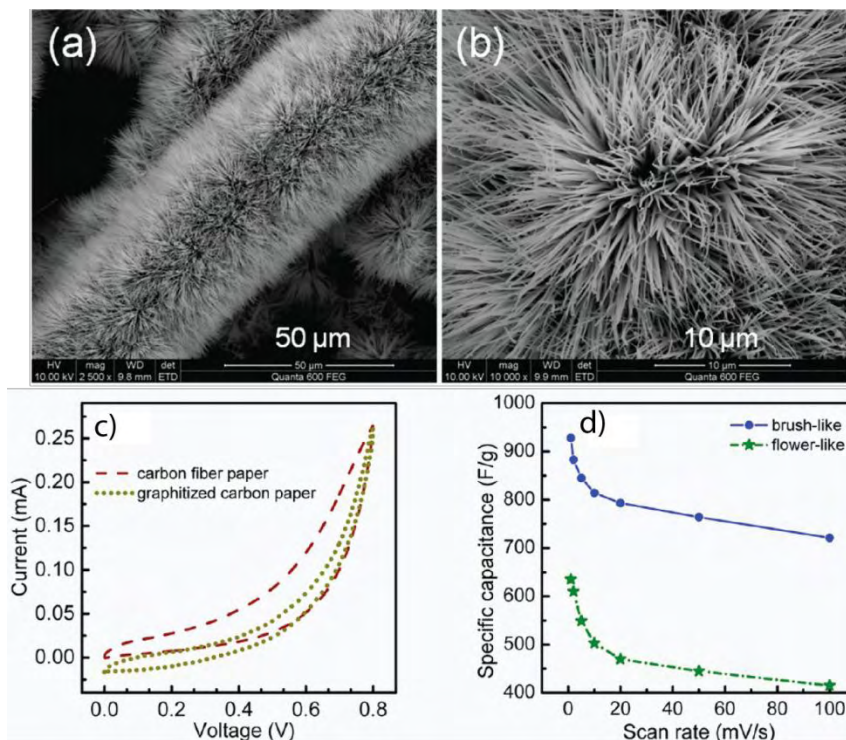


Figure 1.24: (a) Low and (b) high magnification SEM images of Co_3O_4 nanowires with brush-like morphology, (c) cyclic voltammograms of carbon substrates at a scan rate of 10 mV s^{-1} and (d) specific capacitances of Co_3O_4 nanowires with brush-like and flower-like morphologies at different scan rates. Adapted with permission from Ref. [169], Copyright, American Chemical Society, 2012).

1.11 Scope and Objectives of the Present Thesis

Critical analysis of the present supercapacitors and dye sensitized solar cells (DSSCs) based on the current research activities, pertaining issues in design, performance, safety and cost clearly reveals the existing hurdles which need to overcome in order to broaden their wider applications. Electrode material is one of the vital factors which has a critical role in deciding the performance of the energy devices listed above. Facile movement of electrons and ions through such electrodes and their electrolyte interfaces thus plays a pivotal role apart from the inherent electrochemical activity of the electrode materials. This requires proper understanding of the double layer structure and mechanism of the concerned devices. Among the various single phase and multi-phase nanomaterials, 1-D carbon supported nanomaterials are ideal for such applications due to their improved activity resulting from enhanced electrode-electrolyte interfaces, amended kinetics *via* facile charge movements, stability etc. Further, such 1-D carbon supports are ideal for devising safer solid polymer electrolyte supercapacitors owing to their ability to form better interfaces with the electrolytes. At the same time, for future flexible applications, development of flexible, thinner electrode materials with stable activity are required. To conceptualize this, there requires highly flexible, thinner electrode materials with high electrochemical activities. The prime focus of the present thesis is thus to develop efficient electrode-electrolyte interfaces in 1-D carbon supported nanomaterials to serve as the charge storage electrodes in supercapacitors and counter electrodes in DSSCs. The thesis also focuses on the attainment of electrode flexibility by creating the efficient active sites and electrode-electrolyte interfaces in flexible substrates. With respect to the supercapacitors, the thesis starts with the development of the liquid-state based devices. The attention then moves to the development of solid-state devices and finally the thesis ends with the demonstration of flexible-solid-state devices. At the same time, DSSC counter electrode devices are applied to a TCO based DSSC counter electrode in the beginning and finally ends with TCO-free flexible counter electrode. The specific objectives of the research activities covered by the thesis are as listed as below:

Objectives

- To study the effects and benefits of 1-D nano-confinement of materials on the electrode-electrolyte interfacial processes. Evaluation of the ionic and electric mobility changes during the 1-D confinement in the electrochemical charge storage and tri-iodide reduction is a focusing area of the work.
- Application of the 1-D confined materials in supercapacitor and DSSC devices and to evaluate their performance characteristics with adequate comparison and stability analysis.
- To study the effect of the relative electrode-electrolyte interfaces in solid-state supercapacitors with varying electrode mass loading.
- To design new approaches, from materials preparation to system design, for improving the electrode-electrolyte interfaces and explore the applications of such materials in real solid-state supercapacitors with an aim to achieve redefined performance characteristics and design aspects.
- To study the performance of the solid-state devices under the conditions of varied temperature and humidity with proper comparisons with the performance characteristics of their liquid-state counterparts under the identical test conditions.
- Controlling the electrodeposition technique to manipulate the nanomaterials' structure to attain high electric as well as ionic mobility and to utilise such materials in charge-storage devices using liquid and well as solid electrolytes.
- To develop simple and scalable strategies for making flexible thin conducting substrates by utilising simple surfactant-free interfacial polymerisation techniques. Further, understanding the chemistry behind the process and utilising such large scale method of electrode preparation for developing flexible all-solid-state supercapacitors and flexible counter electrode for DSSCs.
- To understand the rate of polymerisation of the conducting polymers and its effect on dictating the polymer chain alignment as well as the doping level and to understand the outcome of these effects in deciding the conductivity of the matrix.

1.12 References

- [1] M. Gratzel, *Nature* **2001**, *414*, 338-344.
- [2] R. Vajtai, *Springer Handbook of Nanomaterials*, Springer, **2013**.
- [3] W. A. H. Helmholtz, *Physik. Tech. Reichsanst Alt* **1879**, *1*, 925.
- [4] A. Gouy, *Ann. Chim. Phys.* **1903**, *29*, 145.
- [5] O. Stem, *Z. Electrochem.* **1924**, 508.
- [6] S. Srinivasan, *Fuel Cells: From Fundamentals to Applications*, Springer, **2006**.
- [7] L. L. Zhang, X. S. Zhao, *Chem Soc Rev* **2009**, *38*, 2520-2531.
- [8] O. A. E. a. B. F. Markov, *Zh. Fiz. Khim.* **1939**, 318.
- [9] D. C. Grahame, *J. Electrochem. Soc.* **1952**, *98*, 313
- [10] M. A. V. Devanathan, *Trans. Faraday Soc.* **1954**, *50*, 373
- [11] M. A. V. D. J. O'M Bockris, and K. Mueller, *Proc. Roy. Soc, Ser. A.* **1963**, *274*, 55
- [12] M. R. Palacin, *Chem. Soc. Rev.* **2009**, *38*, 2565-2575.
- [13] N.-S. Choi, Z. Chen, S. A. Freunberger, X. Ji, Y.-K. Sun, K. Amine, G. Yushin, L. F. Nazar, J. Cho, P. G. Bruce, *Angew. Chem. Int. Ed.* **2012**, *51*, 9994-10024.
- [14] F. Béguin, V. Presser, A. Balducci, E. Frackowiak, *Adv. Mater.* **2014**, *26*, 2219-2251.
- [15] W.-D. Zhang, B. Xu, L.-C. Jiang, *J. Mater. Chem* **2010**, *20*, 6383-6391.
- [16] E. Frackowiak, G. Lota, J. Machnikowski, C. Vix-Guterl, F. Béguin, *Electrochim. Acta.* **2006**, *51*, 2209-2214.
- [17] L. Madec, A. Bouvree, P. Blanchard, C. Cougnon, T. Brousse, B. Lestriez, D. Guyomard, J. Gaubicher, *Energy & Environmental Science* **2012**, *5*, 5379-5386.
- [18] S. Roldán, M. Granda, R. Menéndez, R. Santamaría, C. Blanco, *J. Phys. Chem. C* **2011**, *115*, 17606-17611.
- [19] B. E. Conway, *Electrochemical Supercapacitors: Scientific Fundamentals and Technological Applications*, Springer, **1999**.
- [20] B. E. Conway, W. G. Pell, *J. Solid State Electrochem.* **2003**, *7*, 637-644.
- [21] B. E. Conway, V. Birss, J. Wojtowicz, *J. Power Sources* **1997**, *66*, 1-14.
- [22] (a) X. Dong, W. Shen, J. Gu, L. Xiong, Y. Zhu, H. Li, J. Shi, *J. Phys. Chem. B* **2006**, *110*, 6015-6019; (b) B. You, N. Li, H. Zhu, X. Zhu, J. Yang, *ChemSusChem* **2013**, *6*, 474-480; (c) H. Jiang, Y. Dai, Y. Hu, W. Chen, C. Li, *ACS Sustainable Chem. Eng.* **2013**, *2*, 70-74; (d) Z. Tang, C.-h. Tang, H. Gong, *Adv. Funct. Mater.* **2012**, *22*, 1272-1278; (e) Y. G. Zhu, Y. Wang, Y. Shi, J. I. Wong, H. Y. Yang, *Nano Energy* **2014**, *3*, 46-54.
- [23] (a) Q. Xiao, X. Zhou, *Electrochim. Acta.* **2003**, *48*, 575-580; (b) Y. Hou, Y. Cheng, T. Hobson, J. Liu, *Nano Letters* **2010**, *10*, 2727-2733.

- [24] T. Lee, T. Yun, B. Park, B. Sharma, H.-K. Song, B.-S. Kim, *J. Mater. Chem* **2012**, 22, 21092-21099.
- [25] W. Wang, S. Guo, I. Lee, K. Ahmed, J. Zhong, Z. Favors, F. Zaera, M. Ozkan, C. S. Ozkan, *Sci. Rep.* **2014**, 4.
- [26] X. Lu, M. Yu, T. Zhai, G. Wang, S. Xie, T. Liu, C. Liang, Y. Tong, Y. Li, *Nano Lett* **2013**, 13, 2628-2633.
- [27] C. Peng, S. Zhang, X. Zhou, G. Z. Chen, *Energy & Environmental Science* **2010**, 3, 1499.
- [28] (a) K. Fic, G. Lota, M. Meller, E. Frackowiak, *Energy & Environmental Science* **2012**, 5, 5842; (b) J. H. Chae, G. Z. Chen, *Electrochim. Acta.* **2012**, 86, 248-254.
- [29] A. Du Pasquier, I. Plitz, S. Menocal, G. Amatucci, *J. Power Sources* **2003**, 115, 171-178.
- [30] (a) H. Li, L. Cheng, Y. Xia, *Electrochem. Solid State Lett.* **2005**, 8, A433-A436; (b) D. Puthusseri, V. Aravindan, B. Anothumakkool, S. Kurungot, S. Madhavi, S. Ogale, *Small* **2014**, 10, 4395-4402.
- [31] V. L. Pushparaj, M. M. Shaijumon, A. Kumar, S. Murugesan, L. Ci, R. Vajtai, R. J. Linhardt, O. Nalamasu, P. M. Ajayan, *Proc. Natl. Acad. Sci.* **2007**, 104, 13574-13577.
- [32] M. D. Stoller, S. Murali, N. Quarles, Y. Zhu, J. R. Potts, X. Zhu, H.-W. Ha, R. S. Ruoff, *Phys. Chem. Chem. Phys.* **2012**, 14, 3388-3391.
- [33] V. Aravindan, J. Gnanaraj, Y.-S. Lee, S. Madhavi, *Chem. Rev.* **2014**, 114, 11619-11635.
- [34] M. Yoshio, H. Nakamura, H. Wang, *Electrochem. Solid State Lett.* **2006**, 9, A561-A563.
- [35] A. G. Pandolfo, A. F. Hollenkamp, *J. Power Sources* **2006**, 157, 11-27.
- [36] E. Frackowiak, *Phys. Chem. Chem. Phys.* **2007**, 9, 1774-1785.
- [37] C. Y. Yin, M. K. Aroua, W. M. A. W. Daud, *Sep. Purif. Technol.* **2007**, 52, 403-415.
- [38] (a) C. O. Ania, V. Khomenko, E. Raymundo-Piñero, J. B. Parra, F. Béguin, *Adv. Funct. Mater.* **2007**, 17, 1828-1836; (b) H. Wang, Q. Gao, J. Hu, Z. Chen, *Carbon* **2009**, 47, 2259-2268.
- [39] (a) C. Vix-Guterl, E. Frackowiak, K. Jurewicz, M. Friebe, J. Parmentier, F. Béguin, *Carbon* **2005**, 43, 1293-1302; (b) W. Li, D. Chen, Z. Li, Y. Shi, Y. Wan, G. Wang, Z. Jiang, D. Zhao, *Carbon* **2007**, 45, 1757-1763.
- [40] (a) B. Liu, H. Shioyama, H. Jiang, X. Zhang, Q. Xu, *Carbon* **2010**, 48, 456-463; (b) J. Hu, H. Wang, Q. Gao, H. Guo, *Carbon* **2010**, 48, 3599-3606.
- [41] (a) J. Chmiola, G. Yushin, R. Dash, Y. Gogotsi, *J. Power Sources* **2006**, 158, 765-772; (b) J. Chmiola, G. Yushin, Y. Gogotsi, C. Portet, P. Simon, P. L. Taberna,

- Science* **2006**, *313*, 1760-1763; (c) Y. Korenblit, M. Rose, E. Kockrick, L. Borchardt, A. Kvit, S. Kaskel, G. Yushin, *ACS Nano* **2010**, *4*, 1337-1344.
- [42] Y. Gogotsi, A. Nikitin, H. Ye, W. Zhou, J. E. Fischer, B. Yi, H. C. Foley, M. W. Barsoum, *Nat. Mater.* **2003**, *2*, 591-594.
- [43] (a) D. N. Futaba, K. Hata, T. Yamada, T. Hiraoka, Y. Hayamizu, Y. Kakudate, O. Tanaike, H. Hatori, M. Yumura, S. Iijima, *Nat. Mater.* **2006**, *5*, 987-994; (b) M. Kaempgen, C. K. Chan, J. Ma, Y. Cui, G. Gruner, *Nano Letters* **2009**, *9*, 1872-1876.
- [44] C. Niu, E. K. Sichel, R. Hoch, D. Moy, H. Tennent, *Appl. Phys. Lett.* **1997**, *70*, 1480-1482.
- [45] Y.-T. Kim, Y. Ito, K. Tadai, T. Mitani, U.-S. Kim, H.-S. Kim, B.-W. Cho, *Appl. Phys. Lett.* **2005**, *87*, -.
- [46] C. Yuan, L. Shen, D. Li, F. Zhang, X. Lu, X. Zhang, *Appl. Surf. Sci.* **2010**, *257*, 440-445.
- [47] F. Béguin, K. Szostak, G. Lota, E. Frackowiak, *Adv. Mater.* **2005**, *17*, 2380-2384.
- [48] C. Kim, B. T. N. Ngoc, K. S. Yang, M. Kojima, Y. A. Kim, Y. J. Kim, M. Endo, S. C. Yang, *Adv. Mater.* **2007**, *19*, 2341-2346.
- [49] L. Yang, S. Cheng, Y. Ding, X. Zhu, Z. L. Wang, M. Liu, *Nano Letters* **2011**, *12*, 321-325.
- [50] (a) J. Jang, J. Bae, M. Choi, S.-H. Yoon, *Carbon* **2005**, *43*, 2730-2736; (b) X. Yan, Z. Tai, J. Chen, Q. Xue, *Nanoscale* **2011**, *3*, 212-216.
- [51] C. Kim, Y.-O. Choi, W.-J. Lee, K.-S. Yang, *Electrochim. Acta.* **2004**, *50*, 883-887.
- [52] S. Hou, X. Cai, Y. Fu, Z. Lv, D. Wang, H. Wu, C. Zhang, Z. Chu, D. Zou, *J. Mater. Chem.* **2011**, *21*, 13776-13779.
- [53] M. Endo, Y. A. Kim, T. Hayashi, K. Nishimura, T. Matusita, K. Miyashita, M. S. Dresselhaus, *Carbon* **2001**, *39*, 1287-1297.
- [54] E. S. Steigerwalt, G. A. Deluga, C. M. Lukehart, *J. Phys. Chem. B* **2002**, *106*, 760-766.
- [55] T. Kim, S. Lim, K. Kwon, S.-H. Hong, W. Qiao, C. K. Rhee, S.-H. Yoon, I. Mochida, *Langmuir* **2006**, *22*, 9086-9088.
- [56] A. K. Geim, K. S. Novoselov, *Nat. Mater.* **2007**, *6*, 183-191.
- [57] K. S. Novoselov, A. K. Geim, S. V. Morozov, D. Jiang, Y. Zhang, S. V. Dubonos, I. V. Grigorieva, A. A. Firsov, *Science* **2004**, *306*, 666-669.
- [58] V. C. Tung, M. J. Allen, Y. Yang, R. B. Kaner, *Nat. Nanotechnol.* **2009**, *4*, 25-29.
- [59] D. B. Shinde, J. Debgupta, A. Kushwaha, M. Aslam, V. K. Pillai, *J. Am. Chem. Soc.* **2011**, *133*, 4168-4171.
- [60] M. Choucair, P. Thordarson, J. A. Stride, *Nat. Nanotechnol.* **2009**, *4*, 30-33.

- [61] K. V. Emtsev, A. Bostwick, K. Horn, J. Jobst, G. L. Kellogg, L. Ley, J. L. McChesney, T. Ohta, S. A. Reshanov, J. Rohrl, E. Rotenberg, A. K. Schmid, D. Waldmann, H. B. Weber, T. Seyller, *Nat. Mater.* **2009**, *8*, 203-207.
- [62] P. W. Sutter, J.-I. Flege, E. A. Sutter, *Nat. Mater.* **2008**, *7*, 406-411.
- [63] K. S. Kim, Y. Zhao, H. Jang, S. Y. Lee, J. M. Kim, K. S. Kim, J.-H. Ahn, P. Kim, J.-Y. Choi, B. H. Hong, *Nature* **2009**, *457*, 706-710.
- [64] X. Yang, X. Dou, A. Rouhanipour, L. Zhi, H. J. Räder, K. Müllen, *J. Am. Chem. Soc.* **2008**, *130*, 4216-4217.
- [65] W. S. Hummers, R. E. Offeman, *J. Am. Chem. Soc.* **1958**, *80*, 1339-1339.
- [66] N. I. Kovtyukhova, P. J. Ollivier, B. R. Martin, T. E. Mallouk, S. A. Chizhik, E. V. Buzaneva, A. D. Gorchinskiy, *Chem. Mater.* **1999**, *11*, 771-778.
- [67] S. R. C. Vivekchand, C. Rout, K. S. Subrahmanyam, A. Govindaraj, C. N. R. Rao, *J. Chem. Sci.* **2008**, *120*, 9-13.
- [68] M. D. Stoller, S. Park, Y. Zhu, J. An, R. S. Ruoff, *Nano Letters* **2008**, *8*, 3498-3502.
- [69] (a) C. Liu, Z. Yu, D. Neff, A. Zhamu, B. Z. Jang, *Nano Letters* **2010**, *10*, 4863-4868; (b) Y. Xu, Z. Lin, X. Zhong, X. Huang, N. O. Weiss, Y. Huang, X. Duan, *Nat. Commun.* **2014**, *5*; (c) X. Yang, C. Cheng, Y. Wang, L. Qiu, D. Li, *Science* **2013**, *341*, 534-537; (d) Y. Zhu, S. Murali, M. D. Stoller, K. J. Ganesh, W. Cai, P. J. Ferreira, A. Pirkle, R. M. Wallace, K. A. Cychosz, M. Thommes, D. Su, E. A. Stach, R. S. Ruoff, *Science* **2011**, *332*, 1537-1541.
- [70] S. Trasatti, G. Buzzanca, *J. Electroanal. Chem. Interfac* **1971**, *29*, A1-A5.
- [71] D. Michell, D. A. J. Rand, R. Woods, *J. Electroanal. Chem. Interfac* **1978**, *89*, 11-27.
- [72] V. Ozolins, F. Zhou, M. Asta, *Acc. Chem. Res.* **2013**, *46*, 1084-1093.
- [73] R. Fu, Z. Ma, J. P. Zheng, *J. Phys. Chem. B* **2002**, *106*, 3592-3596.
- [74] (a) G. Wang, L. Zhang, J. Zhang, *Chem. Soc. Rev.* **2012**, *41*, 797-828; (b) W. Sugimoto, H. Iwata, K. Yokoshima, Y. Murakami, Y. Takasu, *J. Phys. Chem. B* **2005**, *109*, 7330-7338.
- [75] M. Toupin, T. Brousse, D. Bélanger, *Chem. Mater.* **2004**, *16*, 3184-3190.
- [76] J. N. Broughton, M. J. Brett, *Electrochim. Acta.* **2005**, *50*, 4814-4819.
- [77] (a) D.-W. Wang, F. Li, H.-M. Cheng, *J. Power Sources* **2008**, *185*, 1563-1568; (b) H. Jiang, T. Zhao, C. Li, J. Ma, *J. Mater. Chem* **2011**, *21*, 3818-3823.
- [78] (a) T. Zhao, H. Jiang, J. Ma, *J. Power Sources* **2011**, *196*, 860-864; (b) J. Xu, L. Gao, J. Cao, W. Wang, Z. Chen, *Electrochim. Acta.* **2010**, *56*, 732-736.
- [79] Q. Qu, S. Yang, X. Feng, *Adv. Mater.* **2011**, *23*, 5574-5580.
- [80] S. Boukhalifa, K. Evanoff, G. Yushin, *Energy & Environmental Science* **2012**, *5*, 6872-6879.
- [81] K. Rajendra Prasad, N. Miura, *Electrochem. Commun.* **2004**, *6*, 849-852.

- [82] D. P. Dubal, D. S. Dhawale, R. R. Salunkhe, V. S. Jamdade, C. D. Lokhande, J. *Alloys Compd.* **2010**, *492*, 26-30.
- [83] (a) R. B. Kaner, A. G. MacDiarmid, *J. Chem. Soc., Faraday Trans. 1: Physical Chemistry in Condensed Phases* **1984**, *80*, 2109-2118; (b) R. B. Kaner, A. G. Macdiarmid, *Synth. Met.* **1986**, *14*, 3-12.
- [84] S. Gottesfeld, A. Redondo, S. W. Feldberg, *J. Electrochem. Soc.* **1987**, *134*, 271-272.
- [85] B. E. Conway, in *Power Sources Symposium, 1990., Proceedings of the 34th International*, **1990**, pp. 319-327.
- [86] Y. Wang, *Journal of Physics: Conference Series* **2009**, *152*, 012023.
- [87] M. Ue, *J. Electrochem. Soc.* **1994**, *141*, 3336-3342.
- [88] M. Galiński, A. Lewandowski, I. Stępnia, *Electrochim. Acta.* **2006**, *51*, 5567-5580.
- [89] M. Armand, F. Endres, D. R. MacFarlane, H. Ohno, B. Scrosati, *Nat. Mater.* **2009**, *8*, 621-629.
- [90] C. A. Kelly, F. Farzad, D. W. Thompson, G. J. Meyer, *Langmuir* **1999**, *15*, 731-737.
- [91] F. Farzad, D. W. Thompson, C. A. Kelly, G. J. Meyer, *J. Am. Chem. Soc.* **1999**, *121*, 5577-5578.
- [92] K. C. D. Robson, P. G. Bomben, C. P. Berlinguette, *Dalton Trans.* **2012**, *41*, 7814-7829.
- [93] M. Ikegami, K. Miyoshi, T. Miyasaka, K. Teshima, T. C. Wei, C. C. Wan, Y. Y. Wang, *Appl. Phys. Lett.* **2007**, *90*, 153122.
- [94] G. Wang, R. Lin, Y. Lin, X. Li, X. Zhou, X. Xiao, *Electrochim. Acta.* **2005**, *50*, 5546-5552.
- [95] S.-S. Kim, Y.-C. Nah, Y.-Y. Noh, J. Jo, D.-Y. Kim, *Electrochim. Acta.* **2006**, *51*, 3814-3819.
- [96] L. Chen, W. Tan, J. Zhang, X. Zhou, X. Zhang, Y. Lin, *Electrochim. Acta.* **2010**, *55*, 3721-3726.
- [97] M. Wu, T. Ma, *ChemSusChem* **2012**, *5*, 1343-1357.
- [98] X. Fang, T. Ma, G. Guan, M. Akiyama, T. Kida, E. Abe, *J. Electroanal. Chem.* **2004**, *570*, 257-263.
- [99] H. Jeong, Y. Pak, Y. Hwang, H. Song, K. H. Lee, H. C. Ko, G. Y. Jung, *Small* **2012**, *8*, 3757-3761.
- [100] C.-K. Hsieh, M.-C. Tsai, C.-Y. Su, S.-Y. Wei, M.-Y. Yen, C.-C. M. Ma, F.-R. Chen, C.-H. Tsai, *Chem. Commun.* **2011**, *47*, 11528-11530.
- [101] Y.-S. Chien, P.-Y. Yang, I.-C. Lee, C.-C. Chu, C.-H. Chou, H.-C. Cheng, W.-E. Fu, *Appl. Phys. Lett.* **2014**, *104*, -.
- [102] M.-Y. Yen, C.-C. Teng, M.-C. Hsiao, P.-I. Liu, W.-P. Chuang, C.-C. M. Ma, C.-K. Hsieh, M.-C. Tsai, C.-H. Tsai, *J. Mater. Chem.* **2011**, *21*, 12880-12888.

- [103] A. Thiangkaew, K. Keothongkham, W. Maiaugree, W. Jareenboon, T. Kamwanna, S. Pimanpang, V. Amornkitbamrung, *J. Korean Phys. Soc.* **2014**, *64*, 1356-1362.
- [104] L. Fan, J. Wu, Y. Huang, J. Lin, *Electronic Components & Materials* **2003**, *22*, 1-3.
- [105] E. Olsen, G. Hagen, S. Eric Lindquist, *Sol. Energy Mater. Sol. Cells* **2000**, *63*, 267-273.
- [106] S. A. Sapp, C. M. Elliott, C. Contado, S. Caramori, C. A. Bignozzi, *J. Am. Chem. Soc.* **2002**, *124*, 11215-11222.
- [107] Y.-L. Lee, Y.-S. Lo, *Adv. Funct. Mater.* **2009**, *19*, 604-609.
- [108] M. Wu, Q. Zhang, J. Xiao, C. Ma, X. Lin, C. Miao, Y. He, Y. Gao, A. Hagfeldt, T. Ma, *J. Mater. Chem* **2011**, *21*, 10761-10766.
- [109] M. Wang, A. M. Anghel, B. Marsan, N.-L. Cevey Ha, N. Pootrakulchote, S. M. Zakeeruddin, M. Grätzel, *J. Am. Chem. Soc.* **2009**, *131*, 15976-15977.
- [110] (a) X. Xin, M. He, W. Han, J. Jung, Z. Lin, *Angew. Chem. Int. Ed.* **2011**, *50*, 11739-11742; (b) Y. C. Wang, D. Y. Wang, Y. T. Jiang, H. A. Chen, C. C. Chen, K. C. Ho, H. L. Chou, C. W. Chen, *Angew. Chem. Int. Ed* **2013**, *52*, 6694-6698; (c) X. Miao, K. Pan, G. Wang, Y. Liao, L. Wang, W. Zhou, B. Jiang, Q. Pan, G. Tian, *Chem. Eur. J.* **2014**, *20*, 474-482.
- [111] Y. Y. Dou, G. R. Li, J. Song, X. P. Gao, *Phys. Chem. Chem. Phys.* **2012**, *14*, 1339-1342.
- [112] (a) M. Wu, X. Lin, Y. Wang, L. Wang, W. Guo, D. Qi, X. Peng, A. Hagfeldt, M. Gratzel, T. Ma, *J Am Chem Soc* **2012**, *134*, 3419-3428; (b) G. R. Li, F. Wang, Q. W. Jiang, X. P. Gao, P. W. Shen, *Angew. Chem. Int. Ed.* **2010**, *49*, 3653-3656.
- [113] J. Xia, C. Yuan, S. Yanagida, *ACS Appl. Mater. Interfaces.* **2010**, *2*, 2136-2139.
- [114] C.-W. Kung, H.-W. Chen, C.-Y. Lin, K.-C. Huang, R. Vittal, K.-C. Ho, *ACS Nano* **2012**, *6*, 7016-7025.
- [115] S.-H. Chang, M.-D. Lu, Y.-L. Tung, H.-Y. Tuan, *ACS Nano* **2013**, *7*, 9443-9451.
- [116] Y. Xiao, G. Han, H. Zhou, Y. Li, J.-Y. Lin, *Electrochim. Acta.* **2015**, *155*, 103-109.
- [117] J. Song, G. R. Li, C. Y. Wu, X. P. Gao, *J. Power Sources* **2014**, *266*, 464-470.
- [118] L. Zhang, H. K. Mulmudi, S. K. Batabyal, Y. M. Lam, S. G. Mhaisalkar, *Phys. Chem. Chem. Phys.* **2012**, *14*, 9906-9911.
- [119] F. Gong, H. Wang, X. Xu, G. Zhou, Z. S. Wang, *J. Am. Chem. Soc.* **2012**, *134*, 10953-10958.
- [120] C.-T. Lee, J.-D. Peng, C.-T. Li, Y.-L. Tsai, R. Vittal, K.-C. Ho, *Nano Energy* **2014**, *10*, 201-211.
- [121] I. A. Ji, H. M. Choi, J. H. Bang, *Mater. Lett.* **2014**, *123*, 51-54.
- [122] Y. Duan, Q. Tang, J. Liu, B. He, L. Yu, *Angew. Chem. Int. Ed.* **2014**, *53*, 14569-14574.

- [123] A. Kay, M. Grätzel, *Sol. Energy Mater. Sol. Cells* **1996**, *44*, 99.
- [124] K. Imoto, K. Takahashi, T. Yamaguchi, T. Komura, J.-i. Nakamura, K. Murata, *Sol. Energy Mater. Sol. Cells* **2003**, *79*, 459-469.
- [125] B. Zhao, H. Huang, P. Jiang, H. Zhao, X. Huang, P. Shen, D. Wu, R. Fu, S. Tan, *J. Phys. Chem. C* **2011**, *115*, 22615-22621.
- [126] (a) J. W. Guo, B. Zhang, Y. Hou, S. Yang, X. H. Yang, H. G. Yang, *J. Mater. Chem. A* **2013**, *1*, 1982; (b) J.-G. Park, M. S. Akhtar, Z. Y. Li, D.-S. Cho, W. Lee, O. B. Yang, *Electrochim. Acta* **2012**, *85*, 600-604; (c) J. Han, H. Kim, D. Y. Kim, S. M. Jo, S.-Y. Jang, *ACS Nano* **2010**, *4*, 3503-3509; (d) H. Kim, H. Choi, S. Hwang, Y. Kim, M. Jeon, *Nanoscale Res. Lett.* **2012**, *7*, 53; (e) E. Ramasamy, W. J. Lee, D. Y. Lee, J. S. Song, *Electrochem. Commun.* **2008**, *10*, 1087-1089.
- [127] (a) D. Sebastián, V. Baglio, M. Girolamo, R. Moliner, M. J. Lázaro, A. S. Aricò, *J. Power Sources* **2014**, *250*, 242-249; (b) S. M. Mahpeykar, M. K. Tabatabaei, H. Ghafoori-fard, H. Habibiyani, J. Koohsorkhi, *Nanotechnology* **2013**, *24*, 435402.
- [128] (a) M.-Y. Yen, C.-K. Hsieh, C.-C. Teng, M.-C. Hsiao, P.-I. Liu, C.-C. M. Ma, M.-C. Tsai, C.-H. Tsai, Y.-R. Lin, T.-Y. Chou, *RSC Advances* **2012**, *2*, 2725; (b) J. Velten, A. J. Mozer, D. Li, D. Officer, G. Wallace, R. Baughman, A. Zakhidov, *Nanotechnology* **2012**, *23*, 085201; (c) H. Wang, K. Sun, F. Tao, D. J. Stacchiola, Y. H. Hu, *Angew. Chem. Int. Ed.* **2013**, *52*, 9210-9214; (d) Y. Xue, J. Liu, H. Chen, R. Wang, D. Li, J. Qu, L. Dai, *Angew. Chem. Int. Ed.* **2012**, *51*, 12124-12127.
- [129] M. J. Ju, J. C. Kim, H.-J. Choi, I. T. Choi, S. G. Kim, K. Lim, J. Ko, J.-J. Lee, I.-Y. Jeon, J.-B. Baek, H. K. Kim, *ACS Nano* **2013**, *7*, 5243-5250.
- [130] E. Ramasamy, W. J. Lee, D. Y. Lee, J. S. Song, *Appl. Phys. Lett.* **2007**, *90*, -.
- [131] L. Kavan, J. H. Yum, M. Grätzel, *ACS Nano* **2010**, *5*, 165-172.
- [132] J. D. Roy-Mayhew, D. J. Bozym, C. Punckt, I. A. Aksay, *ACS Nano* **2010**, *4*, 6203-6211.
- [133] H. Zhu, H. Zeng, V. Subramanian, C. Masarapu, K.-H. Hung, B. Wei, *Nanotechnology* **2008**, *19*, 465204.
- [134] J. G. Nam, Y. J. Park, B. S. Kim, J. S. Lee, *Scripta Materialia* **2010**, *62*, 148-150.
- [135] M. Wu, T. Ma, *ChemSusChem* **2012**, *5*, 1343-1357.
- [136] (a) F. D. Jonas, G. D. Heywang, W. Schmidtberg, J. P. D. Heinze, M. Dietrich, Google Patents, **1989**; (b) S. K. Andreas Elschner, Wilfried Lovenich, Udo Merker, Knud Reuter *PEDOT: Principles and Applications of an Intrinsically Conductive Polymer*, CRC, **2011**.
- [137] L. Groenendaal, F. Jonas, D. Freitag, H. Pielartzik, J. R. Reynolds, *Adv. Mater.* **2000**, *12*, 481-494.
- [138] T. Yohannes, O. Inganäs, *Sol. Energy Mater. Sol. Cells* **1998**, *51*, 193-202.

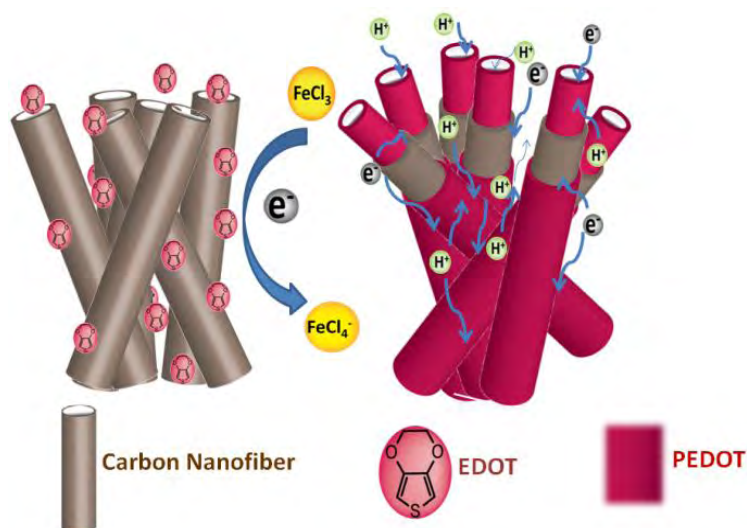
- [139] (a) D. Alemu Mengistie, P.-C. Wang, C.-W. Chu, *J. Mater. Chem. A* **2013**, *1*, 9907-9915; (b) M. Vosgueritchian, D. J. Lipomi, Z. Bao, *Adv. Funct. Mater.* **2012**, *22*, 421-428.
- [140] J. Xia, N. Masaki, K. Jiang, S. Yanagida, *J. Mater. Chem* **2007**, *17*, 2845-2850.
- [141] J. M. Pringle, V. Armel, D. R. MacFarlane, *Chem Commun (Camb)* **2010**, *46*, 5367-5369.
- [142] T. H. Lee, K. Do, Y. W. Lee, S. S. Jeon, C. Kim, J. Ko, S. S. Im, *J. Mater. Chem* **2012**, *22*, 21624-21629.
- [143] (a) H.-J. Shin, S. S. Jeon, S. S. Im, *Synth. Met.* **2011**, *161*, 1284-1288; (b) J. Zhang, X. Li, W. Guo, T. Hreid, J. Hou, H. Su, Z. Yuan, *Electrochim. Acta.* **2011**, *56*, 3147-3152.
- [144] (a) K. S. Lee, H. K. Lee, D. H. Wang, N. G. Park, J. Y. Lee, O. O. Park, J. H. Park, *Chem Commun (Camb)* **2010**, *46*, 4505-4507; (b) S. Ahmad, E. Dell'Orto, J. H. Yum, F. Kessler, M. K. Nazeeruddin, M. Gratzel, *Chem Commun (Camb)* **2012**, *48*, 9714-9716; (c) S. Nagarajan, P. Sudhagar, V. Raman, W. Cho, K. S. Dhathathreyan, Y. S. Kang, *J. Mater. Chem. A* **2013**, *1*, 1048; (d) J. Kwon, V. Ganapathy, Y. H. Kim, K. D. Song, H. G. Park, Y. Jun, P. J. Yoo, J. H. Park, *Nanoscale* **2013**, *5*, 7838-7843; (e) T. L. Zhang, H. Y. Chen, C. Y. Su, D. B. Kuang, *J. Mater. Chem. A* **2013**, *1*, 1724-1730.
- [145] (a) K.-M. Lee, C.-Y. Hsu, P.-Y. Chen, M. Ikegami, T. Miyasaka, K.-C. Ho, *Phys. Chem. Chem. Phys.* **2009**, *11*, 3375-3379; (b) L. Kun-Mu, C. Po-Yen, H. Chih-Yu, H. Jen-Hsien, H. Wen-Hsien, C. Hung-Chang, H. Kuo-Chuan, *J. Power Sources* **2009**, *188*.
- [146] (a) J. Luo, H.-j. Niu, W.-j. Wu, C. Wang, X.-d. Bai, W. Wang, *Solid State Sci.* **2012**, *14*, 145-149; (b) M. R. Karim, A. Islam, S. P. Singh, L. Han, *Adv. Opt. Electron. mic* **2011**, *2011*, 7.
- [147] J. Wu, Q. Li, L. Fan, Z. Lan, P. Li, J. Lin, S. Hao, *J. Power Sources* **2008**, *181*, 172-176.
- [148] L.-Y. Chang, C.-T. Li, Y.-Y. Li, C.-P. Lee, M.-H. Yeh, K.-C. Ho, J.-J. Lin, *Electrochim. Acta.* **2015**, *155*, 263-271.
- [149] J. Xia, L. Chen, S. Yanagida, *J. Mater. Chem* **2011**, *21*, 4644-4649.
- [150] (a) J. Luo, H.-j. Niu, H.-l. Wen, W.-j. Wu, P. Zhao, C. Wang, X.-d. Bai, W. Wang, *Mater. Res. Bull.* **2013**, *48*, 988-994; (b) S. P. Lim, A. Pandikumar, Y. S. Lim, N. M. Huang, H. N. Lim, *Sci. Rep.* **2014**, *4*, 5305.
- [151] W. Liu, Y. Fang, P. Xu, Y. Lin, X. Yin, G. Tang, M. He, *ACS Appl. Mater. Inter.* **2014**, *6*, 16249-16256.

- [152] G. Yue, L. Wang, X. a. Zhang, J. Wu, Q. Jiang, W. Zhang, M. Huang, J. Lin, *Energy (Oxford, U. K.)* **2014**, *67*, 460-467.
- [153] T. Peng, W. Sun, C. Huang, W. Yu, B. Sebo, Z. Dai, S. Guo, X. Z. Zhao, *ACS Appl. Mater. Inter.* **2014**, *6*, 14-17.
- [154] D. K. Hwang, D. Song, S. S. Jeon, T. H. Han, Y. S. Kang, S. S. Im, *J. Mater. Chem. A* **2014**, *2*, 859-865.
- [155] L. Qinghua, W. Jihuai, T. Qunwei, L. Zhang, L. Pinjiang, L. Jianming, F. Leqing, *Electrochem. Commun.* **2008**, *10*.
- [156] Q. Tai, B. Chen, F. Guo, S. Xu, H. Hu, B. Sebo, X.-Z. Zhao, *ACS Nano* **2011**, *5*, 3795-3799.
- [157] (a) B. He, Q. Tang, M. Wang, H. Chen, S. Yuan, *ACS Appl. Mater. Inter.* **2014**, *6*, 8230-8236; (b) Y.-S. Wang, S.-M. Li, S.-T. Hsiao, H. Wei, S.-Y. Yang, H.-W. Tien, C.-C. M. Ma, C.-C. Hu, *J. Power Sources* **2014**, *260*, 326-337.
- [158] M. Wang, Q. Tang, H. Chen, B. He, *Electrochim. Acta.* **2014**, *125*, 510-515.
- [159] Y. W. Lee, K. Do, T. H. Lee, S. S. Jeon, W. J. Yoon, C. Kim, J. Ko, S. S. Im, *Synth. Met.* **2013**, *174*, 6-13.
- [160] Q. Tang, H. Cai, S. Yuan, X. Wang, *J. Mater. Chem. A* **2013**, *1*, 317-323.
- [161] A. Kancierzewska, E. Dobruchowska, A. Baranzahi, E. Carlegrim, M. Fahlman, M. A. Girtu, *J. Optoelectron. Adv. Mater.* **2007**, *9*, 1052-1059.
- [162] S. Biallozor, A. Kupniewska, *Electrochem. Commun.* **2000**, *2*, 480-486.
- [163] R. Liu, J. Duay, S. B. Lee, *Chem. Commun.* **2011**, *47*, 1384-1404.
- [164] H.-X. Zhang, C. Feng, Y.-C. Zhai, K.-L. Jiang, Q.-Q. Li, S.-S. Fan, *Adv. Mater.* **2009**, *21*, 2299-2304.
- [165] K. H. An, K. K. Jeon, J. K. Heo, S. C. Lim, D. J. Bae, Y. H. Lee, *J. Electrochem. Soc.* **2002**, *149*, A1058-A1062.
- [166] L. Ji, X. Zhang, *Carbon* **2009**, *47*, 3219-3226.
- [167] G.-r. Li, F. Wang, Q.-w. Jiang, X.-p. Gao, P.-w. Shen, *Angew. Chem. Int. Ed.* **2010**, *49*, 3653-3656.
- [168] J. Li, L. Cui, X. Zhang, *Appl. Surface Science* **2010**, *256*, 4339-4343.
- [169] R. B. Rakhi, W. Chen, D. Cha, H. N. Alshareef, *Nano Letters* **2012**, *12*, 2559-2567.
- [170] R. Liu, S. B. Lee, *J Am Chem Soc* **2008**, *130*, 2942-2943.

Chapter-2

1-D Confinement of PEDOT Using Hollow Carbon Nanofiber: An Efficient Charge Storage Material with High Catalytic Activity for Tri-iodide Reduction in DSSC

In this chapter, preparation of a highly conducting porous 1-dimensionally (1-D) aligned nanohybrid of polyethylenedioxythiophene (PEDOT) using a cup-stacked hollow carbon nanofiber (CNF) and its applications as a solid template for potential



charge storage and DSSC counter electrode are reported. The unique features of the nano confinement involve the significantly high porosity and conductivity with the establishment of the 1-D architecture. This preferential orientation along the pore axis during the slow polymerization brings an order in the polymer chain which

enhances the π conjugation length, leading to higher electrical conductivity. The tubular morphology of CNF with open tips provides facile routes for the electrolyte and, thereby, to achieve low charge transfer resistance. Apart from this, the solid CNF backbone helps in improving the stability and surface area of PEDOT. Thus, the overall improvement in conductivity, surface area, charge-transfer resistance, stability etc. make the derived 1-D nanohybrid material as a potential material for supercapacitor and a counter electrode for DSSC.

Content in this chapter is published in the following articles:

Nanoscale, 2014, 6, 10332-10339

(<http://pubs.rsc.org/en/content/articlelanding/2014/nr/c4nr00717d#!divAbstract>)

RSC Adv, 2013, 3, 11877-11887

(<http://pubs.rsc.org/en/content/articlelanding/2013/ra/c3ra40853a#!divAbstract>)

Reproduced by permission of The Royal Society of Chemistry

2.1 Introduction

Recently, there has been a great interest in developing various nanostructured hybrid materials for energy applications^[1] due to the efficiency of many of such materials to overcome the pertinent issues on performance and durability. The growing presence of such materials in niche applications such as electrodes for fuel cells,^[2] supercapacitors,^[3] Li ion batteries,^[4] solar cells^[5] etc. underlines the wide prospects of these materials. The issues related to the performance, efficiency, cost and durability of the electrodes are continuing to be the daunting challenges in the ongoing efforts for bringing many of these systems in the main stream. Therefore, realization of new materials which can make revolutionary changes in the key limiting areas is of profound importance. Especially in the case of supercapacitors and dye-sensitized solar cells (DSSCs)^[5], nanostructured inorganic-organic hybrids^[1a, 3a, 6] have great scope. As one of the key advantages, the inorganic part of the nanocomposite can serve as a solid template to dictate the polymer growth, leading to nanoconfinement and enhancement in the electrode-electrolyte interfacial area. Thus, the added properties of the two materials at the nano regime help such hybrid materials to outperform in functions compared to the constituent materials. Such nano hybrid materials based on conducting polymer^[7] are more interesting in the electrochemical energy devices due to their high electrical conductivity, low band gap, cost and processability.^[8] Among the various conducting polymers which are widely essayed in literature, polyethylenedioxythiophene (PEDOT)^[9] has been evolved as one of the most successful material from both fundamental and practical perspectives for various applications beyond electrochemistry. PEDOT possesses several beneficial features over its competitors, which include its low oxidation potential, wide potential window (1.2-1.5 V) and moderate band gap.^[10] In addition to its reasonable conductivity, the material is also found to be transparent, easy to process and environmentally stable. Due to these exceptionally unique properties, PEDOT has emerged as a promising material in various energy devices, especially as an “active material” for the energy storage devices^[11] and DSSC counter electrode applications.

2.1.1 PEDOT as a Charge Storage Material

PEDOT as a charge storage material has gained its identity irrespective of the

facts that the material possesses only moderate theoretical specific capacitance of 210 F g^{-1} due to its high molecular weight (142 g mol^{-1}) and low doping level (0.33) compared to its competitors.^[12] Considering the cost competitiveness of the material, the theoretical capacitance of 210 F g^{-1} itself is a good advantage. However, the reported capacitance of bulk PEDOT prepared by various methods is in a significantly low range of $50\text{-}90 \text{ F g}^{-1}$ ^[11b, 11c, 13] due to its low surface area and difficulties associated with low conductivity. More importantly, PEDOT suffers from a stability issue during cycling^[14] and it also possesses an inability to retain constant energy delivery at high power demands. This is due to the slow faradaic redox charge storage mechanism involved in the system.^[15] During charging and discharging, insertion and re-insertion of ions occur, which leads to swelling and shrinking of the polymer matrix.^[6b] Consequently, the stability of the polymer matrix reduces, which affects ion diffusion in the system and the capacitance, especially as the current demand increases.

2.1.2 PEDOT as a Counter Electrode in Dye Sensitized Solar Cell (DSSC)

PEDOT^[9] is a promising counter electrode^[16] in DSSC over costly Pt for the tri-iodide (I_3^-) reduction. This is in conjunction with its unique properties such as high catalytic activity for I_3^- reduction^[16d], low cost and high-conductivity^[10]. However, low conductivity as well as surface area in its bulk form results in poor catalytic activity. Low conductivity and surface area in the bulk synthesized PEDOT occur mainly due to the fast polymerization rate of PEDOT^[17]. Such a fast polymerization results in aggregated polymer grains which may precipitate out in the medium. In such cases, processability will become difficult due to the low solubility of PEDOT.

2.1.3 Solution for the Existing Problems

Establishing both nanomorphology of PEDOT and better mechanical stability to the system are important for improving the electrochemical properties for the above two applications and to attain overall durability. Such morphological fine tuning is expected to improve the porosity and this can facilitate ion transport to assist the fast and efficient electrode reaction. Among the various morphologies of PEDOT, the 1-D nanostructure^[18] can minimize the existing drawbacks in a better way. Among the various reported processes, the hard template assisted synthesis using electrochemical^[18-19] and chemical methods^[20] give low yield, which restricts the practical implementation of these methods. On the other hand, the soft template

assisted synthesis^[20-21] often fails to provide the required property characteristics of PEDOT.

Here, a synthetic strategy of PEDOT is developed in order to overcome its drawbacks such as fast polymerization rate, low conductivity, low surface area and low stability. This is achieved by 1-D aligning of PEDOT over a high aspect ratio carbon nanofiber (CNF) with diameter of $\sim 50-70$ nm and length of several micrometres. This method offers unique nano architecture for PEDOT by providing the mechanically stable and electrically conductive CNF as the core material and by concomitantly maintaining both high aspect ratio and interfacial areas. Formation of PEDOT as a thin layer improves the electrical conductivity and the aligned growth along the surfaces of CNF provides well defined pathways for faster movement of ions in and out of the polymer matrix. Consequently, during the electrode reactions, the nanostructured hybrid morphology helps the system to display high electrochemical activity and stability.

2.2 Experimental Section

2.2.1 Materials

Carbon nanofiber (CNF) used as the solid template was procured from Pyrograf Corporation, USA. Ethylenedioxythiophene (EDOT), 1,3-dimethylimidazolium iodide (DMII) and FeCl_3 were purchased from Aldrich Chemicals. Acetonitrile, dimethylsulfoxide (DMSO) and sulfuric acid (H_2SO_4) were procured from Rankem Chemicals. All the chemicals were used as received without any further purification. A polytetrafluoroethylene (PTFE) filter paper (pore size of $0.45 \mu\text{m}$; Rankem) was used for the filtration. A copper grid with a carbon support (Icon Analytical) was used for the HR-TEM observations. Fluorine doped Tin Oxide (FTO) glass electrode with $15 \Omega/\square$ sheet resistances was purchased from Solaronix (TCO22-15) and was used as a substrate for the counter and working electrodes.

2.2.2 Functionalization of Carbon Nanofiber (FCNF)

Functionalization of CNF was carried out by hydrogen peroxide (H_2O_2) treatment. In a typical experiment, 1 g of CNF was well dispersed in 200 ml of 30 % H_2O_2 for 15 minutes followed by refluxing at 60°C for 5 h. Subsequently, the solid mass was filtered out, washed repeatedly with deionized water and finally dried at

100 °C in an oven for 5 h. The sample which is designated as FCNF was used for the nanocomposite preparation.

2.2.3 PEDOT-FCNF Composite Preparation

50 mg of FCNF was dispersed in 10 ml of acetonitrile (HPLC) in 100 ml round bottom flask by sonication for 15 min to get proper wetting of FCNF by the solvent. To the above solution, required amount of the monomer, EDOT (3, 4-ethylenedioxy thiophene), in 10 ml acetonitrile was added drop-wise. The mixture was kept for probe sonication for 30 min. followed by vigorous stirring for 24 h at room temperature. For executing polymerization, anhydrous FeCl₃ (keeping 1:4 molar ratio with the monomer) in acetonitrile (10 ml) was added drop-wise to the above mixture. The solution becomes pale blue in colour after the addition of the oxidizing agent. The reaction mixture was kept for 48 h for stirring followed by filtering using the PTFE filter paper (pore size, 0.45 µm; Rankem). The wet cake was thoroughly washed with acetonitrile and DI water to ensure the complete removal of the unreacted monomer and excess FeCl₃. The solid mass was kept at 100 °C in an oven for overnight for drying. Keeping the preparation protocol the same and by varying the monomer content, four composites of PEDOT-CNF containing 25, 40, 60 and 80 wt. % of PEDOT were synthesized. The samples are respectively denoted as CP-25, CP-40, CP-60 and CP-80. Finally, for a comparison purpose, bulk PEDOT was also synthesized from the EDOT monomer using the similar procedure.

2.2.4 Counter Electrode Preparation

FTO plate was washed by ultra-sonication in soap solution, deionized water and absolute ethanol and 0.5 cm² of area was confined by adhesive spacer. 3 mg of the sample was dispersed well in 500 µl DMSO using a mortar pestle and 25 µl of the above solution was drop coated onto the confined area of the FTO plate. Electrodes were dried overnight at 100 °C under vacuum. Two such electrodes were sandwiched together for the symmetric cell experiments by facing each other and keeping an adhesive tape piece as a spacer. The electrolyte composition was DMII, 0.05 M LiI, 0.05 M I₂ and 0.5 M tert-butyl pyridine in 1:1 (v:v) acetonitrile and valeronitrile mixed solvent. All the electrolyte components except DMII were purchased from Sigma-Aldrich and used without further purification.

2.2.5 Dye Sensitized Solar Cell (DSSC) Fabrication

Standard P25 paste was prepared using a reported method^[22]. FTO substrates for working electrode were washed by ultra-sonication in soap solution, deionized water and absolute ethanol. The P25 paste was doctor bladed on the washed FTO plate and the plate was heated at 450 °C for 10 min. A thickness of 12-13 microns was achieved by multiple coatings. The final annealing was done for 1 h. TiCl₄ treatment on the working electrodes was done according to a reported method^[22] and the electrodes were reheated at 450 °C for 30 min. The working electrodes were soaked in 0.5 mM N719 dye solution for overnight. DSSCs were assembled using a sandwich assembly of the working electrode and counter electrode. The electrolyte composition was 1 M DMII, 0.05 M LiI, 0.05 M I₂ and 0.5 M tert-butyl pyridine. *I-V* (current vs. voltage) measurements were done under Newport Solar Simulator attached to Keithley 2420 source meter. In order to check the stability of the counter electrode for the best case, the working and counter electrodes were sealed using Surllyn.

2.2.6 Characterization

Structure and morphology of the hybrid materials were analyzed using a high-resolution transmission electron microscope (HR-TEM) Tecnai-T 30 model at an accelerated voltage of 300 kV. TEM samples were prepared by placing a drop of the catalyst sample in ethanol onto a carbon-coated Cu grid, dried in air, and loaded into the electron microscopic chamber. X-ray Diffraction (XRD) was conducted using a Philips X'pert pro powder X-ray diffractometer (Cu K α radiation, Ni filter). Thermogravimetric Analysis (TGA) was performed on a PERKIN ELMER STA 6000 analyzer from 50 to 900 °C with 10 °C min⁻¹ temperature ramp under air. X-ray Photoelectron Spectroscopic (XPS) measurements were carried out on a VG Micro Tech ESCA 300° instrument at a pressure of $> 1 \times 10^{-9}$ Torr (pass energy of 50 eV, electron take off angle of 60° and the overall resolution of ~ 0.1 eV). The Fourier Transform (FT) IR spectra was taken on a BRUKER Alpha model in ATR mode. Raman analysis was carried out on Horiba JobinYvon Inverted LabRAM HR800 VIS-NIR using 532 nm solid-state diode laser beams. Nitrogen adsorption-desorption experiments were conducted at 77 K using QuantachromeQuadratorb automatic volumetric instrument. Ultra pure N₂ (99.999%) was purified further by using calcium aluminosilicate adsorbents to remove trace amounts of water and other impurities

before introduction into the system. For measurements at 77 K, a standard low-temperature liquid nitrogen Dewar vessel was used. Before the gas adsorption measurements, the sample was activated at room temperature (for 24 h) and 100 °C (for 36 h) under ultrahigh vacuum (10⁻⁸ mbar) for overnight. About 50 mg of the samples was loaded for gas adsorption, and the weight of each sample was recorded before and after out gassing to confirm the complete removal of all guest molecules including the coordinated H₂O in the sample. Electrical conductivity was measured using four-probe conductivity method at room temperature with a probe distance of 0.2 cm ± 2 %. Variable current source (mA) and micro voltmeter were used for the experiments. Sample in the form of a thick pellet with a diameter of 13 mm and a thickness of ~0.5 mm was prepared using a pellet maker. All the samples were given the same hydraulic pressure of 150 kg cm⁻² for 3 min. Conductivity was measured by placing the sample pellets on a non-conducting surface and the measurement was done by the four probe method by using the following equation:

$$K = \frac{1}{\rho} \rho = \frac{2 \pi S \frac{V}{I}}{G_7 \left(\frac{W}{S}\right)}$$

where, K = conductivity (S cm⁻¹), ρ = resistivity (Ω cm), G₇($\frac{W}{S}$) = correction factor, W = thickness of the pellet, S = probe spacing (2mm), V = voltage (V) and I = current (A).

2.2.7 Electrochemical Studies

All the electrochemical studies for charge-storage properties were carried in a Bio-Logic SP-300 Potentio-Galvanostat using a two-electrode test cell containing 0.5 M H₂SO₄ as the electrolyte. For preparing the electrodes, 4 mg of the sample was dispersed in 2 ml of EtOH:H₂O (3:2). From this, 1 mg of the catalyst was drop coated on to 1 cm² area of a Toray carbon paper (non-teflonated) having a dimension of 1 x 5 cm². After the coating, the carbon paper was dried at 100 °C for overnight. The required electrical contacts from the electrodes were made by using metal crocodile clips. The CV measurements were taken at different scan rates from 10 to 800 mV s⁻¹ by maintaining a potential window of 1 V. Charge-discharge measurement was done at different current densities (0.5 to 10 A g⁻¹) in the potential range of 0-1 V. Electrochemical impedance (EIS) analysis was carried out from 10⁶ Hz to 0.1 Hz

frequency sweep against the open circuit potential with a sinus amplitude of 10 mV ($V_{\text{rms}} = 7.07$ mV). All the EIS data were analyzed using an EC-Lab Software V10.19. Capacitance calculated from the CV and charge-discharge for the hybrid material is converted into specific capacitance in terms of the weight of the active material (PEDOT) in the composites.

Capacitance (F g^{-1}) was calculated from the cyclic voltamogram using the following equation:

$$C = 2 * \left(\frac{I}{\text{ScanRate} \left(\frac{dv}{dt} \right) * V * M} \right)$$

Capacitance was also calculated from the charge-discharge experiments using the following equation:

$$C = 2 * \left(\frac{I}{\frac{dv}{dt} * M} \right)$$

in both the cases, 'I' is the average current during the anodic and cathodic sweep, 'V' is the potential window (1 V), 'M' is the weight of the active electrode material coated in one of the electrodes (g) and ' $\left(\frac{dv}{dt} \right)'$ ' is the slope of discharge curve after the IR drop.

Energy density (E_d) and power density (P_d) were calculated from the capacitance value obtained by cyclic voltametry^[23] using the following equations:

$$\text{Energy density } E_d (\text{Wh Kg}^{-1}) = \frac{1}{8} C_s V^2 \text{ and power density } P_d (\text{W Kg}^{-1}) = \frac{E_d}{V} \left(\frac{dv}{dt} \right)$$

here, V= voltage window and $\frac{dv}{dt}$ = scan rate (V s^{-1})

Calculations of the imaginary capacitance and time constant from the EIS measurements^[24] were done using the following equations:

$$\text{Imaginary capacitance } C''(w) = \frac{Z'(w)}{\omega |Z(w)|^2}$$

where, $Z(w)$ is called impedance modulus $|Z(w)|^2 = Z'(w)^2 + Z''(w)^2$

$Z'(W)$ = real Impedance (Ω) and $Z''(w)$ = Imaginary Impedance (Ω)

$$\omega = 2\pi f \quad \text{where } f = \text{AC frequency (Hz)}$$

In the plot of the imaginary capacitance vs. frequency, a maximum occurs at a particular frequency which is known as the relaxation frequency (f_0). Time constant (t) of the material is given by the reciprocal of (f_0).

In case of the counter electrodes, CV was done in distilled acetonitrile containing 0.1 M LiClO₄, 5 mM LiI and 0.5 mM I₂ under N₂ atmosphere. A 3-electrode setup was used for CV in which the prepared counter electrode for DSSC was used as the working electrode and Pt wire which was internally calibrated using ferrocene/ferrocenium (Fc/Fc⁺) couple was used as the reference electrode. Pt foil was used as the counter electrode. Tafel measurements were done in symmetrical cell in which potential was polarised from -1 to +1 V at a scan rate of 10 mV s⁻¹. Impedance analysis was carried out from 10⁶ to 0.1 Hz frequency sweep against the open circuit potential with a sinusoidal amplitude of 10 mV ($V_{\text{rms}} = 7.07$ mV). Impedance data was fitted using EC-Lab Software V10.19.

2.3 Result and Discussion

Polymerization of bulk PEDOT starts very fast in presence of the oxidising agent FeCl₃ and the reaction completes within ~10-20 min^[25]. Whereas, in presence of CNF, the polymerization rate becomes slow and, hence, it takes longer time for completion. This is due to the π - π interaction between the functionalised CNF and EDOT monomers which restricts the motion and thus retards the polymerization rate. Thus, such confined monomers and slow rate of polymerization help formation of a thin film over CNF rather than the polymerization at the bulk. This is essential because the fast polymerization results in a mixture of the 1-D aligned polymer as well as the bulk PEDOT.

2.3.1 HR-TEM and SEM Analyses

Microstructural feature of the above materials was examined using TEM. Image of a bare CNF as shown in Figure 2.1a reveals a hollow tubular nature with cup-stacked structure on the inner wall. Inner diameter of the tube is around 60 nm whereas the total diameter is approximately 120 nm. CNF possesses a highly graphitised outer layer (Figure 2.1b) which was activated *via* oxidative

functionalization by H_2O_2 treatment for easy anchoring of the monomer. On the other hand, due to the presence of the slanting graphene layers which terminate along the inner wall, the inner side of the tube is inherently active. The HRTEM images of the composites (Figure 2.1c-k) delineate the morphological modification affected in the nanofiber after the deposition of PEDOT. Since the FCNF core dictates the growth of PEDOT, an effective 1-D hollow tubular confinement of PEDOT is evident from the images. The images corresponding to CP-25, as shown in Figure 2.1c depict the thin layer of PEDOT on the outer wall and patches of the layer along the inner cavity of FCNF. The thickness of the layer formed on the outer wall in this composition is *ca.* ~ 10 nm as can be seen from the highlighted portion in Figure 2.1d. The extent of the polymer coating along the inner and outer surfaces of FCNF increases as the

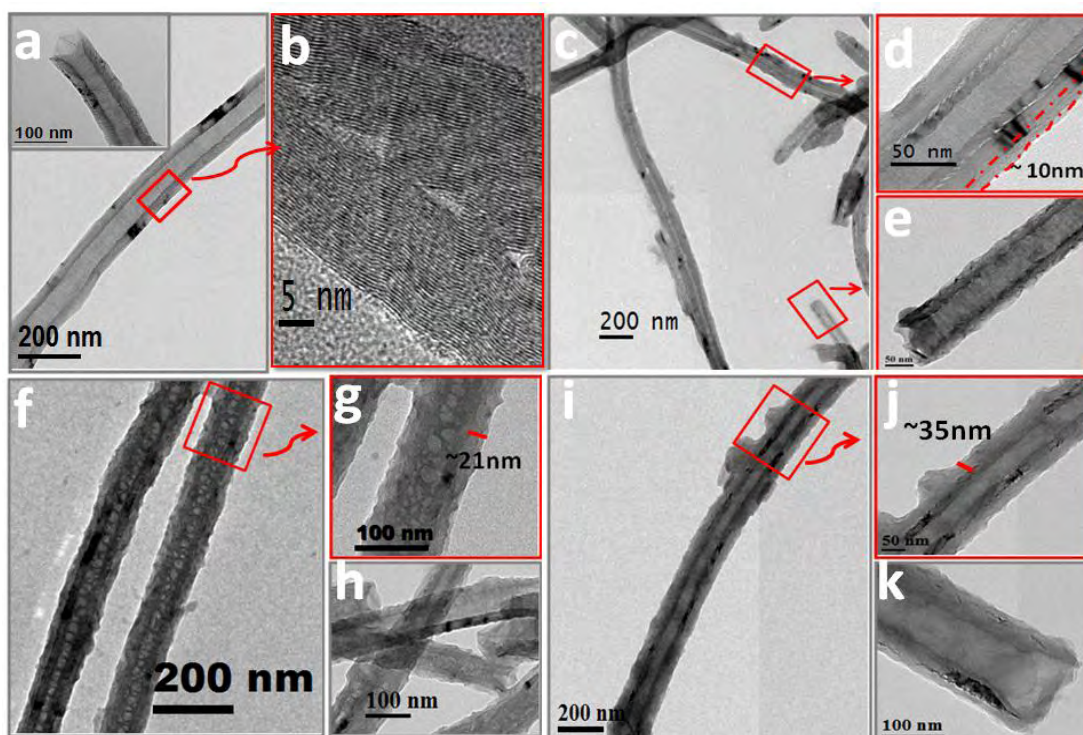


Figure 2.1: HRTEM images of CNF and nanocomposites: a) pristine CNF showing the tubular morphology with its large inner diameter and open tips (inset), b) focused image of the wall of CNF showing the parallel and slanting graphitic layers of the outer and inner walls respectively, c-e) CP-25 with a thin layer of PEDOT and open tips, f-h) CP-40 with prominent PEDOT layers along the inner and outer walls of FCNF possessing a PEDOT thickness of ~ 21 nm along the outer wall and the tip of the tube which is still open and i-k) CP-60 which has more PEDOT content along the outer wall with a thickness of ~ 35 nm and relatively continuous PEDOT layer.

percentage of PEDOT increases as revealed from the images corresponding to CP-40 and CP-60 in Figure 2.1f-k. The thickness of the coating layer has been increased from 10 to 21 nm as the PEDOT content changes from 25 to 40 %, which is associated with a considerable reduction in the number of the vacant pockets in the inner cavity as can be seen by comparing Figure 2.1d and 1g. The thickness of the PEDOT layer further increases to ~35 nm (Figure 2.1j) in the case of CP-60, where the 1D alignment is still retained without any apparent indication of agglomeration (Figure 2.1i). The vacant spaces along the inner wall are considerably less for this composition, indicating a nearly complete wrapping on the inner wall surface with PEDOT. Formation of the porous matrix of PEDOT along the inner wall of CNF is caused by the evaporation of trapped solvent inside CNF. The continuous porosity of the polymer layer inside CNF plays a vital role for the easy movement of the ion species present in the electrolyte.

FE-SEM imaging is used to see the surface morphology of the counter electrodes. Figure 2.2 corresponds to the FESEM images taken at the surface of a counter electrode prepared from CNF, PEDOT and CP-25. Surfaces of CNF (Figure 2.2a) and the composite (CP-25, Figure 2.2b) are more porous than that of the bulk PEDOT. CNF and CP-25 show almost similar morphology even though a distinction between the polymer and carbon entities is difficult due to the lack of contrast difference. Presence of bulk PEDOT outside the CNF surface is negligible in case of CP-25 (Figure 2.2b) and CP-40 (Figure 2.3a).

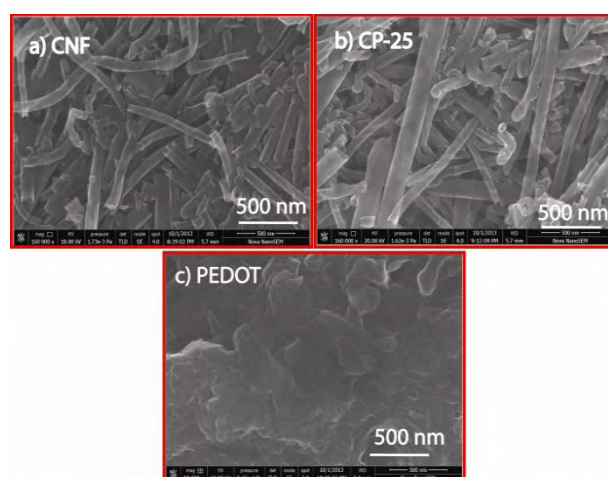


Figure 2.2: FE-SEM images of a) bare CNF, b) CP-25 and d) bulk PEDOT. Images of all the samples are taken using the original counter electrodes.

In case of the composites with even higher loading of PEDOT such as CP-60 and CP-80 (Figure 2.3b & 2.3c), the PEDOT phase is distinct and is clearly visible separately from the CNF surface. Thus, in CP-60 and CP-80, higher concentration of PEDOT leads to deviation from the expected core-shell morphology. Arrow marked portions in Figure 2.3b & 2.3c show the part of bulk PEDOT present in the composites. Higher concentration of EDOT monomer during the synthesis, as in the case CP-60 and CP-80, enhances the chances of polymerization outside the CNF surface at a faster rate compared CP-25 and CP-40.

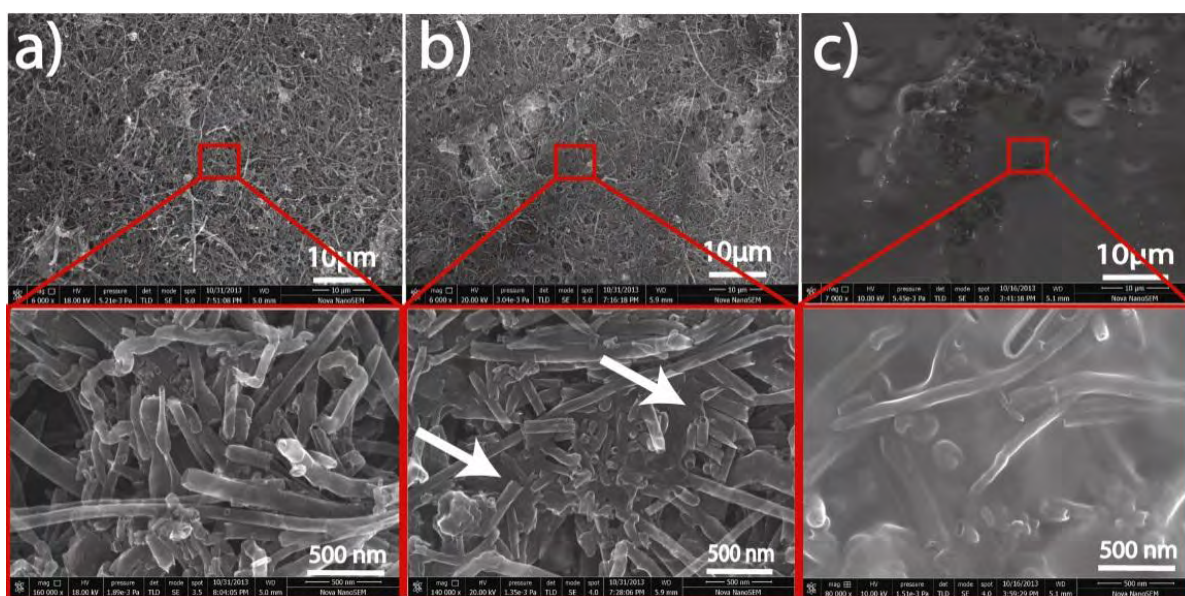


Figure 2.3: FE-SEM images of a) CP-40, b) CP-60 and c) CP-80.

2.3.2 BET-Surface Area Measurements

The HRTEM images clearly provide strong evidences on the attainment of highly exposed surface of PEDOT as the polymer growth has been confined along the surfaces of FCNF. A quantitative estimation on the surface area change upon the nanocomposite formation has been done by measuring the BET surface areas of the samples (Figure 2.4). FCNF and bulk PEDOT possess surfaces areas in two extremes as 55 and 5 m² g⁻¹, respectively. The growth of PEDOT as a thin layer along the surfaces of FCNF has helped the composites to display significantly high surface area compared to the bulk PEDOT. The surface areas of the composite follow the order CP-40 (33 m² g⁻¹) > CP-60 (27 m² g⁻¹) > CP-25 (23 m² g⁻¹) > CP-80 (7 m² g⁻¹). Here, again CP-80 shows a trend which is more similar to that of bulk PEDOT and this can be ascribed to the polymer growth outside the periphery of FCNF. Thus, with the

significantly high conductivity and enhanced surface area of the nanoconfined PEDOT compared to the bulk sample, the hybrid material qualifies two essential requirements for serving as the electrodes for supercapacitors.

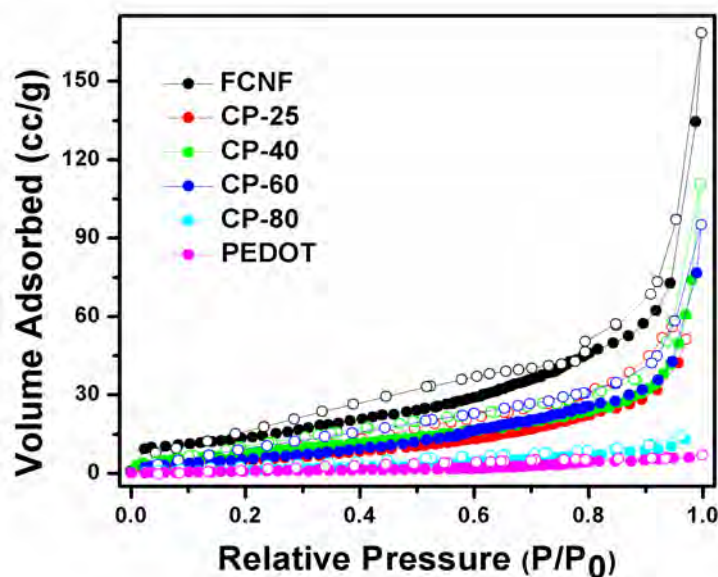


Figure 2.4: Nitrogen adsorption isotherm of CNF, PEDOT and their hybrids.

2.3.3 Electrical Conductivity Measurements

1-D alignment of PEDOT is expected to improve the electrical conductivity not only because of the presence of the conducting carbon core but also due to the efficiency of the strategy to maintain a nearly uniform thickness of the continuous PEDOT layer. The electrical conductivity data, as measured by the four-probe method, is summarized

in Table 1.1. FCNF and bulk PEDOT show conductivities of 5.75 ± 2 and 8.00 ± 2 S cm^{-1} respectively. The conductivity increases significantly as we move to the nanocomposites. In the case of the nanocomposites, the pressed pellet conductivity follows the order CP-60 (106 S cm^{-1}) > CP-40 (92 S cm^{-1}) > CP-25 (66 S cm^{-1}) > CP-80 (38 S cm^{-1}). It should be noted that this value is much higher than the reported conductivity values of PEDOT having different morphologies.^[21c, 21d, 26] It has been observed that the template assisted synthesis of conducting polymers^[27] leading to fibrous structures possesses high electrical conductivity as compared to their bulk counterparts. This was explained by various research groups^[27a] on the basis of the results obtained from Polarized Infrared Absorption Spectroscopy (PIRAS). PIRAS

study points towards formation of well-ordered polymer chains leading to higher conjugation length and hence high electrical conductivity in case of the template assisted

Table 1.1: Comparison of surface area, electrical conductivity and specific capacitance of the samples.

Sample	Surface Area ($\text{m}^2 \text{g}^{-1}$)	Electrical Conductivity (S cm^{-1})
FCNF	55	5.75 ± 2
CP-25	23	66 ± 2
CP-40	33	92 ± 2
CP-60	27	106 ± 2
CP-80	7	38 ± 2
PEDOT	5	8 ± 2

growth. In the case of bulk PEDOT, fast polymerization rate results in the formation of disordered polymer chains resulting in decreased conjugation length and low conductivity^[27a]. The presence of CNF, however, lowers the rate of polymerization of PEDOT and also facilitates the growth of polymer chains in the direction along the axis of the pores of CNF. This preferential orientation along the pore axis (*i.e.* along the length) brings an order in the polymer chain which enhances the π conjugation length leading to higher electrical conductivity in case of CP when compared to bulk PEDOT and pristine-CNF. However, there is a threshold amount of PEDOT that FCNF can accommodate. Once the concentration exceeds this limit as in the case of CP-80, PEDOT is also seen to polymerize outside the CNF surface (Figure 2.3c) leading to departure from the conformal core-shell architecture which makes CP-80's electronic character to lean towards the bulk PEDOT character. This is because of the large proportion of disorder in the polymer matrix of CP-80, which leads to further decrease in conductivity with loading as compared to lower compositions.

This is also experimentally supported by the *I-V* measurements of the material coated in between the two FTO plates in Figure 2.5a. It clearly illustrates the higher conductivity in case of the CP-25 (best case for the counter electrode application) samples. The electrical conductivity of CP-25 is higher as compared to CNF because

of the higher amount of the ordered PEDOT. To examine the long-term stability towards conductivity, the conductivity of the materials was evaluated for different time intervals. PEDOT is known to show degradation in conductivity with exposure to atmosphere^[28]. Figure 2.5b shows the data

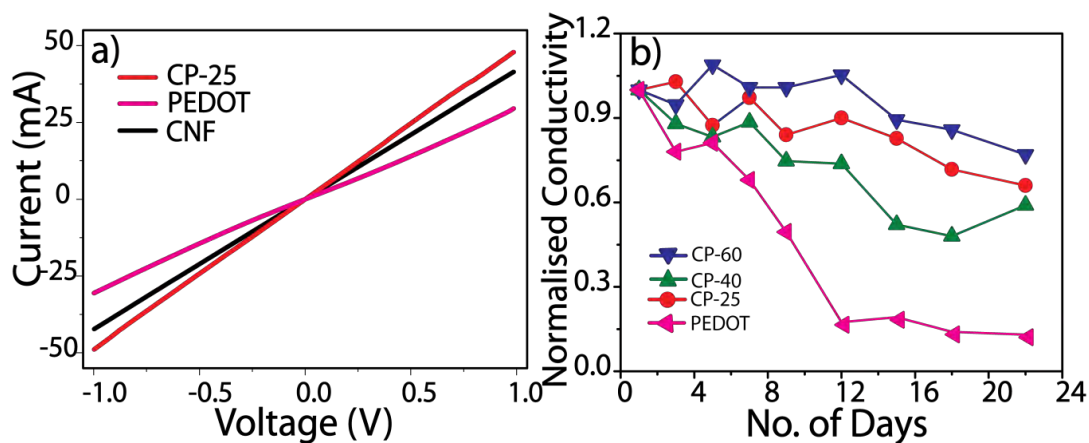


Figure 2.5: a) I-V measurements of the materials coated in between the two FTO plates and b) time dependent conductivity of the materials with exposure to atmosphere.

corresponding to the conductivity evaluation as a function of time for different combinations of PEDOT and CNF. Bulk PEDOT degrades to $\frac{1}{4}^{\text{th}}$ of its initial conductivity within 18 days whereas the composites CP-60, CP-40 and CP-25 retain $\sim\frac{3}{4}^{\text{th}}$ of their initial conductivities for the same duration. Such enhanced stability will help the material to deliver consistent efficiency for longer duration and can avoid costly handling technologies needed for such a humidity sensitive material.

2.3.4 XRD Analysis

The XRD patterns of CNF, FCNF, PEDOT, CP-25, CP-40, CP-60 and CP-80 are shown in Figure 2.6. In all the samples except PEDOT, the XRD patterns display a strong peak at a 2θ value of 26.2° , indicating the (002) graphitic plane of CNF. On the other hand, in the case of bulk PEDOT, a broad peak corresponding to the 2θ of 25.8° due to the (020) reflection has been observed along with some less intense peaks at 6.2 , 9.47 and 14.5° .^[29] Comparison of the full width at half maximum (FWHM) of the graphitic (002) peak (Figure 2.6) clearly shows a gradual broadening with increase in the concentration of PEDOT on the surface. This peak broadening is due to the overlapping of the (020) plane of PEDOT with the (002) plane of the graphitic carbon as the reflections occur almost at the same position in the case of the hybrid materials.

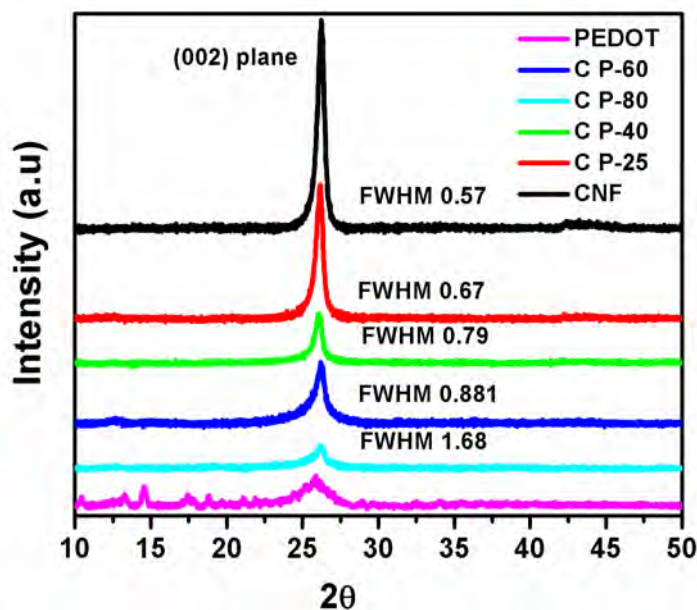


Figure 2.6: XRD patterns of CNF, CP-25, CP-40, CP-60, CP-80 and PEDOT.

2.3.5 Raman Spectroscopy

The mode of interaction between the PEDOT and FCNF and the extent of defects induced in the CNF system are investigated using Raman spectroscopy. Accordingly, Raman spectra of CNF, FCNF, PEDOT and FCNF-PEDOT hybrids are shown in Figure 2.7. The Raman spectra of CNF exhibit two strong peaks at 1320 and 1564 cm^{-1} corresponding to the D and G bands, respectively and a 2D band at 2641 cm^{-1} . After the functionalization of CNF to form FCNF, there is a significant increase in the I_D/I_G ratio from 0.30 to 0.39.^[30] Again, the position of the G band at 1564 cm^{-1} of FCNF is shifted to 1571 cm^{-1} after the polymer incorporation (inset of Figure 2.7). There are reports regarding the positive shift of the G band of carbon materials after functionalization with electron withdrawing groups.^[31] These transitions in the present case clearly indicate that there is a strong electronic interaction between S^+ in the doped PEDOT and the carbon network of FCNF. The same but less prominent trend is observed in the case of the D and 2D bands as well. Apart from the D, G and 2D bands, all the hybrid compositions show the characteristic Raman lines of PEDOT. The intense peak at 1430 cm^{-1} indicates the $C_\alpha=C_\beta$ symmetric stretching band of PEDOT, which provides a valid evidence of the doped state obtained for all the hybrid compositions^[32]. The other peaks obtained at 1362 and 1507 cm^{-1} represent the $C_\beta=C_\beta^1$ stretching. The characteristic peaks such as 499 cm^{-1} (oxyethylene ring deformation), 695 cm^{-1} (symmetric C-S-C deformation), 859 cm^{-1} (asymmetric C-S-C

deformation), 987cm^{-1} (O-C-C-O ring deformation) and 1550 cm^{-1} (asymmetric C–C stretching) ^[32-33] obtained for the pristine PEDOT are not clearly visible in the case of the nanocomposites.

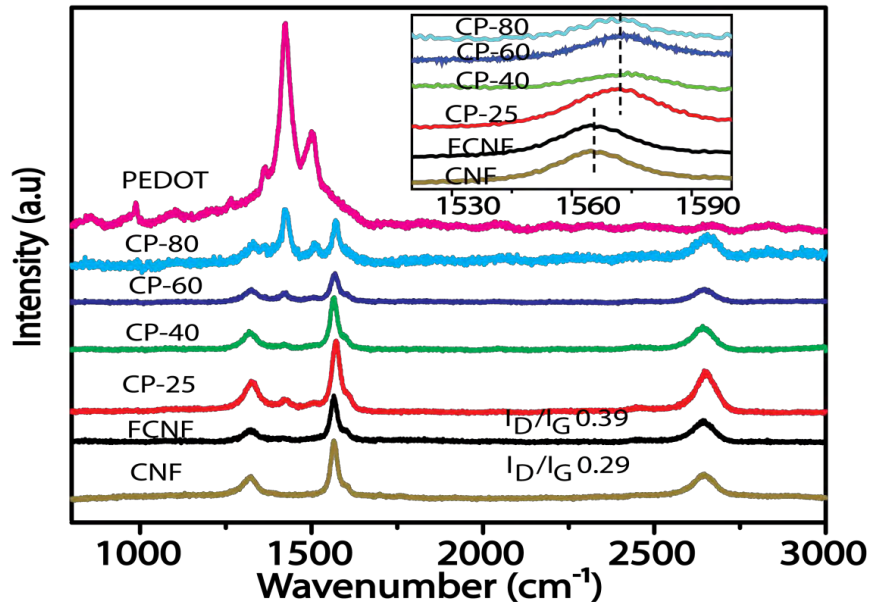


Figure 2.7: Raman spectra of CNF, FCNF, CP-25, CP-40, CP-60, CP-80 and PEDOT. The inset of the figure highlights the G band shift.

2.3.6 FT-IR Spectra

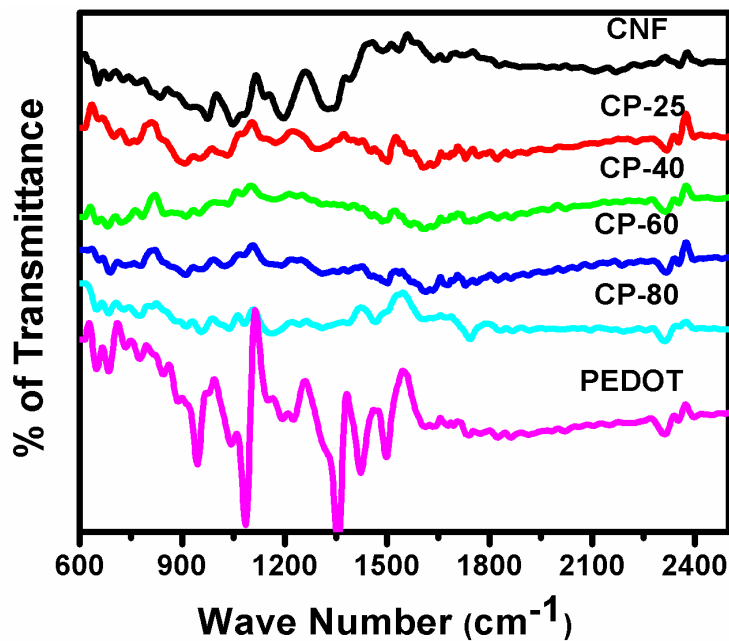


Figure 2.8: FT-IR spectra of CNF, CP-25, CP-40, CP-60, CP-80 and PEDOT.

The FT-IR spectra of the nanocomposites display the characteristic peaks (Figure 2.8) of PEDOT at 651, 683, 736, 847 and 945 cm^{-1} , which correspond to the C-S vibration modes of the thiophene ring in the PEDOT moiety.^[29a, 33a, 34] Apart from this, the peaks at 1357, 1422 and 1494 cm^{-1} indicate the C-C and C=C stretching of the thiophene ring whereas the peaks at 1085, 1147 and 1187 cm^{-1} represent the stretching modes of the C-O-C groups of PEDOT in the nanocomposites.

2.3.7 XPS Analysis

The evidence for the chemical interaction between the FCNF and PEDOT is further deduced from the XPS analysis. Apart from the signatures of C, O and S, the presence of both Fe and Cl confirms that the polymer is in its doped state in which Cl^- or FeCl_4^- is the possible dopant. As shown in Figure 2.9a, the S2p core level spectrum of PEDOT can be deconvoluted into four peaks corresponding to the binding energies of 163.7, 164.9, 166.2 and 167.4 eV. The first two peaks correspond to the spin split doublet, represented as $\text{S}_{3/2}$ and $\text{S}_{1/2}$, of neutral sulfur possessing a binding energy

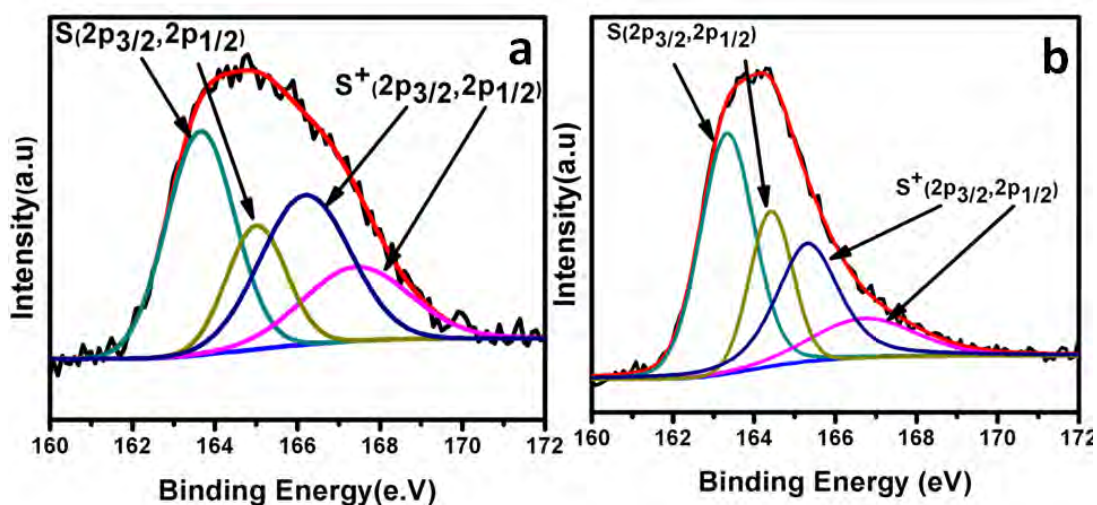


Figure 2.9: Deconvoluted XPS core level spectra of S2p of a) PEDOT and b) CP-40.

difference of 1.2 eV and an intensity ratio of 1:2.^[35] The higher binding energy peaks at 166.2 and 167.4 eV correspond to S^+ and this explicitly reveals that the polymer is in the doped state. Compared to PEDOT, the S2p core level spectrum in the case of CP-40 shows peaks at 163.3, 164.5, 165.3 and 166.5 eV as shown in Figure 2.9b. Here, the binding energy of S has been decreased to 0.5 eV for neutral S and 0.9 eV for S^+ and this shift indicates the influence of the π electrons of CNF to decrease the electronegativity of S especially for S^+ .

2.3.8 Thermogravimetric Analysis

Further, to understand the thermal stability and quantification of polymer in the nanocomposites, thermogravimetric analysis (TGA) of CNF, PEDOT and various CNF-PEDOT hybrids was carried out in air at a heating rate of 10 °C per minute from room temperature to 900 °C (Figure 2.10). There are three major stages of weight loss in the TG curves of PEDOT-FCNF composites. The first weight loss below ~120 °C is ascribed to desorption of water molecule which are physisorbed on the composite. The decomposition of PEDOT in the composites starts at around 250 °C and completes at around 490 °C in comparison to the pristine PEDOT, for which the decomposition completes at nearly 410 °C. The physiochemical interaction of PEDOT with CNF and its confinement inside the more thermally stable shell of CNF apparently enhanced the thermal stability of PEDOT close to

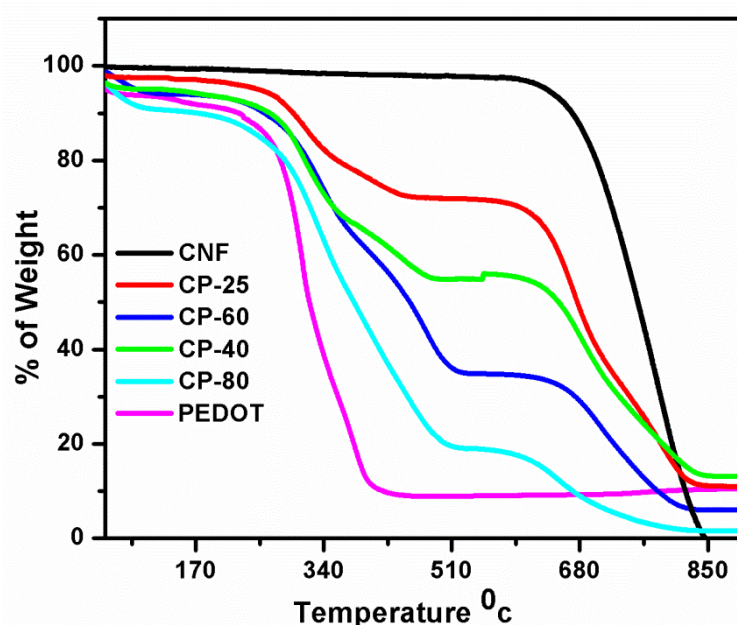


Figure 2.10: TGA of CNF, CP-25, CP-40, CP-60, CP-80 and PEDOT.

the carbon surface. At around 600 °C, a rapid fall in the weight of the carbon in the pristine CNF and the composites is observed. The residues found after the analyses are due to the oxidizing agent that is not completely removed from the polymer matrix and trace amount of Fe impurity present in CNF. TGA profile is used to account the quantitative loading of PEDOT in the composites. These loadings are estimated to be 25.3, 39.5, 60.5 and 79.5 wt. % respectively for CP-25, CP-40, CP-60 and CP-80.

2.3.9 Electrochemical Characterization of Charge Storage Properties

In order to validate the efficiency of the systems for charge storage, measurement of electrochemical capacitance was done by using cyclic voltammetry (CV) and chrono charge-discharge technique in a two electrode set-up containing 1 mg of the respective material and 0.5 M H₂SO₄ as the electrolyte. The contribution of CNF towards the capacitance of the hybrid is negligible as evident from the significantly low capacitance of 1 F g⁻¹ for the pristine CNF.^[7b, 36] Due to this reason, any improvement in the capacitance for the nanocomposites can be correlated to the loading and the peculiar confinement of PEDOT. Since no major contribution in the capacitance is apparent from CNF, for all the calculations to deduce the mass specific capacitance of the samples, the mass of PEDOT as estimated from the TG-DTA analysis was used in the hybrid instead of the total weight of the composite.

2.3.9.1 Cyclic voltammetry

Combined cyclic voltammograms of CNF, PEDOT and their hybrids taken at voltage scan rates of 50 and 2000 mV s⁻¹ are presented in Figures 11a and 11b, respectively. All the hybrid materials show a square type voltammogram even at a high scan rate of 2000 mV s⁻¹, which is a clear indication of the true capacitive nature of the material.^[37] The cyclic voltammogram of PEDOT^[11a, 11b, 18, 38] is quite different from the other conducting polymer such as polyaniline^[39], polypyrrole^[40] etc. as they show typical redox peak in the CV. The square type voltammogram obtained here shows the contribution from double layer capacitance and thus the capacitance of PEDOT clearly depends on the surface area and conductivity of the polymer. Very high retention of the CV feature at higher scan rates comes from fast response of the material to the voltage switching, where unique morphology of the composite helps seamless movements of ion during the redox faradic reaction.⁵⁰ In the case of bulk PEDOT, however, the above feature is apparent only at very low scan rate of 500 mV s⁻¹ and below. For example, a complete deviation from the square type feature of the voltammogram at a scan rate of 2000 mV s⁻¹ is visible in Figure 2.11b. At a scan rate of 50 mV s⁻¹, the pristine PEDOT gives a mass specific capacitance of 76 F g⁻¹, which is well in agreement with the literature reports.^[11-13] However, this value drops to 30 F g⁻¹ as the scan rate increases to 3000 mV s⁻¹. This can be accounted by the low surface area (5 m² g⁻¹) and conductivity (8 S cm⁻¹) of the pristine PEDOT together with the

indisposed features of the polymer matrix which restrict the fast ion movement during the potential cycling. A substantial improvement in the mass specific capacitance has been observed in the case of the nanoconfined samples. At the scan rate of 50 mV s^{-1} , the specific capacitance of the composites follows the order CP-40 (177 F g^{-1}) > CP-25 (151 F g^{-1}) > CP-60 (147 F g^{-1}) > CP-80 (110 F g^{-1}). This nearly 2 fold improvement in the capacitances of CP-25, CP-40 and CP-60 clearly validates the efficiency of nanoconfinement and interfacial area tuning as affected by using carbon nanomorphology as a solid template. The specific capacitance measured from the systems well correlate with the electrical conductivity and surface area data as well, which reveals a controlled interplay of various contributing factors in the hybrid system. Among the systems, CP-40 has registered the highest specific capacitance and this superiority is easily understandable as it possesses the highest surface area, which is crucial over the electrical conductivity for charge storage.

To test the capacitance retention at higher scan rates, the CV profiles were taken by varying the scan rate from 10 to 3000 mV s^{-1} . The capacitance retention of the hybrids is excellent and the combined results are shown in Figure 2.11c. Among the composites, CP-25, CP-40 and CP-60 give retention of 88, 74 and 69 %, respectively from their initial values whereas CP-80 shows retention of 43 % from its initial value. Compared to the nanocomposites, the capacitance retention of the bulk PEDOT with the voltage scan rate is only 33 %. This limitation is linked to the morphology of the polymer matrix which restricts the system to respond effectively during potential cycling at various rates due to the resistances existing in the system for fast ion movements. On the other hand, in the case of the hybrid system, due to its 1-D confinement with optimum PEDOT thickness and overall porosity, better access and fast movements of ions even at very high scan rates can be expected. This eventually helps the system to display better capacitance retention as the scan rate changes. Adding to these structural advantages incurred, the high electrical conductivity of the hybrid also favors the nanoconfined PEDOT to display better performance compared to its bulk counterpart.

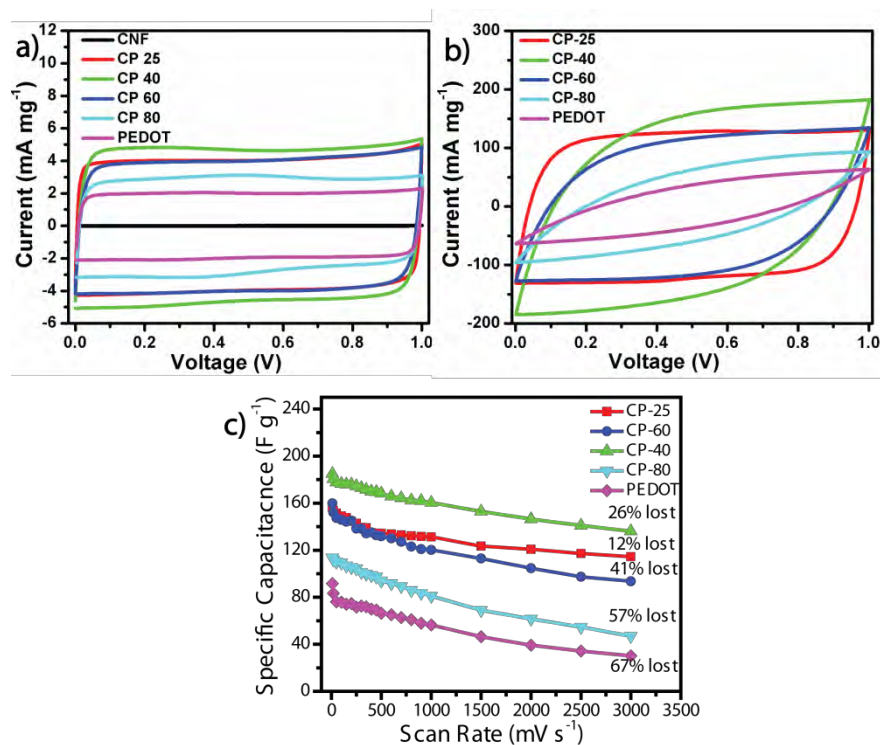


Figure 2.11: Cyclic voltamogram and charge-discharge profiles of CNF, CP-25, CP-40, CP-60, CP-80 and PEDOT; the CV responses in (a) and (b) were taken at scan rates of 50 and 2000 mV s^{-1} , respectively; (c) gives the specific capacitance retention of CP-25, CP-40, CP-60, CP-80 and PEDOT from CV with different scan rates.

2.3.9.2 Galvanostatic charge-discharge experiments

The capacitances measured by the galvanostatic charge-discharge experiments are also in well agreement with the results obtained by the CV measurements. The charge-discharge curves for the samples obtained by maintaining the current density at 1 A g^{-1} are shown in Figure 2.12a. Perfect symmetric nature of the curves for the hybrids indicates the high columbic efficiency which is lacking in the case of bulk PEDOT. In the case of bulk PEDOT, it is clear from the figure that the charging time is slightly higher than the discharging time which leads to a variation in the symmetric nature of the plots. Such behaviour can be seen in the case of CP-80, which possesses aggregates of PEDOT as revealed from the SEM images. The capacitances obtained from the plots are 139, 151, 134, 89 and 80 F g^{-1} for CP-25, CP-40, CP-60, CP-80, and bulk PEDOT respectively. Again, among the hybrids, CP-40 is the one with the maximum performance. For high power demanding situations, charging and discharging of the electrode material at high current density is necessary. One of the best qualities of a perfect capacitive material is to retain its high energy density in

terms of capacitance even at high current density. Due to the unique architecture, hybrids have very high capacitance retention even at a high current density of 10 A g^{-1} (Figure 2.12 b). Pristine PEDOT shows an enormous decrease of 69 % (90 F g^{-1} at 0.5 A g^{-1} to 27.5 F g^{-1} at 10 A g^{-1}) in capacitance at high current density. Compared to this, the hybrids show low to moderate decrease, which are 12.5, 13.0, 14.0, and 23.0 % for CP-25, CP-40, CP-60, and CP-80 respectively from their initial values as shown in Figure 2.12c. It should be noted that effective current density with respect to the active material (PEDOT) will be much higher than that applied to the total electrode material, which depends on the loading of PEDOT in the composite. For example, 10.0 A g^{-1} applied to CP-40 leads to an effective value of 25.0 A g^{-1} in terms of the total PEDOT weight in the composite. In a similar way, normalization with respect to the PEDOT weight for CP-25, CP-60, and CP-80 leads to the effective current density values as 40.0, 16.0 and 12.0 A g^{-1} , respectively. Slight variation in the capacitances of the hybrids calculated using the charge-discharge method with that of CV can also

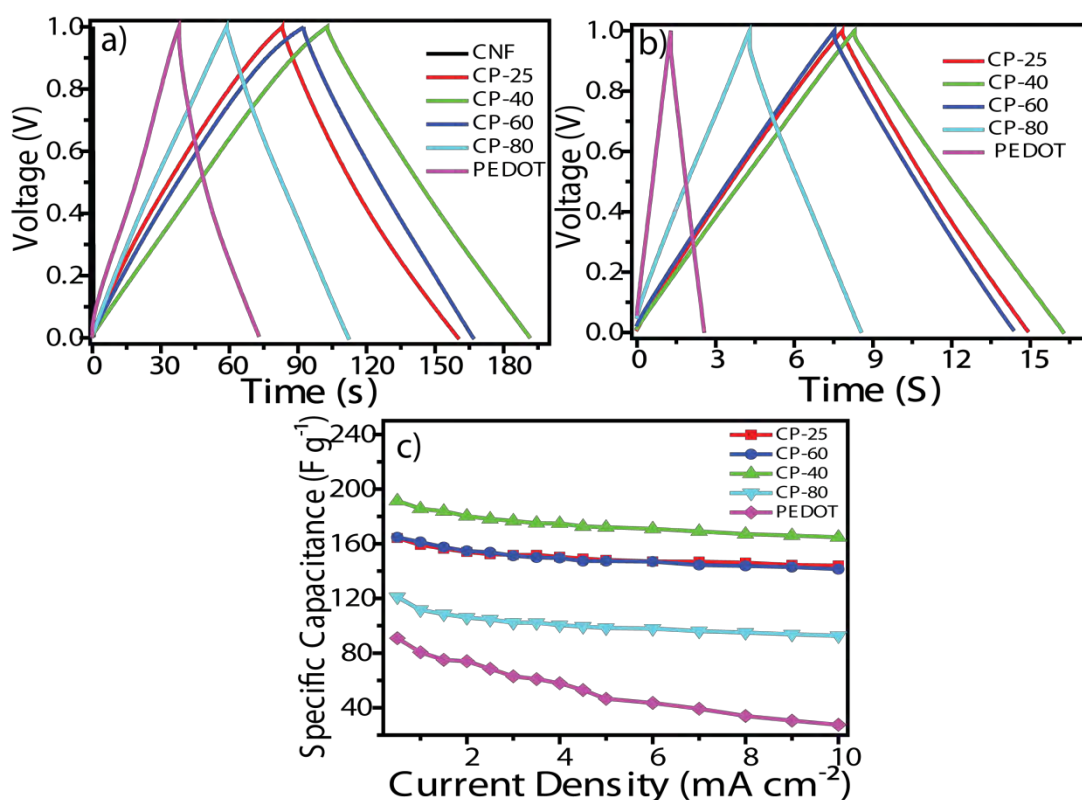


Figure 2.12: a) & b) Represent the charge-discharge experiments performed by maintaining the current densities as 1 and 10 mA cm^{-2} , respectively and (c) gives the specific capacitance retention of CNF, CP-25, CP-40, CP-60, CP-80 and PEDOT from the charge-discharge method with different current density values.

be correlated to the differences in the effective current density values between the samples as shown above.

Extended cycling life is an important requirement for supercapacitors. The electrochemical stability of CP-40 and PEDOT are examined at a current density of 2 A g^{-1} over 4500 charge-discharge cycles, where CP-40 is found to be showing excellent stability (Figure 2.13). The overall decrease in the case of CP-40 is less than 2 % from the initial value after 4500 cycles compared to a loss of 15 % observed with bulk PEDOT. Few cycles in the initial and final charge-discharge cycles are shown in the inset of Figure 2.13. The cyclic degradation issue in the case of the bulk conducting polymers is mainly due to the polymer structural degradation. This happens due to the continuous swelling and shrinking during the repeated charging and discharging (doping-dedoping) processes.^[6b, 7a, 12, 41] In the present case, the hybrid structure helps PEDOT to maintain better mechanical stability by helping proper movements of ions and flexibility during the volume change. It is notable that, this high stability is achieved without the addition of any physical binders like polyvinylidene fluoride (PVDF) which is expected to improve the cycle life further, but at the expense of the capacitance.

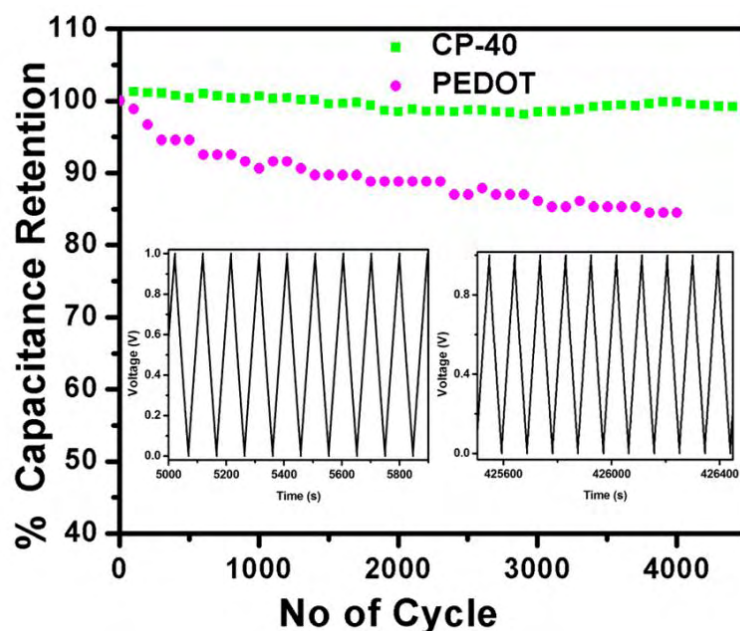


Figure 2.13: Percentage capacitance retention from the galvanostatic charge-discharge cycle over 4500 repetitions at a current density of 2 A g^{-1} .

Energy density (E_d) and power density (P_d) are calculated using the equation given in the experimental section and the typical Ragone plot^[42] is shown in Figure 2.14. Maximum energy density is shown by CP-40, which is 5.89 Wh kg^{-1} at a power density of 212 W kg^{-1} and is able to keep 75 % (4.42 Wh kg^{-1}) at a power density of 12.72 kW kg^{-1} . CP-25 and CP-60 also show similar high values of 5.11 and 5.16 Wh kg^{-1} at power densities of 184 and 186 W kg^{-1} , respectively. These values become 4.49 and 3.64 Wh kg^{-1} at 12.9 and 10.5 kW kg^{-1} , respectively. Compared to the nanohybrid composites, bulk PEDOT shows only a very low energy density of 3 Wh kg^{-1} at a low power density of 110 W kg^{-1} . A drastic drop in the energy density at higher power densities can also be seen.

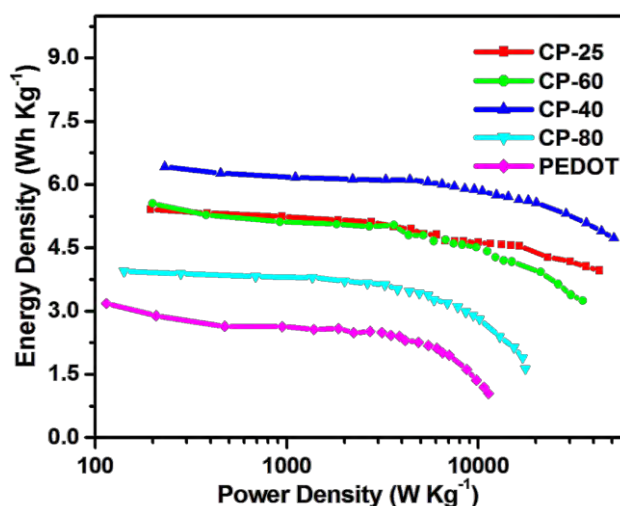


Figure 2.14: Ragone plot calculated from the cyclic voltammetry profile in the scan rate range 10 to 800 mV s^{-1} .

2.3.9.3 Impedance analysis

To support the explanation of the improved capacitance due to fast ion transport in the hybrid, EIS studies were carried out. The Nyquist plot, Z' (real) versus Z'' (imaginary), is presented in Figure 2.15a, which indicates the characteristic capacitive behaviour for the hybrids. At the high frequency region (inset of Figure 2.15a), a small semicircle is observed which arises from the charge transfer resistance between constituent elements in the electrodes as well as the electrolyte within the pores.^[43] It is interesting to note that all the hybrids display very small semicircles. For CP-25, CP-40 and CP-60, the diameters of the semicircles correspond to only 1.18, 1.33 and 2.10Ω , respectively, compared to 2.60 and 8.25Ω respectively for CP-

80 and PEDOT. This result unambiguously proves the very low charge-transfer resistances associated with the hybrids due to their unique 1-D structure with adequate porosity by which the ion transport in the systems is expected to be favoured significantly. Above result also explains why hybrids, especially CP-25, show excellent capacitance retention at high scan rate and current density. In the lower frequency region, ideal capacitor will have an exact parallel line with the Z'' (imaginary) axis in the Nyquist plot.^[24b, 44] The much inclined vertical lines of PEDOT and CP-80 compared to CP-25, CP-40, and CP-60 are due to the surface roughness and non-uniform active layer thickness. On the other hand, CP-25 shows nearly ideal behaviour due to its thin uniform coating compared CP-40 and CP-60. This thin and smooth coating reduces the diffusive resistivity of the system.

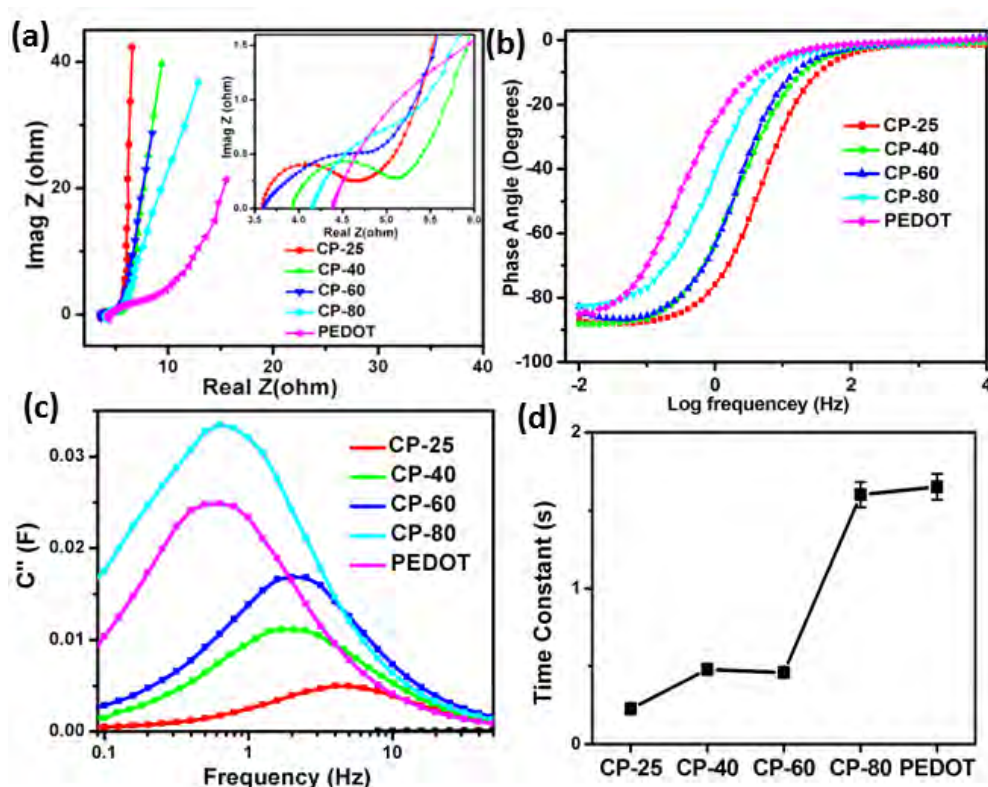


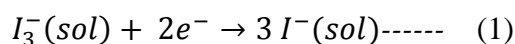
Figure 2.15: a) Nyquist plot of CP-25, CP-40, CP-60, CP-80 and PEDOT (magnified high frequency region of the plots given in the inset), b) plot of impedance phase angle versus frequency (Bode plot). (c) Imaginary capacitance vs. Frequency and (f) calculated time constants.

The Bode plots (frequency vs. phase angle) in Figure 2.15b shows nearly -90° phase angle at 0.1 Hz for the hybrid compositions CP-25, CP-40 and CP-60 represent an ideal capacitive behaviour^[45] compared to PEDOT and CP-80. In addition to this,

for CP-40, CP-60 and CP-25, change from the resistive to capacitive nature, as indicated by the change from 0° phase angle to a favourable negative value, happens at the high frequency regions compared to PEDOT and CP-80. To evaluate the voltage response of the material, relaxation time constant (t_0) has been measured from the plot of imaginary capacitance (C'') vs. frequency (Figure 2.15c). Reciprocal of the frequency ($1/f_0$) corresponding to the peak capacitance gives the time constant (t_0), which is a quantitative measure of how fast a material can be charged and discharged.^[44, 46] Time constants of CP-25, CP-40, CP-60, CP-80 and PEDOT are 0.22, 0.48, 0.46, 1.60 and 1.65 seconds respectively (Figure 2.15d) which clearly indicate the quick potential response of the hybrids compared to bulk PEDOT. These time constants of conducting polymers are very low compared to even EDLC material^[45a, 47]. Very high capacitive retention of CP-25 compared to CP-40 and CP-60 is also understandable from this low time constant of CP-25. The increase in t_0 with the layer thickness of PEDOT on CNF arguments that a thin and smooth coating reduces the diffusive resistivity for the charge transfer process. Overall, the nanoconfinement as conceived by this approach assists PEDOT to mobilize fast charging and discharging processes and helps to achieve high retention of capacitance at high scan rate and current density.

2.3.10 Electrochemical Characterisation of Counter Electrode Activity

Higher surface area and conductivity of CP-25 as compared to CNF and PEDOT are expected to help the hybrid sample to display improved catalytic activity towards the reduction of tri-iodide species to iodide at the counter electrode which is represented as,



where, sol indicates the acetonitrile solution which is generally used as the solvent to make the DSSC electrolyte.

2.3.10.1 Cyclic voltammetry analysis

A typical cyclic voltammogram shows the reduction-oxidation peaks at negative potentials vs. Fc/Fc^+ which are assigned to the reduction and oxidation peaks for I_3^-/I^- couple as clearly depicted in Figure 2.16a. The second redox peak observed at the positive potential is corresponding to the I_2/I_3^- couple. The important parameters

which determine the electrochemical catalytic activity of the counter electrode are the potential difference between the reduction and oxidation peaks of I_3^-/I^- couple as denoted by E_{pp} and the peak reduction current density as indicated by I_p ^[48]. The catalytic activity is negatively correlated to the magnitude of E_{pp} and directly to the current density I_p . CP-25 shows an E_{pp} of 0.27 mV which is very less compared to the E_{pp} values of 0.34 mV for bulk PEDOT and 0.97 mV for CNF which clearly indicates the superior catalytic activity of CP-25 as compared to bulk PEDOT and pristine-CNF. This is further supported by the comparison of the reduction current density I_p among CP-25, PEDOT and CNF. Note that in all the cases, the background current is subtracted to get the pure reduction current for appropriate comparison of I_p . Due to the higher catalytic activity of CP-25, it shows an I_p of 1 mA cm^{-2} as compared to 0.70 mA cm^{-2} for bulk PEDOT and 0.58 mA cm^{-2} for CNF. Comparing to the catalytic activity of Pt (E_{pp} is 0.34 mV), CP-25 shows superiority in terms of its lower E_{pp} value even though Pt retains an edge in terms of its high I_p (1.16 mA cm^{-2}) value compared to CP-25. Thus, the CV results clearly indicate the superior catalytic activity of CP-25 over its constituent components (CNF and PEDOT) and it is interesting to find out that the performance is even comparable to Pt. To understand the effect of 1-D confinement in the catalytic activity, CV of different composites is also carried out and the corresponding voltammograms are given in Figure 2.16c. With increasing the amount of PEDOT, E_{pp} is increasing in the order of CP-25 (0.272 mV) < CP-40 (0.324 mV) < CP-60 (0.329 mV). E_{pp} of CP-10 (0.882 mV) is found to be higher than that of CP-25 (0.272 mV) due to the very low amount of PEDOT content which is not sufficient for the catalytic activity in a system containing higher amount of less active CNF. As it is found from the FE-SEM images, perfect 1-D confinement is destroyed beyond CP-25 which results into lower conductivity and more bulk-like characteristics. Thus, the higher E_{pp} values of the samples with PEDOT loading beyond 25 % can be ascribed to the the cathodic peak current density in the case of CP-25, Pt and CNF. Such a linear relationship lower electrical conductivity as well as to the high charge transport resistance of such samples. Figure 2.16b shows that square root of the scan rate has a linear relationship with indicates the involvement of diffusion limited reaction and absence of any interaction of ionic species with the catalyst during the adsorption^[49]. On the other hand, in the case of bulk PEDOT, the high charge-transfer resistance makes slow ion movement especially at higher scan rate, which leads to a deviation from the linear relationship.

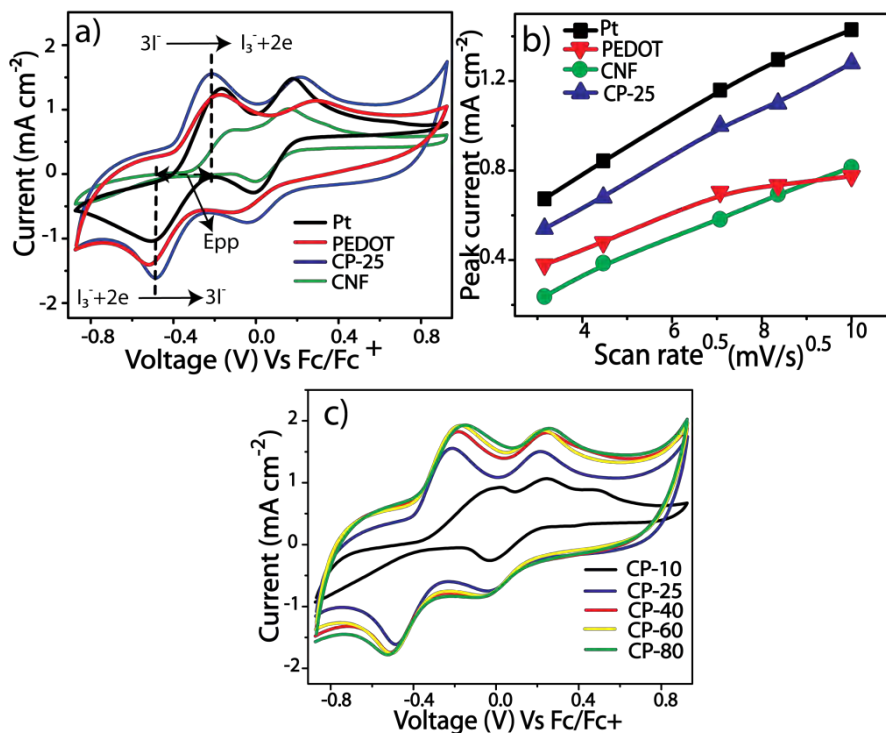


Figure 2.16: a) CV profiles recorded at a scan rate of 50 mV s^{-1} and b) plots showing the relationship between the peak current density and square root of the scan rate and c) cyclic voltammograms of the CP samples with different PEDOT loadings taken at a scan rate of 50 mV s^{-1} .

2.3.10.2 Impedance and Tafel analysis

To reconfirm the superior catalytic activity of CP-25 towards the tri-iodide reduction, EIS measurements were carried out in a symmetrical cell having the CE/electrolyte/CE arrangement. Corresponding Nyquist plots are shown in Figure 2.17a. Experimental data are fitted using Randles-type circuit (Figure 2.17c) and the individual circuit element's values are given in Table 2.2. Real axis intercept at the high frequency region is known as R_s , which corresponds to the equivalent series resistance and is contributed mainly by the sheet resistance of the FTO plate. Sample to sample variations in R_s values are omitted due to the same reason. First semicircle after R_s at the high frequency region corresponds to the charge transfer resistance (R_{ct}) between CE and the electrolyte which is inversely correlated to the tri-iodide catalytic activity. A constant phase element (CPE) having a dimension of capacitance is also introduced to fit the data and is commonly used instead of pure capacitance. CP-25, which is showing highest catalytic activity, shows less R_{ct} value (3.18Ω) compared to

CNF (8.22 Ω) and PEDOT (7.35 Ω). This reconfirms the high catalytic activity of CP-25. The low charge transfer resistance of CP-25 ultimately comes from the 1-D aligning of PEDOT over CNF. Such peculiar morphology helps for achieving high conductivity as well as easy ion transport. Compared to standard Pt (2.55 Ω), CP-25 shows little higher R_{ct} . This is probably due to the higher thickness of the counter electrode (CE) and can be reduced further by process modification. The semicircle loop at the low frequency region is an indication of Warburg diffusion (W_d) impedance due to the diffusion through Nernst's diffusion layer^[50]. W_d increases in the order of Pt (4.76 Ω) < CP-25 (5.26 Ω) < PEDOT (10.33 Ω) < CNF (44.95 Ω), indicating that the diffusion coefficient of tri-iodide is in the reverse order. Thus, the superior catalytic activity of CP-25 over PEDOT and CNF is confirmed by the lower charge transfer resistance (R_{ct}) and high diffusion (lower W_d). Tafel polarisation is also carried out in the above cell and is plotted in Figure 2.17b. Exchange current density for the samples is calculated from the low overpotential region from the plot

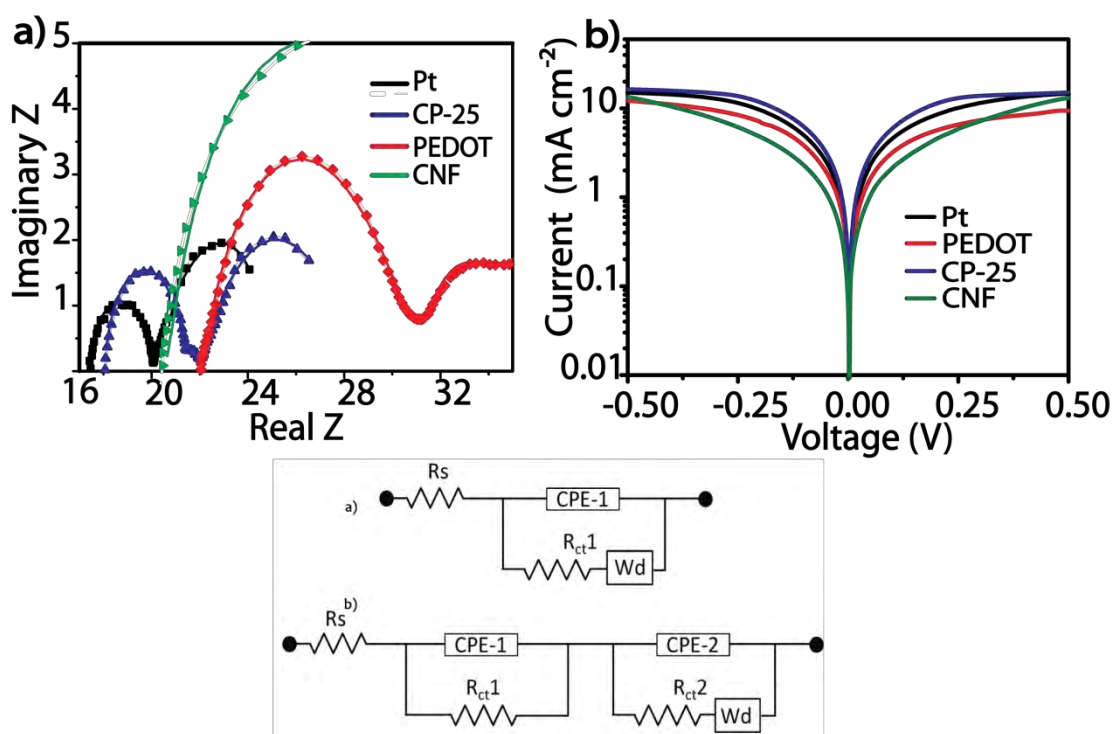


Figure 2.17: a) Nyquist plots obtained from the EIS analysis of the symmetrical cells; symbols are used for the experimental and lines for the fitted data, b) Tafel polarisation plots of the symmetrical cells using different samples and c) circuit diagram used for fitting the EIS data (where, a) Pt and b) PEDOT, CP-25 and CNF).

Table 2.2: EIS equivalent circuit element values as deduced from Figure 2.5a.

	R_s	R_{ct-1}	CPE-1	R_{ct-2}	CPE-2	Wd1
	Ω	Ω	F (10⁻⁶)	Ω	F (10⁻⁶)	Ω
Pt	17.3	2.522	11.3			4.766
CP	18.13	3.184	2.01	0.814	0.020	5.264
PEDOT	21.81	7.35	4.32	5.41	0.019	10.33
CNF	20.4	8.221	3.02	12.92	0.81e-3	44.95

and the corresponding values are 1.40, 1.30, 0.90 and 0.60 mA cm⁻² respectively for Pt, CP-25, PEDOT and CNF. Higher slopes in the anodic and cathodic tales indicate higher exchange current density (J_0) and, thereby, high catalytic activity^[51]. The limiting currents (J_{lim}) in the Tafel plots of CP-25 and Pt are nearly same (Figure 2.17b). Interestingly, it is found that CNF is showing high limiting current even though it has less exchange current density. Thus, it can be concluded that CNF has high overpotential for the tri-iodide reduction compared to PEDOT and CP-25. The J_0 values are also calculated from the EIS measurement using R_{ct} by using the following equation^[51].

$$J_0 = RT/nFR_{ct} \text{ ----- (2)}$$

The calculated values of J_0 from the EIS data are in the same order as obtained from the Tafel slope and the corresponding values are 10.2, 8.1, 3.5, 3.1 mA cm⁻² for Pt, CP-25, PEDOT and CNF respectively.

2.3.10.3 I–V measurement of DSSC

The derived materials were tested as counter electrodes in DSSC under solar illumination of 100 mW cm⁻². Figure 2.18a shows the comparison of *I-V* curves of DSSCs made with different counter electrode materials as compared to standard Pt electrode and Table 2.3 shows the corresponding photovoltaic parameters. Counter electrode made with CP-25 shows superior photo-conversion efficiency of 7.2 % as compared to PEDOT (4.5 %) and CNF (5.6 %). The superior efficiency of CP-25 can be assigned to its high catalytic activity due to the high conductivity and less charge transfer resistance coming from the 1-D alignment of PEDOT^[52]. Compared to PEDOT, the high conversion efficiency of CNF is due to the high open circuit

potential (V_{oc}) and short circuit density (J_{sc}) even though its fill factor was poor due to the low catalytic activity. The low fill factor of CNF is supported by the poor redox couple in CV, low exchange current density in Tafel and high R_{ct} in the EIS measurements. Importantly, CP-25 overcomes the individual drawbacks of its constituents by retaining the high V_{oc} as CNF and high fill factor as PEDOT. The photovoltaic parameters of CP-25 are comparable to Pt (7.3 %), and therefore, CP-25 can be considered to be a promising candidate as an alternative counter electrode in DSSC. Photovoltaic stability of DSSCs made with counter electrodes comprising of CP-25 and PEDOT was also studied. As shown in Figure 2.18b, the efficiency of CP-25 is stabilized to a value of 95 % whereas the efficiency of PEDOT is decreased to 66 % of the starting value. The higher tolerance of CP-25 against deactivation is clearly due to the stable conductivity as well as the mechanical integrity acquainted

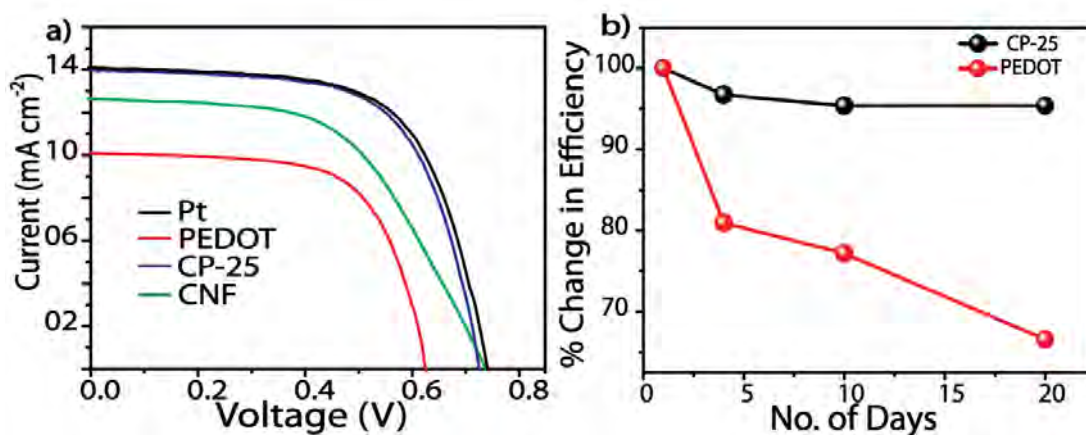


Figure 2.18: a) I-V measurement of DSSC made using the different counter electrodes and b) comparison of the stability of DSSCs made by using CP-25 and bulk PEDOT as the counter electrodes for a duration of 20 days.

Table 2.3: The photovoltaic parameters as deduced from the plots given in Figure 2.6a.

Sample	V_{oc} (V)	J_{sc} (mA cm ⁻²)	Fill Factor (%)	Efficiency (%)
CNF	0.74	12.61	55.08	5.56
PEDOT	0.62	10.02	66.50	4.48
CP-25	0.72	13.96	65.19	7.16
Pt	0.74	14.06	64.78	7.32

from the CNF backbone compared to the bulk PEDOT. Among the counter electrodes with different loading of PEDOT, CP-25 shows superior photovoltaic parameters (Figure 2.19a, Table 2.4), which are in accordance with the catalytic activities obtained from the CV profiles. Further, the performance of CP-25 is compared with a physical mixture containing 25 % of PEDOT. However, the difference in the conversion efficiency is clearly due to the peculiar 1-D alignment of PEDOT in CP-25 which helps to increase the surface area, conductivity and to attain low charge transfer resistance (Figure 2.19 b, Table 2.5). In the case of CP-25, due to the reduced rate of polymerization rate, a film of PEDOT is formed along the inner and outer surfaces of the hollow carbon fiber. On the other hand, in the case of the physical mixture, the system will show an average characteristic of the bulk CNF and PEDOT and result in low fill factor and J_{sc} compared to the bulk PEDOT, likely due to the exposed surfaces of CNF in the electrolyte. In CP-25, the exposed surface is only PEDOT, which has higher surface area, and electrical conductivity resulting in high photo-conversion efficiency.

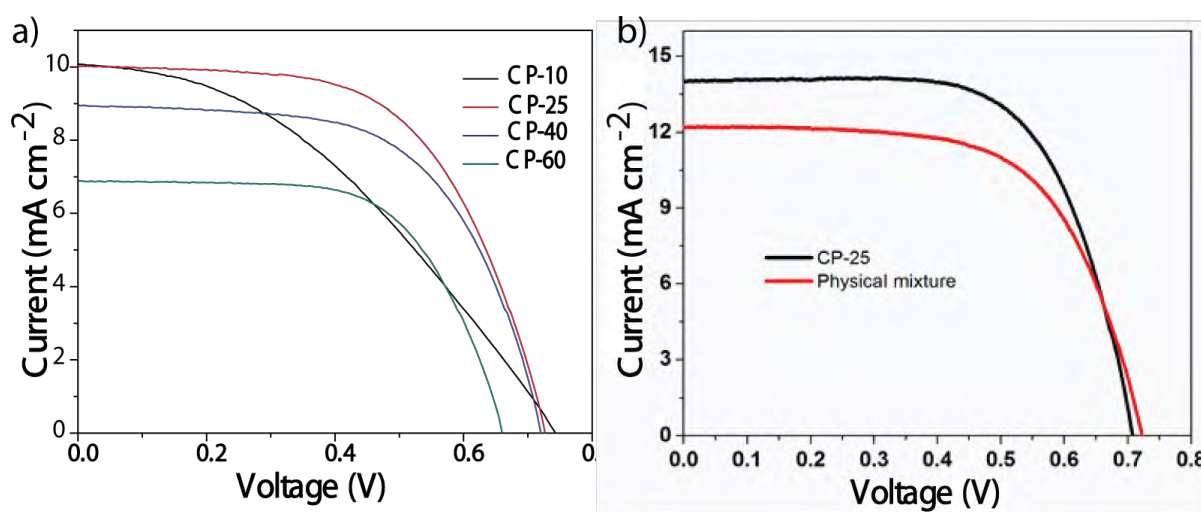


Figure 2.19: (a) I-V data of the composites (only two layer TiO_2 films (total thickness: 6 micron) were used to evaluate the optimum composition of the counter electrode) and b) I-V data of CP-25 and the physical mixture of PEDOT and CNF.

Table 2.4: Values extracted from the photovoltaic performance profiles of the composites with different amount of PEDOT.

Sample	Voc (V)	Jsc (mA cm ⁻²)	Fill Factor (%)	Efficiency (%)
CP-10	0.743	10.01	39.35	3.10
CP-25	0.726	10.00	60.10	4.56
CP-40	0.719	8.933	60.43	4.11
CP-60	0.660	6.873	63.78	3.06

Table 2.5: Values extracted from the photovoltaic performance profiles of CP-25 and the physical mixture.

Sample	Voc (V)	Jsc (mA cm ⁻²)	Fill Factor (%)	Efficiency (%)
CP-25	0.70	14.0	66.5	6.59
Physical-mixture	0.72	12.2	63.3	5.58

2.4 Conclusions

A facile, economical synthetic strategy has been developed for preparing 1-D PEDOT using CNF as a template by adopting a simple *in-situ* polymerization method. The unique structure of CNF provides favourable paths for electrolyte penetration and transportation. A porous structure of PEDOT on FCNF is formed because of the slow polymerization, which plays the key role for the significant electrochemical activity and stability. Nanoconfinement significantly enhanced the conductivity and surface area of PEDOT compared to its bulk counterpart. The overall structural modification assists the system to achieve a high specific capacitance, which is 165 F g⁻¹ for 40 % PEDOT-CNF compared to 75 F g⁻¹ displayed by pure PEDOT. The tubular architecture provided by CNF assists the hybrid for fast ion transport as confirmed from the retention of the initial capacitance, which is 86 % as the scan rate changes in the range of 10 to 800 mV s⁻¹. The CNF backbone also helped the system to provide excellent cycle stability compared to the bulk PEDOT. Along with this, the impedance analysis shows low charge transfer resistance and low time constant for

the hybrid. Poor catalytic activity of bulk PEDOT in DSSC counter electrode could be overcome by the nanoconfinement using CNF. The hybrid material CP-25, which possesses a PEDOT content of 25 wt. %, shows superior catalytic activity as evident from its low E_{pp} and high I_p in the cyclic voltammogram. EIS and Tafel measurements on the symmetrical cell re-confirm the superior catalytic activity of CP-25 over CNF and PEDOT. CP-25 shows low charge transfer resistance and high exchange current density. DSSC made with CP-25 as the counter electrode catalyst shows a conversion efficiency of 7.16 % compared to 4.48 % of PEDOT and 5.56 % of CNF and the value is nearly comparable to that of Pt (7.3 %).

2.5 References

- [1] (a) A. S. Arico, P. Bruce, B. Scrosati, J.-M. Tarascon, W. van Schalkwijk, *Nat. Mater.* **2005**, *4*, 366-377; (b) Y.-G. Guo, J.-S. Hu, L.-J. Wan, *Adv. Mater.* **2008**, *20*, 2878-2887.
- [2] (a) M. L. Anderson, R. M. Stroud, D. R. Rolison, *Nano Letters* **2002**, *2*, 235-240; (b) Y. Qiao, C. M. Li, *J. Mater. Chem* **2011**, *21*, 4027-4036.
- [3] (a) P. Simon, Y. Gogotsi, *Nat. Mater.* **2008**, *7*, 845-854; (b) L. L. Zhang, X. Zhao, M. D. Stoller, Y. Zhu, H. Ji, S. Murali, Y. Wu, S. Perales, B. Clevenger, R. S. Ruoff, *Nano Letters* **2012**, *12*, 1806-1812.
- [4] R. Liu, J. Duay, S. B. Lee, *Chem. Commun.* **2011**, *47*, 1384-1404.
- [5] B. O'Regan, M. Gratzel, *Nature* **1991**, *353*, 737-740.
- [6] (a) A. Malinauskas, J. Malinauskiene, A. Ramanavičius, *Nanotechnology* **2005**, *16*, R51; (b) G. A. Snook, P. Kao, A. S. Best, *J. Power Sources* **2011**, *196*, 1-12; (c) Y. Hou, Y. Cheng, T. Hobson, J. Liu, *Nano Letters* **2010**, *10*, 2727-2733.
- [7] (a) E. Frackowiak, V. Khomenko, K. Jurewicz, K. Lota, F. Béguin, *J. Power Sources* **2006**, *153*, 413-418; (b) J.-H. Kim, A. K. Sharma, Y.-S. Lee, *Mater. Lett.* **2006**, *60*, 1697-1701; (c) C. Zhou, S. Kumar, C. D. Doyle, J. M. Tour, *Chem. Mater.* **2005**, *17*, 1997-2002.
- [8] (a) A. O. Patil, A. J. Heeger, F. Wudl, *Chem. Rev.* **1988**, *88*, 183-200; (b) A. Rudge, J. Davey, I. Raistrick, S. Gottesfeld, J. P. Ferraris, *J. Power Sources* **1994**, *47*, 89-107.
- [9] S. K. Andreas Elschner, Wilfried Lovenich, Udo Merker, Knud Reuter *PEDOT: Principles and Applications of an Intrinsically Conductive Polymer*, CRC, **2011**.
- [10] S. Kirchmeyer, K. Reuter, *J. Mater. Chem* **2005**, *15*, 2077-2088.
- [11] (a) J. C. Carlberg, O. Inganas, *J. Electrochem. Soc.* **1997**, *144*, L61-L64; (b) W. Li, J. Chen, J. Zhao, J. Zhang, J. Zhu, *Mater. Lett.* **2005**, *59*, 800-803; (c) K. S. Ryu, Y.-G. Lee, Y.-S. Hong, Y. J. Park, X. Wu, K. M. Kim, M. G. Kang, N.-G. Park, S. H. Chang, *Electrochim. Acta.* **2004**, *50*, 843-847.
- [12] K. Lota, V. Khomenko, E. Frackowiak, *J. Phys. Chem. Solids.* **2004**, *65*, 295-301.
- [13] L. Chen, C. Yuan, B. Gao, S. Chen, X. Zhang, *J. Solid State Electrochem.* **2009**, *13*, 1925-1933.
- [14] D. Villers, D. Jobin, C. Soucy, D. Cossement, R. Chahine, L. Breau, D. Belanger, *J. Electrochem. Soc.* **2003**, *150*, A747-A752.
- [15] (a) H. Talbi, P. E. Just, L. H. Dao, *J. Appl. Electrochem.* **2003**, *33*, 465-473; (b) P. S. A. Laforguea, *,f, J. F. Fauvarquea,*, M. Mastragostinob,*,z, F. Soavib, J. F. Sarrauc,

- P. Laillerc, M. Conted, E. Rossid and S. Saguattie, *J. Electrochem. Soc.* **2003**, *150*, A645-A651.
- [16] (a) J. Kwon, V. Ganapathy, Y. H. Kim, K. D. Song, H. G. Park, Y. Jun, P. J. Yoo, J. H. Park, *Nanoscale* **2013**, *5*, 7838-7843; (b) T. L. Zhang, H. Y. Chen, C. Y. Su, D. B. Kuang, *J. Mater. Chem. A* **2013**, *1*, 1724-1730; (c) J. M. Pringle, V. Armel, D. R. MacFarlane, *Chem Commun (Camb)* **2010**, *46*, 5367-5369; (d) K.-M. Lee, P.-Y. Chen, C.-Y. Hsu, J.-H. Huang, W.-H. Ho, H.-C. Chen, K.-C. Ho, *J. Power Sources* **2009**, *188*, 313-318.
- [17] J. P. Lock, S. G. Im, K. K. Gleason, *Macromolecules* **2006**, *39*, 5326-5329.
- [18] R. Liu, S. I. Cho, S. B. Lee, *Nanotechnology* **2008**, *19*, 215710.
- [19] (a) S. I. Cho, D. H. Choi, S.-H. Kim, S. B. Lee, *Chem. Mater.* **2005**, *17*, 4564-4566; (b) R. Xiao, S. I. Cho, R. Liu, S. B. Lee, *J. Am. Chem. Soc.* **2007**, *129*, 4483-4489.
- [20] M. G. Han, S. H. Foulger, *Chem. Commun.* **2005**, 3092-3094.
- [21] (a) J. W. Choi, M. G. Han, S. Y. Kim, S. G. Oh, S. S. Im, *Synth. Met.* **2004**, *141*, 293-299; (b) J. Jang, J. Bae, E. Park, *Adv. Mater.* **2006**, *18*, 354-358; (c) J. Wu, Y. Li, W. Feng, *Synth. Met.* **2007**, *157*, 1013-1018; (d) X. Zhang, A. G. MacDiarmid, S. K. Manohar, *Chem. Commun.* **2005**, 5328-5330.
- [22] S. Ito, P. Chen, P. Comte, M. K. Nazeeruddin, P. Liska, P. Péchy, M. Grätzel, *Progress in Photovoltaics: Research and Applications* **2007**, *15*, 603-612.
- [23] J. H. Jang, A. Kato, K. Machida, K. Naoi, *J. Electrochem. Soc.* **2006**, *153*, A321-A328.
- [24] (a) **B. E. Conway**, *Electrochemical Supercapacitors Scientific Fundamentals and Technological Applications*, Springer, **1999**; (b) P. L. Taberna, P. Simon, J. F. Fauvarque *J. Electrochem. Soc.* **2003**, *150*, A292-A300.
- [25] B. Winther-Jensen, K. West, *Macromolecules* **2004**, *37*, 4538-4543.
- [26] H. Mao, X. Lu, D. Chao, L. Cui, Y. Li, W. Zhang, *J. Phys. Chem. C* **2008**, *112*, 20469-20480.
- [27] (a) C. R. Martin, *Acc. Chem. Res.* **1995**, *28*, 61-68; (b) Y.-Z. Long, Z. Chen, C. Gu, M. Wan, J.-L. Duvail, Z. Liu, S. P. Ringer, *A Review on Electronic Transport Properties of Individual Conducting Polymer Nanotubes and Nanowires*, **2010**; (c) Y. Shirai, S. Takami, S. Lasmono, H. Iwai, T. Chikyow, Y. Wakayama, *Journal of Polymer Science Part B: Polymer Physics* **2011**, *49*, 1762-1768.
- [28] D. Alemu Mengistie, P.-C. Wang, C.-W. Chu, *J. Mater. Chem. A* **2013**, *1*, 9907-9915.
- [29] (a) F. Tran-Van, S. Garreau, G. Louarn, G. Froyer, C. Chevrot, *J. Mater. Chem* **2001**, *11*, 1378-1382; (b) A. B. Kaiser, *Rep. Prog. Phys.* **2001**, *64*, 1-49.

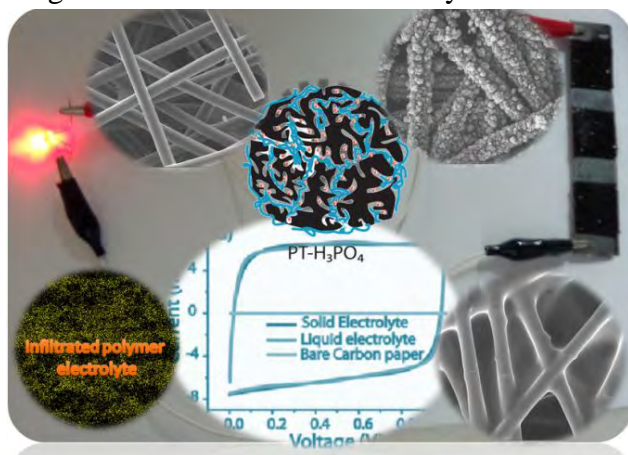
- [30] (a) M. C. Evora, D. Klosterman, K. Lafdi, L. Li, J. L. Abot, *Carbon* **2010**, *48*, 2037-2046; (b) C. Lau, R. Cervini, S. Clarke, M. Markovic, J. Matisons, S. Hawkins, C. Huynh, G. Simon, *J. Nanopart. Res.* **2008**, *10*, 77-88.
- [31] Q. Li, Q. Xue, L. Hao, X. Gao, Q. Zheng, *Compos. Sci. Technol.* **2008**, *68*, 2290-2296.
- [32] W. W. Chiu, J. Travaš-Sejdić, R. P. Cooney, G. A. Bowmaker, *J. Raman Spectrosc.* **2006**, *37*, 1354-1361.
- [33] (a) S. Garreau, G. Louarn, J. P. Buisson, G. Froyer, S. Lefrant, *Macromolecules* **1999**, *32*, 6807-6812; (b) A. Schaarschmidt, A. A. Farah, A. Aby, A. S. Helmy, *J. Phys. Chem. B* **2009**, *113*, 9352-9355; (c) I. Baltog, M. Baibarac, S. Lefrant, P. Gomez-Romero, *Journal of Nanoscience and Nanotechnology* **2009**, *9*, 6204-6209.
- [34] P. A. Christensen, A. Hamnett, A. R. Hillman, *J. Electroanal. Chem. Interfac* **1988**, *242*, 47-62.
- [35] (a) J. H. Scofield, *J. Electron. Spectrosc. Relat. Phenom.* **1976**, *8*, 129-137; (b) D. G. Castner, K. Hinds, D. W. Grainger, *Langmuir* **1996**, *12*, 5083-5086; (c) N. Sakmeche, S. Aeiyaach, J.-J. Aaron, M. Jouini, J. C. Lacroix, P.-C. Lacaze, *Langmuir* **1999**, *15*, 2566-2574; (d) M. G. Han, S. H. Foulger, *Small* **2006**, *2*, 1164-1169.
- [36] I. Y. Jang, H. Ogata, K. C. Park, S. H. Lee, J. S. Park, Y. C. Jung, Y. J. Kim, Y. A. Kim, M. Endo, *J. Phy. Chem. Lett.* **2010**, *1*, 2099-2103.
- [37] (a) M. F. El-Kady, V. Strong, S. Dubin, R. B. Kaner, *Science* **2012**, *335*, 1326-1330; (b) M.-K. Song, S. Cheng, H. Chen, W. Qin, K.-W. Nam, S. Xu, X.-Q. Yang, A. Bongiorno, J. Lee, J. Bai, T. A. Tyson, J. Cho, M. Liu, *Nano Letters* **2012**, *12*, 3483-3490.
- [38] D. Y. Liu, J. R. Reynolds, *ACS Appl. Mater. Interfaces.* **2010**, *2*, 3586-3593.
- [39] C. Peng, D. Hu, G. Z. Chen, *Chem. Commun.* **2011**, *47*, 4105-4107.
- [40] K. A. Noh, D.-W. Kim, C.-S. Jin, K.-H. Shin, J. H. Kim, J. M. Ko, *J. Power Sources* **2003**, *124*, 593-595.
- [41] J. P. Ferraris, M. M. Eissa, I. D. Brotherston, D. C. Loveday, *Chem. Mater.* **1998**, *10*, 3528-3535.
- [42] (a) M. Winter, R. J. Brodd, *Chem. Rev.* **2004**, *104*, 4245-4270; (b) W. G. Pell, B. E. Conway, *J. Power Sources* **1996**, *63*, 255-266.
- [43] V. Noël, H. Randriamahazaka, C. Chevrot, *J. Electroanal. Chem.* **2003**, *558*, 41-48.
- [44] Y. Kou, Y. Xu, Z. Guo, D. Jiang, *Angew. Chem. Int. Ed.* **2011**, *50*, 8753-8757.
- [45] (a) J. R. Miller, R. A. Outlaw, B. C. Holloway, *Science* **2010**, *329*, 1637-1639; (b) K. Sheng, Y. Sun, C. Li, W. Yuan, G. Shi, *Sci. Rep.* **2012**, *2*.
- [46] (a) P. L. Taberna, C. Portet, P. Simon, *Appl. Phys. A* **2006**, *82*, 639-646; (b) B. G. Choi, J. Hong, W. H. Hong, P. T. Hammond, H. Park, *ACS Nano* **2011**, *5*, 7205-7213.

- [47] D. Antiohos, G. Folkes, P. Sherrell, S. Ashraf, G. G. Wallace, P. Aitchison, A. T. Harris, J. Chen, A. I. Minett, *J. Mater. Chem* **2011**, *21*, 15987-15994.
- [48] J. D. Roy-Mayhew, D. J. Bozym, C. Punckt, I. A. Aksay, *ACS Nano* **2010**, *4*, 6203-6211.
- [49] Y.-M. Xiao, J.-Y. Lin, J.-H. Wu, S.-Y. Tai, G.-T. Yue, *Electrochim. Acta.* **2012**, *83*, 221-226.
- [50] L. Kavan, J. H. Yum, M. Grätzel, *ACS Nano* **2010**, *5*, 165-172.
- [51] F. Gong, H. Wang, X. Xu, G. Zhou, Z. S. Wang, *J Am Chem Soc* **2012**, *134*, 10953-10958.
- [52] (a) R. Trevisan, M. Döbbelin, P. P. Boix, E. M. Barea, R. Tena-Zaera, I. Mora-Seró, J. Bisquert, *Adv. Energy Mater.* **2011**, *1*, 781-784; (b) T. H. Lee, K. Do, Y. W. Lee, S. S. Jeon, C. Kim, J. Ko, S. S. Im, *J. Mater. Chem* **2012**, *22*, 21624-21629.

Chapter-3

Active Interface Tuning Of Solid-State Supercapacitor: Studies with Carbon Fiber Supported Conducting Polymers

Replacement of liquid electrolyte from the supercapacitors and Li-ion batteries with a solid counterpart is very promising for developing safe, light-weight and flexible devices. However, conventional polymer film approach is inferior in performance owing to the less effective electrode-electrolyte interface achievable with the solid polymer electrolytes. This chapter deals with the successful demonstration of the tuning of active electrode-electrolyte interface in favorably affecting the charge



storage properties of the solid-state supercapacitors. In the initial section, performance variation of an all-solid-state supercapacitor is explained by intercalating a gel-polymer electrolyte, *i.e.* PVA-H₂SO₄, with different amounts of PANI coated carbon fiber paper. However, this system encountered issues such as low interface and inferior

charge storage properties at higher mass loading conditions. The second section deals with the fabrication of a solid-state supercapacitor which has closely matching performance characteristics as that of its liquid-state counterpart. This has been achieved by electro-depositing PEDOT onto the individual carbon fiber in the paper, followed by polymer-gel electrolyte intercalation. Electrodeposited PEDOT acquired a flower like interconnected growth pattern, which helped to improve the electrode-electrolyte interfacial area. Thus, even under a higher PEDOT loading of 7.56 mg cm⁻², desired interface could be established and, thus, resulted into a high volumetric capacitance of 28 F cm⁻³ while retaining a high specific capacitance of 112 F g⁻¹.

Content in this chapter is published in the following articles.

ACS Appl. Mater. Interfaces, 2013, 5 (24), 13397–13404

(<http://pubs.acs.org/doi/abs/10.1021/am404320e>)

Nanoscale, 2014, 6, 5944-5952

(<http://pubs.rsc.org/en/content/articlelanding/2014/nr/c4nr00659c#!divCitation>)

Reproduced by permission of Royal Society of Chemistry and American Chemical Society

3.1 Introduction

Polymer electrolytes^[1] have been extensively studied as electrolytes in supercapacitors and lithium batteries in place of liquid electrolytes. Liquid electrolyte in conventional electrochemical energy storage devices raise safety issues and thus require high-standard safety encapsulation materials and technologies.^[2] Replacement of liquid electrolyte in the energy storage devices with a solid counterpart is thus very promising for developing thin, light-weight, economically viable and flexible future devices. Among the various polymer electrolytes, gel/plasticised electrolytes^[1b, 1c] show ambient conductivity and desirable mechanical properties. Thus, they are emerging as promising electrolyte materials to replace conventional liquid electrolyte in supercapacitors. Many of the earlier studies utilized gel electrolyte as a film^[1d, 1e, 3] between the electrodes, which resulted in low electrode-electrolyte interfacial area with poor charge storage properties. Apart from the low charge storage properties, total device resistance increases due to high contact resistance arising from the low integrity of the electrode-electrolyte material.^[3c, 4] Very low equivalent series resistance (ESR) is highly desirable for the storage device as the power rate of the device is determined by the relation $P_{\max} = V^2/4R$. In recent studies, researchers have been successful in developing free standing electrode materials for fabricating flexible solid-state devices.^[4a, 5] Here also, these polymer electrolyte films are not intercalated with electrode material which in turn decreases the electrode-electrolyte interfacial area, leading to low capacitance and high ESR. To find a promising solid counterpart for replacing liquid electrolytes in supercapacitors, we need an electrode-electrolyte interface in the solid-state system which mimics the liquid-solid interface in the conventional systems.

Here, we have developed a process wherein we could closely mimic the electrode-electrolyte interface obtainable from a liquid electrolyte for the solid-state supercapacitors by utilizing the high porosity of conducting carbon paper and tunable viscosity characteristics of the gel electrolyte. Carbon paper used for this purpose possesses very low sheet resistance ($0.26 \Omega/\square$), low density (0.4 g/cc) and high porosity (97%), which makes it a versatile candidate for fabricating the supercapacitor electrodes. The polymer electrolyte selected here is a PVA- H_2SO_4 gel/plasticizer, which is known for its high conductivity and flexibility.^[6] Due to the

high porosity of the carbon substrate, PVA-H₂SO₄ is successfully intercalated even after the loading of the electrode material. Apart from acting as a matrix which helps to establish the enhanced electrode-electrolyte interface, the porous carbon backbone plays another important role as an adequate electrical contact within the network, which is critical in maintaining very low ESR. Initial experiments were carried out with polyaniline (PANI)^[7] as an electrode material (Part A). The systematic experiments carried out using PANI provided critical information on the importance of porosity in the electrode for establishing enhanced interfacial network in solid-state supercapacitors for achieving high charge-storage properties. However, one challenge which we faced here was that, at higher mass loading of the electro active material, the performance of the solid-state device becomes inferior to its liquid-state counterpart as the polymer infiltration becomes improper under such conditions. This leads to a drastic decrease in the specific capacitance. This left out an open question on developing appropriate strategies for maintaining high specific capacitance even under high mass loading conditions.

To address this issue, in the second part of this chapter (Part B), a different strategy of electrodepositing the charge storage material directly onto a porous carbon current collector is adopted, which ensures a highly reproducible coating of the electro-active material over each carbon fiber backbone. Due to the low stability and low electrochemical window of the PANI, selected electrode material in the second case (Part B) is polyethylenedioxythiophene (PEDOT)^[8]. Such a stable electrode material, which can be electrodeposited uniformly along the carbon fiber from a non-aqueous solvent, is important for checking the stability aspects of the polymer electrolyte.

3.2 Experimental Section

3.2.1 Materials

Aniline, ammoniumpersulfate (NH₄)₂S₂O₈, polyvinylalcohol (PVA), ethylenedioxythiophene (EDOT), lithium perchlorate (LiClO₄) and N-methylpyrrolidone (NMP) were purchased from Aldrich Chemicals. Concentrated H₃PO₄ and polyvinyl alcohol (PVA) (M.W 1,15,000; 98-99 mol % hydrolyzed) were supplied by Loba Chemie. Sulfuric acid (H₂SO₄), acetonitrile and hydrochloric acid

(HCl) were procured from Rankem Chemicals. All the chemicals were used as received without any further purification. A polytetrafluoroethylene (PTFE) filter paper (pore size, 0.45 μm ; Rankem) was used for the filtration. Carbon paper having a thickness of 0.3 mm was purchased from Toray Japan. Polypropylene membrane of 25 μm from Celgard was used as a separator in specified devices. Supercapacitor grade carbon was purchased from Kuraray chemicals. Conducting carbon filler was purchased from Alfa Aesar. Super-P (PvDF) was procured from Global Nanotech and used as the binder. Grafoil® sheet was purchased from GrafTech. .

3.2.2 Preparation of PVA-H₂SO₄ Solutions and Film

Approximately 2 g of PVA was weighed and transferred onto 100 ml round bottom flask containing 20 ml of de-ionized water to prepare 10 wt. % PVA solutions. The mixture was heated at 85 °C with constant stirring until a clear solution of PVA was obtained. This was subsequently cooled to room temperature. Approximately, 2 g of concentrated H₂SO₄ was added to the solution and stirred gently for 30 min. to obtain 1:1 PVA-H₂SO₄ solution. Films were prepared by pouring 7 g of PVA-H₂SO₄ solution into a glass Petri-dish having 7 cm diameter and was kept in an oven initially at 60 °C for 2 h and later at 40 °C for 6 h to obtain a uniform transparent PVA-H₂SO₄ film.

3.2.3 Synthesis of Polyaniline (PANI)

Polyaniline was prepared by adopting a reported method^[7]. In a typical synthesis, to an ice cold solution of 1 ml of aniline in 50 ml of 1M HCl, pre-cooled solution of (NH₄)₂S₂O₈ in 50 ml 1M HCl was added drop-wise and stirred for 6 h. The green colored PANI solution was filtered and washed with DI water and dried at 60 °C.

3.2.4 Electrochemical Polymerization of EDOT

Polymerization was carried out in a BioLogic SP-300 Potentio-Galvanostat using 3-electrode systems in which carbon paper was used as the working electrode, Pt was used as the counter electrode and Ag/AgCl was used as the reference electrode. Electrolyte used was acetonitrile containing 0.1 M LiClO₄ as the supporting electrolyte and 0.1 M EDOT. Before the experiments, nitrogen was passed through

the electrolyte to remove any dissolved oxygen. 1 cm² area of carbon paper was kept exposed to the electrolyte and the remaining part was masked using a Kapton adhesive tape. The experiments were carried out in constant current mode, by maintaining 10 mA cm⁻² current density. The experiments were repeated for different time durations of 50, 100, 300, 600, 1200 s and the corresponding electrodes are named as CP-50, CP-100, CP-300, CP-600, and CP-1200, respectively. After completion of the electrochemical deposition, the electrodes were washed with acetonitrile solution and dried under IR lamp and preserved for further studies.

3.2.5 PANI Electrode Preparation

A paste of polyaniline was made with NMP and this was coated onto 1 cm² area of a Toray carbon paper (non teflonated) having a total dimension of 1 cm x 2 cm using a K-control coater. The excess dimension outside the PANI coated area was kept to utilize it as the current collector during the measurements. PANI to NMP ratio was fine tuned to get a uniform deposition of PANI inside the carbon matrix. Different loading of PANI was obtained by varying the concentration of PANI in NMP. The electrodes were dried overnight at 100 °C.

3.2.6 Device Fabrication

In order to make the solid-state supercapacitors, the PVA-H₂SO₄ aqueous solution was used as the electrolyte. This was coated onto the both surfaces of the PANI coated carbon paper electrode using a K-control coater and the coated electrodes were dried at 60 °C under vacuum for overnight. In the case of electro deposited PEDOT electrode, both surfaces of the carbon paper were coated with PVA-H₂SO₄ using the same method. Prototype devices were made by attaching together two such electrodes by applying a pressure of 20 Kg cm⁻². Before sandwiching, much care was taken to ensure that a fine layer of PVA-H₂SO₄ was formed on one side of the each electrode to serve as an effective separator between the electrodes once they are pressed together. The film formed in between the electrodes will prevent the short circuit by acting as a separator. For making the liquid-state devices for comparison, the electrodes were separated by using a polypropylene membrane as a separator and the device was tested by dipping in 0.5 M H₂SO₄.

3.2.7 Characterization

Structure and morphology of the materials and device were analyzed using Quanta™ Scanning Electron Microscope. All the electrochemical studies were carried out in a Bio-Logic SP-300 Potentio-Galvanostat. The CV measurements were taken at different scan rates by maintaining a potential window of 0.8 V for the PANI devices and 1.0 V for the PEDOT and carbon devices. The charge-discharge measurement was done at the same potential range as that of CV. Cycling stability was done by chrono charge-discharge method at 5 A g⁻¹ current density. Electrochemical impedance (EIS) analysis was carried out from 10⁶ to 0.01 Hz frequency against the open circuit potential with a sinus amplitude of 10 mV ($V_{\text{rms}} = 7.07$ mV). The EIS data was analyzed using an EC-Lab Software V10.19

Weight calculation for the electro-deposited PEDOT:

$$W = \frac{\text{Charge passed (C)} * 142 \text{ (Mol. weight of EDOT)}}{96485 * 2.33 \text{ (no electron released per EDOT)}}$$

Specific capacitance (F g⁻¹), volumetric capacitance (F cm⁻³) and areal capacitance (F cm⁻²) of the electrode were calculated from the cyclic voltammogram using the following equation [9]:

$$C = 2 * \frac{Q}{(E_1 - E_2) * v * M/V/A} \text{ ----- (1)}$$

In case of the charge-discharge experiments, the following equation was used for measuring the capacitance:

$$C = 2 * \left(\frac{I \Delta t}{(E_1 - E_2) * M/V/A} \right) \text{ ----- (2)}$$

where, $Q(\text{charge}) = \frac{\int_{E_1}^{E_2} I(E) dE}{v}$ is the average charge obtained by the integration of the cathodic and anodic parts of the voltammogram, $E_1 - E_2$ is the potential window, M is the weight of the active material in the one of the electrodes (g), V is the volume of the single electrode, A is the area of the single electrode, v is the scan rate (mV s⁻¹), Δt is the discharge time and I is the constant current used for charging and discharging.

- As the experiments are done in symmetrical 2-electrode fashion, *i.e.* capacitance of the cell will be the half of the single electrode capacitance,

multiplication of the capacitance by a factor of 2 is included in the above equations.

- Contribution of carbon paper towards the capacitance is negligible and not considered for the calculations.

Energy density (E_d) and power density (P_d) for the whole device were calculated from the capacitance value obtained from the charge-discharge method.

$$\text{Volumetric energy density } E_{V/m} \text{ (Wh cm}^{-3}\text{)} = \frac{1}{2} * \frac{C_{V/m} V^2}{3600}$$

$$\text{Power density } P_{V/m} \text{ (W cm}^{-3}\text{)} = \frac{E_{V/m}}{t}$$

where, C_V is the volumetric capacitance for the whole device ($F \text{ cm}^{-3}$), C_m is the specific capacitance for the whole device ($F \text{ g}^{-1}$), V is the voltage window and t is the discharge time.

3.3 Result and Discussion

Part A. Effect of Mass Loading of PANI in the Relative Electrode-Electrolyte Interface

Doped PANI was synthesized by chemical oxidation of aniline using ammonium persulfate in acidic condition. The solvent selected here was N-methyl-2-pyrrolidone (NMP), and the concentration was carefully adjusted to get the proper distribution of PANI particles on to the carbon fibers without blocking the pores. This was essential for attaining enough space for the penetration of the solid electrolyte. PANI solution was manually coated onto the porous carbon paper using a steel rod over a smaller area, while coating on larger areas was performed by an automated K-coater. For incorporating the solid-electrolyte in the solid-state device, an aqueous solution of PVA- H_2SO_4 was applied on to the PANI coated porous carbon paper. The density of PVA was tuned for easy penetration of the solid electrolyte into the pores of the PANI coated carbon paper. Two such electrodes are sandwiched together to form the device. The device fabrication steps are shown schematically in Figure 3A.1a. Optical images of a single cell device and 4-cells in series powering an LED are shown in Figure 3A.1b and 1c, respectively.

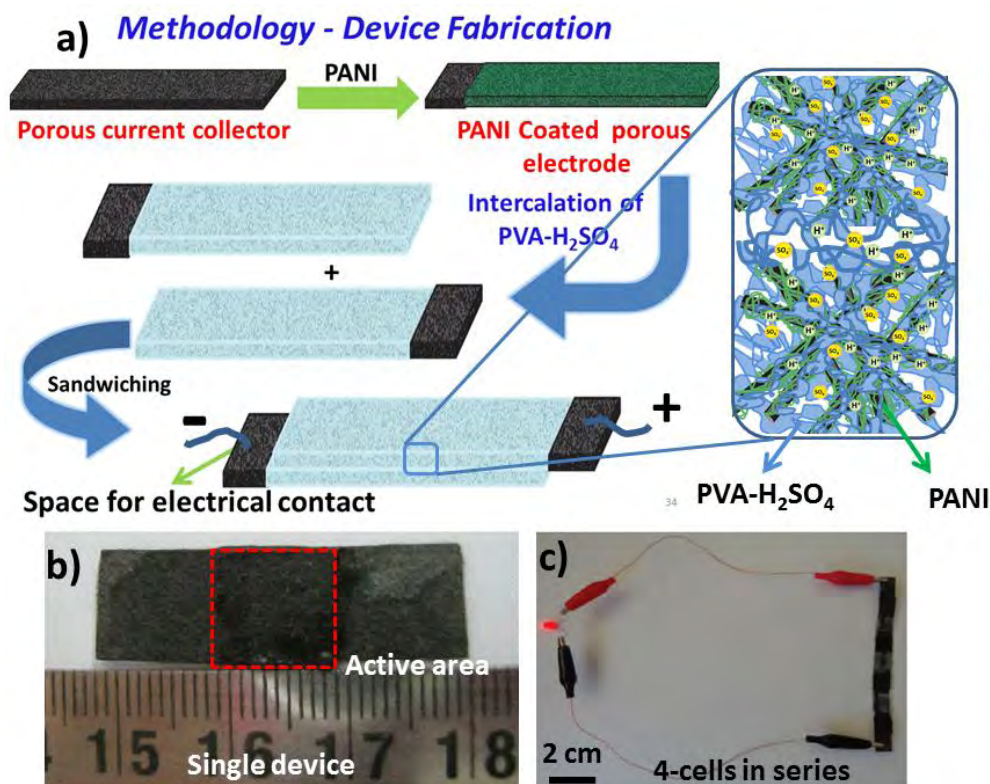


Figure 3A.1: a) Schematics of the all-solid-state-supercapacitor (ASSP) representing the steps involving the coating of PANI onto the carbon paper, incorporation of PVA-H₂SO₄ into the porous PANI/carbon paper and sandwiching of electrodes by applying pressure to make the all-solid-state-supercapacitor, b) optical images of the 1 cm² prototype ASSP and c) LED powered by a four-cell assembly connected in series.

3.3.A1 SEM and EDX Analysis

Scanning electron microscopy (SEM) and elemental mapping of the surface of the carbon paper using energy-dispersive X-ray spectroscopy (EDX) show a clear picture of the surface morphology of the device. The SEM images of the bare carbon paper in Figure 3A.2a show high porosity of the matrix which is formed by homogenous alignment of uniform fibers having a diameter of ~5 μm. In order to validate the role of the porous matrix of the carbon paper, Grafoil® sheet also was used as a current collector, which is a plain nonporous conducting substrate. The corresponding SEM image of Grafoil® is given in Figure 3A.2c. Figure 3A.2e shows the SEM image of the carbon paper loaded with 1.5 mg cm⁻² PANI (for the images corresponding to the different loading of PANI as 0.3 and 5 mg cm⁻², refer Figure 3A.2d & 2f). The particle size of PANI is small due to the higher solubility of PANI in NMP, which helps in attaining uniform coating along the individual fibers of the carbon paper

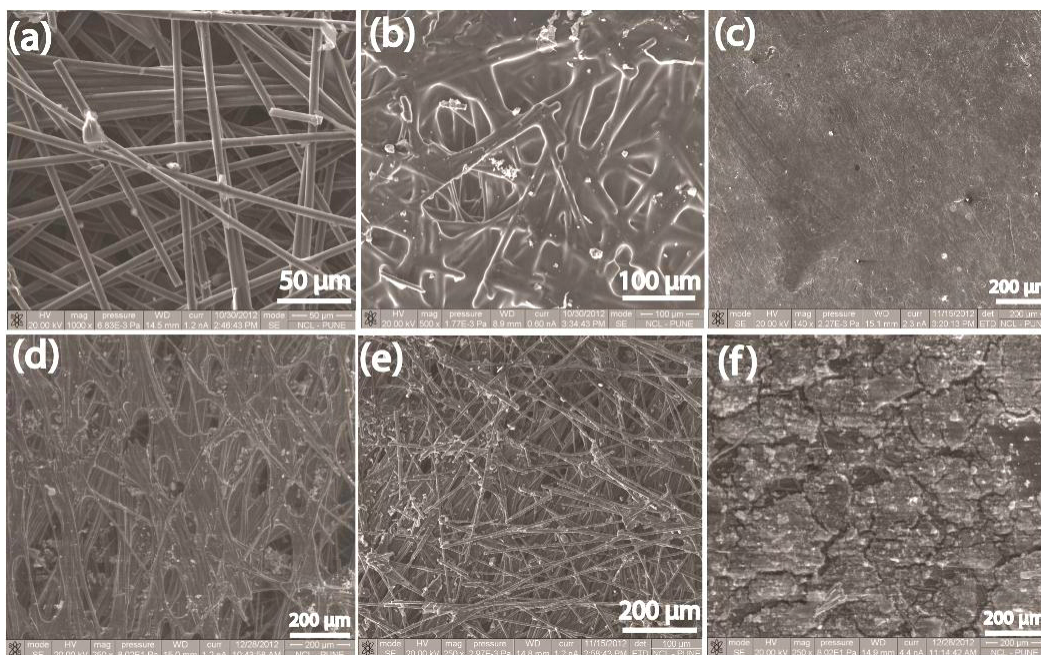


Figure 3A.2: SEM images of (a) porous carbon paper, (b) intercalated gel-electrolyte inside the PANI/carbon paper PANI (1.5 mg cm^{-2}) coated carbon paper and (c) Grafoil®, which was used as the nonporous substrate for the comparative study. Images d) to f) indicate the PANI/carbon paper with different PANI loadings as d) 0.3 mg cm^{-2} , e) 1.5 mg cm^{-2} and f) 5.0 mg cm^{-2} .

throughout the matrix. However, at higher loading, more PANI particles get accumulated at the surface which in turn reduces the porosity, which is evident from Figure 3A.2f. The carbon surface after the PVA- H_2SO_4 coating is shown in Figure 3A.2b which reveals well intercalated PVA- H_2SO_4 matrix.

Cross-sectional SEM images and elemental mapping along the cross-section of the device gives a clear picture of the expected high integrity and enhanced electrode-electrolyte interface within the system (Figure 3A.3a-c). The total thickness of the device is only 0.80 mm which comprises a fine film of the gel electrolyte possessing a thickness of 0.12 mm in between the PANI coated carbon paper. The EDX elemental mapping shows the intercalated PANI particles and PVA- H_2SO_4 inside the carbon fiber matrix. Sulphur (S) mapping at the same location as shown in Figure 3A.3a indicates the presence of S into the either side of the PVA- H_2SO_4 film. This unambiguously confirms the diffusion of PVA- H_2SO_4 through the carbon fibers, which leads to an intimate electrode-electrolyte interface in the system. Further, the diffusive nature of the solid-electrolyte is appeared to be decreasing with higher

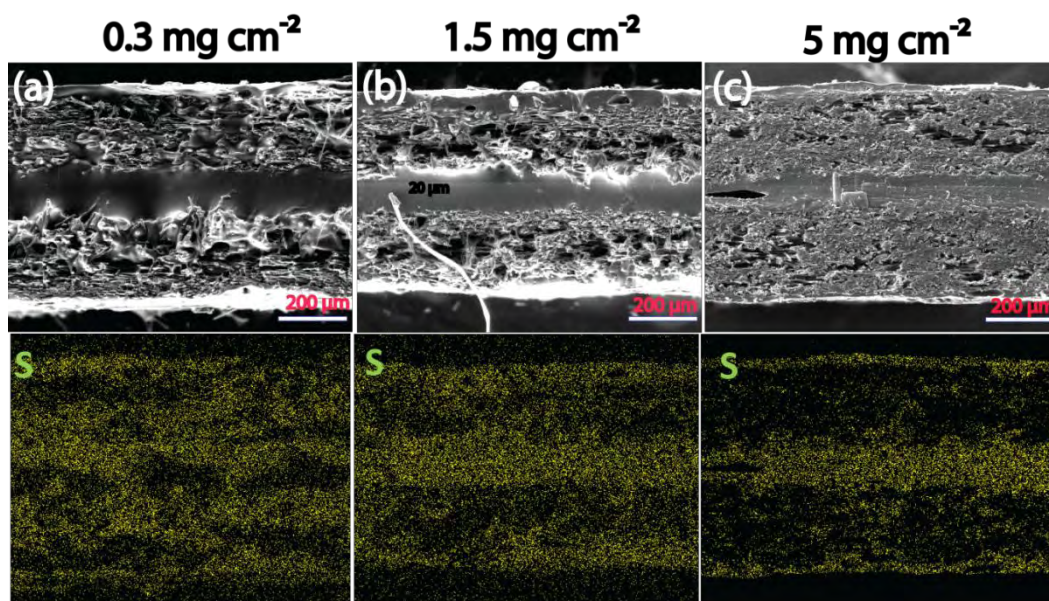


Figure 3A.3: Cross-sectional SEM images and the corresponding S-elemental mapping of the ASSP with different loading of PANI: (a) 0.3 mg cm^{-2} , (b) 1.5 mg cm^{-2} and (c) 5.0 mg cm^{-2} .

loading of PANI, which is clear from the cross-sectional mapping of the corresponding devices which are having different PANI loading as shown in Figure 3A.3b and 3c. The gradual change in the porosity of the carbon paper with the loading of PANI is clear from Figure 3A.2d-f. It is clear from these sets of figures that, higher loading of PANI leads to filling of the pores heavily so that the space available for the intercalation of the polymer electrolyte is decreasing. The SEM cross-section images and elemental mapping also emphasize the need for special attention to be taken with higher loading of PANI in order to establish adequate integrity. Such benefits in establishing extended electrode-electrolyte interfaces will help to achieve very high areal capacitance without compromising the specific capacitance. This extended and well-distributed interfacial structure nearly mimics an interfacial structure which can be expected in a system based on the conventional liquid electrolytes.

3.3.A2 Electrochemical Characterization

Electrochemical charge storage properties of the PANI coated electrodes were analyzed initially in acidic medium containing $0.5 \text{ M H}_2\text{SO}_4$ and subsequently the tests were done using the systems based on the gel electrolyte. As mentioned before, non-porous electrodes are prepared by coating PANI on Grafoil® along with the PANI coated porous carbon electrodes. Grafoil® with a PANI loading of 1.5 mg cm^{-2}

displays a capacitance of 300 F g^{-1} when the CV was recorded at a voltage scan rate of 10 mV s^{-1} (Figure 3A.4a). This value is in good agreement with the reported capacitance of polyaniline^[10] prepared by the same synthetic procedure. Now, looking at the performance of the porous carbon paper based electrode possessing the same PANI loading, an interesting leap in capacitance of 2.3 fold, leading to a value of 693 F g^{-1} at 10 mV s^{-1} has been achieved in $0.5 \text{ M H}_2\text{SO}_4$ as shown in Figure 3A.4a. It should be noted that the contribution of the porous carbon paper towards the capacitance is only $40 \mu\text{F cm}^{-2}$ (Figure 3A.4b), and, hence, can be neglected while considering the overall capacitance. The charge-discharge method also displays similar results in which the PANI coated carbon paper gives a mass specific capacitance of 700 F g^{-1} and an areal capacitance of 1.05 F cm^{-2} . Contrary to this, the corresponding values with the Grafoil® counterpart are only 300 F g^{-1} and 0.45 F cm^{-2} respectively at 0.5 A g^{-1} current density (Figure 3A.4c). The obtained specific capacitance of 700 F g^{-1} for PANI and an areal capacitance of 1.05 F cm^{-2} are much higher than the corresponding reported capacitance values for pure polyaniline.^[10a, 10c, 11] Apart from this, Figure 3A.4d shows an excellent capacitance retention of 72 % for the PANI coated carbon paper even at a fast discharging rate of 20 A g^{-1} compared 50 % retention of the PANI/Grafoil® system. Thus, the CV and charge-discharge methods reveal a huge difference in the capacitance values when the substrate morphology changes from non-porous to porous even though both are having the same PANI content. This difference can be clearly attributed to the utilization of high porosity carbon paper for achieving enhanced electrode-electrolyte interface for PANI upon its coating on the surface.

Fabrication of the all-solid-state supercapacitor (ASSP) requires replacement of the liquid electrolyte with the solid electrolyte. The above results using the liquid electrolyte clearly indicate the superiority of the porous substrate as the current collector in order to establish higher area of the electroactive material. Once this condition is maintained, a proper intercalation by a solid electrolyte which gives a closely matching interfacial structure with the electrode material is expected to narrow down the differences in the performances between the solid and liquid systems. In order to conceive this condition, the solid electrolyte, which will mimic the nature of the liquid electrolyte, should lead to very high interfacial area inside the porous current collector. This issue could be overcome by using PVA- H_2SO_4 gel polymer electrolyte by *in situ* solidifying inside the porous current collector which is

already coated with PANI, but still bearing enough porosity to accommodate the gel electrolyte. Since the porosity is still sufficient inside the PANI/carbon paper for making intercalated electrode-gel electrolyte interface, the system more or less mimics an interfacial structure similar to a case where a liquid electrolyte is used.

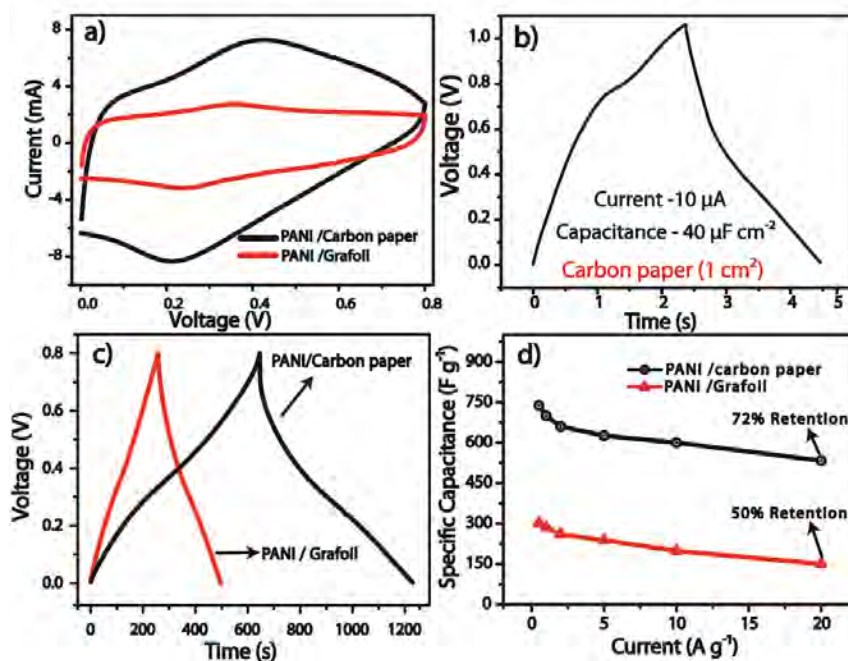


Figure 3A.4: Comparison of (a) CVs at a scan rate of 10 mV s^{-1} for the systems made by using porous carbon and Grafoil® as the substrates, (b) charge-discharge curve of blank carbon paper at a current density of $10 \mu\text{A}$, (c) charge-discharge profiles at a current density of 0.5 A g^{-1} of the PANI coated carbon paper and Grafoil® and (d) the plots indicating the change in the specific capacitance with current density for the carbon paper and Grafoil® based systems.

This strategy has been realized successfully as reflected from the measured capacitance of the ASSP (active material is 1.5 mg cm^{-2}), which shows a capacitance of 647 F g^{-1} at a current density of 0.5 A g^{-1} by the galvanostatic charge-discharge method (Figure 3A.5a). The retention of capacitance of the ASSP with the current density as shown in Figure 3A.5b shows that the ASSP could retain 400 F g^{-1} even at a high current density of 20 A g^{-1} . The capacitance value obtained by the cyclic voltametry is 568 F g^{-1} at 10 mV s^{-1} compared to 700 F g^{-1} measured by using the liquid electrolyte (Figure 3A.5c). The CV profiles of the solid and liquid based systems have similar features even though at higher potentials, the solid-state system shows lower current. In both the cases, closely comparable capacitance retention has

been observed with respect to the variation of the voltage scan rate from low to high. The capacitance value of the ASSP is almost 93 % of the capacitance obtained for the liquid state system using 0.5 M H_2SO_4 by the charge-discharge method. The areal capacitance is estimated to be $1 F cm^{-2}$ for PANI with its loading of $1.5 mg cm^{-2}$.

Variation of specific capacitance vs. areal capacitance is given in Figure 3A.5d which is calculated from the charge-discharge method. Even at a very high areal capacitance of $2 F cm^{-2}$, the device shows a specific capacitance of $400 F g^{-1}$. It should be noted that, many of the ASSPs reported have very low areal capacitances in microfarads even though they have high specific capacitance^[5, 11c, 12]. The specific capacitance could be reached to $850 F g^{-1}$ with a low PANI loading of $0.3 mg cm^{-2}$, where the areal capacitance is $0.28 F cm^{-2}$. These variations are expected and are in accordance with the aforementioned results of the SEM and elemental mapping of the cross-section of the devices possessing varying loading of PANI. As the PANI content increases, the pores are getting filled and subsequently most of the PANI particles stays at the surface and prevents penetration of PVA- H_2SO_4 into the carbon

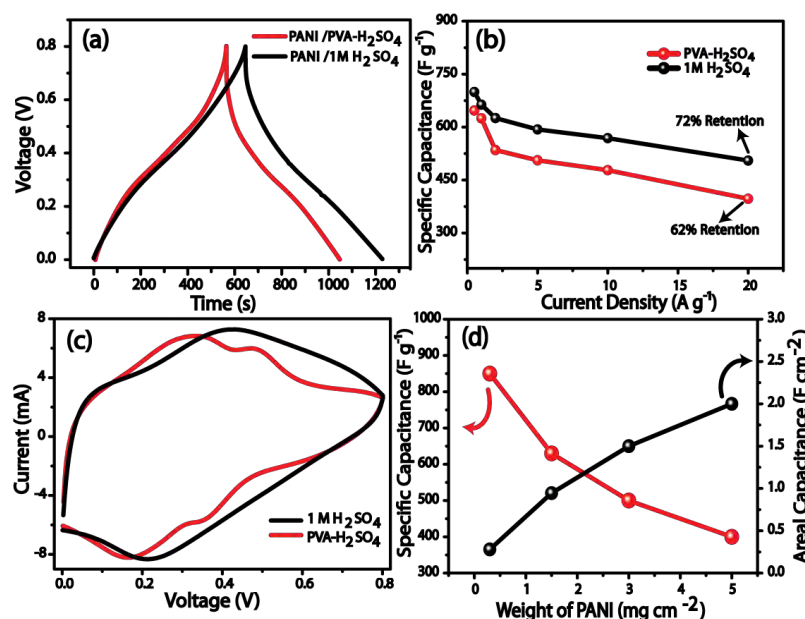


Figure 3A.5: Comparison of (a) charge–discharge profiles at a current density of $0.5 A g^{-1}$ of the PANI coated carbon paper in $0.5 M H_2SO_4$ and PVA- H_2SO_4 , (b) plots indicating the change in the specific capacitance with current density for the solid and liquid-state systems, (c) CV for the solid and liquid-state systems taken at a scan rate of $10 mV s^{-1}$ and (d) plots corresponding to the specific capacitance vs. areal capacitance of the solid-state system.

paper. This leads to lower electrode-electrolyte interface, which is clear from the comparative S elemental mapping in Figure 3A.3a-c.

For comparing the design of the electrode-electrolyte interface with the conventional approach involving an ion conducting membrane as a separator between the electrodes, a device is fabricated by sandwiching a PVA-H₂SO₄ film in between the PANI coated carbon papers by hot pressing. Due to the lower electrode-electrolyte contact, the system gives a significantly low specific capacitance of 150 F g⁻¹ at 0.5 A g⁻¹ and a PANI loading of 1.5 mg cm⁻² (Figure 3A.6 a-b) compared to 647 F g⁻¹ as obtained in the previous case by applying the gel-electrolyte directly on the electrodes. Apart from the lower specific capacitance, the device also shows very low capacitance retention (27 % when the current is directly increased to 20 A g⁻¹ from 0.5 A g⁻¹). The high internal resistance of 20 Ω cm⁻² (Figure 3A.6c) measured from the x-intersect of the Nyquist plot of impedance analysis validates the reason for the poor capacitance retention of the system. This clearly shows the advantages of our design to enhance the electrode-electrolyte interface rather than having a solid film between the electrodes.

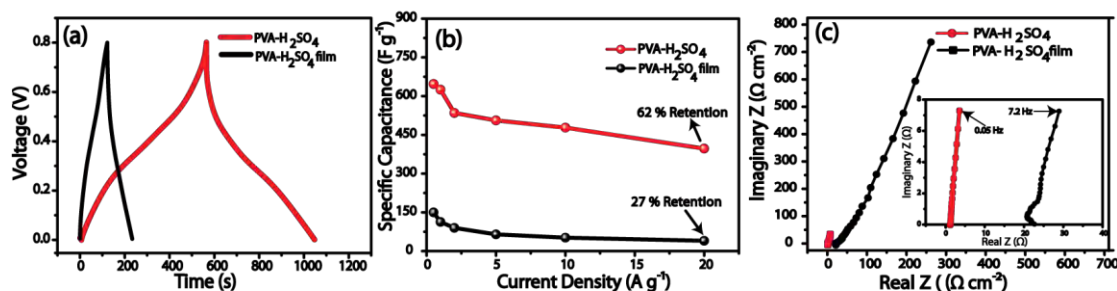


Figure 3A.6: Performance characteristics of the solid-state devices formed by the present approach and the one made by using a polymer film as in the case of the conventional systems: (a) comparison of the charge-discharge profiles measured at 0.5 A g⁻¹ current density, (b) comparison of the change in specific capacitance with varied current and (c) Nyquist plot of the ASSP using PVA-H₂SO₄ in the resent strategy and conventional solid film method with enlarged part of the high frequency region in the inset.

Impedance analysis of the ASSP confirms the high charge storage properties obtained by both the CV and chrono charge-discharge methods. The high retention of capacitance under fast charge-discharge conditions is possible only if the system assists very fast ion diffusion in response to the large perturbation. Two factors which have the key role here are the ESR and the charge-transfer resistance. Estimated ESR

from the Nyquist plot of the device is only $1 \Omega \text{ cm}^{-2}$ (Figure 3A.7a). The liquid and solid systems have only 0.1Ω differences, which explain the superior power rate and high retention of the ASSP. It is also interesting to note that the ESR of the solid device made by using the PVA- H_2SO_4 film shows a huge ESR of $20 \Omega \text{ cm}^{-2}$ (Figure 3A.6c). Further, in ASSP, any characteristic high frequency semicircle could not resolve even in the zoomed image in Figure 3A.7a, confirming that there is very less charge-transfer resistance in the system.

Energy density and power density are calculated from the charge-discharge method after excluding the weight of the carbon paper and electrolyte. The corresponding Ragone plot is shown in Figure 3A.7b. The polyaniline in the solid device shows an energy density of 14.3 Wh kg^{-1} at a power density of 105 W kg^{-1} compared to 3.3 Wh kg^{-1} of the device which uses a polymer film. At a higher power rate of 5.6 kW kg^{-1} , the ASSP based on the current approach could keep an energy density of 8.8 Wh kg^{-1} whereas the film based system shows an energy density of only 1.1 Wh kg^{-1} at a power rate of 2.3 kW kg^{-1} . The volumetric energy density of the whole device including the carbon paper and the solid electrolyte is 0.53 mWh cm^{-3} .

Extended cycling stability is an essential criterion for any charge storage devices. It is found that the architecture improves the stability along with the capacitance. 10000 continuous cycling was carried out at a current density of 5 A g^{-1} of ASSP which was showing a capacitance of 638 F g^{-1} . Percentage capacitance retention and coulombic efficiency during the 10000 cycles are plotted in Figure 3A.7c. Excellent stability was obtained during the cycling with less than 2 % degradation and nearly 100 % coulombic efficiency during the entire cycling. In contrast to the low stability of PANI in the liquid electrolyte (Figure 3A.7d), the enhanced stability of PANI in ASSP is clearly explained by the role of PVA as the binder. Apart from the role as the electrolyte matrix in the device, PVA also plays an integral role by providing a means to hold the polyaniline moiety tightly. On the other hand, in the liquid electrolyte, the relative movement of the electrolyte will enhance the detachment of the electrode material from the electrode as any extra binder is not applied for ensuring mechanical stability. The obtained cycle stability of the solid supercapacitors is much superior to the literature reports.^[4a, 10a, 13]

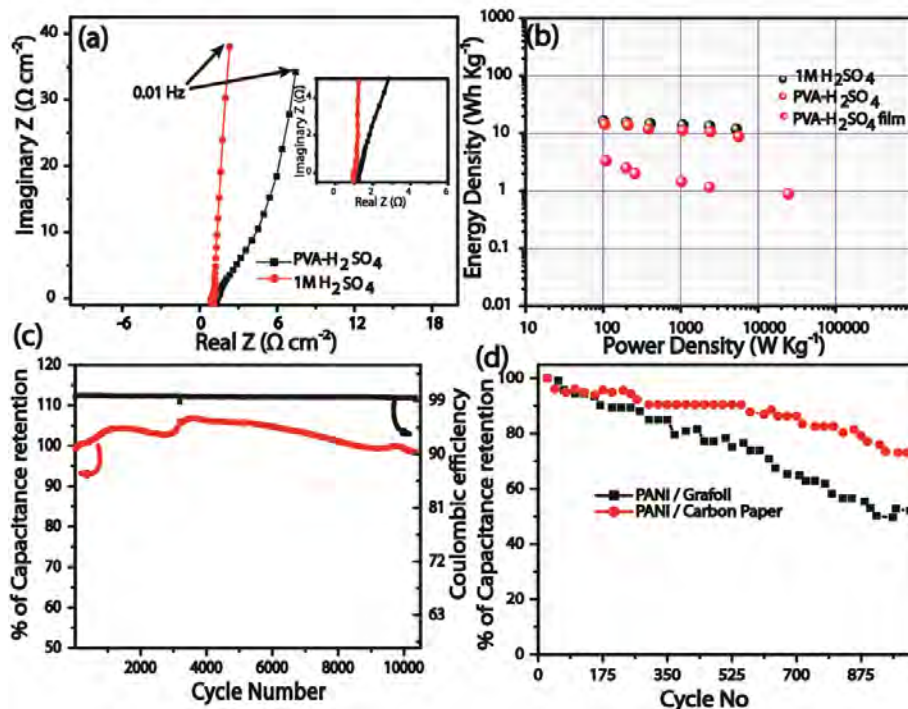


Figure 3A.7: (a) Comparison of the Nyquist plots of the ASSP using PVA- H_2SO_4 as the electrolyte with the corresponding liquid-state system made by using 0.5 M H_2SO_4 , (b) Ragone plots created by calculating the energy density and power density from the charge–discharge method, (c) cycle stability test extending for a period of 10000 cycles of the ASSP carried at a current density of 5 A g^{-1} and (d) comparative cycle stability done at a charge–discharge current density of 5 A g^{-1} in 0.5 M H_2SO_4 for Grafoil® and carbon paper each having a PANI loading of 1.5 mg cm^{-2} .

The prototype device made here is a significantly light weight assembly due to the low density of the carbon paper. The whole device has a weight of only 110 mg including the space given for the contact, which is inactive in terms of charge storage. The whole device including the electrolyte shows a capacitance of 12.5 F g^{-1} , which is double as compared to the commercially available supercapacitors with liquid electrolytes.^[14] It should be noted that the amount of the polymer electrolyte can still be reduced as there is extra thickness ($120 \mu\text{m}$) between the electrodes. This will further decrease the whole device weight. The whole device dimension is also very promising as the thickness is only 0.8 mm. Further, a LED is glow by connecting such 4 devices in series whose minimum working potential was 2 V as shown in Figure 3A.1c. The LED could be glowed more than 1 min. and the intensity of its illumination diminishes when the potential reaches to 2 V.

Part B: Electrodeposited PEDOT as a Solution for Establishing Enhanced Electrode-Electrolyte Interface

In the above section (Part A), the adopted strategy highlights the importance of porosity in the electrode for establishing enhanced interfacial network in solid-state supercapacitors for achieving high charge-storage properties. However, one challenge here noticed was that at higher mass loading of the electroactive material, the performance of the solid-state device becomes inferior to its liquid-state counterpart. This leads to a drastic decrease in the specific capacitance (Figure 3A.5d). Thus, there is a need to develop appropriate strategies for maintaining high specific capacitance even under high mass loading conditions. To address this issue, a new strategy has been adopted by electrodepositing the charge storage material directly onto a porous carbon current collector, which ensures highly reproducible coating of the electroactive material over each fiber of the conducting carbon paper backbone. The selected charge storage material in the present case is PEDOT, which could be electrochemically grown on carbon fibers from a solution containing its monomer, ethelenedioxythiophene (EDOT). PEDOT has many advantages such as high electrical conductivity of $>500 \text{ S cm}^{-1}$ and sustainability for a large potential window of 1.2 V, which is higher than that of the other conducting polymers such as polyaniline and polythiophene.

A schematic representation of the solid-state device and the synthetic procedure adopted here are represented in Figure 3B.1. This strategy helps to get a homogeneous and enhanced electrode-electrolyte interface compared to a case where only a solid electrolyte film is used. Polyvinyl alcohol-sulphuric acid (PVA- H_2SO_4) gel electrolyte has been used as the solid-electrolyte component^[4a, 15]. The main attraction of PVA- H_2SO_4 gel electrolyte apart from its flexibility, ambient conductivity (0.14 S cm^{-1})^[16] and desirable mechanical properties is its ability to diffuse into the porous substrate matrix to ensure extended electrode-electrolyte interfacial structure. Even with 50 % of H_2SO_4 in the matrix, PVA films show a high viscosity of $0.6 \times 10^5 \text{ Pa.S}$ ^[16], attributing its solid nature. The porosity of the carbon paper and the freedom to control the viscosity of PVA by means of water further enable easy penetration and coating of PVA- H_2SO_4 on the surface of the PEDOT grown carbon fibers. Thus, the effort gives a viable way to the conceptualization of a

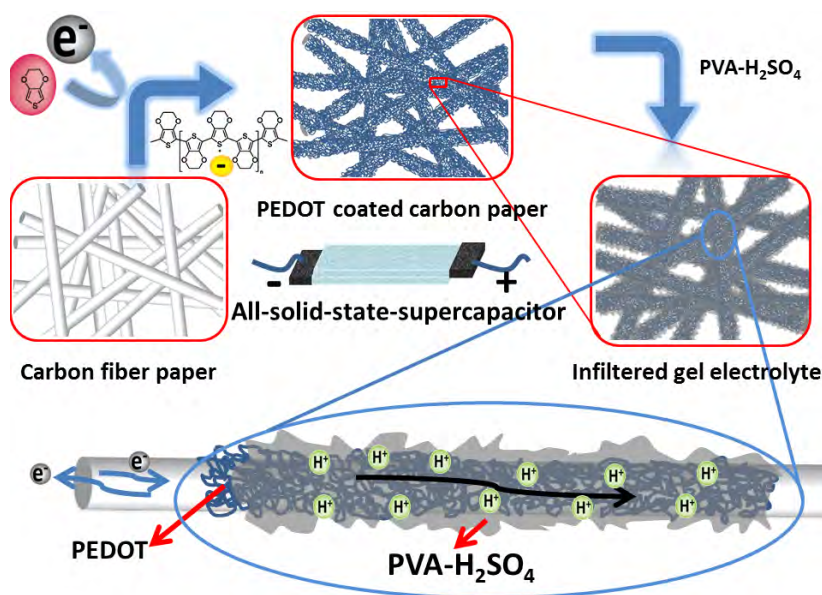


Figure 3B.1: Schematic representation of the preparation stages involved in the development of the all-solid-state supercapacitor through electro-deposition of PEDOT onto the highly porous carbon paper and intercalation of PVA-H₂SO₄ gel-polymer electrolyte into the matrix.

solid-state supercapacitor possessing a closely mimicking electrode-electrolyte interfacial structure as that of its liquid-state counterpart.

3.3.B1 SEM and EDX Analysis

Electrochemical deposition of PEDOT on the carbon paper was carried out in acetonitrile due to the low solubility of EDOT in aqueous medium along with the hydrophobic nature of the carbon paper. The solvent selection is very important in order to ensure uniform deposition of PEDOT as the solvent has to reach inside the fibers and thus to assist maintaining supply of the EDOT monomer while the set potential triggers polymerization of EDOT. Scanning electron microscope (SEM) images of the electrodes clearly reveal the growth patterns of the electro-deposited PEDOT over the carbon fibers. For comparison, the SEM image of the blank carbon paper is shown in Figure 3B.2e. The electro-deposition was conducted by maintaining different time intervals of the polymerization reaction from 50 s and up to 1200 s with a constant current density of 10 mA cm⁻² for all the samples. A close inspection of the formed PEDOT reveals a ‘3-dimensional (3-D) flower’ shaped growth pattern

possessing 1-dimensional (1-D) orientation along each carbon fiber. The deposition becomes denser and branchy as the time increases to 600 and 1200 s (Figure 3B.2c-d). Images corresponding to 300, 600 and 1200 s clearly show the well covered and rough layer of PEDOT without leaving any exposed carbon fiber surface whereas for lower deposition times of 50 and 100 s (Figure 3B.2a), PEDOT amount was not sufficient for the full coverage. Overall, the peculiar growth pattern and the uniform distribution of PEDOT in the matrix of the carbon paper are expected to provide high surface area for the electro-active material while ensuring good conductivity from the conducting backbone of the carbon fibers. It should be noted that for the deposition corresponding to 600 and 1200 s, the amount of the polymer on the individual carbon fiber is too heavy, but still the pores of the carbon paper are vacant especially in case of CP-600. The amount of the deposited polymer is calculated from the electrical charge in coulombs passed and by taking the efficiency of the process as 100 % (details of the calculation are given in experimental section). Accordingly, the estimated weights of the deposited PEDOT for the time intervals of 50, 100, 300, 600 and 1200 s are 0.32, 0.63, 1.89, 3.78 and 7.56 mg cm⁻² respectively and the corresponding samples are designated as CP-50, CP-100, CP-300, CP-600 and CP-1200.

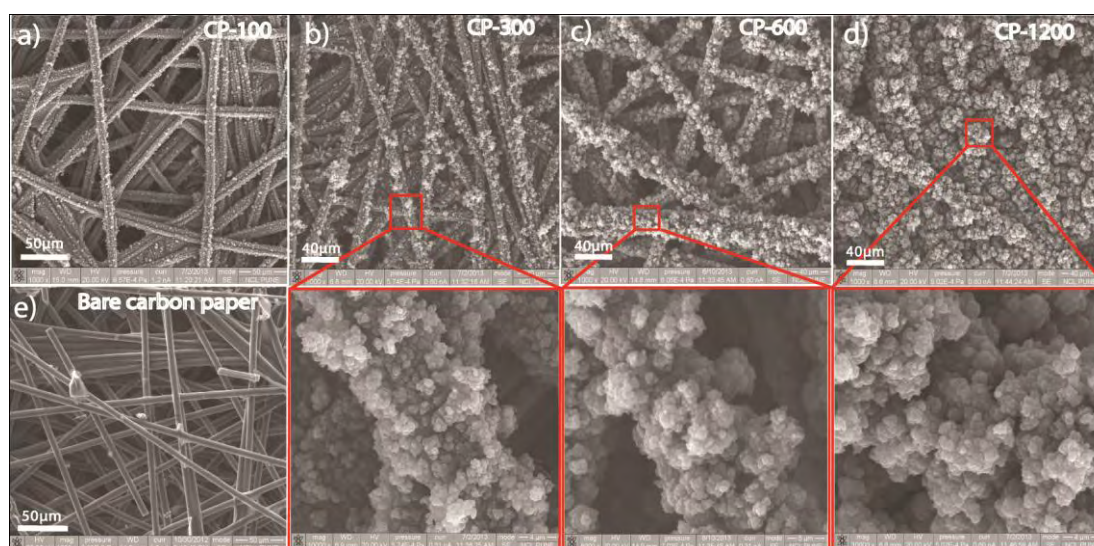


Figure 3B.2: SEM images of the electro-deposited PEDOT on carbon paper; (a) CP-100, (b) CP-300, (c) CP-600, (d) CP-1200 and (e) bare carbon paper; SEM images in the red boxes are the enlarged portion of the corresponding images on the left side.

Subsequent to the electro-deposition of PEDOT, the interface with the PVA- H_2SO_4 gel electrolyte has been achieved by applying an aqueous solution of the electrolyte on both surfaces of the porous PEDOT coated carbon paper. After repeated coating of PVA- H_2SO_4 , two such electrodes were hot-pressed together while ensuring the formation of a thin PVA- H_2SO_4 film between the electrodes. A detailed preparation protocol is given in the experimental section. Cross-sectional SEM image of the all-solid-state devices made from CP-300 as given in Figure 3B.3a reveals that the whole device is having a thickness of 0.70 mm which includes the excess PVA- H_2SO_4 gel electrolyte layer sitting as a separator in between the electrodes (marked with a yellow arrow). In addition to this, the enhanced electrode-electrolyte interface can be visualized from the clear distribution of the gel electrolyte inside the porous electrode from the enlarged sections of the images as shown in

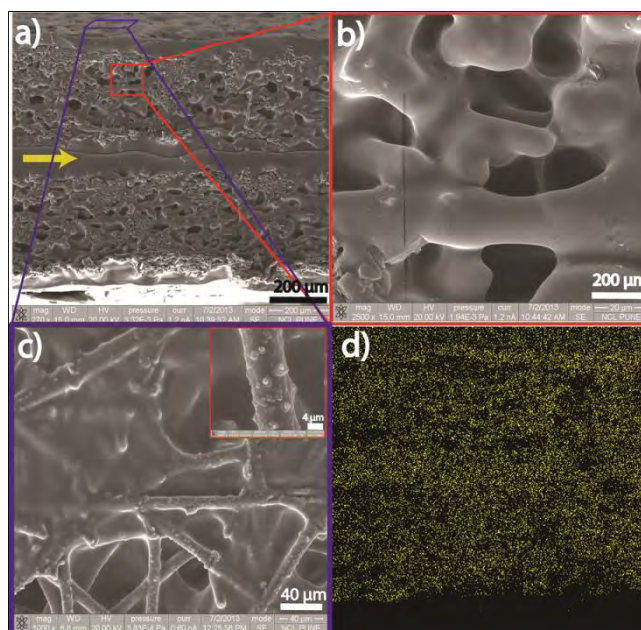


Figure 3B.3: Cross-sectional SEM images of (a) a solid-state-device made from CP-300; yellow arrow indicates the PVA- H_2SO_4 film formed between the electrodes while pressing them together, which serves as a separator between the two sandwiched electrodes, (b) enlarged image of PVA- H_2SO_4 covered PEDOT-carbon fibers corresponding to the red box in image (a), highlighting the high integrity of the electrode's components, (c) enlarged image corresponding to the area marked within the blue box in the SEM image (a), which indicates the upper surface of the device showing highly penetrated PVA- H_2SO_4 gel through the PEDOT-coated carbon matrix and (d) S-elemental mapping along the cross-section of the device as shown in the image (a).

Figure 3B.3b and 3c. This is complemented by the image corresponding to the elemental mapping of sulphur (S) (Figure 3B.3d), which gives highly uniform distribution of S in the entire area of scanning. Sulphur from PEDOT as well as PVA-H₂SO₄ is likely to contribute simultaneously towards the overall distribution. However, the nature of the distribution of S is apparently similar for the electrodes corresponding to a lower (50 and 100 s) as well as a higher (300 s and higher) deposition time. This can be ascribed to the effective infiltration and coating of the electrode surface by PVA-H₂SO₄.

3.3.B2 Four Probe Conductivity Measurements

It is clear from Table 3B.1 that, with the increase in the amount of PEDOT, conductivity of the carbon strip is increasing (from 142 S cm⁻¹ to 179 S cm⁻¹). As more amount of conducting PEDOT is filled inside the pores of the porous paper by electro-deposition, it leads to better connectivity between the individual carbon fibers. Better interconnectivity between the fibers decreases the contact resistance and leads to high conductivity. However, the conductivity enhancement achieved by the higher mass loading of PEDOT brings in restrictions to concomitantly establish the electrode-electrolyte interface as pore-filling by PEDOT can reduce the accessible channels for the gel electrolyte.

Table 3B.1. 4-Probe electrical conductivity data of the PEDOT coated carbon paper.

Sample	Conductivity (S cm ⁻¹)
CP-100	142
CP-300	154
CP-600	162
CP-1200	179

3.3.B3 Electrochemical Characterization

Electrochemical charge storage properties are characterized by cyclic voltammetry (CV), charge-discharge method and electrochemical impedance spectroscopy (EIS). All the experiments are carried out by making a 1 cm² prototype solid-state supercapacitor and the performance aspects are compared with a similar liquid-state device prepared by replacing PVA-H₂SO₄ with 0.5 M H₂SO₄. Capacitance contribution from the bare carbon paper is 40 μF cm⁻², which is negligible and, hence,

omitted from the calculation (Figure 3A.4b). The capacitance values estimated for CP-300 at a scan rate of 50 mV s^{-1} are 142 and 138 F g^{-1} in the corresponding combinations using the solid and liquid electrolytes, respectively (Figure 3B.4a). Even at higher voltage scan rates (up to 2000 mV s^{-1}), closely matching performance characteristics of the solid- and liquid-state systems could also be observed (Figure 3B.4b). Charge-discharge profile of CP-300 at a current density of 0.5 A g^{-1} is shown in Figure 3B.4c and the capacitances obtained are 145 and 147 F g^{-1} respectively with the liquid and solid electrolytes (Figure 3B.4d). For the lower deposition time of 50 s for PEDOT, the maximum capacitance obtained is 181 F g^{-1} in the case of the solid-state system (CP-50; Figure 3B.5d) which is even higher than the reported values for the PEDOT based supercapacitors in liquid electrolyte^[17]. A very large volumetric capacitance of 28 F cm^{-3} is displayed by CP-1200 due to its higher mass loading of PEDOT (7.56 mg cm^{-2}).

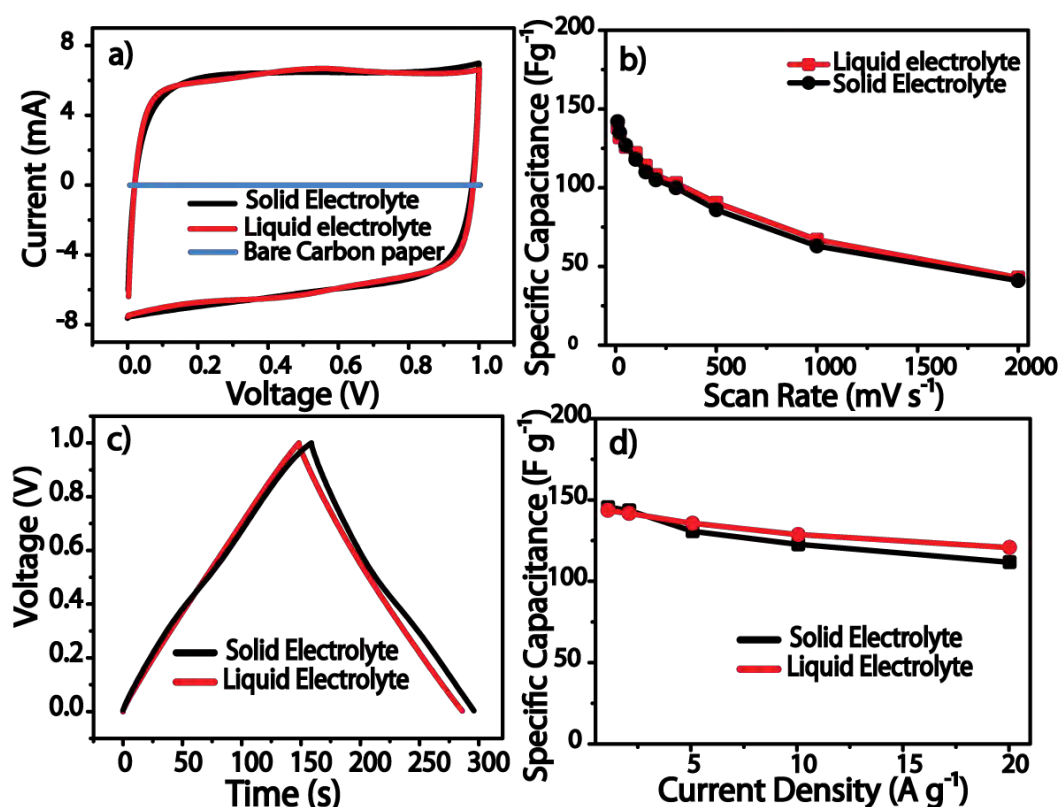


Figure 3B.4: Comparison of the performances of the solid- and liquid-state devices made from CP-300: (a) comparison of the cyclic voltammograms of the devices taken at 50 mV s^{-1} , (b) specific capacitance of PEDOT in the devices measured at different scan rates, (c) charge-discharge profile of the devices taken at 0.5 A g^{-1} and (d) specific capacitance of PEDOT in the devices measured at different current densities.

The corresponding areal capacitance of the system is 836 mF cm^{-2} . It should be noted that that even under the high mass loading condition of CP-1200, a specific capacitance of 111 F g^{-1} is retained by the system. This is associated with the ability of the process to maintain high mass loading of PEDOT without scarifying its 1-D flower like structure (Figure 3B.2) all the while keeping the vacant pores within the carbon paper well accessible for the solid electrolyte. A plot of specific capacitance vs. volumetric capacitance is shown in Figure 3B.6a.

The perfect fit of the voltammograms and charge-discharge condition profiles of the solid- and liquid-state systems as shown in Figure 3B.4a and 4c is attained due to the enhanced electrode-electrolyte interface conceived with the help of the gel electrolyte which closely mimics the extent of the interface obtainable by using the liquid electrolyte. Along with the absolute value of the capacitance, there has been a similar close fit in terms of the capacitance retention of the solid- and liquid-state systems. Normally, the solid-state supercapacitors are prone to sudden decrease in capacitance with fast scan rates due to their inherently high internal resistance (ESR)^[4, 18] compared to their liquid-state counterparts. Figure 3B.4b and 4d clearly highlight this prospect of the solid-state device made from CP-300. Generally, in the case of conducting the polymer based systems, the capacitive retention with fast scan rate is determined by the mobility of the counter ion between the polymer matrix and the electrolyte. Due to the level of precautions taken in the present strategy to establish a 'solid-liquid' like interface, the solid-state system attains a low charge transfer resistance and thus enables it to display similar retention features as that of the liquid-state counterpart. In the case of CP-300, even at a high scan rate of 500 mV s^{-1} , the system derived from the gel electrolyte displays only 40 % degradation in capacitance, which is exactly matching with its liquid-state counterpart (Figure 3B.4b). Detailed plots are shown in Figure 3B.5. The charge-discharge profile of CP-300, taken at 10 A g^{-1} , shows 25 % degradation compared to the capacitance measured at 0.5 A g^{-1} (Figure 3B.4d) in the solid electrolyte. High degradation rates for CP-1200 (80 %) compared to CP-50 (28 %), CP-100 (21 %) and CP-600 (34 %) have been observed under similar testing conditions. This trend on the solid-state devices is analogous to the corresponding liquid-state devices as well (Figure 3B.5c and Figure 3B.5d). When the amount of PEDOT increases, the electrode electrolyte interface reduces owing to the pore blocking by excess PEDOT. Also, the electrical contact to the carbon fiber and PEDOT reduces as PEDOT loading exceeds a

threshold level. This degradation is prominent in CP-1200 due to the presence of overfilled PEDOT in the electrode which leads to the low electrode-electrolyte interface with the gel electrolyte compared to its liquid-state counterpart. This leads to poor specific capacitance as well as retention in capacitance at high current density for CP-1200.

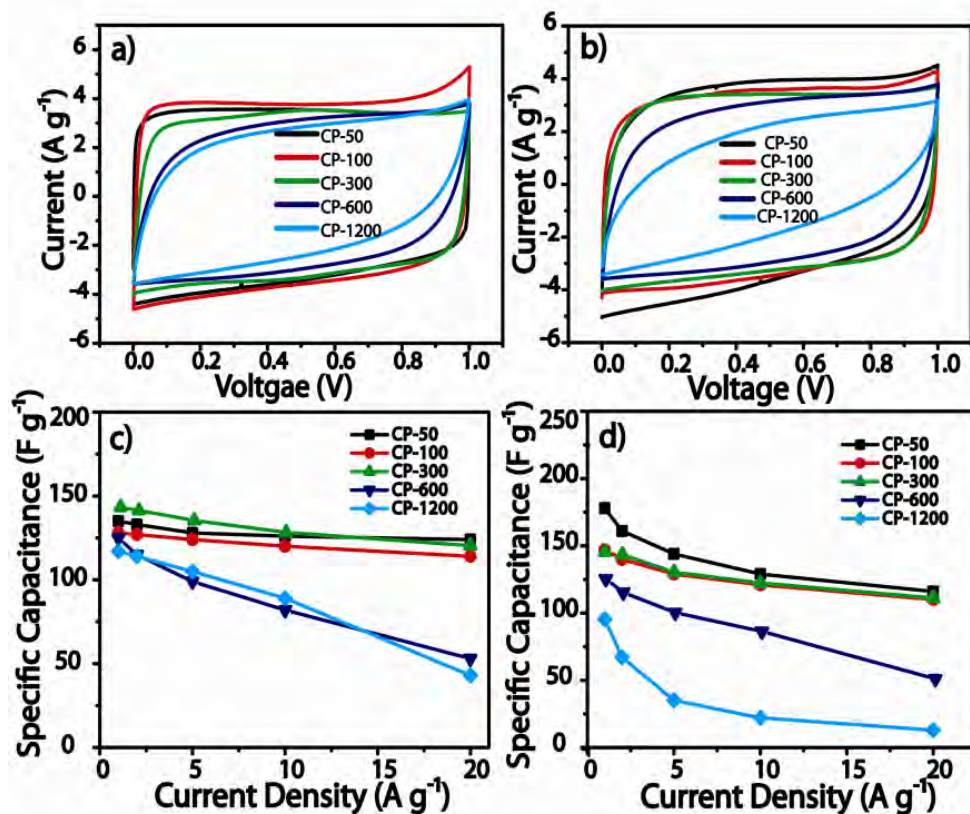


Figure 3B.5: Cyclic voltammograms of PEDOT coated carbon paper for different time of deposition carried out at a scan rate of 50 mV s^{-1} : a) in $0.5 \text{ M H}_2\text{SO}_4$ and b) using PVA- H_2SO_4 . The corresponding specific capacitance vs. current density plots of the samples are given in c) and d), respectively.

Electrochemical impedance spectroscopy (EIS) is one of the efficient tools to investigate the characteristic transient features of supercapacitors through an a.c frequency response. Impedance Nyquist plot in which the real part of the impedance (Z') is plotted against the imaginary part (Z'') of CP-300 is given in Figure 3B.6b. At the high frequency region, the Nyquist plot starts from the x-axis and progresses vertically parallel to the y-axis at the low frequency, which indicates the ideal capacitive nature of the system^[19]. The unique design through the electro-deposition of the charge storage material ensures enough space for the solid electrolyte for its intercalation even under the situation of high mass loading as in the case of CP-1200.

A close inspection of the plot corresponding to the solid-state system indicates a small deviation in the low frequency region compared to its liquid-state counterpart and this is expected due to the lower ionic mobility in PVA-H₂SO₄ compared to that in liquid H₂SO₄. Absence of a semicircle loop at the high frequency region (inset of Figure 3B.6b) depicts very low charge-transfer resistance (CTR) in both the medium. The ESR of the solid-state device made from CP-300 is only 1.1 Ω which is lower than its liquid-state counterpart (1.6 Ω) (Figure 3B.6b) determined from the x-intersect of the Nyquist plot. This difference is accounted by the hydrophobic nature of the carbon paper where the PVA based gel electrolyte outperforms the aqueous electrolyte to form an effective interface in the system. Impedance phase angle and time constant [19a, 20] are two important factors which are considered as figures of merits of supercapacitors. Impedance phase angle of CP-300 in both the phases is

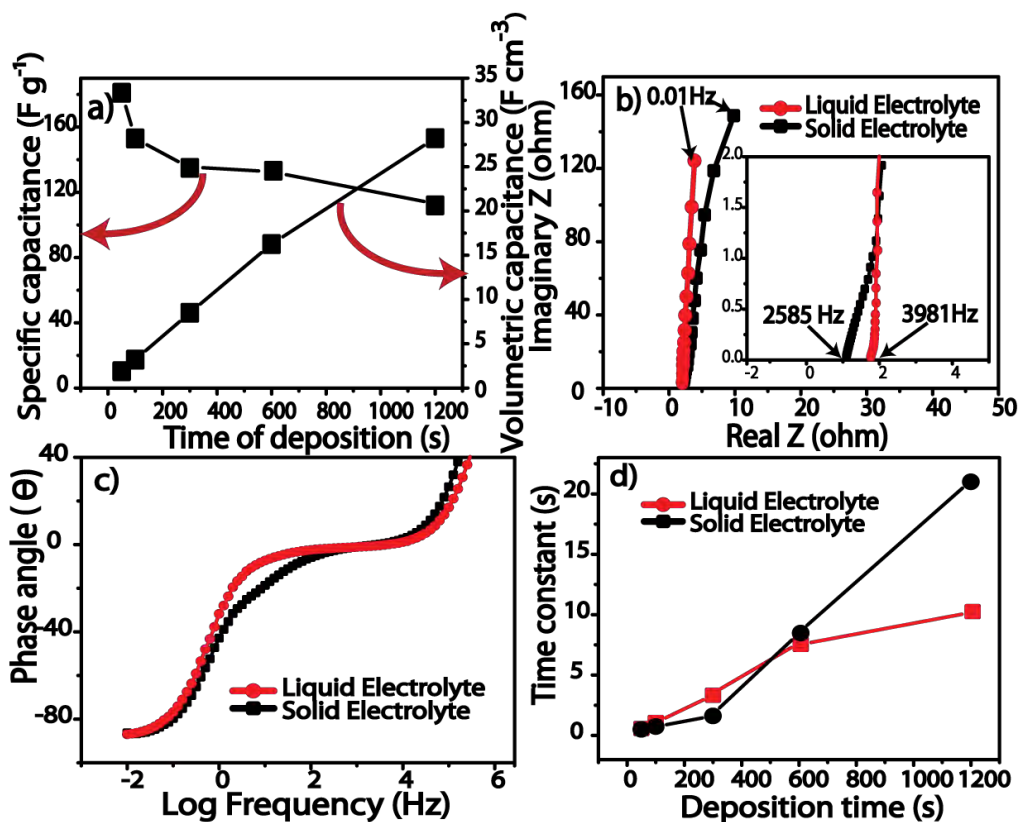


Figure 3B.6: (a) Specific capacitance vs. volumetric capacitance of the solid-state device made from CP-300, (b) Nyquist plot of CP-300 in solid and liquid electrolytes with zoomed high-frequency regions in the inset, (c) Bode plot, which represents the relationship of phase angle vs. frequency, for the solid- and liquid-state devices made from CP-300 and (d) time constant calculated for CP-300 in solid and liquid electrolytes from the corresponding impedance data.

shown in Figure 3B.6c. This clearly dictates the nature of the charge storage properties with the frequency. Normally, at the high frequency region, a supercapacitor will show resistive nature with 0 phase lag between voltage and current and at low frequency region it will show a -90 degree phase lag. Here, the nature of the phase angle with frequency is similar in both cases of liquid and solid electrolytes and it reaches nearly -90° at low frequency showing ideal capacitive nature in both cases (Figure 3B.6c). This explains why similar capacitive retention is obtained in liquid and solid electrolyte with the faster rate.

As that of impedance, complex form of frequency dependent capacitance can be defined in terms of real capacitance (C^I) and imaginary capacitance (C^{II}) as follows [19a, 20b, 21]

$$C(w) = C^I(w) + C^{II}(w)$$

where,

$$C^I(w) = \frac{Z^{II}(W)}{\omega|Z(w)|^2} \text{ and } C^{II}(w) = \frac{Z^I(W)}{\omega|Z(w)|^2}$$

$$\text{Where } |Z(w)|^2 = Z(w)'^2 + Z(w)''^2$$

The real part of the cell capacitance calculated from the impedance analysis matches with the CV and charge-discharge method. At 0.01 Hz, CP-300 shows a capacitance of 116 F g⁻¹ with a phase angle of -90° shown in the plot of frequency vs. capacitance (Figure 3B.7). The imaginary part of the capacitance, on the other hand, depicts the energy lost during the charge-discharge cycle. A plot of imaginary capacitance vs. frequency will have a maximum, normally happens at -45° phase angle and the corresponding frequency is called the relaxation frequency (Figure 3B.7). Comparative plots are given in Figure 3B.8 for the systems based on the solid and liquid electrolytes. The inverse of the above frequency is called the time constant which measures the kinetics of the capacitor and is known to be as ‘figure of merit of a capacitor’. Another method to calculate the time constant is the inverse of the frequency at which phase difference is -45° (Figure 3B.7). In both the methods, CP-300 shows a time constant of 1.5 seconds. Time constants of the systems corresponding to the lower deposition time are less due to the better contact of PEDOT with the carbon fibers leading to better sensitivity with voltage switching during the fast charge-discharge cycles. CP-50 and CP-100 show the time constants of 0.50 and 0.73 s respectively in the solid electrolyte whereas the corresponding values

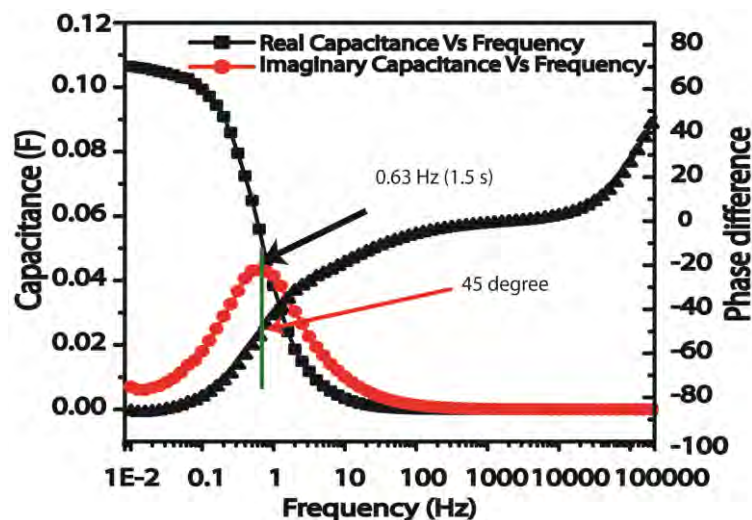


Figure 3B.7: Frequency dependant imaginary and real capacitances and phase difference of CP-300 in PVA-H₂SO₄.

change to 0.57 and 1.07 s respectively during the measurements using the liquid electrolyte (Figure 3B.6d). This explains why the lower deposition time leads to capacitance retention with faster charge-discharge. The time constant for CP-300 is 1.6 s in the solid state, which is a highly appreciable value for a conducting polymer-solid electrolyte combination compared to many of the reported time constants of the systems based on liquid electrolytes and carbon materials^[19a]. In case of CP-600 and CP-1200, due to the lower electrode-electrolyte contact, higher time constants have been observed and this accounts the sudden drops in capacitance with faster scan rates. The increased time constant of CP-1200 in solid state (21.0 s) compared liquid

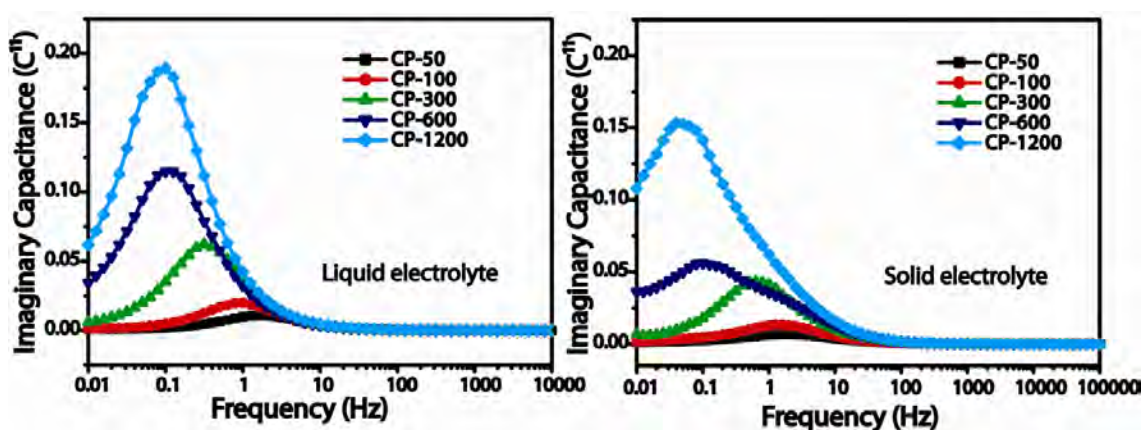


Figure 3B.8: Frequency dependent imaginary capacitance of PEDOT coated carbon paper for different time of deposition: a) in 0.5 M H₂SO₄ and b) using PVA-H₂SO₄.

state (10.2 s) is due to the less available porosity for solid electrolyte, which leads to substantial reduction in the interface.

The cycle stability of the present solid-state device is also found to be excellent as compared to the literature reports. 12000 continuous charge-discharge cycles is carried out for the solid-state device made from CP-300 electrodes at a current density of 5 A g^{-1} (Figure 3B.9a). The columbic efficiency is estimated to be 100 % during the whole charge-discharge cycle. After 2000 cycles, a decrease of 10 % in the capacitance (116 F g^{-1} to 105 F g^{-1}) is occurred which remained almost constant thereafter for the remaining 10000 cycles. It is worth mentioning that the same device, which was tested for 12000 charge-discharge cycles, storing under ambient room conditions, retained a capacitance value of 130 F g^{-1} at 0.5 A g^{-1} . This indicates the evaporation of small amount of water entrapped in the polymer matrix. This is probably due to the rise in temperature with the continuous charge-discharge cycling and also due to the low humidity of the environment (20-30 %). Convincible evidence on this possible changeover is obtained from the EIS analysis of the corresponding sample before and after its charge-discharge cycling process (Figure 3B.9b). An increase in the ESR from 1.1 to 2.1Ω after the execution of the cycling process and a recovery of ESR to 1.4Ω after 2 days of its storage clearly validate the sensitive role of water in the gel electrolyte. It is also worth mentioning that, due to the highly intercalated nature of PVA- H_2SO_4 inside the porous electrode, unlike a liquid electrolyte, it also functions as a binder for PEDOT. Due to this binding effect, PVA- H_2SO_4 helps to decrease the detachment rate of PEDOT from the electrode during the expected volume changes in the charge-discharge process. This is validated more extensively by carrying out the charge-discharge measurements of the same device after the stability cycling in 7 days intervals for 3 months. It is found that the solid-state-device is highly stable even after the 8 weeks assessment period (Figure 3B.10a-b).

In order to understand the dependence of humidity and temperature on the charge-storage properties of the solid-state device, the charge-discharge and EIS measurements were carried out by subjecting the system under thermal cycling by varying the temperature from room-temperature ($30 \text{ }^\circ\text{C}$) to $80 \text{ }^\circ\text{C}$ and then cooling down to $-10 \text{ }^\circ\text{C}$ (Figure 3B.9c). Humidity dependent charge-storage behaviour is

observed by keeping the system inside a humidity chamber where the temperature is maintained at 25 °C and humidity is varied from 30-80 %. As can be seen from Figure 3B.9c, as the temperature increases, capacitance also increases as expected due to the increase in the mobility of ions in the gel electrolyte. It is remarkable that these changes are highly reversible as the capacitance values closely retrace the forward path even during the cooling cycle. To validate this further, 150 charge-discharge cycles were carried out at 80 °C using 5 A g⁻¹ current density followed by cooling the device to 10 °C where this was subjected to 100 cycles (Figure 3B.9d). The system was again brought back to 80 °C. It has been observed that the device is quite stable

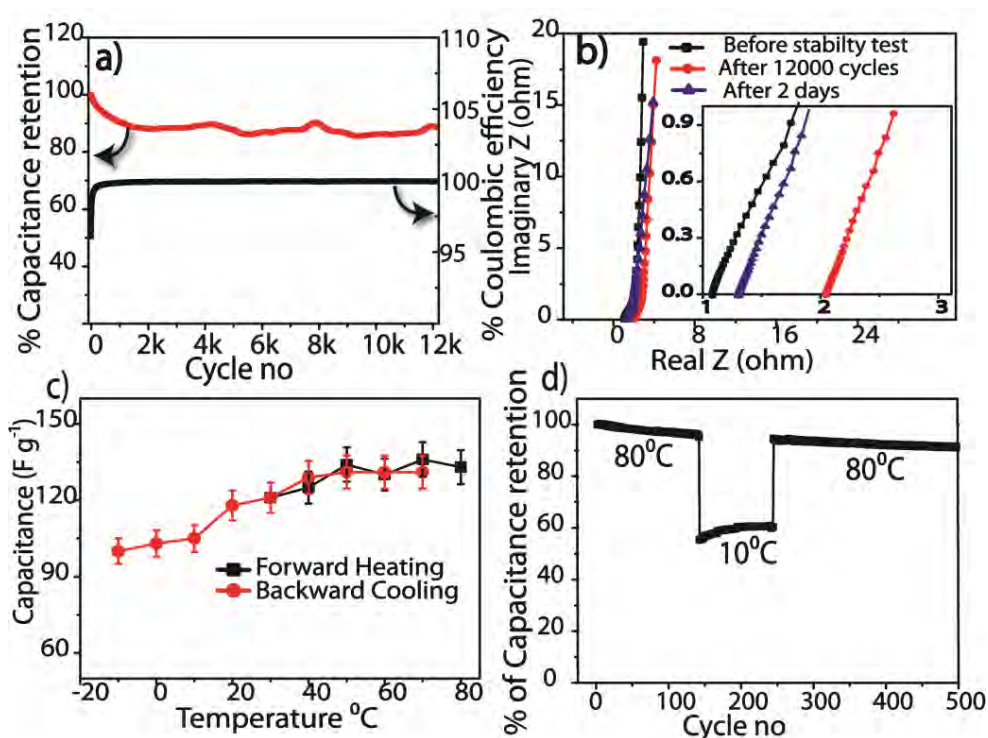


Figure 3B.9: Various performance features of the solid-state supercapacitor made from CP-300: (a) cycle stability and coulombic efficiency at 5 A g⁻¹ current density, (b) Nyquist plots of the device before and after the stability test; the magnified view of the high frequency region is given in the inset, (c) temperature-dependent capacitance and (d) stability in terms of its capacitance with respect to the cycling of the operating temperature.

even after subjecting these extreme variations. It is also noticed that change in humidity has an effect on the capacitance (Figure 3B.9d) probably due to the sensitivity of humidity on the conductivity of the solid electrolyte. Clearly, increase in humidity level decreases the ESR (Figure 3B.9c), which ultimately helps the system to attain an improved capacitance value.

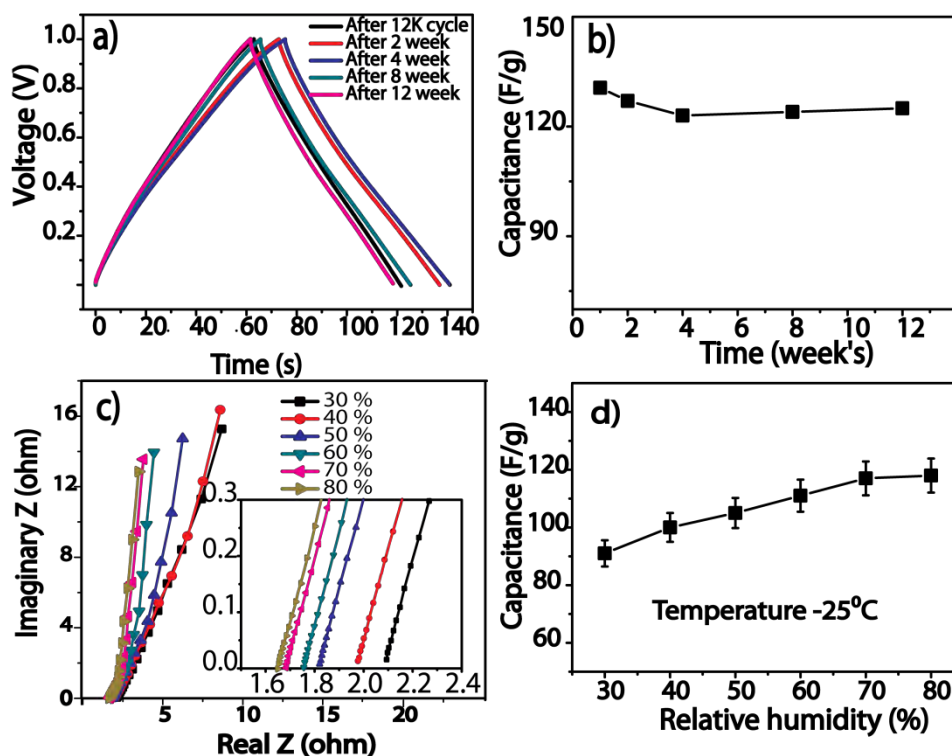


Figure 3B.10: a) Charge-discharge profiles taken at 0.5 A g^{-1} during different time intervals and b) is the capacitance values calculated. c) Nyquist plots taken under different humidity conditions; the zoomed high frequency region of the Nyquist plot in the inset and d) humidity dependent capacitance. All the experiments were carried out using the solid-state devices based on CP-300.

The energy density and power density of the solid- and liquid-state devices are calculated from the capacitance, and the corresponding Ragone plots are presented in Figure 3B.11a. Volumetric energy density for the whole device including the volume of the solid electrolyte is 0.28 mWh cm^{-3} at a power density of 6.8 mWh cm^{-3} . The system is able to keep the energy density as high as 0.22 mWh cm^{-3} at an elevated power demand of 271 mW cm^{-3} . The response of the solid-state system is a perfect fit of its liquid-state counterpart. The gravimetric energy density also has been estimated, in which the solid-state device displays a maximum energy density of 5.1 Wh kg^{-1} . Table 3B.2, summarizes the mass specific capacitance values of the devices, which include the weight of PEDOT, carbon paper and electrolyte. Among the devices, CP-1200 displays the highest capacitance of 7.1 F g^{-1} .

Looking into the practical scalability aspects of the adopted method here, a four-time larger area device has also been made by following the same fabrication protocol which also highlights the excellent prospects of scaling up the process. For

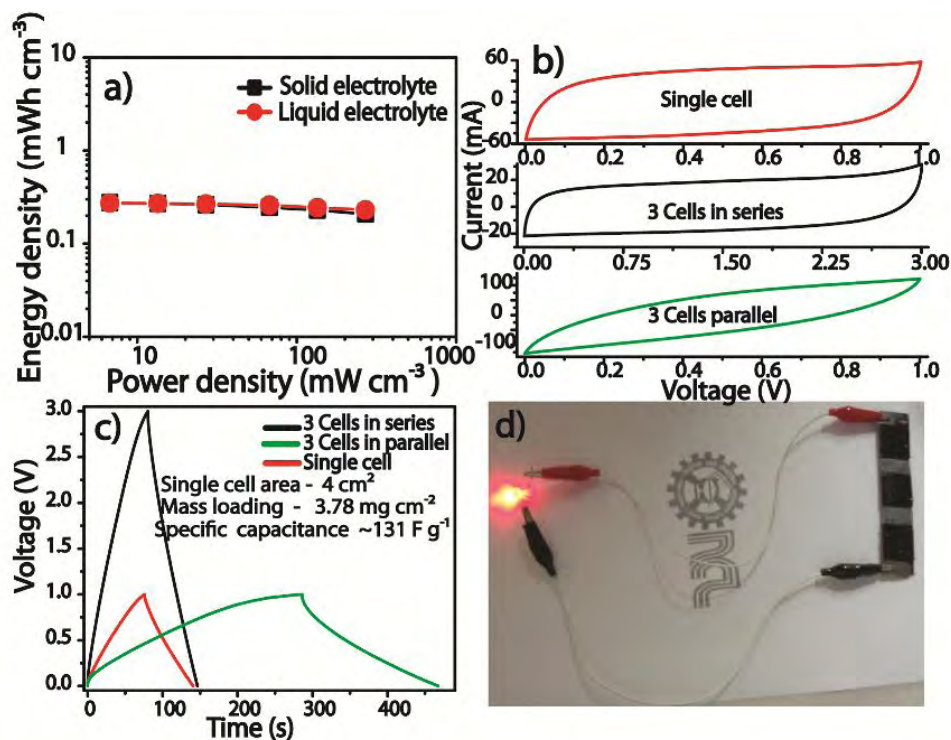


Figure 3B.11: (a) Comparison of the Ragone plots of the solid- and liquid-state devices made from CP-600, (b) cyclic voltammograms of the single cell, three-cell (parallel) and three-cell (series) devices made from CP-600 having 4 cm² area at 50 mV s⁻¹ scan rate, (c) charge-discharge profiles taken at 1 A g⁻¹ current density of the single cell, three cell (parallel) and three cell (series) having a 4 cm² area and (d) LED powered using the solid-state three-cell series connection.

Table 3B.2. Total specific capacitance obtained from the solid-state devices including the weight of the current collector and carbon paper.

Sample	Loading of PEDOT (mg)	Weight of Carbon paper (mg)	Total weight of device (mg, ± 5%)	Capacitance obtained (mF)	Capacitance of the device (F g ⁻¹ , ±5%)
CP-50	0.63	13	45	28.5	0.6
CP-100	2.52	13	46	48.2	1.0
CP-300	3.78	13	47	127.6	2.7
CP-600	7.56	13	51	249.5	4.9
CP-1200	15.12	13	59	419.6	7.1

the demonstration purpose, three 4 cm² area solid devices were made from CP-600 containing a mass loading of 3.78 mg cm⁻² of PEDOT and tested by connecting in series and parallel methods. The CV profiles of the single cell and stack cell taken at

50 mV s⁻¹ scan rate are given in Figure 3B.11b. Single cell, 3 cells in series and in parallel combinations show a specific capacitance of ~131 F g⁻¹ for PEDOT at 15 mA (1 A g⁻¹) (Figure 3B.11c), which is comparable to the single cell having an area of 1 cm² (132 F g⁻¹). This small variation is accounted by the variation of weights deposited which was calculated by taking 100 % columbic efficiency. A detailed comparison is given in Table 3B.2. For practical demonstration of the electric charge storage, an LED having a minimum working potential of 1.8 V could be lightened using 3 single cells connected in series (Figure 3B.11d).

3.4 Conclusion

The chapter deals with the successful strategies adopted to establish efficient electrode-electrolyte interface in order to enhance the charge storage properties of the solid-state supercapacitors. The initial section of the chapter deals with the performance variation of the all-solid-state supercapacitor by intercalating a gel-polymer electrolyte, *i.e.* PVA-H₂SO₄, with the PANI coated carbon fiber paper having different loading of PANI. The cross-sectional elemental mapping and SEM images were used to confirm the relative changes in the interface. The enhanced interface with optimum mass loading helps the solid device to perform like a liquid counterpart showing a specific capacitance of 647 F g⁻¹ for PANI with retention of 62 % of its capacitance at a current density of 20 A g⁻¹. High integrity of the electrode and electrolyte phases helps the device to attain a very low ESR of 1 Ω cm⁻². Further, to address the low interface and inferior charge storage properties at the higher mass loading of PANI, another approach, involving the electro-deposition of PEDOT onto the individual carbon fiber followed by intercalating the carbon paper matrix with PVA-H₂SO₄ polymer-gel electrolyte, was adopted. The second part of the chapter deals with the important aspects of this work. In this case, even under the higher PEDOT loading of 7.56 mg cm⁻², the desired interface formation is established which leads to a high volumetric capacitance of 28 F cm⁻³ while retaining a high specific capacitance of 112 F g⁻¹. Excellent capacitance retention for the solid device is observed with faster scan rates with a close fitting performance profile as its liquid-state counterpart. The solid-state device displayed outstanding cycling stability and even after 12000 charge-discharge cycles at 5 A g⁻¹, only 3 % loss in capacitance is observed.

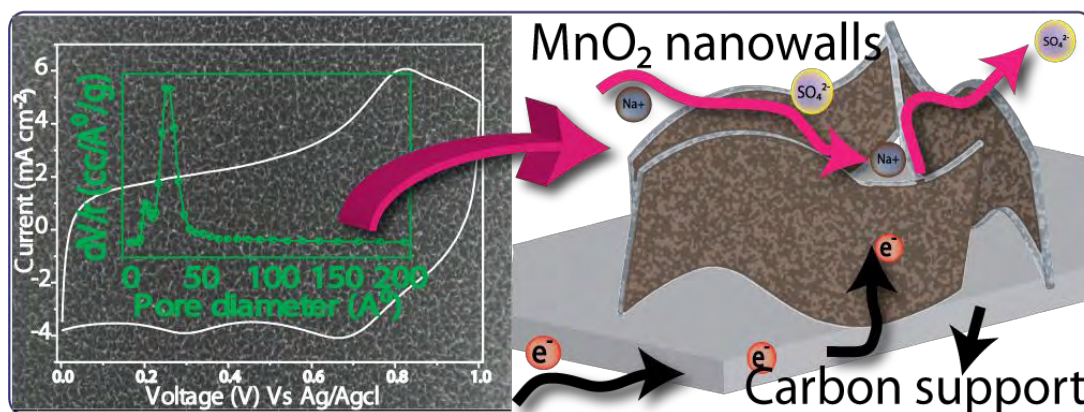
3.5 References

- [1] (a) P. V. Wright, *Electrochim. Acta.* **1998**, *43*, 1137-1143; (b) J. Y. Song, Y. Y. Wang, C. C. Wan, *J. Power Sources* **1999**, *77*, 183-197; (c) R. C. Agrawal, G. P. Pandey, *J. Phys. D: Appl. Phys.* **2008**, *41*, 223001; (d) P. Kyung-Won, A. Hyo-Jin, S. Yung-Eun, *J. Power Sources* **2002**, *109*, 500-506; (e) A. Lewandowski, *Electrochim. Acta.* **2001**, *46*, 2777-2780; (f) A. M. White, R. C. T. Slade, *Synth. Met.* **2003**, *139*.
- [2] A. Catia, B. Maurizio, C. Dario, L. Mariachiara, S. Francesca, M. Marina, *J. Power Sources* **2008**, *185*, 1575-1579.
- [3] (a) R. Dhanraj, V. Meenu, I. Nazrul, K. Ramaiyan, K. Ulhas, K. Sreekumar, P. Vijayamohanan, *Journal of Applied Electrochemistry* **2009**, *39*, 1097-1103; (b) X. Wang, B. Liu, Q. Wang, W. Song, X. Hou, D. Chen, Y.-B. Cheng, G. Shen, *Adv. Mater.* **2012**; (c) M. Kaempgen, C. K. Chan, J. Ma, Y. Cui, G. Gruner, *Nano Letters* **2009**, *9*, 1872-1876.
- [4] (a) C. Meng, C. Liu, L. Chen, C. Hu, S. Fan, *Nano Letters* **2010**, *10*, 4025-4031; (b) L. Yuan, X. Xiao, T. Ding, J. Zhong, X. Zhang, Y. Shen, B. Hu, Y. Huang, J. Zhou, Z. Wang, *Angew. Chem. Int. Ed.* **2012**, *51*, 4934-4938.
- [5] L. Yuan, X.-H. Lu, X. Xiao, T. Zhai, J. Dai, F. Zhang, B. Hu, X. Wang, L. Gong, J. Chen, C. Hu, Y. Tong, J. Zhou, Z. Wang, *ACS Nano* **2012**, *6*, 656-661.
- [6] Y. Haijun, W. Jihuai, F. Leqing, L. Youzhen, X. Kaiqing, T. Ziyang, C. Cunxi, T. Shen, L. Jianming, H. Miaoliang, L. Zhang, *J. Power Sources* **2012**, *198*, 402-407.
- [7] A. G. MacDiarmid, A. J. Epstein, *J. Chem. Soc. Faraday Trans.* **1989**, *88*, 317.
- [8] S. K. Andreas Elschner, Wilfried Lovenich, Udo Merker, Knud Reuter *PEDOT: Principles and Applications of an Intrinsically Conductive Polymer*, CRC, **2011**.
- [9] W. Chen, Z. Fan, L. Gu, X. Bao, C. Wang, *Chem. Commun.* **2010**, *46*, 3905-3907.
- [10] (a) Q. Wu, Y. Xu, Z. Yao, A. Liu, G. Shi, *ACS Nano* **2010**, *4*, 1963-1970; (b) D. Ghosh, S. Giri, A. Mandal, C. K. Das, *RSC Advances* **2013**, *3*, 11676-11685; (c) H. Zhang, J. Wang, Y. Chen, Z. Wang, S. Wang, *Electrochim. Acta.* **2013**, *105*, 69-74.
- [11] (a) J. Liu, M. Zhou, L.-Z. Fan, P. Li, X. Qu, *Electrochim. Acta.* **2010**, *55*, 5819-5822 ; (b) J. Jyongsik, B. Joonwon, C. Moonjung, Y. Seong-Ho, *Carbon* **2005**, *43*, 2730-2736; (c) L. Yuan, X. Xiao, T. Ding, J. Zhong, X. Zhang, Y. Shen, B. Hu, Y. Huang, J. Zhou, Z. Wang, *Angew. Chem. Int. Ed.* **2012**, *51*, 4934-4938.
- [12] F. Meng, Y. Ding, *Adv. Mater.* **2011**, *23*, 4098-4102.
- [13] H. Ying-Ying, L. Yi-Chen, H. Yu-Kuei, C. Chia-Chun, C. Li-Chyong, C. Kuei-Hsien, *J. Power Sources* **2010**, *195*.
- [14] A. Chu, P. Braatz, *J. Power Sources* **2002**, *112*, 236-246.

- [15] (a) B. G. Choi, S.-J. Chang, H.-W. Kang, C. P. Park, H. J. Kim, W. H. Hong, S. Lee, Y. S. Huh, *Nanoscale* **2012**, *4*, 4983-4988; (b) Y. Xu, Z. Lin, X. Huang, Y. Liu, Y. Huang, X. Duan, *ACS Nano* **2013**, *7*, 4042-4049.
- [16] B. Anothumakkool, A. T. A. Torris, S. N. Bhange, M. V. Badiger, S. Kurungot, *Nanoscale* **2014**, *6*, 5944-5952.
- [17] (a) W. Li, J. Chen, J. Zhao, J. Zhang, J. Zhu, *Mater. Lett.* **2005**, *59*, 800-803; (b) R. Liu, S. I. Cho, S. B. Lee, *Nanotechnology* **2008**, *19*, 215710; (c) L. Chen, C. Yuan, B. Gao, S. Chen, X. Zhang, *J. Solid State Electrochem.* **2009**, *13*, 1925-1933; (d) D. Antiohos, G. Folkes, P. Sherrell, S. Ashraf, G. G. Wallace, P. Aitchison, A. T. Harris, J. Chen, A. I. Minett, *J. Mater. Chem* **2011**, *21*, 15987-15994; (e) A. K. Cuentas Gallegos, M. E. Rincón, *J. Power Sources* **2006**, *162*, 743-747; (f) K. Lota, V. Khomenko, E. Frackowiak, *J. Phys. Chem. Solids.* **2004**, *65*, 295-301; (g) J. Jang, J. Bae, E. Park, *Adv. Mater.* **2006**, *18*, 354-358.
- [18] M. Kaempgen, C. Chan, J. Ma, Y. Cui, G. Gruner, *Nano Letters* **2009**, *9*, 1872-1876.
- [19] (a) P. L. Taberna, P. Simon, J. F. Fauvarque *J. Electrochem. Soc.* **2003**, *150*, A292-A300; (b) V. Noël, H. Randriamahazaka, C. Chevrot, *J. Electroanal. Chem.* **2003**, *558*, 41-48.
- [20] (a) K. Sheng, Y. Sun, C. Li, W. Yuan, G. Shi, *Sci. Rep.* **2012**, *2*; (b) J. R. Miller, R. A. Outlaw, B. C. Holloway, *Science* **2010**, *329*, 1637-1639.
- [21] P. L. Taberna, C. Portet, P. Simon, *Appl. Phys. A* **2006**, *82*, 639-646.

Chapter-4

Electrochemically Grown MnO₂ Nanowall Forest on a Carbon Fiber Substrate as a Supercapacitor Charge Storage Material



Even though metal oxides, especially manganese oxides (MnO₂), are highly promising materials for energy storage application, their low electrical and ionic conductivities are challenging for achieving high specific capacitance. Here, in this chapter, an efficient electro-deposition method to achieve a uniform growth of MnO₂ nano-wall forest along the carbon fiber threads in a conducting carbon paper is reported. Each nanowall unit is separated from the neighboring unit by 25-65 nm and the units retain surface pores having a uniform pore diameter of 2-5 nm, which could be confirmed by surface area studies and TEM imaging. Due to the ordered nano channels demarcated by the MnO₂ walls for easy ion transport and continuous electron path created by the carbon backbone, the system achieves a specific capacitance of 1149 F g⁻¹ and it retains 565 m² g⁻¹ of that even at a dragging condition as high as 100 A g⁻¹. Impedance analysis has been carried to explain the easy ion transport through the nano-channels by analyzing the low charge-transfer resistance. Stability of the formed structure could be analyzed by FE-SEM images and it is found that the nanowalls are intact even after continuous 8500 charge-discharge cycles.

Content in this chapter is published in the following article.

Chem. Commun., 2014, **50**, 7188-7190

(<http://pubs.rsc.org/en/content/articlelanding/2014/cc/c4cc00927d#!divAbstract>)

Reproduced by permission of The Royal Society of Chemistry

4.1 Introduction

The present applications of supercapacitors are mainly limited to high power demanding situations like start-up solutions, memory backup, circuit smoothening etc. Apart from the high power density, other lineaments like excellent cycle life, high columbic efficiency, environmental benign nature etc.^[1] of a supercapacitor are ideal for various energy storage applications. However, for wider applications, high energy densities are required and this cannot be fulfilled by 5-10 Wh kg⁻¹ of energy available from the conventional supercapacitors which utilize high surface area carbon (AC) (100-250 F g⁻¹) as active materials^[1a]. Replacing AC with various metal oxides^[2], especially less costly and environmentally friendly MnO₂ is looking promising at this context owing to their high potential storage capacities (1200 F g⁻¹) and high potential window (1-1.6 V)^[3]. Nevertheless, due to low electrical (10⁻⁵-10⁻⁶ S/cm) and ionic conductivity, bulk MnO₂ delivers low mass specific capacitance (100-200 F g⁻¹)^[3b]. Especially, thick coating of MnO₂ on a plain current collector leads majority of the bulk MnO₂ inaccessible for electrons as well as ions in the electrolyte. A common approach to augment the capacitance of MnO₂ is to composite it with various carbon materials like carbon nanotubes, graphene, carbon fiber, metals, conducting polymers etc.^[3b]. However, many of the above composites lack continuous electron path due to the presence of semiconducting MnO₂ grains between the conducting ingredients, which restricts their performance towards the theoretical maximum. One excellent solution for this issue is the electrochemical synthesis of MnO₂ layer directly onto a conducting substrate^[4]. Further improvement on the ion transport can be accomplished by creating a porous architecture of MnO₂, which can be achieved with the help of templates. However, usage of hard templates for improving the porosity of MnO₂ during the electro-deposition is not a viable choice as it requires complicated template preparation and removal processes^[4a, 5].

As a solution to the above problems, highly uniform MnO₂ porous nanowall forest is synthesized directly onto a conducting porous carbon fiber paper electrochemically without employing any templates (Figure 4.1). The process of the synthesis is simple and the architecture yields excellent charge storage properties for MnO₂. Continuous electron movement is ensured by the carbon fiber support whereas high ionic mobility and enhanced electrode-electrolyte interface are achieved by the

high porosity of the nanowall assembly. Apart from these specialties, the inherent porosity of the carbon fiber paper and uniform deposition ensure relatively high MnO_2 amount per unit area of the electrode.

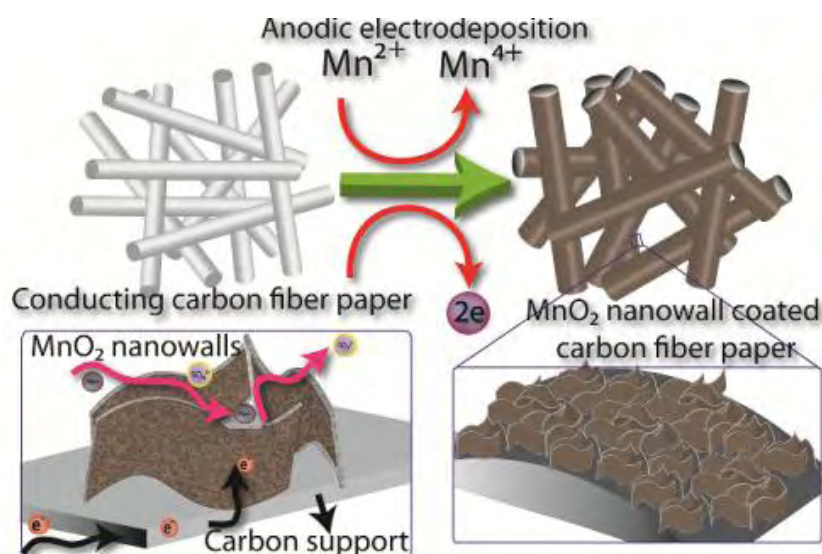


Figure 4.1: Schematic representation of the MnO_2 nanowall preparation

4.2 Experimental Section

4.2.1 Materials

Manganese acetate (MnAc_2), ammonium acetate (NH_4Ac) and sodium sulfate (Na_2SO_4) were purchased from Rankem Chemicals. All the chemicals were used as received without any further purification. Carbon paper having a thickness of 0.3 mm was purchased from Toray.

4.2.2 Preparation of MnO_2 Coated Carbon Paper

Electrochemical synthesis was carried out in Bio-Logic SP-300 Potentiogalvanostat using 3-electrode systems in which carbon paper was used as the working electrode, Pt was used as the counter electrode and Ag/AgCl was used as the reference electrode. Deposition was carried out in a solution containing 0.1 M (0.49 g) $\text{Mn}(\text{Ac})_2$ and 0.1 M (0.154 g) NH_4Ac salt in 20 ml of deionized water. 1 cm^2 area of carbon paper was kept exposed to the electrolyte and the remaining part was masked using Kapton adhesive tape. Experiments were carried out at a constant potential of 0.6 V vs Ag/AgCl for different time intervals. Carbon paper was dipped in ethanol before the

electro-deposition to enhance the hydrophilic nature. After the deposition, the electrode was washed and dried at 60 °C. For comparison purpose, MnO₂/CNF was also prepared by hydrothermal method. In a typical experiment, 100 mg of CNF and 150 mg of KMnO₄ were dispersed in 40 mL water using a probe sonicator. The solution was poured into a hydrothermal bomb and was kept at 140 °C for 24 h followed by filtration. The filtrate was washed and kept for drying at 60 °C.

The amount of MnO₂ deposited was calculated by using Faraday's law of electrolysis:

$$W = \frac{\text{Charge passed (C)} * 87(\text{Mol. weight of MnO}_2)}{96485 * 2 (\text{no electron released per MnO}_2)}$$

4.2.3 Characterization

Structure and morphology of the materials were analyzed using Nova Nano SEM 450 and Quanta™ Scanning Electron Microscope. High-resolution transmission electron microscope (HR-TEM) was carried out in Tecnai-T 30 at an accelerated voltage of 300 kV. The X-ray diffraction patterns of the prepared specimens were done using PAN X'pert Pro instrument, data collection was done at a scan rate of 1.5°/min using Cu K α radiation. Raman analysis was carried out on Horiba Jobin Yvon Inverted LabRAM HR800 VIS-NIR using 632 nm solid-state diode laser beams. X-ray Photoelectron Spectroscopic (XPS) measurements were carried out on a VG Micro Tech ESCA 300° instrument at a pressure of $> 1 \times 10^{-9}$ Torr (pass energy of 50 eV, electron take off angle of 60° and the overall resolution of ~ 0.1 eV). Nitrogen adsorption-desorption experiments were conducted at 77 K using Quantachrome Quadraorb automatic volumetric instrument. Before the gas adsorption measurements, the sample was activated at room temperature (for 24 h) and 100 °C (for 36 h) under ultrahigh vacuum (10⁻⁸ mbar) for overnight. The deposited MnO₂ was carefully scratched from the carbon surface and analyzed for gas adsorption. Surface area was calculated from the N₂-adsorption isotherm up to 0.3 relative pressures. Pore size distribution was measured by the DFT method.

4.2.4 Electrochemical Characterization

All the electrochemical studies were carried out in a BioLogic SP-300 Potentiogalvanostat. Metal crocodile clips were used for the required electrical contacts from the electrodes. Cyclic Voltammetry (CV) was carried out in a 3-electrode setup where

MnO₂ coated carbon paper was used as a working electrode and Ag/AgCl was used as a reference electrode and Pt mesh as a counter electrode. The CV measurements were taken at different scan rates from 10 to 1500 mV s⁻¹ by maintaining a potential window between 0 to 1 V vs Ag/AgCl. Mass specific capacitance of MnO₂ was calculated from the CV and charge discharge method using the equations used in the Chapter 3.2.7.

The charge-discharge measurement was done at different current densities (1 to 100 A g⁻¹) in the same potential range which was used for CV. Cycling stability was done by chrono charge-discharge method at 5 A g⁻¹ current density for 1000 continuous cycles. Coulombic efficiency was calculated during the charge-discharge cycling by taking the percentage of charging time coulombs by discharge coulombs. Electrochemical impedance (EIS) analysis was carried out from 10⁶ Hz to 0.01 Hz frequency against the open circuit potential with a sinus amplitude of 10 mV ($V_{\text{rms}} = 7.07$ mV). All the EIS data were analyzed using an EC-Lab Software V10.19.

Asymmetric capacitor was assembled by using activated carbon (AC) as the negative electrode and MnO₂/carbon paper as the positive electrode. AC was made into a paste with conducting carbon and binder in a ratio of 80:15:5 in N-methyl 2-pyrrolidone. The above made paste was brush coated to the carbon paper with an area of 1 cm² and the loading was adjusted according to the specific capacitance of AC (180 F g⁻¹). Measurements were carried out in 1 M Na₂SO₄.

4.3 Result and Discussion

4.3.1 SEM and HR-TEM Analysis

SEM image of the carbon fiber paper clearly indicates the presence of smooth fibers with 5-7 μm diameter (Figure 4.4.2a). Figure 4.4.2b, 2c and 2d represent field emission scanning electron microscope (FE-SEM) images of the formed MnO₂ nanowalls on the carbon fiber (Mn-CP) backbone at different magnifications. The FE-SEM image in Figure 4.4.2b clearly shows a highly uniform layer of MnO₂ deposited individually on each carbon fiber having a thickness of 365 nm. Elemental mapping in Figure 4.4.3 also confirms the uniform distribution of Mn along the fiber surface. Figure 4.4.2c is an enlarged portion of a small area in Figure 4.4.2b, which gives a clear view of the 3D growth pattern of the MnO₂ circular nanowalls having individual

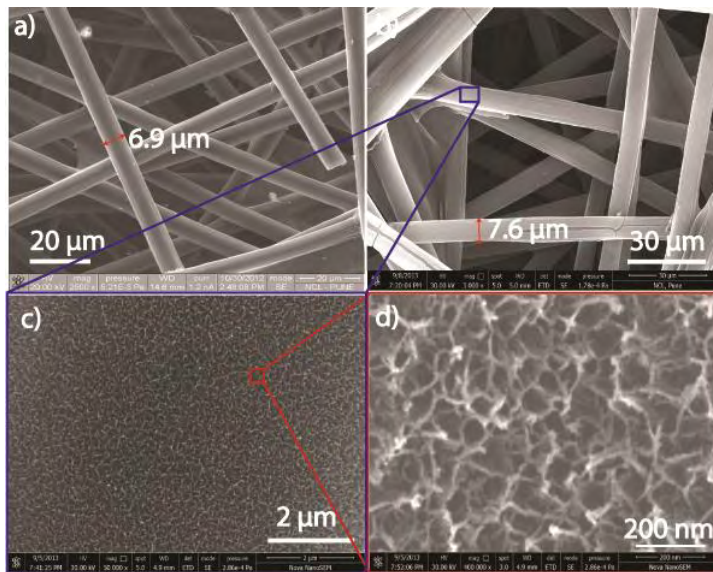


Figure 4.2: FE-SEM images of a) bare carbon paper, b) MnO₂ coated carbon paper, c) enlarged view of the portion marked in b) and c) focused view of the portion marked in c) which shows the growth pattern of the nanowalls.

wall thickness of 5-8 nm. The alignment of the nanowalls in Figure 4.4.2d indicates clear vertical growth patterns of the MnO₂ layers with adequate space of 25-65 nm between the enclosed boundaries of the walls.

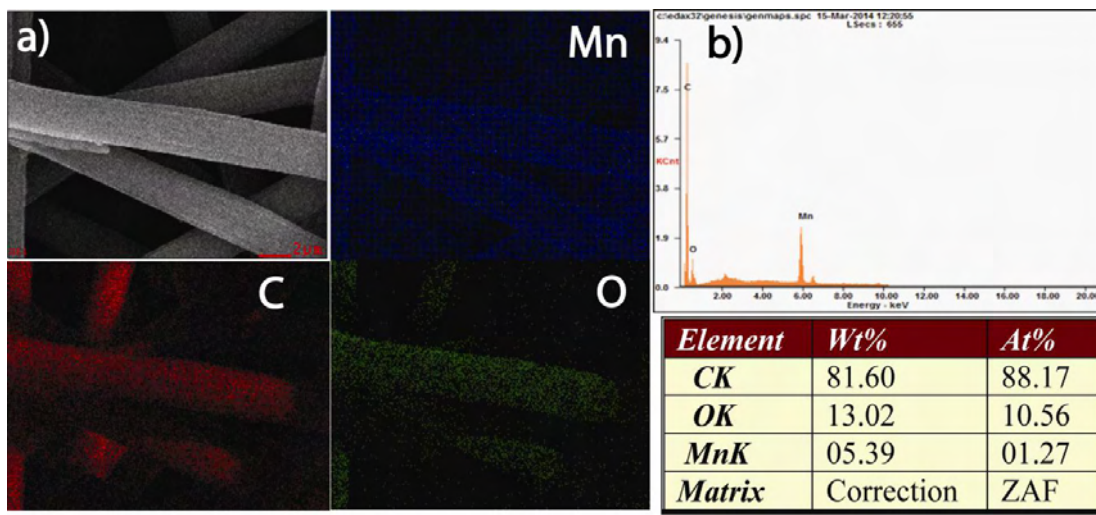


Figure 4.3: a) EDAX elemental mapping of the MnO₂ nanowalls, b) EDAX spectrum and the table indicating the % of the elements present in the area of Figure 4.3a.

Figure 4.4 is the high resolution transmission electron microscopy (HR-TEM) images of the surface of the MnO₂ wall. HR-TEM (Figure 4.3b) image clearly shows partial crystallinity in the selected area. This was contradictory to the XRD spectra

(Figure 4.5d), which lack characteristic peaks of MnO_2 probably due to the high amorphous content. Selected area diffraction (SAED) patterns in Figure 4.3c shows (110), (111) and (220) planes corresponding to the d-spacing of 0.32, 0.26 and 0.15 nm which are also found in accordance with the values deduced from the HRTEM image presented in Figure 4.4b^[6]. A d-spacing of 0.22 nm indicates the presence of the (211) crystal plane, which can probably be due to the presence of Mn_3O_4 . Thus, XRD, HRTEM and SAED results show high amount of amorphous MnO_2 in the nanowalls with partial crystalline phase which is difficult to ascertain to a particular MnO_2 phase due to polycrystalline nature as indicated by the SAED images.

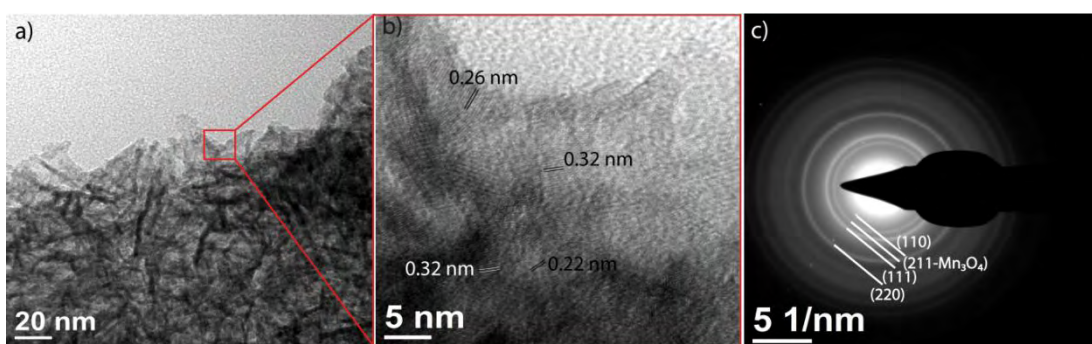


Figure 4.4: a) HR-TEM image of the MnO_2 nanowalls, b) enlarged part of the marked portion of a) (different crystal planes are marked by lines) and c) SAED image of the MnO_2 nanowall.

4.3.2 Surface Area Measurements

Interestingly, the nanowall itself is porous, which could be confirmed from the pore size distribution profile as indicated in the inset of Figure 4.5b. The intense peak at 3.5 nm and a small one at 1.7 nm are explicitly indicating the porosity of the walls. The measured surface area of the MnO_2 layer is $98 \text{ m}^2 \text{ g}^{-1}$ (Figure 4.5a). This peculiar morphological growth pattern of MnO_2 having both active surface and room for easy access by electrolytes helps to simultaneously establish both high active interfacial area and pathways for seamless ion movement within the electrode. BET surface area measurement of the carbon fiber paper shows merely $1 \text{ m}^2 \text{ g}^{-1}$ surface area for the paper which indicates there are nanopores at nano regime.

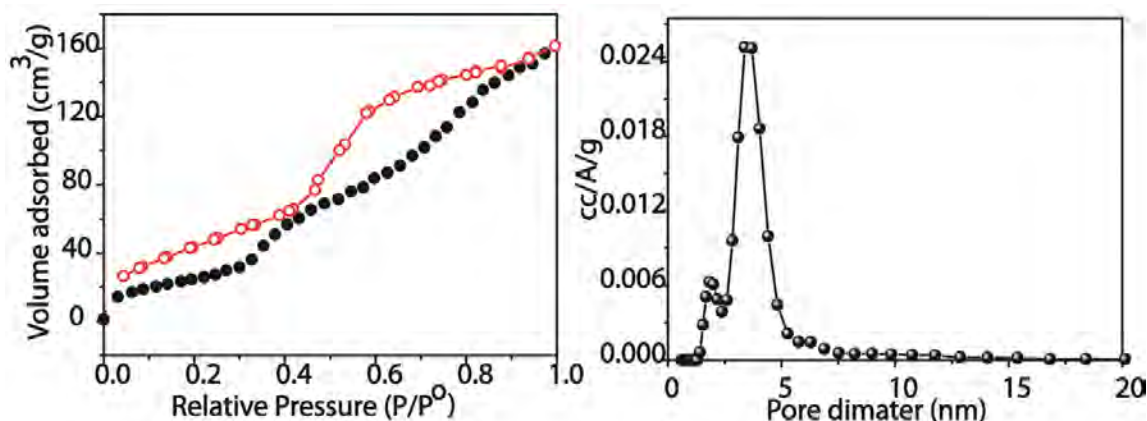


Figure 4.5: a) Nitrogen adsorption isotherm of Mn/CP-300 and b) pore distribution profile.

4.3.4 Raman, XRD and XPS Spectral Analyses

Raman spectrum of Mn-CP in Figure 4.6a & 4.6b comprises of a strong peak at 650 cm⁻¹ which corresponds to symmetric stretching vibration of Mn-O^[7]. Two weak peaks are also observed at 576 and 474 cm⁻¹ in which the former one is due to the stretching of the basal plane of MnO₂^[7a]. The above peaks indicate the presence of birnessite-type of MnO₂ in the nanowalls. Raman spectrum also indicates the presence

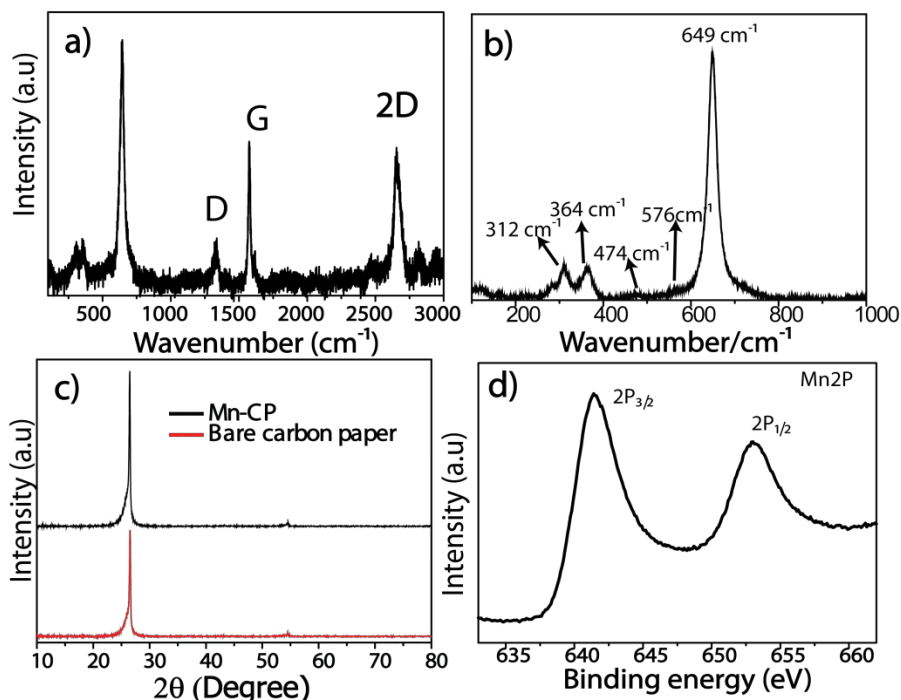


Figure 4.6: a) Full scale Raman spectrum, b) enlarged view of the spectrum below 1000 cm⁻¹ where the characteristic MnO₂ peaks are present, c) XRD spectra and d) Mn2p XPS; the measurements are done by using the MnO₂ coated carbon paper.

of Mn_3O_4 phase due to the peaks obtained at 312 and 364 cm^{-1} which correspond to the T_{2g} , and E_g active modes of Mn_3O_4 apart from the normal MnO_2 peaks^[8]. Apart from this, strong peaks at 1329, 1575 and 2657 cm^{-1} are also observed, which represent the D, G and 2D bands of carbon originated from the carbon fiber surface. Presence of the characteristic carbon peaks in surface sensitive Raman spectroscopy also provides indirect evidence on the presence of nanovoids between the areas demarcated by the MnO_2 walls. In the XRD spectrum, the characteristic peaks of MnO_2 are absent, indicating the prominent amorphous nature of the deposited layer (Figure 4.6c). On the other hand, the HRTEM and SAED images (Figure 4.4b & 4.4c) show partial crystallinity of the MnO_2 phase. Mn 2P X-ray photoelectron spectrum (XPS) is shown in Figure 4.6d. It possesses two peaks at 653.0 and 642.4 eV respectively which are corresponding to $2P_{3/2}$ and $2P_{1/2}$ with a binding energy difference of 11.58 eV. These values are very similar to the reported values in the literature^[9].

4.3.5 Electrochemical Analysis

Electrochemical charge storage properties of the MnO_2 nanowall-modified carbon fiber are examined in 1 M Na_2SO_4 in a 3-electrode cell in which Ag/AgCl and Pt foil were used as the reference and counter electrodes respectively. Figure 4.7a shows cyclic voltamogram of Mn-CP-300 at various scan rates and Figure 4.6b shows the CV profile of CP-300 to CP-2400 at 50 mV s^{-1} . At lower scan rates, the redox peaks corresponding to the Na^+ intercalation inside the MnO_2 bulk^[6a] is more prominent and at higher scan rates, such peaks are absent due to dominance of contributions by surface adsorption compared to the intercalation. Figure 4.7c shows the chrono charge-discharge profiles for the MnO_2 based systems at 5 A g^{-1} . The highest capacitance of 1149 F g^{-1} at 1 A g^{-1} current density is observed for Mn-CP-300 where the MnO_2 nanowall thickness is only 73 nm. The continuous electron path from the carbon fiber backbone and the nano-corridor for ion movement inside the nanowalls along with its porosity help to provide high capacitance. Fast ion transportation through the nanowalls is playing a significant role for excellent capacitance retention as well. To look at the capacitance contribution from the support carbon fiber, the charge-discharge study of bare carbon paper was carried out which shows a capacitance of 40 $\mu\text{F cm}^{-2}$ due to the extreme low surface area (1 $\text{m}^2 \text{g}^{-1}$).

Thus, highly macroporous carbon paper compared to a plane current collector helps for the high mass loading of MnO_2 but at the same time it gives adequate conducting support with negligible capacitance contribution. Even at a high current dragging condition of 100 A g^{-1} , Mn-CP-300 could retain a capacitance of 558 F g^{-1} , which is 56 % of the capacitance obtained at a low current density of 2 A g^{-1} (Figure 4.7d). When the deposition time is doubled, the thickness of the MnO_2 coating also is increased in the order of 70 (Mn-CP-300), 365 (Mn-CP-600), 560 (Mn-CP-1200) and 1210 nm (Mn-CP-2400). In accordance with this, the specific capacitance displayed a decreasing trend as 1000 F g^{-1} (Mn-CP-300) > 790 F g^{-1} (Mn-CP-600) > 619 F g^{-1} (Mn-CP-1200) > 339 F g^{-1} (Mn-CP-2400). Lowering of the specific capacitance with increasing the MnO_2 wall thickness is apparent as the electron needs to travel long distance through the non-conducting MnO_2 phase for storing charges. Hence, as the thickness of the MnO_2 wall increases, surface charge storage becomes prominent than that due to Na^+ intercalation especially in the case of Mn-2400. Considering the

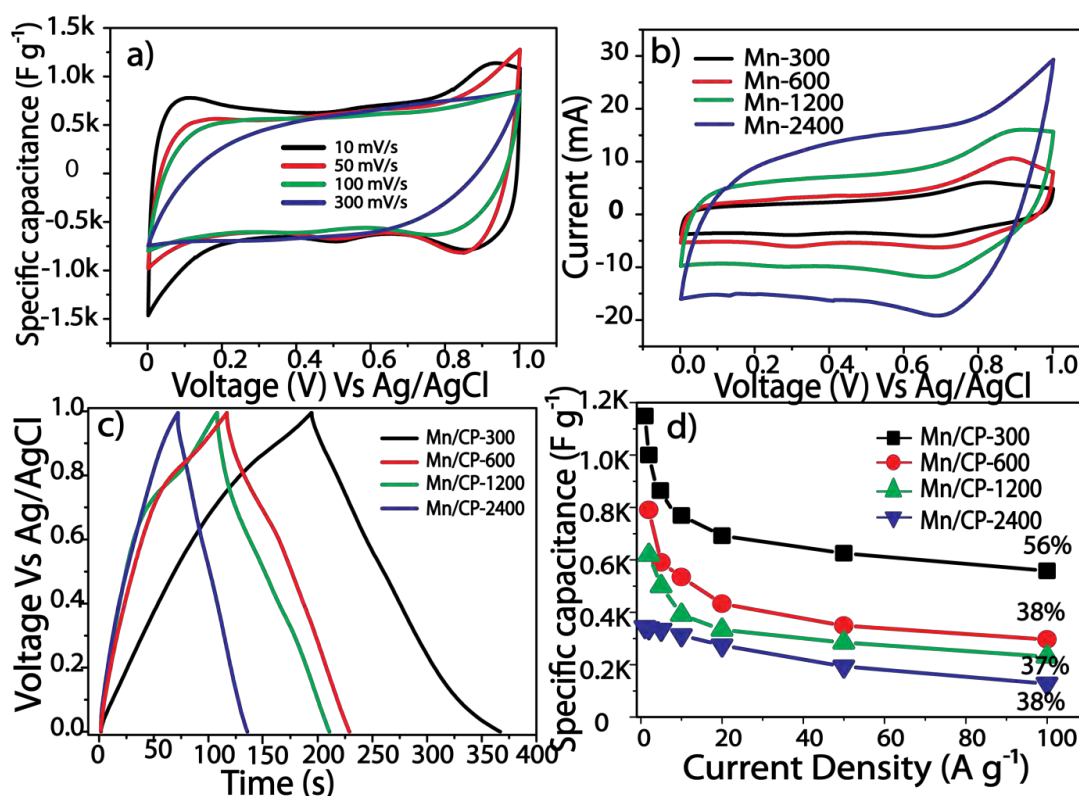


Figure 4.7: a) Cyclic voltammograms of Mn-300 at various scan rates, b) combined cyclic voltammograms of Mn/CP-300 to Mn/CP-2400 carried out at a scan rate of 50 mV s^{-1} c) charge-discharge profiles at 5 A g^{-1} current density and d) specific capacitance for various time of deposition at varied current density.

capacitance retention, Mn-CP-300 shows the highest retention of 56 % at 100 A g^{-1} current density compared to $\sim 38 \%$ for the rest of the samples. Retention in capacitance is more influenced by the fast ion transport than that of electrical conductivity. Thus, good retention in capacitance is credited to the establishment of proper ion channels for fast ion transport up to Mn-CP-1200 which is confirmed by the SEM images of the various MnO_2 samples. On the other hand, in case of Mn-CP-2400, its high retention is mainly because of its prominent surface charge storage, rather than intercalation of Na^+ , as the process can respond fast with respect to the potential switching^[6a]. It is remarkable that a sudden decrease in capacitance is found in all cases (30-35 %) except for Mn-CP-2400 (9 %) in the current density region of $1\text{-}10 \text{ A g}^{-1}$. This is clearly because of the dominance of pseudocapacitance in the case of Mn-CP-300, Mn-CP-600 and Mn-CP-1200 due to Na^+ intercalation which is more affected by the fast potential switching compared to surface adsorption which is prominent in case Mn-CP-2400.

Finally, in order to validate the advantages of the involvement of both electrically conducting backbone and structural benefits for ion diffusion, MnO_2 nanowalls are compared with a composite, designated as CNF/ MnO_2 , consisting of

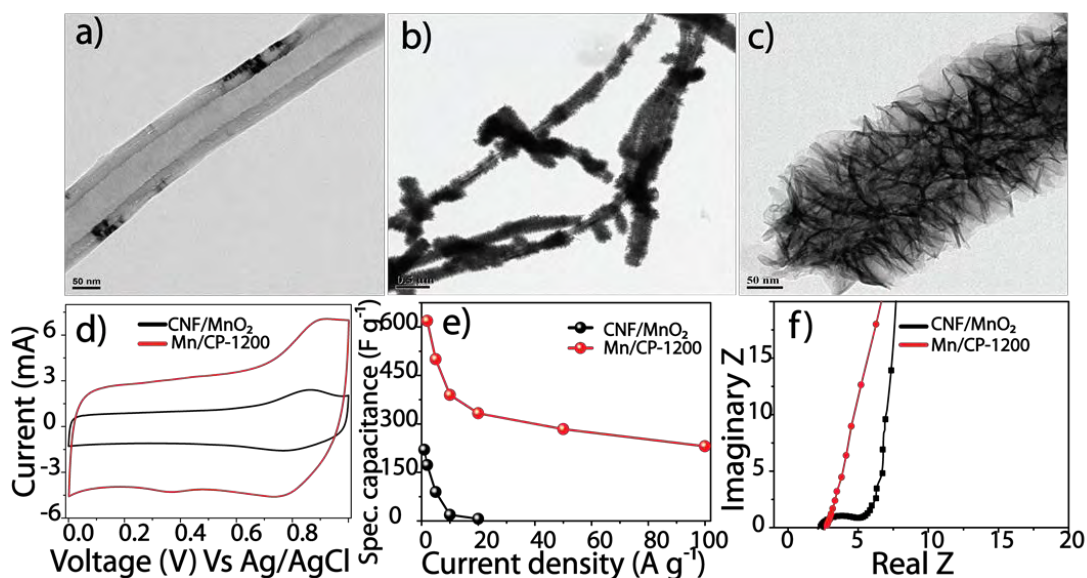


Figure 4.8: TEM image of a) bare CNF, b) & c) CNF/ MnO_2 composites, d) cyclic voltammograms of CNF/ MnO_2 and Mn/CP-1200 recorded at 50 mV s^{-1} , e) specific capacitance measured at varies current densities and f) comparative Nyquist plot of CNF/ MnO_2 and Mn-CP-1200.

MnO₂ layers grown on a hollow carbon nanofiber (CNF). Details are given in Figure 4.8. Compared to the MnO₂-carbon paper composite, CNF/MnO₂ lacks continuous electron path due to the possible presence of low conducting MnO₂ grains between the tubes, thus affecting the electrical conductivity. This is reflected in the capacitance of CNF/MnO₂, which delivers only 220 F g⁻¹ at 1 A g⁻¹ and the value drops nearly to 7 F g⁻¹ at a higher current density of 20 A g⁻¹ (Figure 4.8e). In order to quantify the low charge-transfer resistance in the MnO₂ nanowall system, electrochemical impedance spectroscopic (EIS) analysis was carried out and the corresponding Nyquist plots are given in Figure 4.8f. CNF/MnO₂ shows a clear semicircle loop at high frequency, indicating the high charge-transfer resistance (3.5 Ω). Conversely, the electrode based on the MnO₂ nanowall shows a very small semicircle loop (0.7 Ω) at the high frequency region (Figure 4.8f), indicating its high charge-mobility due to the well-connected and accessible channels generated during the synthesis.

Structure and morphology of MnO₂ formed clearly depend on various factors. During the electrodeposition, apart from the selected precursors, the derived structure also has dependency on the mode of deposition (constant current or potential), amount of current passed per second and the nature of the substrate as well. To testify this, electrodeposition is controlled by maintaining two conditions in which the amount of charge passed remains the same (1200 mC). This includes (Case-I) deposition at constant potential (*i.e.* chrono-amperometry, 0.6 V Vs Ag/AgCl) and (Case-II) deposition at constant current (*i.e.* chrono-potentiometry, 1 mA). SEM images of the formed MnO₂ in both the cases are shown in Figure 4.9 which clearly indicates that the morphology quite varies with the method adopted for electrodeposition. Compared to the nanowall forest in Case-I, which was obtained at 0.6 V, Case-II shows nanoflower structure. Surface area obtained for the material formed in Case-I is 19 m² g⁻¹ and in Case-II is 12 m² g⁻¹ (Figure 4.9e; this includes the weight of carbon paper and MnO₂ and the carbon paper alone shows a surface area of 1 m² g⁻¹). Apart from this, the pore volume is 1.5 times lower in the case of the nanoflower formed in Case-II compared to the nanowall forest formed in Case-I (Figure 4.9d). This unambiguously confirms that the nanowall architecture possesses high surface area with perfect pore distribution, which helps for attaining high specific capacitance (Figure 4.9a). At 0.6 V, the reaction is limited by the diffusion of Mn²⁺ due to the

high oxidation potential which results in high current of 15 mA in the beginning, which decreases gradually to 2-5 mA. Thus, since the potential is controlled throughout the experiment in Case-I, the diffused Mn^{2+} ions will be consumed fast and be grown vertically where nucleation starts rather filling in the vacant space. Diffusion controlled electrodeposition is the possible reason for the formation of nanowalls^[10]. On the other hand, in Case-II, due to the low current of 1 mA, there is no such diffusion limitation. At 0.6 V (Case-I), oxygen evolution is also observed at small rates, which is also expected to have a role in controlling the growth pattern and porosity of the system.

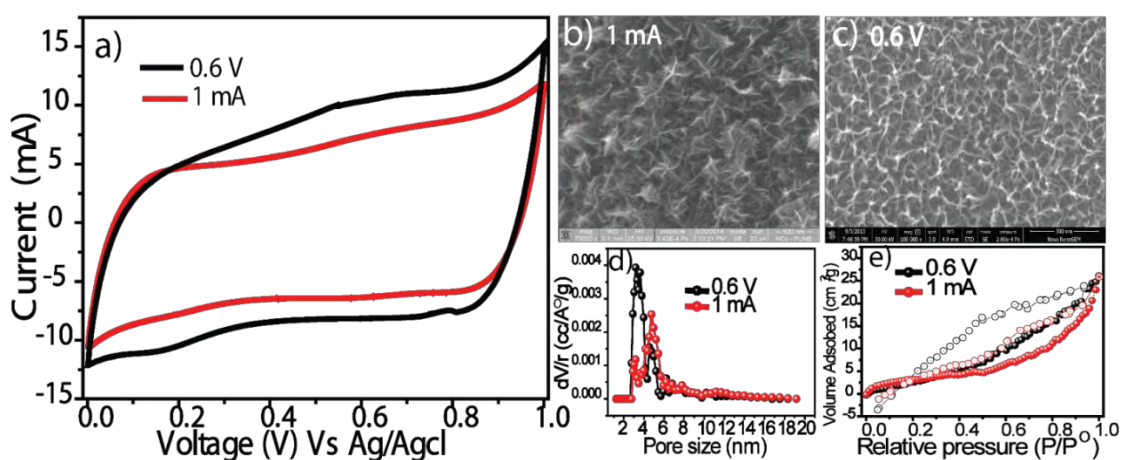


Figure 4.9: a) Cyclic voltammograms recorded at 50 mV s^{-1} for MnO_2 nanowalls forest which was deposited at 0.6 V (black line) and nanoflower formed at 1 mA (red line), b) & c) corresponding SEM images for the MnO_2 nanoflower and nanowall forest formed at different deposition conditions, d) pore distribution patterns for the MnO_2 nanoflower and nanowall forest obtained at different deposition conditions and e) N_2 -adsorption isotherms recorded over the MnO_2 nanoflower and nanowall forest.

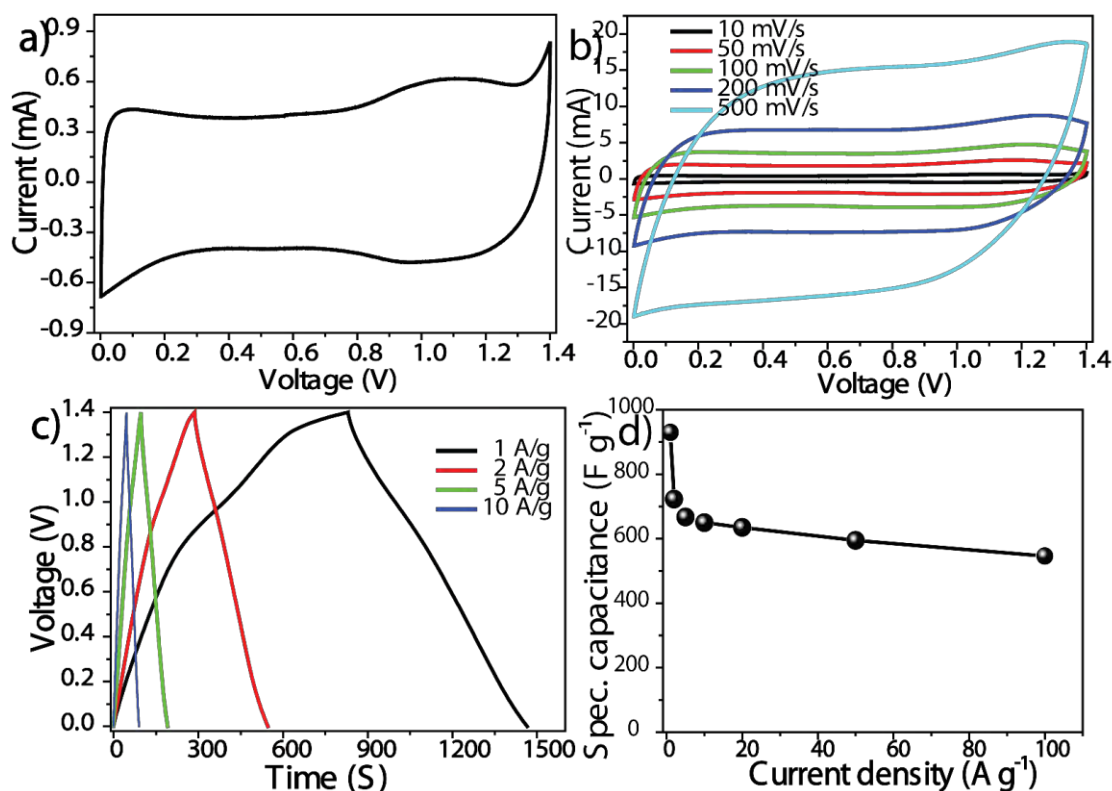


Figure 4.10: Charge storage properties of an asymmetric capacitor using Mn/CP-300: a) cyclic voltammogram recorded at a scan rate of 10 mV s⁻¹, b) the CV profiles obtained at various scan rates, c) charge discharge profiles and d) specific capacitance at varied scan rates.

Even though Mn/CP-300 had shown a high specific capacitance of 1149 F g⁻¹ in a 3-electrode fashion, its reproducibility in an actual supercapacitor which works in 2-electrode fashion is very important. Here, two sets of experiments are carried out by using Mn/CP-300 (where the mass loading is 0.135 mg cm⁻²) and Mn/CP-1200 (where the mass loading is 1 mg cm⁻²) as the positive electrodes. To utilise the full ability of the asymmetric capacitor, potential window is increased from 1 V to 1.4 V. It is interesting to note that still Mn/CP-300 in the 2-electrode configuration shows a high specific capacitance of 930 F g⁻¹. Even at a current density of 100 A g⁻¹, 60 % of its initial capacitance is retained. Details are given Figure 4.10. In the case of Mn/CP-2400, where a high mass loading of 1 mg cm⁻² could be maintained, a capacitance of 402 F g⁻¹ in a potential window 1.5 V could be achieved. The above obtained

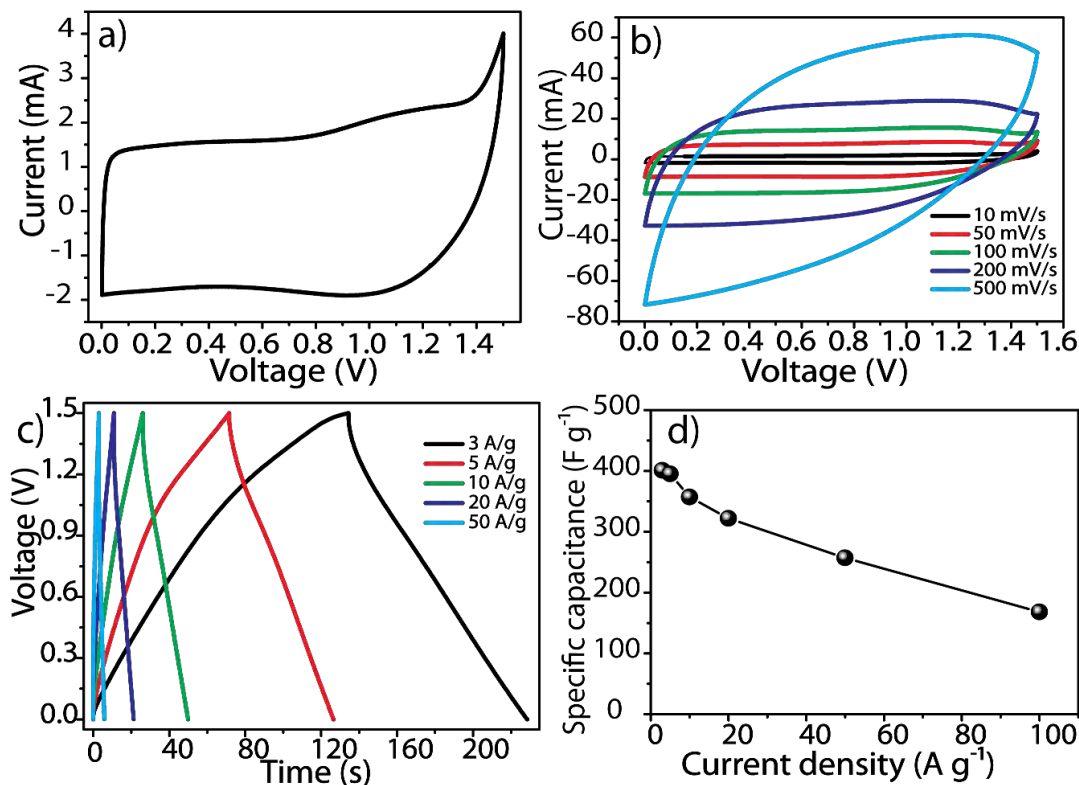


Figure 4.11: Charge storage properties of an asymmetric capacitor using Mn/CP-2400: a) cyclic voltammogram recorded at a scan rate of 10 mV s⁻¹, b) the CV profiles taken at various scan rates, c) charge-discharge profiles and d) specific capacitance at varied scan rates.

capacitance of Mn/CP-2400 is even slightly higher than the obtained capacitance (340 F g⁻¹) in a 3-electrode system (Figure 4.11). Thus, the obtained capacitance of the nanowall forest indicates its prospects for device applications. Details of charge storage measurement are shown in Figure 4.11. In case of Mn/CP-300, oxygen evolution restricts the window around 1.4 V.

Cycle stability of the electrode is evaluated for 8500 continuous cycles in 1 M Na₂SO₄ (Figure 4.12a) at 5 A g⁻¹ current density. Columbic efficiency is nearly 100 % during the whole cycling and less than 10 % degradation in capacitance is happened during the process. To see the structural stability of the nanowalls during the cycles, FE-SEM was carried out after the stability cycling. Figure 4.12b shows the images of the nanowall forest before and after the cycling test, which unambiguously confirm that the nanowalls are almost structurally intact during the charge-discharge cycling.

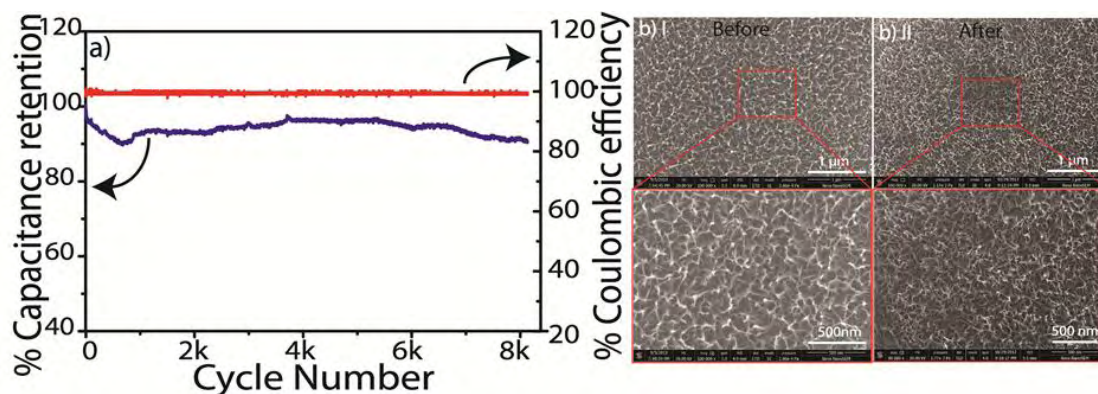


Figure 4.12: a) Cycle stability and columbic efficiency at 5 A g^{-1} current density and (b) FE-SEM images of the surface taken I) before and II) after the stability cycles.

4.3.6 Application in Solid-State Supercapacitor

To utilize the high porosity of the $\text{MnO}_2/\text{carbon}$ paper, a solid-state supercapacitor is made by utilizing polyvinyl alcohol-LiCl (PVA-LiCl) gel electrolyte which is more eco-friendly than the liquid electrolyte. PVA-LiCl was prepared by a similar protocol used in Chapter-3 (3.2.2). The high porosity left even after the MnO_2 coating inside the carbon paper can be utilized for gel electrolyte intercalation which results in high electrode-electrolyte interface. Figure 4.13 shows the detailed electrochemistry of the solid device made from Mn-1200. During the solid-state device testing, Mn-1200 shows a maximum capacitance of 400 F g^{-1} compared to 620 F g^{-1} obtained by using the liquid electrolyte. This deviation is obvious as the conductivity of PVA-LiCl is far lower than that of $1 \text{ M Na}_2\text{SO}_4$. Due to the enhanced electrode-electrolyte interface owing to the high porosity of the nanowalls, excellent capacitance retention also observed at high current drag conditions. Even at a current density of 20 A g^{-1} , 150 F g^{-1} is retained by the system. Such high retention is clearly due to the facile ionic mobility through uniform porous nanowalls. Impedance analysis also shows low charge-transfer resistance in the solid-state device which was measured from the high frequency semicircle of the Nyquist plot.

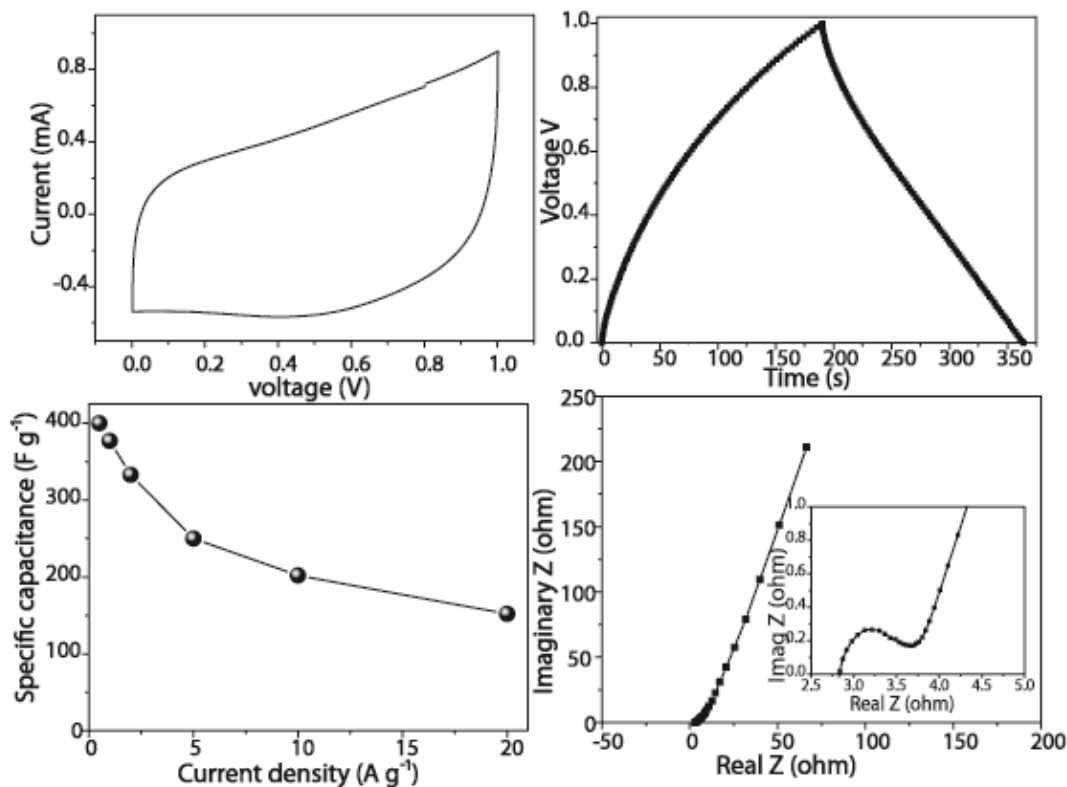


Figure 4.12: Electrochemical performance of the solid-state device made from Mn-1200: a) Cyclic Voltamogram recorded at 50 mV s^{-1} , b) charge–discharge profile taken at a current density of 1 A g^{-1} , c) specific capacitance measured at varied current density values and d) Nyquist plot of the solid-state device and inset shows the high frequency region.

4.4 Conclusion

In conclusion, uniform deposition of nanowall forest could be accomplished electrochemically on the fibers of a conducting and porous carbon paper. The peculiar growth pattern of the vertical MnO_2 walls having microporosity concomitantly provided spacious and accessible corridors along the surface, which act as facile channels for ion transport after electrolyte filling. At the same time, the carbon fiber backbone helped to overcome the issue of the inherent electrical resistance associated with MnO_2 . Thus formed electrode appeared to display a specific capacitance as high as 1149 F g^{-1} at a dragging current of 1 A g^{-1} and the electrode retains a capacitance of 565 F g^{-1} even at a high current dragging condition of 100 A g^{-1} . Even after 8000 continuous cycles, the nanowalls appeared to be structurally stable with no significant degradation in its capacitance.

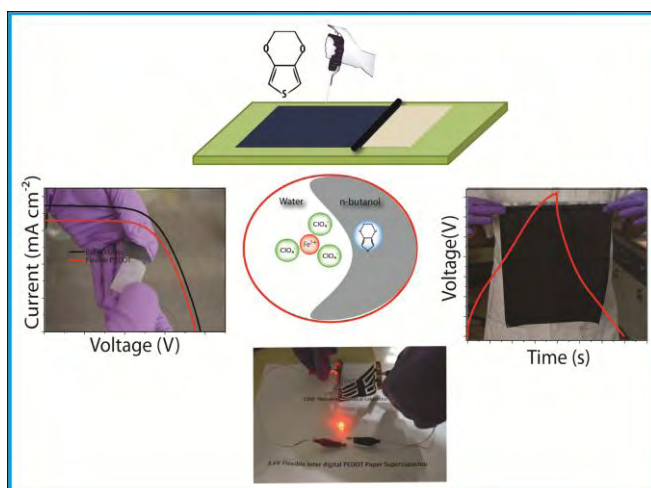
4.5 References

- [1] (a) P. Simon, Y. Gogotsi, *Nat. Mater.* **2008**, *7*, 845-854; (b) Y. Zhang, H. Feng, X. Wu, L. Wang, A. Zhang, T. Xia, H. Dong, X. Li, L. Zhang, *Int. J. Hydrogen Energy* **2009**, *34*, 4889-4899.
- [2] H. Chen, L. Hu, M. Chen, Y. Yan, L. Wu, *Adv. Funct. Mater.* **2014**, *24*, 934-942.
- [3] (a) H. Y. Lee, J. B. Goodenough, *Journal of Solid State Chemistry* **1999**, *144*, 220-223; (b) W. Wei, X. Cui, W. Chen, D. G. Ivey, *Chem Soc Rev* **2011**, *40*, 1697-1721; (c) T. Mathieu, B. Thierry, B. Daniel, *Chem. Mater.* **2004**, *16*, 3184-3190.
- [4] (a) R. Liu, S. B. Lee, *J. Am. Chem. Soc.* **2008**, *130*, 2942-2943; (b) Z. Sun, S. Firdoz, E. Ying-Xuan Yap, L. Li, X. Lu, *Nanoscale* **2013**, *5*, 4379-4387; (c) J. H. Kim, K. H. Lee, L. J. Overzet, G. S. Lee, *Nano Lett* **2011**, *11*, 2611-2617; (d) G.-R. Li, H. Xu, X.-F. Lu, J.-X. Feng, Y.-X. Tong, C.-Y. Su, *Nanoscale* **2013**, *5*, 4056-4069.
- [5] Z. Yu, B. Duong, D. Abbitt, J. Thomas, *Adv Mater* **2013**, *25*, 3302-3306.
- [6] (a) L. Mai, H. Li, Y. Zhao, L. Xu, X. Xu, Y. Luo, Z. Zhang, W. Ke, C. Niu, Q. Zhang, *Sci Rep* **2013**, *3*, 1718; (b) S. Devaraj, N. Munichandraiah, *J. Phys. Chem. C* **2008**, *112*, 4406-4417.
- [7] (a) Y.-K. Hsu, Y.-C. Chen, Y.-G. Lin, L.-C. Chen, K.-H. Chen, *Chem. Commun.* **2011**, *47*, 1252-1254; (b) J. Luo, H. T. Zhu, H. M. Fan, J. K. Liang, H. L. Shi, G. H. Rao, J. B. Li, Z. M. Du, Z. X. Shen, *J. Phys. Chem. C* **2008**, *112*, 12594-12598.
- [8] Z.-Y. Tian, P. Mountapmbeme Kouotou, N. Bahlawane, P. H. Tchoua Ngamou, *J. Phys. Chem. C* **2013**, *117*, 6218-6224.
- [9] (a) S. Dong, X. Chen, L. Gu, X. Zhou, L. Li, Z. Liu, P. Han, H. Xu, J. Yao, H. Wang, X. Zhang, C. Shang, G. Cui, L. Chen, *Energy & Environmental Science* **2011**, *4*, 3502-3508; (b) L. Hu, W. Chen, X. Xie, N. Liu, Y. Yang, H. Wu, Y. Yao, M. Pasta, H. N. Alshareef, Y. Cui, *ACS Nano* **2011**, *5*, 8904-8913.
- [10] S. I. Cho, S. B. Lee, *Acc. Chem. Res.* **2008**, *41*, 699-707.

Chapter-5

Surfactant-Free Interfacial Polymerization of PEDOT through Simple Roll Coating: Scalable Method for Flexible, Conducting Substrate for Energy Conversion and Storage Applications

The chapter deals with a novel synthetic strategy to prepare a highly conducting PEDOT phase on flexible cellulose paper formed by inducing surfactant-free interfacial polymerization at the interface of two immiscible liquids. The illustrated process is highly scalable in such a way that very large flexible PEDOT paper can be prepared in 2-3 h under laboratory conditions. The obtained PEDOT-paper possesses efficiently packed π -conjugated chains and increased doping level. This helps for



better inter-chain and intra-chain charge mobility, leading to conductivity as high as 375 S cm^{-1} compared to 30 S cm^{-1} of the PEDOT prepared in n-butanol. A low sheet resistance of $3 \Omega/\square$ is achieved by multiple coating, which is found to be stable even after two months under ambient conditions and at various flexible and bending conditions. A flexible solid-state supercapacitor

with an overall thickness of 0.17 mm made from the PEDOT paper and PVA- H_2SO_4 as the solid electrolyte exhibits a volumetric energy density of 1 mWh cm^{-3} . The flexible devices are found to be very stable during the charge-discharge cycling under twisted and bending conditions for more than 3800 cycles. A 3.6 V inter-digitized flexible device could also be made in a single PEDOT paper, which is found to be powered enough to glow an LED under flexible conditions. Apart from the supercapacitor application, DSSC made by using the PEDOT paper as the counter electrode shows a high conversion efficiency of 6.5 % in comparison with 7.0 % given by Pt/FTO.

Content in this chapter is published in the following articles.

RSC Energy and Environmental Science, **2015**, DOI: 10.1039/C5EE00142K

Reproduced by permission of The Royal Society of Chemistry.

5.1 Introduction

The entire material designing and device fabrication strategies discussed from Chapter 2 to Chapter 4 were based on the concept of establishing enhanced electrode-electrolyte interface, which can ensure faster ionic and electric mobility. However, the entire devices explained in those chapters hold solid current collectors such as carbon paper, FTO etc., and, thus making such devices heavier and rigid. However, future flexible and light weight electronic and electrical gadgets demand flexibility and weight reduction in the energy managing devices^[1]. Lack of flexibility in the present commercial DSSCs, supercapacitors, Li-ion batteries etc, gives major restrictions in integrating such systems with the future electronic and electric devices. Thus, it is highly important to have lighter, thinner and flexible energy converting and storing devices, which in turn help the whole family of electric and electronic devices to become much cheaper and eco-friendly. Exchange of the individual key components such as current collector, electrode material as well as the electrolyte with lighter and flexible alternatives is the key to the success of such devices. However, this transformation to flexibility and lighter qualities always accompanies with compromise in conductivity and electrochemical activity of the components due to the trade-off between form/property tolerance accommodation and functionality therein.

A single material possessing both high electrochemical activity and flexibility will be promising in this context as it can play the role of both current collector and an electrode material, which results in flexible, lighter, thinner, and cheaper energy devices. This approach is very challenging in the present situation due to the lack of materials which possess the required conductivity, flexibility and electrochemical activity concomitantly. Among the various materials, flexible metal foils^[2] and metal coated flexible substrates^[3] possess high conductivity, and, thus, are being used as the current collectors in most of the electrochemical devices^[4]. However, issues related to electrochemical activity, cost, corrosion and density make them less viable candidates for such flexible applications. Various carbon morphologies like carbon nanotubes^[5] and graphene^[6] are looking very promising due to their low cost and high conductivity. However, large area electrode production from highly graphitized CNT's^[7] and graphene^[8] is still challenging due to the difficulties associated with processing in solution phase. On the other hand, conducting polymers^[9] are promising

in this context due to their easy processability, conductivity etc. compared to the carbon analogues. Polyethylenedioxythiophene (PEDOT)^[10] is a versatile conducting polymer among its counterparts owing to its very high theoretical conductivity ($> 500 \text{ S cm}^{-1}$), chemical and physical stability, large operable potential window etc^[11]. Thus, PEDOT is being used in various photovoltaic cells, Li-ion batteries and supercapacitors. One of the promising applications of PEDOT is in dye sensitized solar cells (DSSCs) to replace the costly Pt coated FTO counter electrode^[12]. At the same time, due to its high conductivity, extensive research is also going on to use it as a potential electrode material in supercapacitors^[13].

For flexible counter electrode as well as for the supercapacitor applications, achieving low sheet resistance for PEDOT on a flexible substrate is necessary. Among the various methods available for the preparation of the PEDOT electrodes, vapour phase^[14] and electrochemical deposition^[15] produce highly conducting films. However, practical issues to produce larger area films as well as the inability to attain comparable coating with a low sheet resistance make PEDOT a less viable choice for conceiving current collector-free electrodes. A simple and common method compared to the aforementioned two methods is direct coating of the chemically synthesized PEDOT on a flexible substrate *via* various techniques like spin coating, brush coating or bar coating. The main drawback of this method is the low processability and low conductivity of the chemically synthesized PEDOT^[16] owing to the fast polymerization rate which leads to disordered and short polymer chains with shorter π conjugation^[17]. One of the attempted solutions to overcome this issue is the use of a retardant, normally a Lewis base^[18], which slows down the polymerization rate. However, harmful nature of the retardants^[19] and their inability to make a significant reduction in the sheet resistance make the process less viable and attractive.

To address all these issues, in this chapter, an efficient and scalable method to prepare highly conducting PEDOT flexible paper which possesses a very low sheet resistance is discussed. This is achieved by manipulating the polymerization at the interface of two immiscible liquids^[20] on a cellulose paper to trigger PEDOT growth along the fibers of the cellulose paper. This type of substrate assisted alignment is found to have a key impact on the conductivity as well as the electrochemical activity of the PEDOT films. The prepared PEDOT film possesses highly ordered polymer

chains and increased doping level, which help the paper to display excellent conductivity even under flexible conditions. The prepared film adheres strongly to the substrate and retains the flexible nature of the cellulose paper and maintains long-term stability on the conductivity. Using the flexible PEDOT paper thus obtained, two promising applications of the paper are also demonstrated, one in flexible all-solid-state supercapacitor and the other in flexible counter electrode in DSSC.

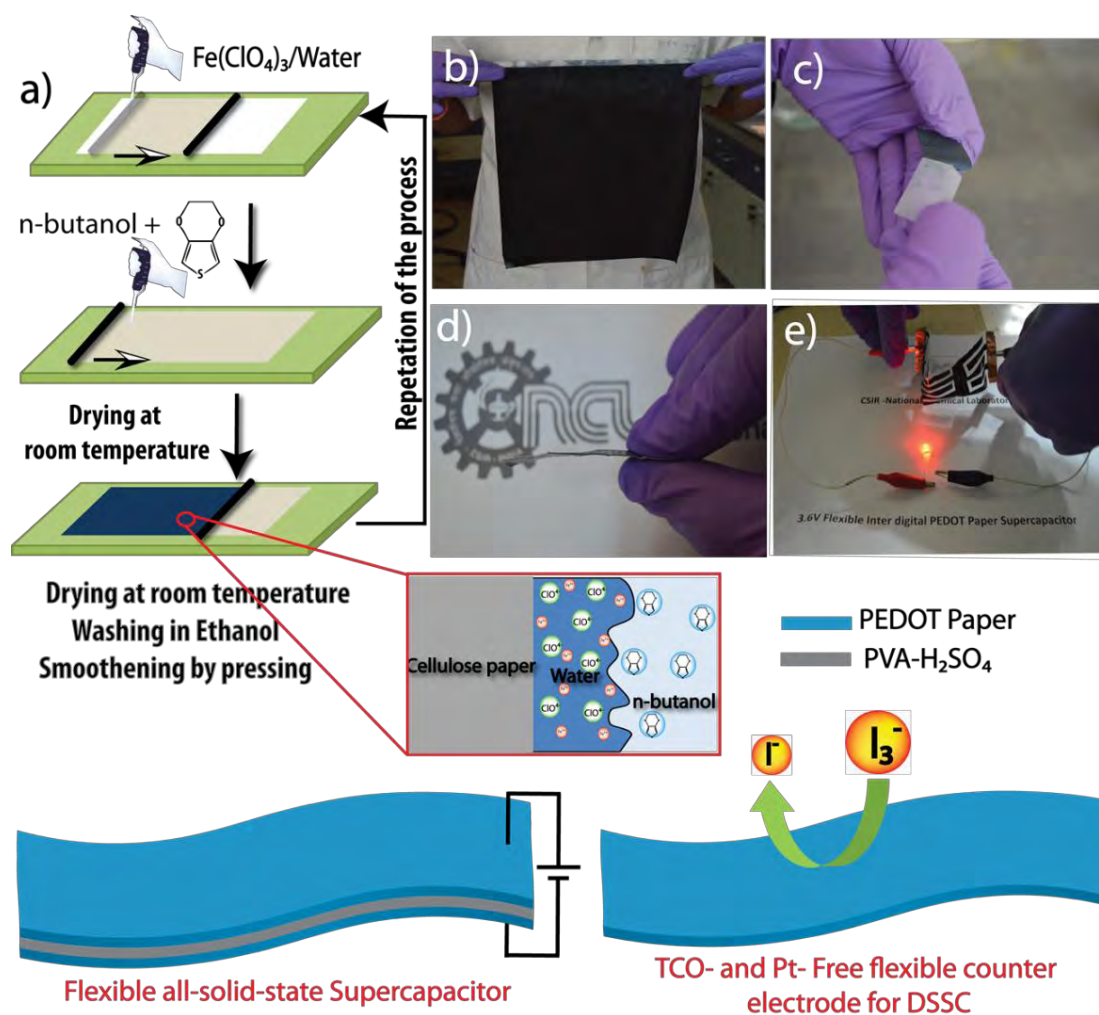


Figure 5.1: a) Schematic representation of the synthetic strategy adopted for the PEDOT-paper preparation, b) larger area PEDOT-paper (40 cm x 25 cm) made from the present strategy, c) an image showing the surface of a clean scotch tape after peeling it from PEDOT-paper surface, d) a flexible thin all-solid-state capacitor of thickness 0.17 mm made from the PEDOT-paper and e) an image of 3.6 V interdigital supercapacitor made from a single layer PEDOT-paper which glows an LED under flexible conditions.

5.2 Experimental Section

5.2.1 Materials

Ethylenedioxythiophene (EDOT) and iron perchlorate $[\text{Fe}(\text{ClO}_4)_3]$ were purchased from Aldrich Chemicals. n-Butanol was procured from Thomas Baker and cellulose paper was purchased from the local market. Polyvinyl alcohol (PVA) (M.W 1,15,000; 98-99 mol % hydrolysed) was supplied by Loba Chemie. Sulphuric acid (H_2SO_4) was procured from Rankem Chemicals. EDOT was distilled before usage. Other chemicals were used as received without any further purification. Carbon paper having a thickness of 0.3 mm was purchased from Toray. Coating was done by using RK K303 Multi Coater.

5.2.2 Preparation of the PEDOT Paper

In a typical preparation method, a cellulose paper having an area of 9 cm x 11 cm was placed over a bar coater and 340 mg of FeClO_4 in 0.5 ml water was coated over it using a rod with a groove spacing of 40 μm at a speed of 3 meter/minute. The paper was kept for drying at room temperature. Further, 25 μl of EDOT in 0.5 ml n-butanol was bar coated over $\text{Fe}(\text{ClO}_4)_3$ coated paper with the same speed. The paper was left for drying and polymerization. After 30 min, the paper was washed several times in ethanol until the excess $\text{Fe}(\text{ClO}_4)_3$ was removed. The paper was dried and smoothed by keeping in a press (Carver) at a pressure of 12 t for 2 min. For achieving a low sheet resistance, the process was repeated several times. From the second layer onwards, $\text{Fe}(\text{ClO}_4)_3$ was coated initially in n-butanol instead of water as the PEDOT layer is hydrophobic. After drying out the n-butanol, the paper was kept under a humidity chamber by maintaining a relative humidity of 70 % for 15 min. for allowing $\text{Fe}(\text{ClO}_4)_3$ to absorb water. Except this step, all the remaining processes were kept same as that of the first coating step.

5.2.3 Preparation of PVA- H_2SO_4 Solution and Film

1 g of PVA was dissolved with vigorous stirring at 85 $^\circ\text{C}$ for 2 h in 50 ml round bottom flask containing 10 ml of de-ionized water. The above solution was left for cooling to room temperature and at this stage, drop-wise addition of 1.0 g H_2SO_4 was carried out under stirring condition.

5.2.4 Prototype Flexible Supercapacitor Fabrication

The above prepared PEDOT paper was laminated using a PVA film (2 μm) by hot pressing at 120 $^{\circ}\text{C}$ for 2 min on the non-conducting side. The laminated PEDOT paper was then cut into pieces having specific areas (here 2.5 cm^2) and was coated with a PVA- H_2SO_4 solution using a bar coater. Small region was left vacant for giving electrical contacts. The space kept for the electrical contact in the butter paper was coated with Ag paste. For making interdigital supercapacitor, the PEDOT paper was cut into specific dimensions and sealed with PVA films. A 3-cell assembly was made in a single paper in series with a total size of 14 cm x 3.8 cm which includes the free space between the electrodes.

5.2.5 Characterization

Structure and morphology of the materials was analyzed by QuantaTM Scanning Electron Microscope and Nova Nano SEM 450. High-resolution transmission electron microscope (HR-TEM) analysis was carried out in Tecnai-T 30 at an accelerated voltage of 300 kV. Philips X'pert pro powder X-ray diffractometer (Cu $K\alpha$ radiation, Ni filter) was used for X-ray Diffraction (XRD). X-ray Photoelectron Spectroscopic (XPS) measurements were carried out on a VG Micro Tech ESCA 300 $^{\circ}$ instrument at a pressure of $> 1 \times 10^{-9}$ Torr (pass energy of 50 eV, electron take off angle of 60 $^{\circ}$ and the overall resolution of ~ 0.1 eV) Horiba JobinYvon Inverted Lab RAM HR800 VIS-NIR using 532 nm solid-state diode laser beam was used for Raman analysis. All the electrochemical studies were carried out in a BioLogic VMP3 multichannel Potentiostat-Galvanostat. The CV measurements were taken at different scan rates from 10 to 100 mV s^{-1} by maintaining a potential window of 1.2 V for single devices. The charge-discharge measurement was done at different current densities (0.5 to 10 mA) in the potential range of 0-1.2 V. Cycling stability was done by chrono charge-discharge method at a current density of 5 mA for 2500 continuous cycles, followed by 3800 cycles including bending and twisting modes. Electrochemical impedance (EIS) analysis was carried in an a.c frequency range of 106-0.01 Hz in the open circuit potential with a sinus amplitude of 10 mV ($V_{\text{rms}} = 7.07$ mV). All the EIS data were analyzed and fitted using an EC-Lab Software V10.19. Inter-digital flexible capacitor was tested by charge-discharge method at a current density of 0.5 mA in a voltage window of 3.6 V in bended, flexible and folded modes. Four-probe conductivity

meter having a probe spacing of 0.2 mm was used for the electrical conductivity measurements. Conductivity changes in the flexible conditions were measured by 2 probe method using linear sweep voltametry (LSV). Capacitance, energy density and power density were calculated using the equations used in Chapter 3 (Section 3.2.7)

5.2.6 Counter Electrode Characterization

The CV measurements were carried out in distilled acetonitrile containing 0.1 M LiClO₄, 5 mM LiI and 0.5 mM I₂ under N₂ atmosphere. A 3-electrode setup was used for the CV measurement in which the prepared counter electrode for DSSC was used as the working electrode and Pt wire which was internally calibrated using ferrocene/ferrocenium (Fc/Fc⁺) couple was used as the reference electrode. 0.64 cm² area of PEDOT-p working electrode was exposed to the electrolyte by masking the remaining portion with an adhesive tape. Pt foil was used as the counter electrode. Tafel measurements were done in a symmetrical cell in which the potential was polarised from -1 to +1 V at a scan rate of 10 mV s⁻¹.

5.2.7 Dye Sensitized Solar Cell (DSSC) Fabrication

The FTO working electrodes were washed by ultra-sonication in soap solution, deionized water and absolute ethanol. The P25 paste was doctor bladed on the washed FTO until 12-13 microns was achieved by multiple coatings, followed by annealing for 1 h. Following a previous method, TiCl₄ treatment was done over the working electrodes, followed by heating at 450 °C for 30 min. The working electrodes were soaked in 0.5 mM N719 dye solution for overnight. DSSCs were assembled using a sandwich assembly of the working electrode and flexible PEDOT counter electrode. The electrolyte used was a mixture of 1 M DMPII, 0.05 M LiI, 0.05 M I₂ and 0.5 M tert-butyl pyridine. I-V (current vs. voltage) measurements were done under Newport Solar Simulator attached to Keithley 2420 source meter.

5.3 Result and Discussion

A schematic representation of the synthetic procedure adopted here is shown in Figure 5.1a. One of the key highlights of the synthetic strategy adopted here is its scalability compared to the other reported methods. PEDOT film impregnated flexible paper (hereinafter called PEDOT-p) can be prepared in a scalable way by bar coating.

Photograph of a prepared PEDOT-p having an area of 40 cm x 25 cm is shown in Figure 5.1b. The PEDOT layer attains strong adhesion with the substrate as revealed from the scotch tape experiment (Figure 5.1c).

5.3.1 Conductivity Studies

Initially, the sheet resistance and conductivity were measured using the four-probe method. The sheet resistance obtained for PEDOT-p-1 is $26 \Omega/\square$ (Figure 5.2a), which could be further reduced up to $3 \Omega/\square$ (PEDOT-p-5) by multiple coating. For comparison, PEDOT was prepared by dissolving both EDOT and $\text{Fe}(\text{ClO}_4)_3$ in pure n-butanol on the cellulose paper (PEDOT-p-bulk) using the same protocol (details are given in the experimental section). Due to the poor control on the polymerization process in this case, the sheet resistance has been shoot up to $10 \text{ M}\Omega/\square$, compared to $24 \Omega/\square$ for PEDOT-1. The measured conductivity of PEDOT-p-5 is $375 \pm 25 \text{ S cm}^{-1}$ considering the thickness of the PEDOT film as $8 \pm 1 \mu\text{m}$, which is higher than the conductivity values reported in the recent literatures^[14b, 21]. For comparative studies, PEDOT powder was also prepared from pure n-butanol by normal solution method, which hereafter is termed as PEDOT-bulk. Compared to PEDOT-p-5 ($375 \pm 25 \text{ S cm}^{-1}$), the conductivity of PEDOT-bulk is only 30 S cm^{-1} . The observed low sheet resistance of PEDOT-p-5 is stable even after 90 days which was kept at ambient conditions (Figure 5.2b). This conductivity retention is far better than a previous report^[22] and the PEDOT prepared using a wet chemistry method, which was reported in our previous paper^[12a]. High hydrophobic nature of the PEDOT paper, which repels the water moisture from entering its matrix, helps for displaying the enhanced stability at the ambient conditions. Contact angle measurement supports its hydrophobic nature with a water contact angle of 131° , which is much higher than that displayed by PEDOT-bulk (55°) and the samples listed in the previous few reports^[23] (inset of Figure 5.2b). Further, *I-V* (current-voltage) measurement is found to be very stable, even with the twisted and bending conditions, where superimposed *I-V* of the PEDOT paper was obtained at various bending and twisting conditions (Figure 5.2c and 2d). The minimum sheet resistance obtained in the present case is $3 \Omega/\square$, which is much lower than the sheet resistance displayed by the present ITO and FTO coated glass plates ($7\text{-}14 \Omega/\square$) and Au sputtered substrates ($5 \Omega/\square$ for a 30-35 nm thick Au film)^[24]. Thus, such a low sheet resistance in flexible and twisted conditions, derived

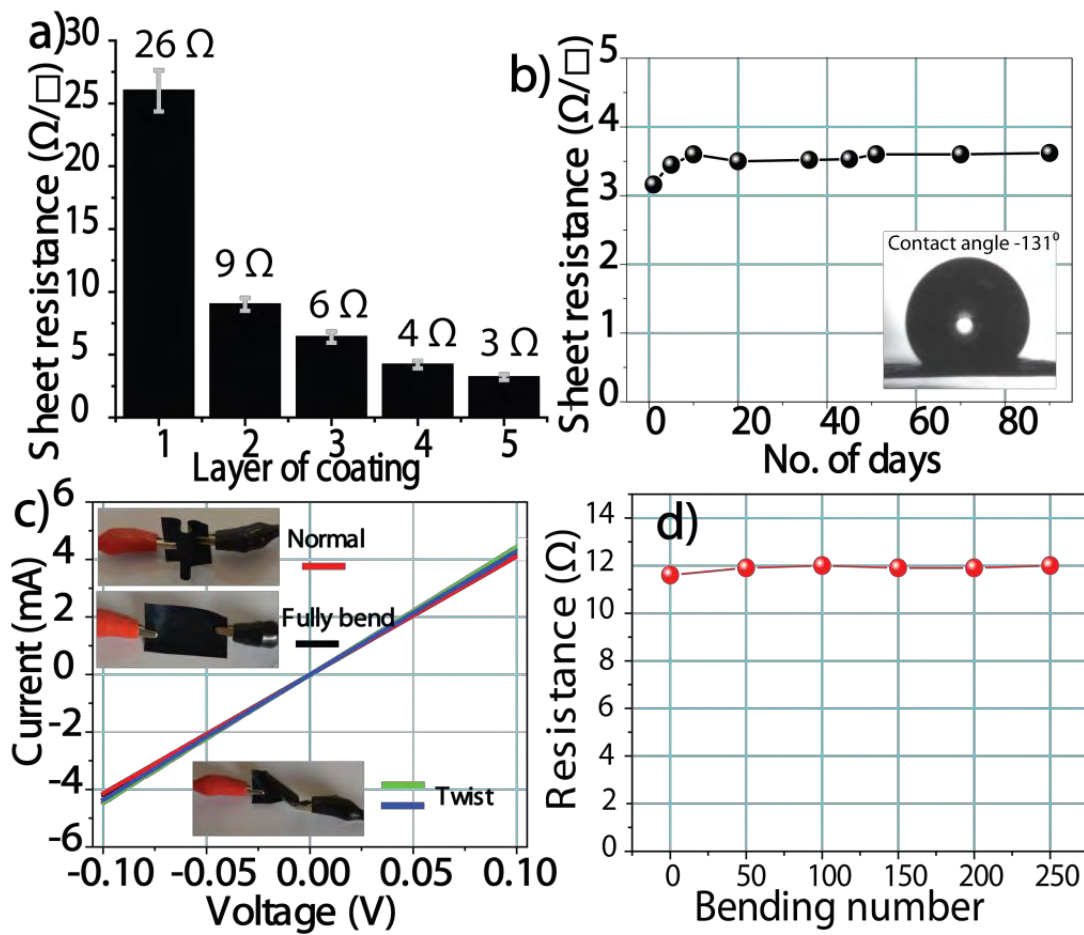


Figure 5.2:(a) Variation in sheet resistance with the number of layers of PEDOT on the paper, (b) a plot presenting the change in sheet resistance with respect to time, while maintaining the PEDOT paper under ambient conditions (the inset shows the contact angle of water on PEDOT-p-5), and (c) conductivity variations under various flexible conditions. (d) Changes in resistance with continuous bending cycles.

through simple scalable method, provides an essential characteristic to the material to serve as a potential candidate for flexible energy applications.

5.3.2 SEM and TEM Analysis

In order to understand the morphological characteristics of the interfacial polymerized PEDOT phase, the PEDOT paper along with the counter samples were analyzed initially with the help of a scanning electron microscope (SEM). Figure 5.3a shows the surface morphology of the bare cellulose paper, where the surface of the paper is found to have micron sized cellulose fibers. After the PEDOT coating, the surface morphology does not have any visible changes (Figure 5.3b and 3c). This is due to the

uniform coating of PEDOT along the cellulose fibers rather than at the vacant spaces. This can be explained from the hydrophilic interaction between the $-OH$ groups in the cellulose with $Fe(ClO_4)_3$. This eventually helps the PEDOT for maintaining polymerization only on the fiber surface. Due to the same reason, the formed PEDOT displays strong adhesion to the substrate in such a way that the polymer layer could withstand while trying to peel it out with the help of a scotch tape (Figure 5.1c). This type of strong interaction is not observed in most of the PEDOT films formed by the conventional ways due to the lack of any interaction between the substrates and the PEDOT films. Figure 5.3d shows the SEM surface images corresponding to the PEDOT-p-bulk. It is clearly visible in this case that the PEDOT is not formed uniformly, rather, it has short and orderless bulk PEDOT structure with relatively low yield. Further, Transmission Electron Microscopy (TEM) images in Figure 5.3e & 5.3f reveal that the PEDOT formed during the interfacial polymerization possess 3-D porous structures.

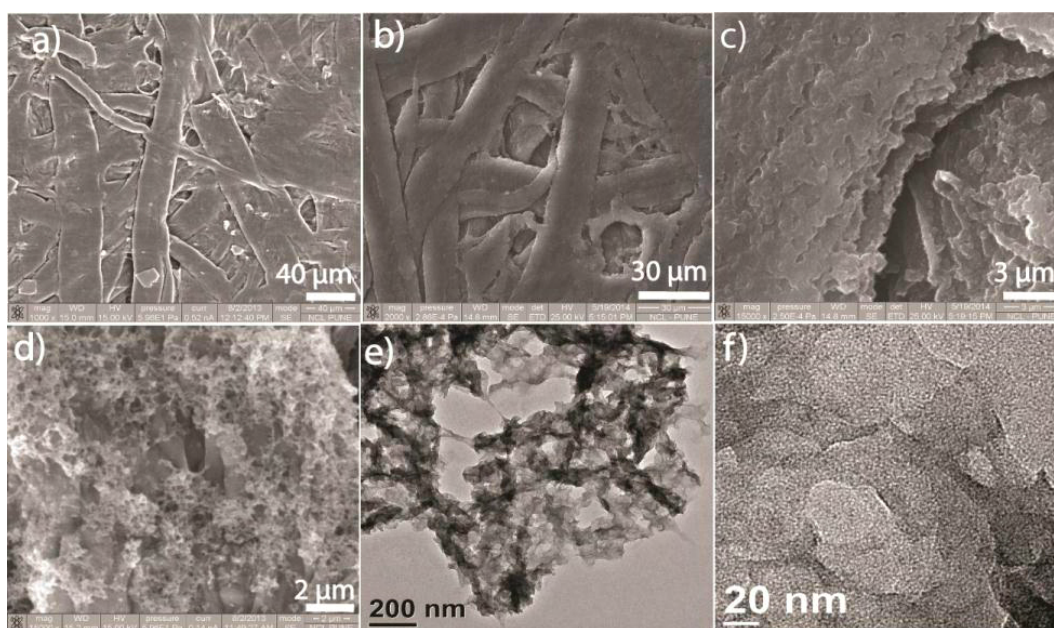


Figure 5.3: SEM images of a) bare cellulose paper, b) & c) PEDOT-p-5 formed by interfacial polymerization, d) PEDOT-p-bulk formed when complete reaction happened in pure *n*-butanol and e) and f) TEM images of the PEDOT formed through interfacial polymerization.

5.3.3 XRD Analysis

Further, to analyse the structural difference of the interfacial polymerized PEDOT (PEDOT-p-5) with PEDOT-bulk, X-ray Diffraction (XRD) analysis was carried out. XRD spectra (Figure 5.4) show two strong peaks at 15.7° (110) and 22.5° (002) for the cellulose paper, which are the characteristic peaks of cellulose^[25]. Apart from the above peaks, characteristic peaks of PEDOT at 6.7° and 26.3° , corresponding to the (100) and (020) planes, respectively, are visible in PEDOT-p-5 and PEDOT-bulk. The (100) spacing is in relation with the inter- π -conjugated chain distance of the stacked PEDOT polymer^[26]. Interestingly, the relative intensity of the (100) to (020) planes is higher in PEDOT-p-5 compared to that in PEDOT-bulk. This serves as an indirect evidence for the existence of more ordered PEDOT chains in PEDOT-p-5, which helps for the better inter-chain interaction and, thereby, efficient charge-hopping between the chains^[26b, 26c, 27] compared to PEDOT-bulk.

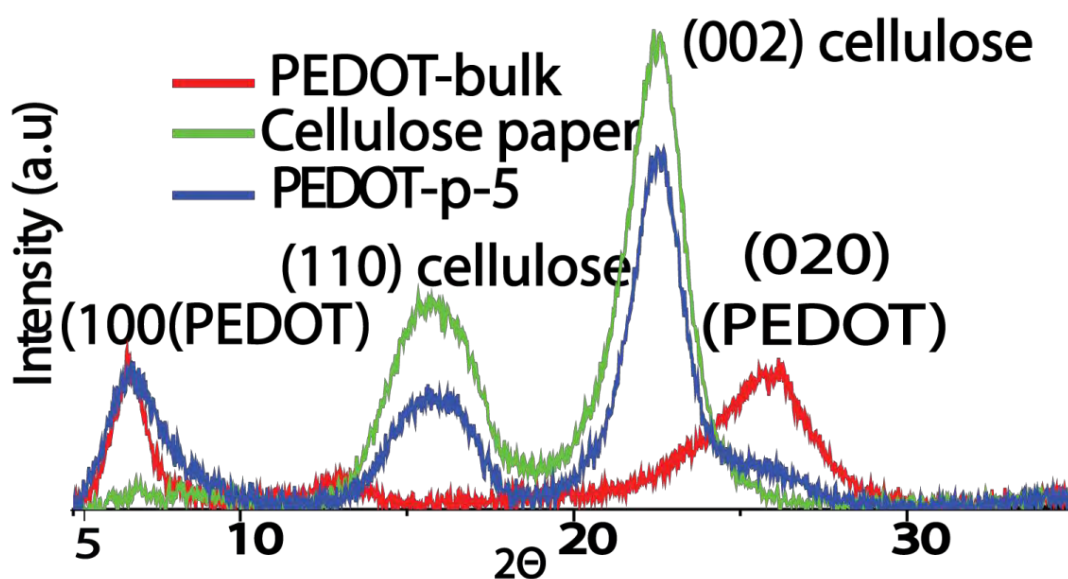


Figure 5.4: XRD spectra of various samples.

5.3.4 XPS Analysis

Extent of removal of electron from the neutral π -conjugated polymer chains primarily decides the conductivity. Such a creation of positive charges in the polymer backbone is balanced by the counter ion which is known as the dopant. Thus, increased delocalized mobility of charges in the polymer helps for enhanced conductivity. Conclusive evidence about the level of doping has been obtained from

the sulphur XPS spectra of PEDOT-p-5 and PEDOT-bulk presented in Figure 5.5a and 5b, respectively. The deconvoluted peaks appeared at 162.3 and 163.6 eV correspond to the S2p_{3/2} and S2p_{1/2} states, which show a ratio of 2:1 for the area under the peak and a B.E difference of 1.3 eV^[28]. The third peak (166.3 eV) corresponds to the partially oxidised sulphur (S^{δ+}), which is balanced by the doped counter ion ClO₄⁻ or Cl⁻^[29]. Remarkable difference is found in the relative intensity of S^{δ+} with neutral S in PEDOT-p-5, indicating the pronounced doped counter ion. Quantification of the doping level is done by taking the ratio of the area under the peaks of Cl 2p to S 2p, which is found to be 0.32 in case of PEDOT-p and 0.23 for PEDOT-bulk (Table 5.1 and 5.2)^[29]. This is re-confirmed by the ratio of the area under the peak of S^{δ+} to the total area of S2p, which is found to be similar to the previous values (PEDOT-p-5 (0.32) and PEDOT-bulk (0.23)). Increased doping level, which is higher than the reported values^[21b, 29-30] and is close to the theoretical maximum doping level (0.33) of PEDOT, substantiates the observed high conductivity of the interfacial polymerized PEDOT-p-5 compared to PEDOT-bulk. However, the measured conductivity of 375 S cm⁻¹ of PEDOT-p-5 is less compared to the other reported PEDOT films^[22, 31] (where the film thickness is < 1000 nm) due to

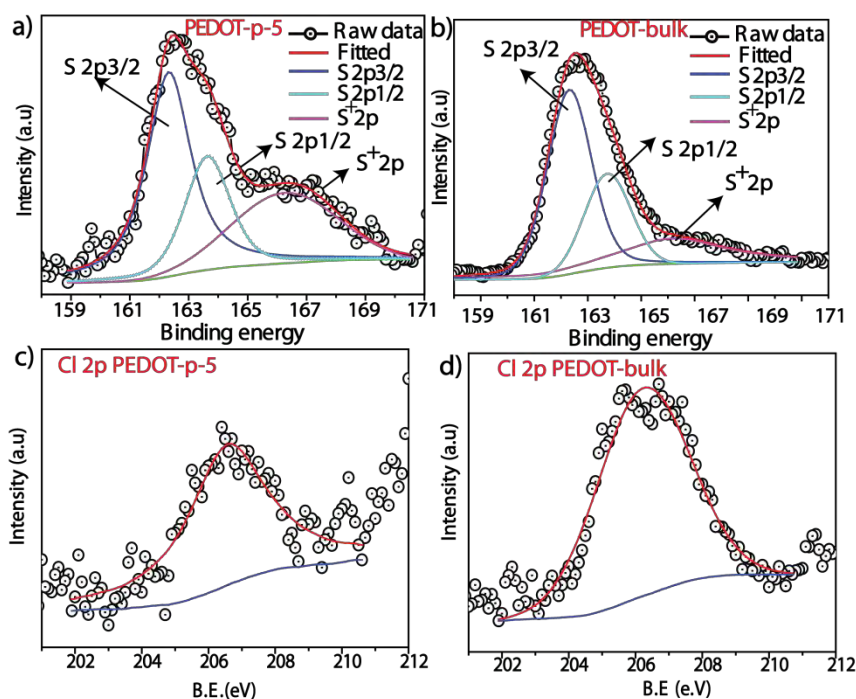


Figure 5.5: S2p XPS spectra of a) PEDOT-p-5 and b) PEDOT-bulk. Cl2p Spectra of c) PEDOT-p-5 and d) PEDOT-bulk.

the grain boundary resistance arises in the relatively thick (8 μm thick) PEDOT film in the present case. However, high conductivity ($> 1000 \text{ S cm}^{-1}$) could be observed in the case of PEDOT-p-1, which possesses a relatively thin film of PEDOT compared to that in PEDOT-p-5. However, for practical usage, the sheet resistance is found to be more critical rather than the conductivity.

Table 5.1: Peak parameters of PEDOT-p-5.

Peak	Position (eV)	Area	FWHM (eV)
0 (S2p 3/2)	162.32	2983.91	1.79
1(S2p 1/2)	163.63	1421.95	3.62
2 (Sδ^+)	166.27	2026.22	4.29
Cl 2p	206.55	2702.51	2.84

Table 5.2: Peak parameters of PEDOT-bulk.

Peak	Position (eV)	Area	FWHM (eV)
0 (S2p 3/2)	162.31	12945.40	1.95
1(S2p 1/2)	163.73	6291.28	2.03
2 (Sδ^+)	166.20	5619.56	4.57
Cl 2p	206.23	7880.31	3.27

Doping level is calculated by the following two methods.

First method: By taking the ratio of the area under the peak of Cl 2p to S 2p.

$$\text{Doping level} = (\text{Area of Cl 2p/ASF of Cl 2p}) / (\text{Area of S2p/ASF of S 2p})$$

ASF (atomic sensitivity factor, which is 0.54 for S 2p and 0.73 for Cl 2p)

Second method: Doping level = Area under the peak of S δ^+ / Total area under the peak of S 2p

5.3.5 UV-Visible Spectral Analysis

Increased doping/electron removal creates more delocalized charges in the polymer backbone and raises the highest occupied molecular orbital (HOMO) position which leads to more of metallic conduction^[32]. Reduction in the band gap during the doping creates a red shift in the absorption and can be probed by UV-

visible spectra^[33]. As expected, in the interfacial polymerized PEDOT, a clear red shift has been observed in the maximum absorption region due to higher doping compared to PEDOT-bulk (Figure 5.6). Insufficient doping in PEDOT-bulk could also be confirmed from the less intense peak at around 560 nm, which is a trademark of the π - π^* transition of neutral PEDOT^[29, 34], and will vanish after complete oxidation as occurred in the interfacial polymerized PEDOT sample. In conclusion, XPS and UV-visible spectra serve as evidences of increased level of doping, which helps for the charge delocalisation, resulting in improved conductivity. Also, the more ordered PEDOT chains in PEDOT-p-5 is helping for the efficient inter-chain charge hopping as substantiated by XRD. Thus, the above two critical factors help for PEDOT-p-5 to achieve a high conductivity of 375 S cm⁻¹ compared to 30 S cm⁻¹ obtained for PEDOT-bulk. Further, the ordered polymer chains as confirmed by XRD also explain the hydrophobic nature of PEDOT-p.

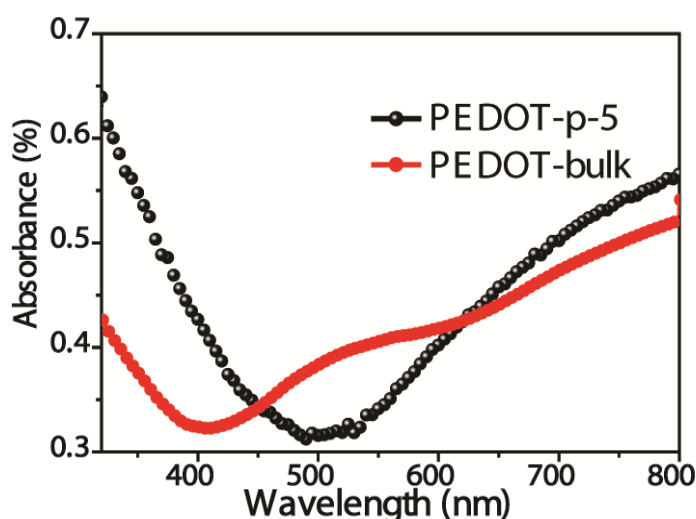


Figure 5.6: UV-visible spectra of PEDOT-p-5 and PEDOT-bulk.

5.3.6 Mechanism of Interfacial Polymerization

Even though interfacial polymerization is common for polyaniline^[35], polypyrrole^[36] and polythiophene^[37], few reports on the interfacial polymerization are available for PEDOT. Most of the reports utilize surfactants^[38], however, surfactant always has a negative impact on the conductivity of the formed PEDOT. Yang *et al.*^[39] prepared semiconducting PEDOT nano-needles at a water/dichloromethane interface. However, lengthy reaction time (3 days) and poor yield are the main limitations of such a method. Images shown in Figure 5.7 give insights on the

mechanism of interfacial polymerization in the cellulose paper. In Figure 5.7 I to 7 III, the experiments were carried out by changing the concentration of the monomer (EDOT) from 0.46 mM to 1.84 mM in n-butanol, while keeping 4 times higher molar concentration for $\text{Fe}(\text{ClO}_4)_3$ in water with the monomer. n-Butanol/EDOT was further added slowly through the walls of a vial to the aqueous phase. In Figure 5.7 Ia, even after 5 min, there is no visible polymerization happens as there is very less interface is available, and, overall the polymerization rate is found to be less. No bulk polymerization is found in the organic phase as there is no diffusion of $\text{Fe}(\text{ClO}_4)_3$ from the aqueous phase to the organic phase owing to the less solubility of $\text{Fe}(\text{ClO}_4)_3$ in n-butanol compared to water. Possible interfacial polymerization rate is very less under static condition, even though it can be increased further by shaking, which creates large number of droplets of n-butanol inside the aqueous phase. Figure 5.7 Ib & Ic show the presence of PEDOT, which is formed at the interface of the droplets after the shaking and joining together during settling. It can be seen that some PEDOT is formed in the organic phase as well, which is obvious due to the diffusion of $\text{Fe}(\text{ClO}_4)_3$ into the organic phase during the shaking process.

While going from low to high concentration, bulk polymerization in the organic phase is happening at a faster rate, which is due to the easy diffusion of the high concentrated $\text{Fe}(\text{ClO}_4)_3$ from water to the organic phase through the interface. This gradual change is visible from Figure 5.7 I-III. Thus, concentration has a key role in the surfactant-free interfacial polymerization carried out here. Hence, an EDOT concentration of 0.46 mM was used, which will preferably result in the interfacial polymerization. However, lengthy reaction time as well as poor yields (Figure 5.7 I) makes the pot synthesis less viable choice. High concentration can result in higher yield, but the bulk polymerized PEDOT will be predominant in such cases (Figure 5.7 III). For comparison, PEDOT formation in pure n-butanol has also been carried out (Figure 5.7 IV), and the reaction is found to be very fast as compared to that in aqueous/organic mixture while maintaining the same concentration. The conductivity of the formed PEDOT formed in this case is measured and is found to be 10 times lesser than PEDOT-bulk (31 S cm^{-1}) compared to PEDOT-p-5

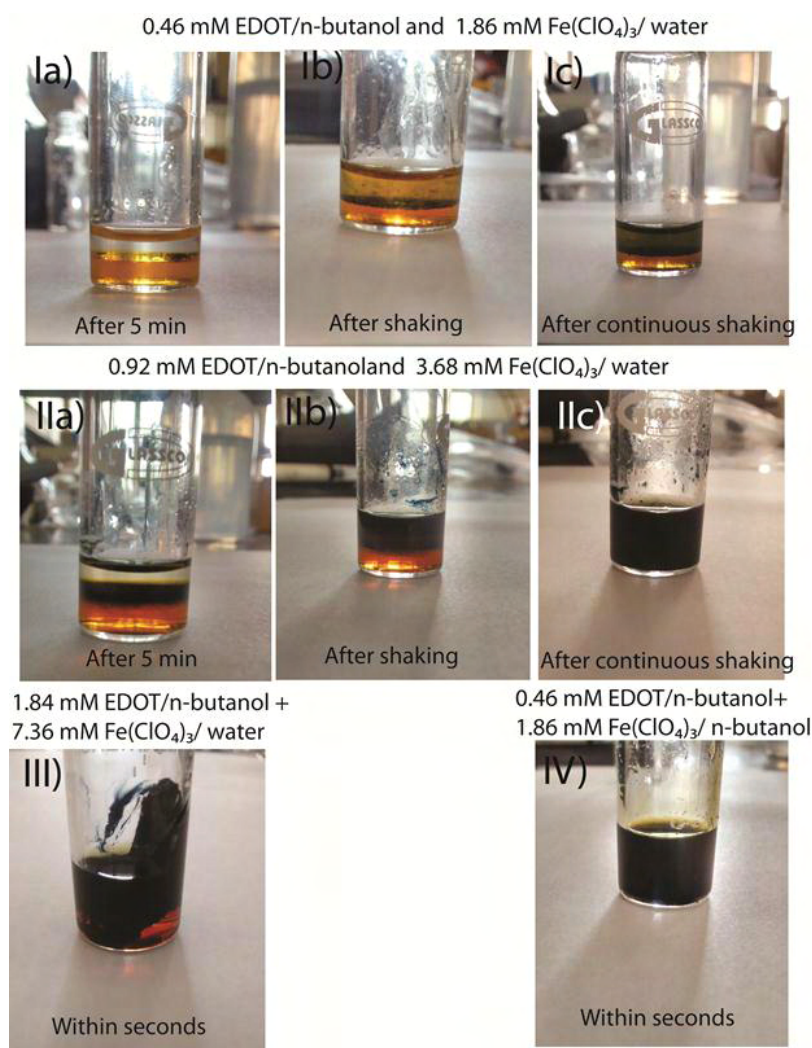


Figure 5.7: Pot syntheses of PEDOT in various conditions: I) 0.46 mM EDOT, II) 0.92 mM EDOT, III) 1.84 mM EDOT in n-butanol after adding to $Fe(ClO_4)_3$ /water solution and IV) formation of PEDOT in n-butanol by mixing 0.46 mM EDOT with $Fe(ClO_4)_3$ in n-butanol.

By transferring the experiments (Figure 5.7 I) judiciously on a cellulose paper, formation of extremely uniform and highly conducting interfacial polymerized PEDOT in short duration with excellent yield could be ensured. This is clearly due to the dominance of the interfacial polymerization compared to the bulk polymerization resulted from the enhanced interface formed along the cellulose fibers having thin layer of water layer. However, increasing the concentration can result in bulk polymerization in this case. Figure 5.7 clearly elucidates this difference. When 4 times higher concentration of $Fe(ClO_4)_3$ was used instead of multi-layer coating, $Fe(ClO_4)_3$ easily diffuses to the organic phase and triggers polymerization there. This results in higher sheet resistance for the formed PEDOT.

After optimising the concentration of $\text{Fe}(\text{ClO}_4)_3$ to 0.46 mM from the previous experiments, coatings were carried out on cellulose paper having an area of 9 cm x 11 cm. Figure 5.8 shows the sheet resistance data of the various experiments. In Sample I, the reaction was carried out in pure n-butanol and as found previously in the case of pot synthesis (Figure 5.7 IV), the present process resulted into low conducting PEDOT. The paper is showing a sheet resistance of around $10 \text{ M}\Omega/\square$ and this high value is associated with the low yield of PEDOT as well as its low conductivity. On the other hand, when $\text{Fe}(\text{ClO}_4)_3$ in n-butanol was coated initially on the cellulose paper, followed by EDOT/n-butanol (Sample II), drastic improvement in the conductance has been observed and the sheet resistance is found to be decreased to $32 \Omega/\square$. This improvement is clearly attributed to the hydrophilic nature of $\text{Fe}(\text{ClO}_4)_3$, which absorbs moisture after removal of n-butanol, leading to the triggering of the interfacial polymerization. In this case, it is observed that the sheet resistance was varying according to the humidity conditions in the atmosphere. Sample III (PEDOT-p-1) was derived purely through interfacial polymerization which resulted in very low sheet resistance among the all samples as $\text{Fe}(\text{ClO}_4)_3$ was dissolved in water. As found in the previous case of pot synthesis, the concentration of $\text{Fe}(\text{ClO}_4)_3$ plays a crucial role for confining $\text{Fe}(\text{ClO}_4)_3$ in the aqueous phase (Figure 5.7). Thus, the preferred interfacial polymerization helps to achieve very low sheet resistance. In Sample VII, the same combination as that of Sample III was used and the only difference was that EDOT/n-butanol was coated initially on the cellulose paper which was followed by coating of FeClO_4 in the aqueous phase. As expected, there is no polymerization occurring in the aqueous phase due to the insolubility of EDOT in this phase.

One question can be arisen in this context as what about the conductivity of PEDOT produced in a solvent where both EDOT and $\text{Fe}(\text{ClO}_4)_3$ are soluble and possessing high dielectric constant and polarity (e.g. acetonitrile, $\epsilon = 37.5$, $D = 3.9$) compared to butanol? To answer this, a similar experiment in acetonitrile (Sample IV) was also carried out. Due to the relatively fast polymerization in this case, non-uniform polymer film over the cellulose paper has been formed and displayed a conductivity value which is substantially lower than that of the polymer formed by the interfacial polymerization process. However, the PEDOT synthesised in acetonitrile is superior in terms of the conductivity ($38 \Omega/\square$) compared to the PEDOT formed in pure n-butanol ($10 \text{ M}\Omega/\square$). This is due to the high dielectric constant in the former

case, which helps for better doping of the counter ions in PEDOT. There is no possibility of interfacial polymerization in water/acetonitrile combination, as the both solvents are miscible with each other and such an experiment rather results into a sample possessing high sheet resistance (Sample V). This further confirms that, not only high dielectric constant but interfacial polymerization (which slows down the polymerization rate) also is crucial for better attaining chain packing and doping for ensuring an overall improvement on the conductivity of the PEDOT.

Second question that can arise is, what will the outcome of a PEDOT formed through interfacial polymerization at an interface of water with another immiscible solvent (like hexane)? Sheet resistance of PEDOT-p formed at the interface of water/hexane (Sample VI) is $38 \Omega/\square$, which is far less than that of Sample I which is formed in butanol ($10 \text{ M}\Omega$). However, the above value is still less than that measured on the water/butanol based system due to the low dielectric constant of the total interface compared to the later. In conclusion, butanol/water at proper concentration gives pure interfacial polymerization at a boundary which possesses highest dielectric constant in total compared to the other combinations experimented here. Further, this polymerization yield is many folds higher in the cellulose paper due to the enhanced surface area on the fibers.

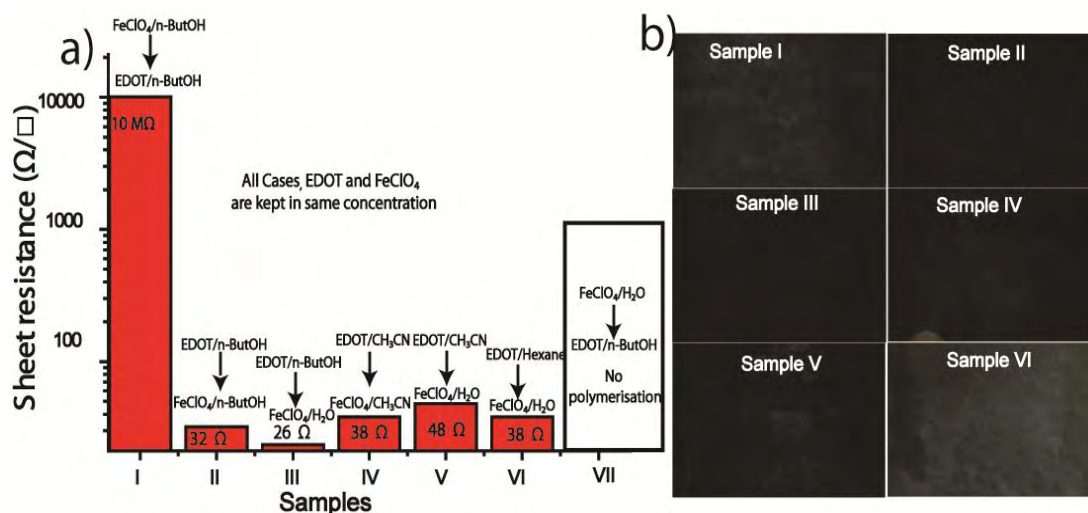


Figure 5.8: a) PEDOT polymerization on the cellulose paper through various solvent combinations and b) optical images of the corresponding PEDOT papers.

As Suh *et al.*^[26b] reported, a solvent with high dielectric constant or polarity results in a polymer with high conductivity due to efficient chain packing as well as

hydrogen bonding between the counter ions associated with the polymer. In case of n-butanol (dielectric constant $\epsilon = 18$ and dipole moment $D = 1.63$), the low dissociation $\text{Fe}(\text{ClO}_4)_3$ results in disordered polymer packing as well as less doping, which result in low conductivity for PEDOT-bulk. Compared to this, in the case of polymerization at the water/butanol interface, high dielectric constant ($\epsilon = 80$) and polarity ($D = 1.85$) of water assist for better packing of the π -conjugated chains and more doping due to the intervention by the hydrogen bonding^[26b, 27a]. Apart from the high dielectric constant, slow polymerization happens at the interface further helps for the generation of better packed and doped polymer chains^[17]. Total polarity of water/n-butanol interface is much higher than the other immiscible interface such as water/hexane (Figure 5.8) or water/DCM, which results in higher conductivity of the polymer formed in the former case. As the EDOT is insoluble in water and the solubility of $\text{Fe}(\text{ClO}_4)_3$ in butanol is relatively low, polymerization mainly occurs at the interface, resulting in the formation of highly doped and more crystalline PEDOT. Thus, concentration of $\text{Fe}(\text{ClO}_4)_3$ has a key role in confining the polymerization at the interface (Figure 5.7 and Figure 5.8). It should be noted that, the relative interface formed between the two immiscible liquids on the cellulose paper will be many times larger than that derived through the pot synthesis due to the large accessible surface area in the former case. Chance of the bulk polymerization in the remaining bulk n-butanol phase will be very less due to the less solubility of $\text{Fe}(\text{ClO}_4)_3$ in butanol and further most of the $\text{Fe}(\text{ClO}_4)_3$ will be utilised at the interface during the diffusion. Here, one of the key highlights of our work lies in the fact that the process involving interfacial polymerization on the cellulose paper surface is highly scalable for practical applications (Figure 5.1a).

As PEDOT-paper could prove its excellent conductivity under flexible conditions along with long-term stability, validation of its application in a realistic perspective will be more interesting. PEDOT is known for its applications as electrodes in supercapacitors (theoretical capacitance is 210 F g^{-1}) and counter electrode in DSSC. In line with these thoughts and considerations, the applications of the PEDOT-paper for making a solid-state supercapacitor and counter electrode for DSSC are demonstrated. A discussion on these demonstrations is given in the following sections.

5.3.7 Application in Flexible Solid-State Supercapacitor

For flexible solid-state-supercapacitor, PVA-H₂SO₄ gel electrolyte was used as the electrolyte, which was prepared by following the procedure reported in Chapter 3.2.2. PVA-H₂SO₄ was coated onto PEDOT-p using the roll coating procedure. Enough time was given for drying to ensure intercalation and proper wetting by the gel electrolyte inside the PEDOT matrix. Two pieces of PEDOT-p having a size of 2.5 cm² each were sandwiched together to form a device. Electrochemical charge-storage properties were measured using cyclic voltammetry (CV), chrono charge-discharge method (CD) and electrochemical impedance analysis (EIS). CV and CD were carried out in a higher potential window of 1.2 V, which helps the system to achieve high energy density. Figure 5.9a and 9b show the CV and CD profiles obtained from the solid-state devices made from PEDOT-p-1 to PEDOT-p-5.

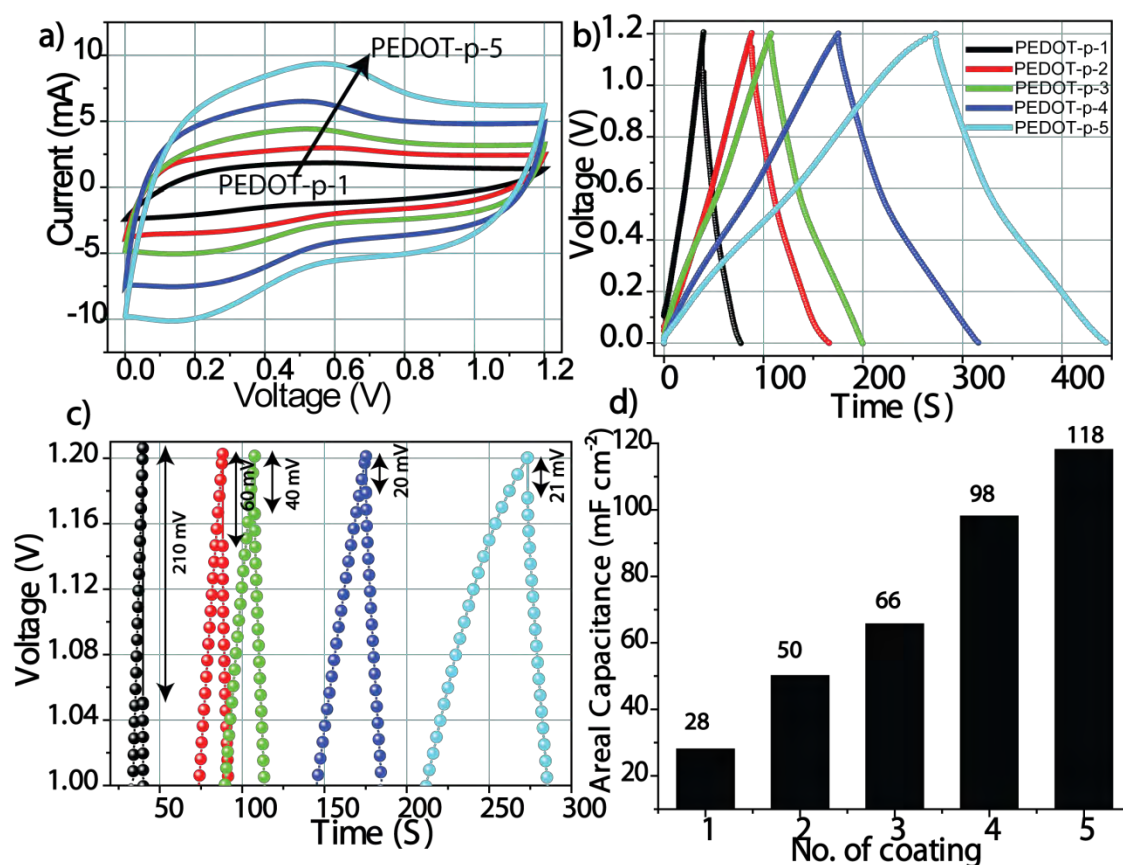


Figure 5.9: a) Cyclic voltammograms recorded at 50 mV s⁻¹, b) charge-discharge (CD) profiles of PEDOT-p taken at a current density of 0.4 mA cm⁻² with different layers of the PEDOT coating, c) enlarged view of the CD profiles given in 'b' indicating the differences in the IR drop and d) areal capacitance measured for the various PEDOT-p.

Capacitance properties are found to improve linearly with increasing the PEDOT layer (28 mF cm^{-2} to 115 mF cm^{-2}) in the paper as expected due to the progressively reduced sheet resistance (Figure 5.9d). The PEDOT amount on PEDOT-p-5 is around 1 mg cm^{-2} and the corresponding mass specific capacitance is estimated to be 115 F g^{-1} (Figure 5.10a), which is substantially higher than that of PEDOT-bulk (60 F g^{-1}) (tested by coating on a carbon paper, Figure 5.10b). By considering the weight of the cellulose paper into account, the capacitance of the electrode has been calculated as 20 F g^{-1} . Considering the highest capacitance registered by the system derived from PEDOT-p-5, detailed investigations are restricted by focusing on this system. Rather than mass specific capacitance, it is desirable to state the capacitance in volumetric and areal density basis, as they are the two important parameters for judging the feasibility of the material for practical usage. A volumetric capacitance of 144 mF cm^{-3} is obtained at a current drag of 0.5 A cm^{-3}

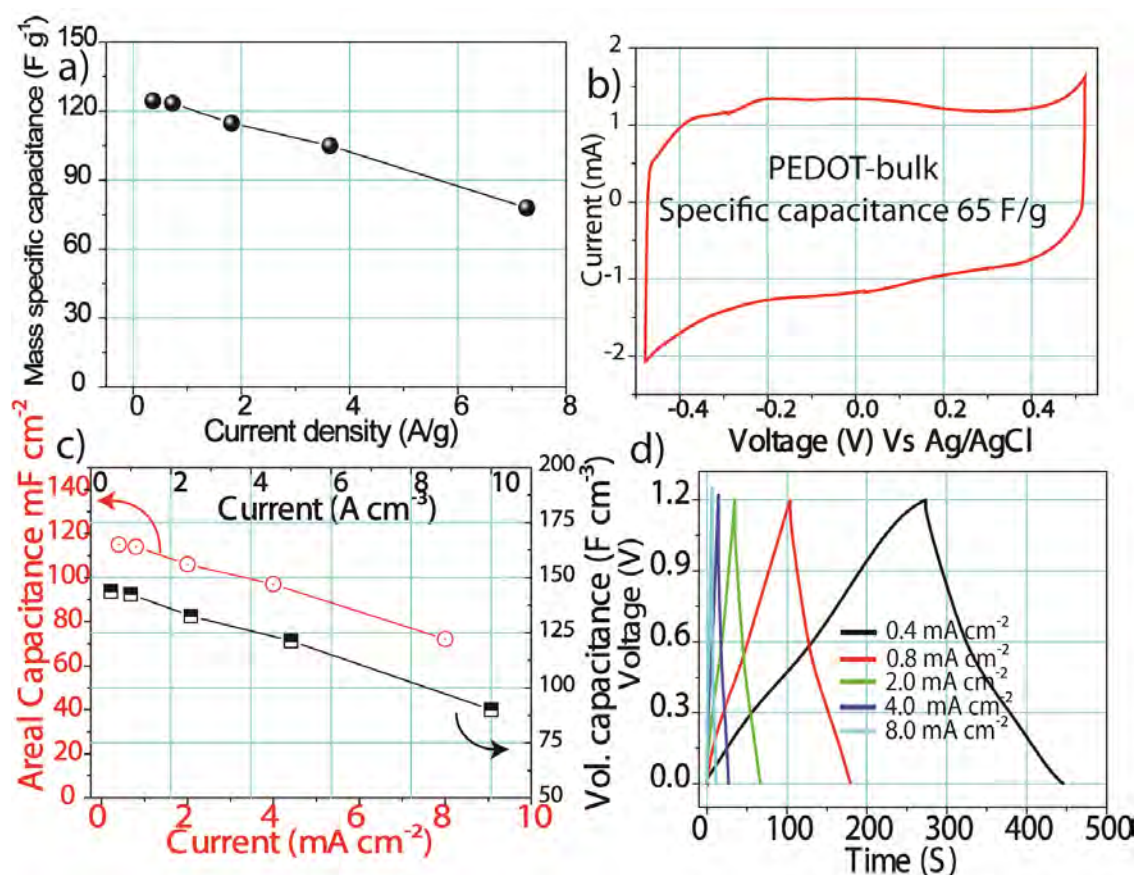


Figure 5.10: a) Mass specific capacitance of PEDOT-p-5 at varying current density values, b) CV profile at 10 mV s^{-1} of PEDOT-bulk coated on a solid current collector, c) CD profiles of PEDOT-p-5 taken at various current densities and d) graphical representation of the capacitance changes of PEDOT-p-5 with respect to the varying current density values.

by considering the thickness of PEDOT as 8 μm in PEDOT-p-5 (Figure 5.10c). Considering the total thickness of the electrode, the measured volumetric capacitance is estimated to be 35 F cm^{-3} . Even at a high current drag of 10 A cm^{-3} , the present system retains up to 90 mF cm^{-3} (Figure 5.10e), indicating the superior power rate of the device. Apart from the high conductivity of PEDOT ($> 375 \text{ S cm}^{-1}$), the porous structure of PEDOT as found in the TEM images is also appeared to be helping in maintaining the high capacitance by achieving high electrode-electrolyte interface during the intercalation of the polymer gel electrolyte^[40]. In addition to the improvement in capacitance, the electrochemical series resistance (ESR) measured from the IR drop in the CD profiles (Figure 5.5c) is found to be going down as expected with the number of PEDOT coating.

EIS is one of the effective tools in analysing the charge storage properties by measuring the response of the system to the varied a.c frequency. Fitted Nyquist plot of the flexible device made from PEDOT-p-5 is shown in Figure 5.11a. As that of an ideal capacitor, the Nyquist plot shows a linear behaviour by intersecting the x-axis at the high frequency region and aligning parallel to the y-axis at the low frequency region with a small deviation. ESR measured is found to be 6.5Ω , which is far better than the flexible supercapacitors reported recently in the literature^[3, 41]. This measured ESR is promising for a thin capacitor which does not contain a separate current collector. It should be noted that hardly any semicircle loop corresponding to the charge-transfer resistance is found at the high frequency region of the Nyquist plot (inset of Figure 5.11a). Without using any conducting current collector, achieving an ideal Nyquist plot as obtained in the present case validates the very low sheet resistance of the PEDOT paper resulting from the high conductivity of the interfacial polymerized PEDOT. This is concomitantly assisted by the proper sink of the gel electrolyte with the porous PEDOT. It is also noted that the capacitance is linearly increasing with the loading of PEDOT (*i.e.* from PEDOT-p-1 to PEDOT-p-5), indicating the ability of PVA-H₂SO₄ to penetrate through the porous PEDOT phase.

Further, the devices have undergone stringent stability tests at various bending and flexible conditions. Initially, the CD profile at various bending and twisted conditions (Figure 5.11b) was measured and the data is found to be closely superimposable. Due to the highly flexible nature of the individual components like cellulose, PEDOT and

PVA-H₂SO₄ gel, the device appears quite robust to the various flexible conditions. Further, long-term stability test was carried out under normal condition for 2500 cycles by applying continuously a current density of 2 mA cm⁻². The performance of the system is found to be very stable (~9 % degradation) while maintaining high coulombic efficiency (~99 %) throughout the cycles. Long-term cycle stability of the devices at various bending and twisted conditions also was monitored and was found to be very stable even after 3800 cycles (Figure 5.11c and 1d). Small reduction found in capacitance is due to the loss of water from the gel due to the heat generation

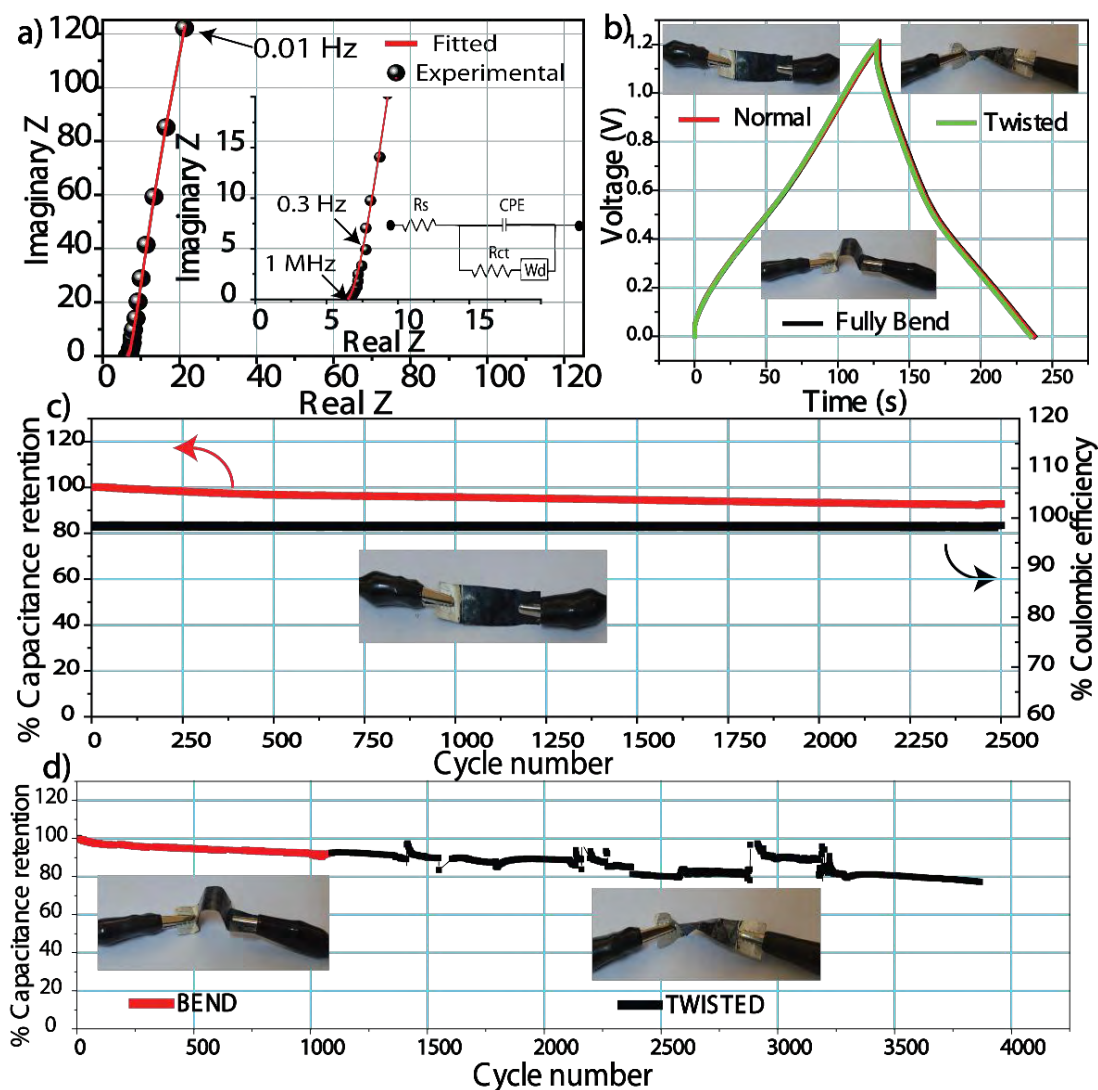


Figure 5.11: a) Nyquist plot of the flexible device made from PEDOT-p-5 with the enlarged high frequency region along with the circuit diagram is given in the inset, b) CD profile of PEDOT-p-5 at a various bending and flexible conditions and c) -d) represent the long-term cycle stability data.

during the cycles, which is in accordance with the observations in Chapter 3 (Figure 3B.10).

The energy density and power density of the device are calculated and the values are tabulated in the form of a Ragone plot in Figure 5.12b. A maximum energy density of 28 mWh cm^{-3} is obtained for PEDOT. The calculated the energy density by considering the whole device thickness (0.17 mm, Figure 5.12b) is found to be $\sim 1 \text{ mWh cm}^{-3}$ at a power density of 52 mW cm^{-3} and the system could retain an energy density of 0.61 mWh cm^{-3} even at a higher power drag condition of 1 W cm^{-3} . As it was mentioned earlier, large scale production of PEDOT paper is simple and can be improvised into various designs and shapes. It should be noted that the total device thickness is only 0.17 mm which includes electrode and electrolyte in the integrated form. The thickness can be further reduced by reducing the thicknesses of the polymer electrolyte (0.1 mm) and cellulose paper (0.6 mm), which come around 90 % of the total thickness in the present device. An inter-digital flexible solid-state-supercapacitor is made from a PEDOT paper with a working potential of 3.6 V (Figure 5.1e and 12a). The device consists of 3 capacitors connected in series in a single PEDOT paper, where, the PEDOT phase itself acts as the electric connector between them. The CD profile of the device is shown in Figure 5.12a and the image of a glowing L.E.D using the device in the flexible condition is shown in the inset of Figure 5.12a. Similar to the sandwiched supercapacitor, the inter-digital supercapacitor has also been found to be very stable to the flexible conditions, where

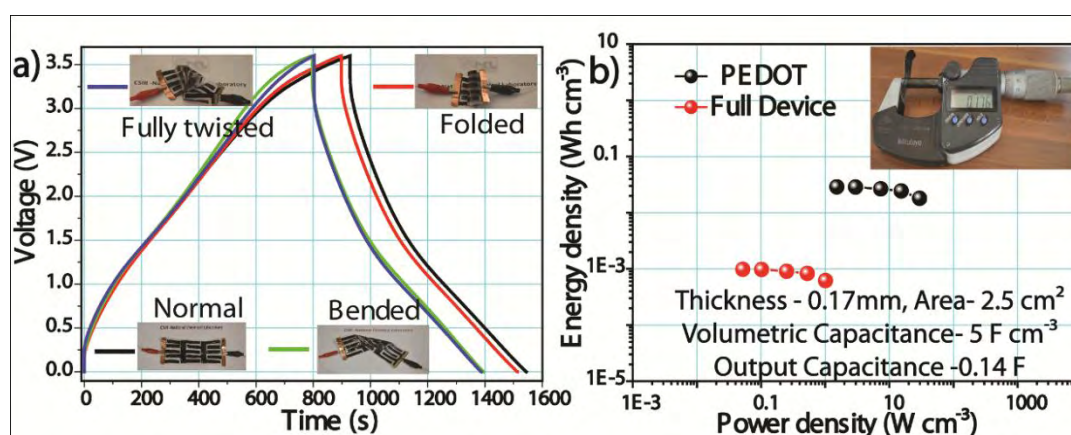


Figure 5.12: a) CD profiles of the inter-digital supercapacitor in a voltage window of 3.6 V at various bending and flexible conditions and b) Ragone plot; inset image shows the thickness of the sandwiched device.

the CD profiles are superimposable in the bending and twisting conditions. This gives a confidence that the method of preparation of the highly conducting PEDOT-p as illustrated here can be further extended to screen printing and can be used to prepare designer flexible supercapacitors.

5.3.8 Pt- and TCO-Free DSSC Counter Electrode Application

Dye sensitized solar cell^[42] utilizes costly Pt coated FTO for the tri-iodide reduction in the counter electrode. Thus, Pt- and TCO-free flexible counter electrodes are highly desirable to make cost-effective flexible DSSCs. As PEDOT is known for its high catalytic activity towards tri-iodide reduction^[43], our flexible PEDOT papers have excellent potential to use as Pt- and TCO-free electrode^[44]. All the characterizations stated below are exclusively done on the PEDOT paper without using any conducting substrate. Tri-iodide catalytic properties were initially screened using CV measurement in 0.1 M LiClO₄ electrolyte containing 5 mM LiI and 0.5 mM I₂. A 3-electrode set-up was used for the CV measurements, in which PEDOT-p was used as the working electrode and Pt wire which was internally calibrated using ferrocene/ferrocenium (Fc/Fc⁺) couple was used as the reference electrode. A Pt foil was used as the counter electrode. Figure 5.13a shows the CV profiles of PEDOT-p-3 to PEDOT-p-5 recorded at a scan rate of 10 mV s⁻¹. As indicated in Figure 5.13a, the first redox peaks correspond to the I⁻/I₃⁻ redox couple and the second one corresponds to the I₃⁻/I₂ couple. Among the various samples, PEDOT-p-4 possesses the highest reduction current as well as the lowest difference between the potential at the current maxima of reduction and oxidation peak for the I⁻/I₃⁻ couple, which are characteristics of the high catalytic activity towards the tri-iodide reduction^[45]. Further, square root of the scan rate has a linear relationship with the peak current density in the case of PEDOT-p-4 (Figure 5.13b & 5.13c), indicating the involvement of a diffusion limited reaction and absence of any interaction of ions with the substrate^[46]. Thus, PEDOT-p-4 is the right candidate for deploying as the counter electrode in real DSSC measurements.

Before going to a real cell, the activity of PEDOT-p-4 was further confirmed by using Tafel polarisation using symmetric cell (details are presented in the experimental section) at a scan rate of 10 mV s⁻¹ (Figure 5.13d). It can be seen that PEDOT-p-4 displays similar limiting current as that of the standard Pt coated FTO

(Pt/FTO). However, the exchange current density, which is measured at a lower overpotential, is high for Pt/FTO (2.2 mA cm^{-2}) than PEDOT-p-4 (1.2 mA cm^{-2})^[47]. This deviation arises due to the movement of I_3^- and I^- inside the PEDOT matrix during the redox reaction, which is hampering the electrical conductivity of PEDOT.

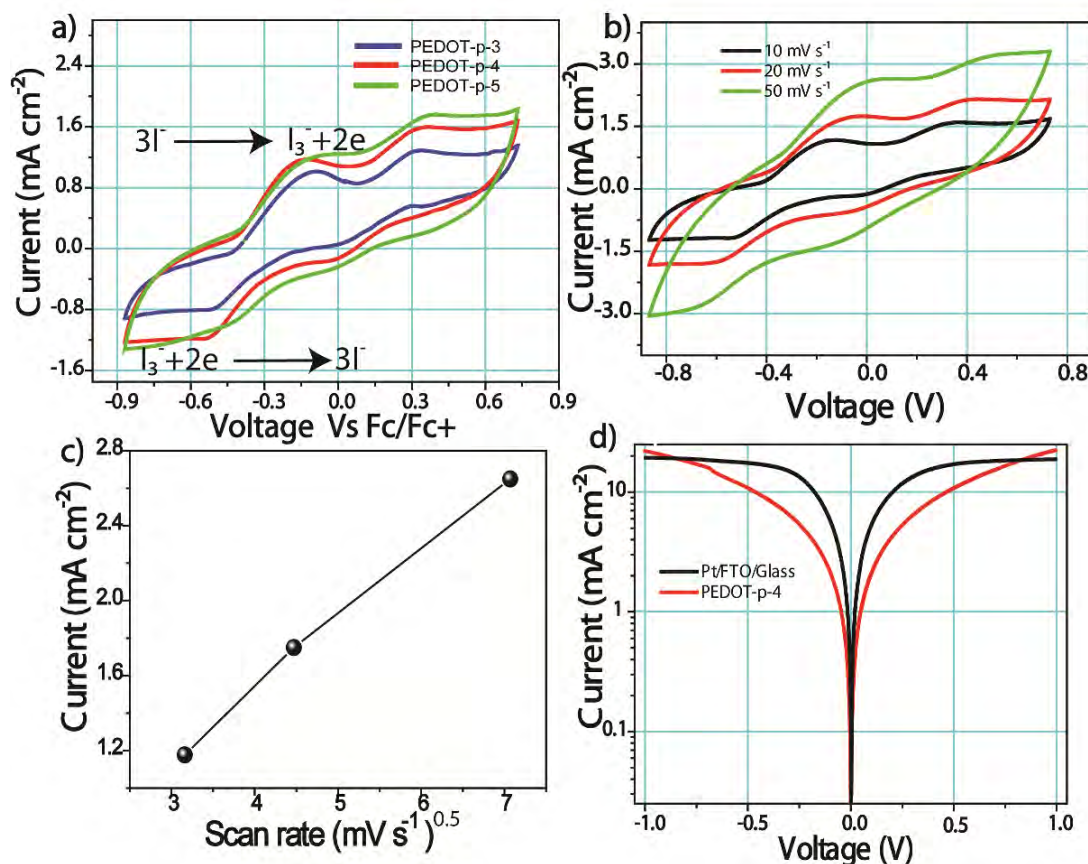


Figure 5.13: a) CV profiles recorded at a scan rate of 10 mV s^{-1} , b) CV profiles of PEDOT-p-4 at various scan rates, c) the plot corresponding to the root square of scan rate vs. peak current and d) Tafel polarization plots in the asymmetrical dummy cell.

A real DSSC cell was fabricated using PEDOT-p-4 as the counter electrode and FTO/TiO₂/Dye as the working electrode (details of the cell fabrication are given in the experimental section). Cell's I - V polarisation plots are given Figure 5.14 and the values extracted from the polarization data are presented in Table 5.3. An overall solar conversion efficiency of 6.5 % has been obtained for the system derived from PEDOT-p-4 compared to 7.0 % efficiency displayed by the system having Pt/FTO as the counter electrode. Coming to the individual parameters, PEDOT-p-4 based system shows a high fill factor of 66 % compared to 62 % of the system made from Pt/FTO, indicating the high catalytic activity of the system. However, lower short circuit current density (J_{sc}) of 13 mA cm^{-2} of PEDOT-p-4 in comparison to 15 mA cm^{-2} of Pt

deleteriously affects the overall efficiency of the present flexible counter electrode. Lower open circuit potential (OCV) and low J_{sc} arise as there is no external current collector, rather the catalyst should play the dual role of I_3^- reduction and charge mobility. However, the presented flexible material is still promising as its catalytic activity is comparable with that of the costly Pt coated FTO. Thus, PEDOT-p-4 shows great potential to replace Pt and TCO from the counter electrode. Among the different PEDOT papers, in accordance with the CV data, PEDOT-p-4 shows superior activity.

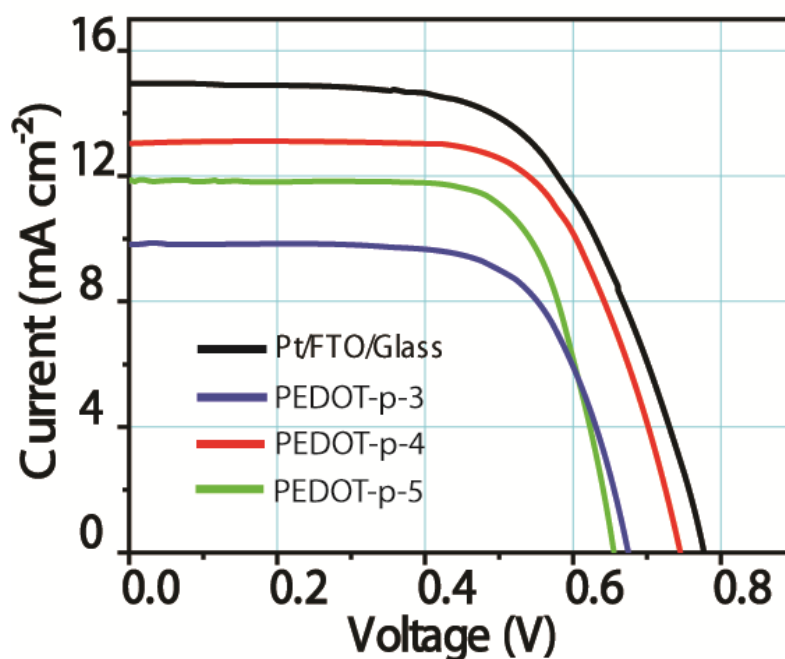


Figure 5.14: I-V profiles of the DSSC with the various PEDOT papers prepared as the counter electrode.

Table 5.3: Parameters extracted from the I-V plots.

Sample	Voc	Fill Factor	Jsc mA cm ⁻²	% Efficiency
PEDOT-p-3	0.67	68.36	9.83	4.53
PEDOT-p-4	0.74	66.45	13.06	6.46
PEDOT-p-5	0.66	70.50	11.86	5.55
Pt/FTO	0.77	61.12	14.94	7.09

5.4 Conclusion

A simple and novel strategy to make a highly conducting PEDOT paper has been developed by manipulating interfacial polymerization at the interface of two immiscible liquids. The process explained here is highly scalable and easy enough to make large PEDOT papers within 2-3 hours. The polymerized PEDOT phase on the paper possesses fibrous structure with more compacted π -conjugated chains and doping level due to the slow polymerization rate and increased polarity of the solvent interface. The paper displays a conductivity value as high as 375 S cm^{-1} and significantly low sheet resistance of $3 \Omega/\square$. The electrical and mechanical properties of the paper are found to be stable even under flexing and bending conditions. A flexible all-solid-state supercapacitor made from the device using PVA- H_2SO_4 gel electrolyte possesses a thickness of 0.17 mm and this system could deliver a power density of 1 mWh cm^{-3} . The flexible devices are found to be very stable during the charge-discharge cycling under twisted and bending conditions for more than 3800 cycles. Apart from the supercapacitor application, DSSC made from the PEDOT-p based counter electrode shows a high conversion efficiency of 6.5 % in comparison with 7% of Pt/FTO as the counter electrode. Even though only two applications are shown here for the PEDOT paper, it can be further extended for various flexible applications like Li-ion battery, sensors etc. owing to its simple and scalable method of preparation and great potential to serve as a highly conducting flexible substrate.

5.5 Reference

- [1] (a) L. Nyholm, G. Nyström, A. Mihranyan, M. Strømme, *Adv. Mater.* **2011**, *23*, 3751-3769; (b) X. Wang, X. Lu, B. Liu, D. Chen, Y. Tong, G. Shen, *Adv. Mater.* **2014**, *26*, 4763-4782.
- [2] F. Meng, Y. Ding, *Adv. Mater.* **2011**, *23*, 4098-4102.
- [3] L. Yuan, X. Xiao, T. Ding, J. Zhong, X. Zhang, Y. Shen, B. Hu, Y. Huang, J. Zhou, Z. Wang, *Angew. Chem. Int. Ed.* **2012**, *51*, 4934-4938.
- [4] S. K. Balasingam, M. G. Kang, Y. Jun, *Chem. Commun.* **2013**, *49*, 11457-11475.
- [5] R. H. Baughman, A. A. Zakhidov, W. A. de Heer, *Science* **2002**, *297*, 787-792.
- [6] K. S. Novoselov, V. I. Falko, L. Colombo, P. R. Gellert, M. G. Schwab, K. Kim, *Nature* **2012**, *490*, 192-200.
- [7] H. Dai, *Acc. Chem. Res.* **2002**, *35*, 1035-1044.
- [8] S. Guo, S. Dong, *Chem. Soc. Rev.* **2011**, *40*, 2644-2672.
- [9] (a) G. A. Snook, P. Kao, A. S. Best, *J. Power Sources* **2011**, *196*, 1-12; (b) K. Gurunathan, A. V. Murugan, R. Marimuthu, U. P. Mulik, D. P. Amalnerkar, *Mater. Chem. Phys.* **1999**, *61*, 173-191; (c) A. O. Patil, A. J. Heeger, F. Wudl, *Chem. Rev.* **1988**, *88*, 183-200.
- [10] S. Kirchmeyer, K. Reuter, *J. Mater. Chem* **2005**, *15*, 2077-2088.
- [11] Y. Wang, *Journal of Physics: Conference Series* **2009**, *152*, 012023.
- [12] (a) B. Anothumakkool, O. Game, S. N. Bhange, T. Kumari, S. B. Ogale, S. Kurungot, *Nanoscale* **2014**, *6*, 10332-10339; (b) K.-M. Lee, P.-Y. Chen, C.-Y. Hsu, J.-H. Huang, W.-H. Ho, H.-C. Chen, K.-C. Ho, *J. Power Sources* **2009**, *188*, 313-318.
- [13] J. C. Carlberg, O. Inganas, *J. Electrochem. Soc.* **1997**, *144*, L61-L64.
- [14] (a) J. Kim, E. Kim, Y. Won, H. Lee, K. Suh, *Synth. Met.* **2003**, *139*, 485-489; (b) J. P. Lock, S. G. Im, K. K. Gleason, *Macromolecules* **2006**, *39*, 5326-5329.
- [15] (a) H. Randriamahazaka, G. Sini, F. Tran Van, *J. Phys. Chem. C* **2007**, *111*, 4553-4560; (b) S. I. Cho, S. B. Lee, *Acc. Chem. Res.* **2008**, *41*, 699-707.
- [16] J. L. Brédas, R. Silbey, *Conjugated Polymers: The Novel Science and Technology of Highly Conducting and Nonlinear Optically Active Materials*, Springer Netherlands, **1991**.
- [17] C. R. Martin, *Acc. Chem. Res.* **1995**, *28*, 61-68.
- [18] L. D. Tsai, Y. C. Du, Oxidizing agent useful for oxidative polymerization of high conductive polymers, US20100099889 A1, **2010**.
- [19] (a) T. Truong, N. Luong, J.-D. Nam, Y. Lee, H. Choi, J. Koo, H. Nguyen, *Macromol. Res.* **2007**, *15*, 465-468; (b) K. S. Lee, H. K. Lee, D. H. Wang, N. G. Park, J. Y. Lee, O. O. Park, J. H. Park, *Chem Commun (Camb)* **2010**, *46*, 4505-4507.

- [20] N. Nuraje, K. Su, N.-I. Yang, H. Matsui, *ACS Nano* **2008**, *2*, 502-506.
- [21] (a) J. A. Lee, M. K. Shin, S. H. Kim, S. J. Kim, G. M. Spinks, G. G. Wallace, R. Ovalle-Robles, M. D. Lima, M. E. Kozlov, R. H. Baughman, *ACS Nano* **2011**, *6*, 327-334; (b) J. M. D'Arcy, M. F. El-Kady, P. P. Khine, L. Zhang, S. H. Lee, N. R. Davis, D. S. Liu, M. T. Yeung, S. Y. Kim, C. L. Turner, A. T. Lech, P. T. Hammond, R. B. Kaner, *ACS Nano* **2014**, *8*, 1500-1510.
- [22] D. Alemu Mengistie, P.-C. Wang, C.-W. Chu, *J. Mater. Chem. A* **2013**, *1*, 9907-9915.
- [23] (a) M. Dobbelin, R. Marcilla, C. Tollan, J. A. Pomposo, J.-R. Sarasua, D. Mecerreyes, *J. Mater. Chem* **2008**, *18*, 5354-5358; (b) H.-E. Yin, F.-H. Huang, W.-Y. Chiu, *J. Mater. Chem* **2012**, *22*, 14042-14051; (c) T. Darmanin, M. Nicolas, F. Guittard, *Phys. Chem. Chem. Phys.* **2008**, *10*, 4322-4326.
- [24] (a) V. Švorčík, P. Slepíčka, J. Švorčíková, M. Špírková, J. Zehentner, V. Hnatowicz, *J. Appl. Poly. Sci.* **2006**, *99*, 1698-1704; (b) J. Mizsei, P. Sipilä, V. Lantto, *Sens. Actuators, B* **1998**, *47*, 139-144.
- [25] S. Andersson, H. Wikberg, E. Pesonen, S. Maunu, R. Serimaa, *Trees* **2004**, *18*, 346 - 353.
- [26] (a) K. E. Aasmundtveit, E. J. Samuelsen, O. Inganas, L. A. A. Pettersson, T. Johansson, S. Ferrer, *Synth. Met.* **2000**, *113*, 93-97; (b) T. Y. Kim, J. E. Kim, K. S. Suh, *Polym. Int.* **2006**, *55*, 80-86; (c) T. Kawai, M. Nakazono, K. Yoshino, *J. Mater. Chem* **1992**, *2*, 903-906.
- [27] (a) H. G. S. J. Joo, Y. C. Chung and J. S. Baeck, *J. Korean Phys. Soc.* **1997**, *30*, 230-236; (b) J. L. Brédas, J. P. Calbert, D. A. da Silva Filho, J. Cornil, *Proceedings of the National Academy of Sciences* **2002**, *99*, 5804-5809.
- [28] D. G. Castner, K. Hinds, D. W. Grainger, *Langmuir* **1996**, *12*, 5083-5086.
- [29] N. Sakmeche, S. Aeiyaeh, J.-J. Aaron, M. Jouini, J. C. Lacroix, P.-C. Lacaze, *Langmuir* **1999**, *15*, 2566-2574.
- [30] W. W. Chiu, J. Travaš-Sejdić, R. P. Cooney, G. A. Bowmaker, *Synth. Met.* **2005**, *155*, 80-88.
- [31] T. L. Zhang, H. Y. Chen, C. Y. Su, D. B. Kuang, *J. Mater. Chem. A* **2013**, *1*, 1724-1730.
- [32] G. Tourillon, F. Garnier, *The Journal of Physical Chemistry* **1983**, *87*, 2289-2292.
- [33] A. G. MacDiarmid, A. J. Epstein, *Synth. Met.* **1995**, *69*, 85-92.
- [34] S. Garreau, G. Louarn, J. P. Buisson, G. Froyer, S. Lefrant, *Macromolecules* **1999**, *32*, 6807-6812.
- [35] (a) J. Huang, S. Virji, B. H. Weiller, R. B. Kaner, *J. Am. Chem. Soc.* **2002**, *125*, 314-315; (b) J. Huang, R. B. Kaner, *J. Am. Chem. Soc.* **2003**, *126*, 851-855.

- [36] (a) U. Sree, Y. Yamamoto, B. Deore, H. Shiigi, T. Nagaoka, *Synth. Met.* **2002**, *131*, 161-165; (b) X. Feng, H. Huang, Q. Ye, J.-J. Zhu, W. Hou, *J. Phys. Chem. C* **2007**, *111*, 8463-8468.
- [37] (a) X.-G. Li, J. Li, Q.-K. Meng, M.-R. Huang, *J. Phys. Chem. B* **2009**, *113*, 9718-9727; (b) C. Bora, R. Pegu, B. J. Saikia, S. K. Dolui, *Polym. Int.* **2014**, *63*, 2061-2067.
- [38] (a) J. Jang, M. Chang, H. Yoon, *Adv. Mater.* **2005**, *17*, 1616-1620; (b) J. Jang, J. Bae, E. Park, *Adv. Mater.* **2006**, *18*, 354-358; (c) H. Mao, X. Liu, D. Chao, L. Cui, Y. Li, W. Zhang, C. Wang, *J. Mater. Chem* **2010**, *20*, 10277-10284; (d) H. Yoon, M. Chang, J. Jang, *Adv. Funct. Mater.* **2007**, *17*, 431-436.
- [39] K. Su, N. Nuraje, L. Zhang, I. W. Chu, R. M. Peetz, H. Matsui, N. L. Yang, *Adv. Mater.* **2007**, *19*, 669-672.
- [40] (a) B. Anothumakkool, A. T. A. Torris, S. N. Bhange, S. M. Unni, M. V. Badiger, S. Kurungot, *ACS Appl Mater Interfaces* **2013**, *5*, 13397-13404; (b) B. Anothumakkool, A. T. A. Torris, S. N. Bhange, M. V. Badiger, S. Kurungot, *Nanoscale* **2014**, *6*, 5944-5952.
- [41] C. Meng, C. Liu, L. Chen, C. Hu, S. Fan, *Nano Letters* **2010**, *10*, 4025-4031.
- [42] B. O'Regan, M. Gratzel, *Nature* **1991**, *353*, 737-740.
- [43] (a) J. M. Pringle, V. Armel, D. R. MacFarlane, *Chem Commun (Camb)* **2010**, *46*, 5367-5369; (b) B. Anothumakkool, O. Game, S. N. Bhange, T. Kumari, S. B. Ogale, S. Kurungot, *Nanoscale* **2014**, *6*, 10332-10339.
- [44] (a) M. Vosgueritchian, D. J. Lipomi, Z. Bao, *Adv. Funct. Mater.* **2012**, *22*, 421-428; (b) S. Ahmad, E. Dell'Orto, J. H. Yum, F. Kessler, M. K. Nazeeruddin, M. Gratzel, *Chem Commun (Camb)* **2012**, *48*, 9714-9716; (c) Y. Wang, M. Wu, X. Lin, Z. Shi, A. Hagfeldt, T. Ma, *J. Mater. Chem* **2012**, *22*, 4009-4014.
- [45] J. D. Roy-Mayhew, D. J. Bozym, C. Punckt, I. A. Aksay, *ACS Nano* **2010**, *4*, 6203-6211.
- [46] Y.-M. Xiao, J.-Y. Lin, J.-H. Wu, S.-Y. Tai, G.-T. Yue, *Electrochim. Acta.* **2012**, *83*, 221-226.
- [47] F. Gong, H. Wang, X. Xu, G. Zhou, Z. S. Wang, *J Am Chem Soc* **2012**, *134*, 10953-10958.

Chapter-6

Summary and Conclusions

This chapter gives an overview of the main observations and conclusion of the different chapters presented in the thesis. Initially, the context of the thesis is



presented where the evolution of the thesis over the theme of 1-D supported materials is narrated. Later, conclusions and main findings of each chapter are overviewed in separate sections.

Conclusions of each chapter contain relevance of each section separately and how they are connected to the main theme of the thesis, *i.e.* 1-D supported nanostructured materials. Further, each section is briefed with some of the important results of supercapacitor and DSSC devices and their performance characteristics in practical conditions. Final part is dedicated to the discussion on the future prospects of the present thesis. This includes a discussion on the importance of the present thesis in terms of the extended applications of the materials evolved, device fabrication methodologies adopted and their scope of improvements etc.

6.1 Summary

Renewable alternatives for the fossil fuels are indispensable requirements of sustainable living for a better tomorrow. However, intermittent nature of such renewable energy sources imposes incorporation of highly efficient energy conversion and storage devices as an inevitable requirement of the power electronics meant for such systems. Among the various energy storing devices, the electrochemical storage and conversion devices are of prime importance, which include batteries, supercapacitors, dye-sensitized solar cells (DSSCs) etc. Heart of such a system comprises a highly active and efficient electrode-electrolyte interface, which requires facile ionic and electron transport throughout the materials in use. Nanosizing of materials, which forms extended interfaces in the above devices, is promising at this context as it imposes tunable physical and chemical properties. However, nanostructuring typically results in low electric and ionic conductivity along with stability. An ingenious way to overcome the low electric and ionic conductivity along with stability is with the help of a support material which comprises high conductivity and surface area. Among the various supported materials, 1-dimensional (1-D) structure holds superior advantages such as higher surface area with continuous electron path and facile ion transport etc. Such confined conducting fibers/tubes can be utilized to grow active materials with tunable morphology and multifunctional properties along with augment in conductivity, low charge transfer resistance and improved stability. Apart from that, high surface area with the 1-D structure provides easy ion flux and buffer volume between the structures, which alleviates the mechanical stress for the materials. Importantly, no need of external binder and conducting ingredients help to reduce the cost of the devices. The present thesis has addressed some of the issues related to the low electrode-electrolyte interfaces of supercapacitors and CEs for DSSCs by utilising various 1-D carbon supported nanomaterials. Further, efficient solid-state supercapacitors could be fabricated with the same strategy by utilising the 1-D carbon support owing to its ability to form better interfaces with the electrolytes. Finally, the future flexible electronic devices require flexibility as an important criterion for the above energy devices which demands highly efficient flexible electrode materials. An important progress in this direction could be made during the course of the work by developing a simple and

scalable method for preparing highly conducting and flexible electrodes, which showed their utilization in flexible applications involving supercapacitor and DSSC.

The major accomplishments of the present thesis are summarised as below:

1-D confinement of PEDOT using hollow carbon nanofibers: an efficient charge storage material with high catalytic activity for tri-iodide reduction in DSSC.

Among the various conducting polymers which are widely essayed in literature, PEDOT has emerged as a promising material in various energy devices, especially as an “active material” for the energy storage devices and counter electrode for DSSCs. However, the reported electrochemical activity of bulk PEDOT prepared by various methods is significantly low due to its reduced surface area, difficulties associated with low conductivity and low stability. Establishing both nanomorphology of PEDOT and better mechanical stability to the system are important for improving the electrochemical properties and to attain overall durability. This section of the thesis deals with a synthetic strategy of PEDOT which could be developed in order to overcome the drawbacks of the bulk PEDOT such as fast polymerization rate, low conductivity, low surface area and low stability. This is achieved by 1-D aligning of PEDOT over a high aspect ratio carbon nanofiber (CNF). This method offers unique nano architecture for PEDOT by providing mechanically stable and electrically conductive CNF as the core material and by concomitantly maintaining both high aspect ratio and interfacial areas. Formation of PEDOT as a thin layer improves the electrical conductivity and the aligned growth along the surfaces of CNF provides well defined pathways for faster movement of ions in and out of the polymer matrix. Since the tubular morphology of the CNF with its open tips provides facile routes for the electrolyte, the overall utilization of the active surface and conductivity increases the charge storage properties. Facile ionic and electric mobility *via* 1-D alignment of PEDOT helps the system to achieve high capacitance retention at high current drag which indicates its high power capability. Moreover, the stable CNF backbone helped to avoid the stress during the stability cycling, leading to excellent cycling stability. Further, electrocatalytic tri-iodide reduction of 1-D PEDOT/CNF is also found to be superior due to the high electrical conductivity, surface area and facile ion diffusion which were characterized by CV, impedance and Tafel measurements. Lastly, DSSCs made out of 1-D PEDOT as CE showed superior conversion efficiency and stability

compared to the CEs based on the bench mark Pt, bulk PEDOT and CNF.

Active interface tuning of solid-state supercapacitor: Studies with carbon fiber supported conducting polymers

Polymer electrolytes have been extensively studied as electrolytes in supercapacitors and lithium batteries in place of liquid electrolytes. Replacement of the liquid electrolyte in the energy storage devices with a solid counterpart is thus very promising for developing safe, thin, light-weight, economically viable and flexible future devices. Many of the earlier studies have utilized gel electrolytes as solid electrolytes in the form of a film between the electrodes, which resulted in low electrode-electrolyte interfacial area and higher ESR for the devices. In the present work, in order to address the low interface and high ESR of the solid-state supercapacitors, the high porosity of a conducting carbon paper and tunable viscosity characteristics of the gel electrolyte are exploited. The well penetrated PVA-H₂SO₄ network along the polyaniline (PANI) coated porous carbon matrix essentially enhanced the electrode-electrolyte interface of the resulting device leading to a very low ESR by establishing an interfacial structure very similar to a liquid electrolyte. Cross-sectional elemental mapping and SEM images display the proof of concept. Apart from acting as an enhanced interface, the porous carbon backbone gives an adequate electrical contact within the network, which helps in maintaining very low ESR. The capacitance obtained was much superior than the conventional film based solid-state supercapacitors. Apart from the higher capacitance, excellent retention in capacitance at high current drag and superior stability were also found in the devices. Using the above experiments, demonstration of the importance of porosity in the electrode for establishing enhanced interfacial network in solid-state supercapacitors for achieving high charge-storage properties also could be completed. However, one challenge noticed here was that, at higher mass loading of the electro-active material, the performance of the solid-state device becomes inferior to its liquid-state counterpart as the polymer infiltration becomes improper under such conditions. To address this issue, a different strategy of electrodepositing the charge storage material directly onto a porous carbon current collector is adopted, which ensures a highly reproducible coating of the electro-active material over the each carbon fiber backbone. Due to the low stability and low electrochemical window of PANI, the

selected electrode material in the case is polyethylenedioxythiophene (PEDOT). The peculiar morphology of the electrodeposited PEDOT and its alignment led to enhanced surface area and electrical conductivity, and the pores in the system enabled effective intercalation of the polymer–gel electrolyte. Consequently, the solid device attained very low internal resistance and a high specific capacitance for PEDOT even with high mass loading. The performance of the device was consistent even under wide-ranging humidity and temperature conditions. Finally, a device fabricated by increasing the electrode area four times was used to light an LED, which validated the scalability of the process.

Electrochemically grown MnO₂ nanowall forest on a carbon fiber substrate as a supercapacitor charge storage material

Replacing active carbon with various metal oxides, especially with less costly and environmentally friendlier MnO₂, is looking promising due to their high potential storage capacities (1200 F g⁻¹) and large potential window (1–1.6 V). However, due to low electrical and ionic conductivity, bulk MnO₂ delivers low mass specific capacitance (100–200 F g⁻¹). In particular, a thick coating of MnO₂ on a plain current collector leads to the majority of the bulk MnO₂ being inaccessible for electrons as well as ions in the electrolyte. As a solution to the above problems, the thesis deals with an approach involving electrochemically synthesizing highly uniform MnO₂ porous nanowalls directly onto a conducting porous carbon fiber paper without employing any templates. The structure of the material deposited is elucidated by XRD, Raman and XPS analyses indicating birnessite-type structure of MnO₂ with some amount of Mn₃O₄ as well. The peculiar growth pattern of the vertical MnO₂ walls, which are microporous concomitantly, provided spacious and accessible corridors along the surface, which act as facile channels for ion transport after electrolyte filling. At the same time, the carbon fiber backbone helped to overcome the issue of the inherent electrical resistance associated with MnO₂. Thus, the formed electrode appeared to display a specific capacitance as high as 1149 F g⁻¹ at a dragging current of 1 A g⁻¹ and the electrode retained a capacitance of 565 F g⁻¹ even at high current dragging conditions of 100 A g⁻¹. Even after 8000 continuous cycles, the nanowalls appeared to be structurally stable with no significant degradation in capacitance. Further, high porosity of the MnO₂ nanowall electrodes is utilised to make a solid-state supercapacitor. Due to the enhanced electrode-electrolyte interface

owing to the high porosity of the nanowalls, the solid-state devices displayed excellent capacitance and low ESR even at high current drag conditions.

Novel scalable synthesis of highly conducting and robust PEDOT paper for high performance flexible supercapacitor and dye sensitized solar cell

Future flexible and light weight electronic and electrical gadgets demand flexibility and weight reduction in the energy managing devices. Lack of flexibility in the present commercial supercapacitors imposes major restrictions in integrating such systems with the future electronic and electric devices. Exchange of the individual key components such as current collector, electrode material as well as the electrolyte with lighter and flexible alternatives is the key to the success of such device systems. However, this transformation to flexibility and lighter qualities always accompanies with compromise in conductivity and charge storage properties of the components due to the trade-off between form/property tolerance accommodation and functionality therein. A single material possessing both high charge storage property, conductivity and flexibility will be promising in this context as it can play the role of both current collector and an electrode material, which results in flexible, lighter, thinner, and cheaper energy devices. This approach is very challenging in the present situation due to the lack of materials which possess the required conductivity, flexibility and capacitance concomitantly. To address this, a novel synthetic strategy is developed to prepare a highly conducting polyethylenedioxythiophene (PEDOT) phase on flexible cellulose paper formed by inducing surfactant-free interfacial polymerization at the interface of two immiscible liquids. The illustrated process is highly scalable in such a way that very large flexible PEDOT paper can be prepared in 2-3 h under laboratory conditions. The obtained PEDOT-paper possesses efficiently packed π -conjugated chains and increased doping level which is proven by XRD, XPS, conductivity and UV-visible measurements. This favourable change has been attained by the slow polymerization coupled with the high di-electric constant of the interface, which stabilises the counter ions through hydrogen bonding. This helps for better inter-chain and intra-chain charge mobility, leading to high conductivity compared to the PEDOT prepared in n-butanol. A low sheet resistance of $3 \Omega/\square$ is achieved by multiple coating, which is found to be stable even after two months under ambient conditions and at various flexible and bending conditions. A flexible solid-state

supercapacitor with an overall thickness of 0.17 mm made from the PEDOT paper and PVA-H₂SO₄ as the solid electrolyte delivered a volumetric energy density of 1 mWh cm⁻³. The flexible device was found to be very stable during the charge-discharge cycling under twisted and bending conditions. A 3.6 V inter-digitised flexible device also could be made in a single PEDOT paper, which is found to be powered enough to glow an LED under flexible conditions. Apart from the supercapacitor application, a dye sensitised solar cell (DSSC) made by using the PEDOT paper without any conducting current collector as the counter electrode shows a comparable conversion efficiency with the costly Pt/FTO.

6.2 Future Prospects

The present thesis has wide potential impact in both fundamental as well as applied research in energy devices due to the unique properties of the materials and methodologies developed during the course of the research work. Some of the key prospects of the thesis are listed below.

Though the current research activities on enhancing the electrode-electrolyte interface *via* 1-D hetero-structured materials as detailed in the thesis are restricted to only supercapacitors and DSSCs, the observations, materials and methodologies have wide impact and potential in other energy devices such as Li-ion batteries, fuel cells, photoelectrochemical cells, sensors etc. The effect of 1-D confinement of PEDOT and its concomitant increment on surface area, conductivity and stability show its prospects for practical applications in other electrochemical devices such as a cathode material in Li-ion batteries and humidity and conductivity sensors. Further, this approach can be utilised to confine other materials 1-dimensionally by employing the inherent hollow core structure of carbon nanofiber. Such type of confinement can result in facile charge transport as proved in Chapter-1. However, more fundamental research is required to unravel the synergic effect which helped in improving the conductivity of the 1-D CNF/PEDOT compared to the individual materials. Nevertheless, we could able to give some insight of slow polymerisation as one of the important contributing factors in attaining better π -chain, leading to better inter-chain charge hopping as described in Chapter-5.

The methodologies used to make the solid-state supercapacitors with infiltrated polymer electrolyte have potential applications in Li-ion battery as well. Especially,

the polymer Li-ion battery is preferred over the liquid systems due to the safety issues. The strategy of usage of the porous electrode and intercalation of Li-conducting polymer electrolyte can result in excellent efficiency and stability for the battery. Further, the method of electro-deposition of conducting polymer and metal oxide as showed in Chapter-3 and Chapter-4 can be utilised to various other group members of the polymers and oxides by targeting activity modulations for various energy applications. Especially, MnO_2 has the potential applications in the areas of fuel cells and electrolysers.

Chapter-5 showed the potential application of the PEDOT-paper *via* a surfactant-free method having excellent conductivity and flexibility. Such a stable low sheet resistance for a thin and flexible substrate can have wide impact in various flexible applications including photovoltaics, sensors, batteries etc. Further, unravelling of the chemistry behind the enhanced conductivity for the PEDOT films resulted from the aligned π -chain and higher doping level will help to develop effective design strategies for conducting polymers to make use in various practical applications.

List of Publications

Patent Filed

- 1) A novel approach in the design of electrode-electrolyte interface towards high a performance all-solid-state-supercapacitor with very low ESR. **WO2014170912-A1 and PCT/IN2014/000233**
- 2) Surfactant free interfacial polymerization of PEDOT through simple roll coating: scalable method for current collector-free flexible thin supercapacitor and TCO-free DSSC counter electrode. **3863-DEL-2014 filing date 23.12.2014**
- 3) *In-situ* polymer generation inside the electrode pores for improved interface **(2015-INV-0058)**

Journal Articles

- 1) “Surfactant-Free Interfacial Polymerization of PEDOT through Simple Roll Coating: Scalable Method for Flexible, Conducting Substrate for Flexible Solid-state-supercapacitor”. **B. Anothumakkool**, R. Soni, S N. Bhangé & S. Kurungot (*Energy and Environmental Science*, **2015**, *8*, 1339 - 1347)
- 2) “Electrochemically grown nanoporous MnO₂ nanowall forest on porous carbon substrate with enhanced capacitance through faster ionic and electrical mobility” **B. Anothumakkool**, S. Kurungot (*Chem. Commun*, **2014**, 50 (54), 7188 - 7190)
- 3) “Enhanced Catalytic Activity of Polyethylenedioxythiophene towards Triiodide Reduction in DSSC via 1-Dimensional Alignment Using Hollow Carbon Nanofiber”. **B. Anothumakkool**, O. Game, S N. Bhangé, T. Kumari, S B. Ogale and S. Kurungot (*Nanoscale*, **2014**, *6*, 10332-10339)
- 4) “Electrodeposited Polyethylenedioxythiophene with Infiltrated Gel Electrolyte Interface: A Close Contest of an All-Solid-State Supercapacitor with its Liquid-State Counterpart”. **B. Anothumakkool**, A Torris A. T, S N. Bhangé, S M. Unni, M V. Badiger and S. Kurungot (*Nanoscale*, **2014**, *6* (11), 5944 - 5952)
- 5) “From waste paper basket to solid state and Li-HEC ultracapacitor electrodes: A value added journey for shredded office paper”. P. Dhanya, V. Aravindan,

- B. Anothumakkool**, S. Kurungot, S. Madhavi, and S. Ogale (*Small*, **2014**, 10 (21), 4395–4402)
- 6) “A unique strategy in the design of a high performance thin all-solid-state supercapacitor mimicking the active interface of its liquid-state counterpart” **B. Anothumakkool**, A. Torris A. T, S N. Bhange, S M. Unni, M V. Badiger and S. Kurungot (*ACS Appl. Mater. Interfaces*, **2013**, 5 (24), 13397–13404)
- 7) “1-Dimensional confinement of porous polyethylenedioxythiophene using carbon nanofibers as a solid template: an efficient charge storage material with improved capacitance retention and cycle stability”. **B. Anothumakkool**, S N. Bhange, S M. Unni and S. Kurungot (*RSC Adv*, **2013**, 3, 11877-11887)
- 8) “Anchored 3-D polyaniline inside pillared graphene: Enhanced interface joined with high conductivity for better charge storage applications”. Sekar Pandiaraj, **B. Anothumakkool**, and S. Kurungot (*ACS Appl. Mater. Interfaces* **2015**, 7, 7661–7669)
- 9) “Water mediated Proton Conduction in an Amine Functionalized H-bonded 3D Ionic Framework” B. Manna, **B. Anothumakkool**, A. V. Desai, S. Kurungot and S K. Ghosh (*ACS Inorganic Chemistry* 2015, Just accepted).
- 10) “From waste paper basket to solid state and Li-HEC ultracapacitor electrodes: A value added journey for shredded office paper”. P. Dhanya, V. Aravindan, **B. Anothumakkool**, S. Kurungot, S. Madhavi, and S. Ogale (*Small*, **2014**, 10 (21), 4395–4402)
- 11) “Redox-Mediated Synthesis of Functionalised Graphene: A Strategy towards 2D Multifunctional Electrocatalysts for Energy Conversion Applications” S M. Unni, S N. Bhange, **B. Anothumakkool**, S. Kurungot (*Chem Plus Chem*, **2013**, 78, 1296–1303)
- 12) “Tuning of multiple luminescence output and white-light emission from a single gelator molecule through ESIPT coupled AIEE process” A. Maity, F. Ali, H. Agarawal, **B. Anothumakkool** and A. Das (*Chem. Commun*, **2015**, 51, 2130-2133).
- 13) “Pt- and TCO-free flexible cathode for DSSC from highly conducting and flexible PEDOT paper prepared via in-situ interfacial polymerisation”. **B. Anothumakkool**, O. Game, S. N. Bhange, R. Soni, I. Agrawal, S. B. Ogale and S. Kurungot (communicated)

- 14) *In-situ* polymer electrolyte generation inside the nanopores of carbon electrode: Facile method to improve the efficiency of solid-state supercapacitor. **B. Anothumakkool**, A. Torris A, Sajna V., Vidyanand V., M V. Badiger & S. Kurungot (under preparation)
- 15) “A chemically stable crystalline metal-organic framework containing water-hydroxide supramolecular chain exhibiting high hydroxide conductivity”. Sanjog Nagarkar, **B. Anothumakkool** , A. Desai, M. Shirolkar , S. Kurungot and Sujit Ghosh (communicated)
- 16) “Surface modification of Buckypaper through interfacial polymerisation of polymer: Towards high energy density, thin solid-state supercapacitor” R. Soni, **B. Anothumakkool** and S. Kurungot (Under preparation)

Erratum